Aeroelastic Analysis of Turbulent Rotor Flows

Thesis submitted in accordance
with the requirements of
the University of Liverpool for
the degree of Doctor of Philosophy
by

Florent Dehaeze

January 2012

Declaration

I hereby declare that this dissertation is a record of work carried out in the School of Engineering at the University of Liverpool during the period from January 2008 to January 2012. The dissertation is original in content except where otherwise indicated.

January 2012

(Florent Dehaeze)

Abstract

This thesis is devoted to the study of rotor flows. A literature survey suggested that possible improvements can be achieved via better simulation of turbulence and prediction of the elastic blade deformation. While the limits of the currently used URANS turbulence models have been shown, accurate predictions can only be achieved if the blade elasticity is taken account due to the large deformations a rotor blade can undergo in flight.

An aeroelastic coupling strategy consists in three steps: computing the flow field, computing the structural deformation and transferring data between the CFD and CSD solvers. The transfer method also needs to deal with the different sizes for the structural and aerodynamic models. Most challenges come from the need to modify the CFD mesh following the blade deformation, and are linked to the higher refinement of the CFD grid. To tackle the problem, a new hybrid mesh deformation technique, adapted to rotor in-flight deformations was developed for the Helicopter Multi-Block solver of Liverpool. Demonstration of the method was presented for multiple test cases: hovering HART-II rotors and forward flying ONERA 7A and HART-II rotors. The method proved quick at deforming the mesh and able to deal with large rotor deformations without downgrading the mesh quality.

Another point of interest in this work was turbulence modelling. Aeroelastic calculations must capture the influence of the flow on the blade structure. Rotorcraft flows are complex and due to the limits of the URANS models in predicting the frequency content in the flow, discrepancies in the structural forcing and the blade deformation might appear. Vibration levels might also see an improvement from a higher frequency content. The potential of DES models for rotorcraft flow was demonstrated using the stalled flow around a NACA0021 wing as a test case. The frequency content obtained through DES was much wider and also allowed for better predictions of the mean flow field properties along with integrated loads. DES was applied to the HART-II rotor in order to assess the possible improvements coming from the use of DES. However, the difference between the URANS and the DES predictions of the flow field were limited, highlighting a grid or time step refinement need.

A strong aeroelastic coupling strategy was also demonstrated, using the UH-60A rotor in high-speed forward flight. The key structural deformation was captured by the coupling strategy, and the dependency of the predictions to many flight and simulation parameters was highlighted.

Publications

Journal Papers

F. Dehaeze and G.N. Barakos, Potential Use of Hybrid Turbulence Models for Rotorcraft Flows, *Submitted to Aerospace Science and Technology*, February 2012.

F. Dehaeze and G.N. Barakos, Hovering Rotor Computations Using an Aeroelastic Blade Model, *Accepted for publication at the Aeronautical Journal*, to be published in May 2012.

S.J. Lawson, F. Dehaeze and G.N. Barakos, Computational Fluid Dynamics Analyses of Ship Air Wakes using Detached-Eddy Simulation, *Submitted to the Journal of Wind Engineering and Industrial Aerodynamics*, January 2011.

F. Dehaeze and G.N. Barakos, Mesh Deformation Method for Rotor Flows, *Journal of Aircraft*, 49(1): 82–92, January–February 2012.

Papers in Conference Proceedings

F. Dehaeze and G.N. Barakos, Aeroelastic CFD Computations for Rotor Flows, *37th European Rotorcraft Forum, Galarate, Italy, 13–15 September*, 2011.

F. Dehaeze and G.N. Barakos, Hybrid Turbulence Models Evaluation for Rotorcraft Flows, *36th European Rotorcraft Forum, Paris, France, 7–9 September*, 2010.

F. Dehaeze and G.N. Barakos, Mesh Deformation Method for Rotor Flows,*RAeS Aerodynamics Conference 2010, Bristol, UK, 27–28 July*, 2010.

F. Dehaeze and G.N. Barakos, Turbulence Modelling for Rotorcraft CFD, *34th European Rotorcraft Forum, Liverpool, UK, 16–18 September*, 2008.

Abstracts Presented at Workshops

F. Dehaeze and G.N. Barakos, Turbulence Modelling for Rotorcraft CFD//Aeroelastic Analysis of Turbulent Rotor Flows, *Helicopter Study Weekend, the Burn, Scotland, 3–5 April*, 2009.

Internal Reports

F. Dehaeze, Aeroelastic Simulations of Hovering Rotors, Technical Note TN11-012, 2011.

F. Dehaeze, Running an Aeroelastic Calculation with a Prescribed Motion, Technical Note TN10-021, 2010.

F. Dehaeze, Blade Structural Modelling and Grid Deformation, Technical Note TN09-002, 2009.

Acknowledgements

I am grateful to the Rotorcraft Aeromechanics Defence and Aerospace Research Project (DARP) partners, namely AgustaWestland, DSTL and the Department of Trade and Industry, for funding this work.

I would like to first thank my supervisors, Professor George Barakos and Professor Ken Badcock. The thorough help and support from Professor George Barakos is especially acknowledged. I would also like to thank all the members of CFD Lab, past and present, for creating a stimulating work environment. Doctor René Steijl's help was especially appreciated.

Last but not least, I would like to thank my family for their moral and financial support during this work. My friends support was also helpful.

Contents

List of Figures

List of Tables

Nomenclature

Roman Symbols

a_∞ Free-stream sound velocity

a, b, c, d Vectors used for the projection of a fluid node on a triangular structural element, as defined in Paragraph 5.1.1

a′, b′, c′, d′ Updated vectors **a, b, c, d** after the structural deformation has been applied

$\arg_1$, $\arg_2$ Arguments to blending functions F_1 and F_2

A_s Sectional area

b Number of nodes along the beam

$B()$ Notation for blending function

c Chord length

c_{b1}, c_{b2}, c_{v1}, c_{w2}, c_{w3}, c_{t1}, c_{t2}, c_{t3}, c_{t4} Closure coefficients for the SA model

CCM Propeller torque coefficient, $CCM = \frac{Q_r}{\rho\left(\frac{\Omega}{2\pi}\right)^2(2R)^5}$

C_D Drag coefficient, $C_D = \frac{D}{0.5\rho_\infty c^2 V_\infty^2}$

C_{DES} Arbitrary constant scaling the mesh length scale in DES models

C_L Lift coefficient, $C_L = \frac{L}{0.5\rho_\infty c^2 V_\infty^2}$

C_μ Closure coefficient for one-equation models

C_μ $k-\varepsilon$ model coefficient

C_P Pressure coefficient, $C_P = \frac{p-P_\infty}{0.5\rho_\infty V_\infty^2}$ for an aerofoil case and $C_P = \frac{p-P_\infty}{0.5\rho_\infty V_{loc}^2}$ for a rotor case

C_Q Rotor torque coefficient, $C_Q = \frac{Q_r}{\frac{1}{2}\rho\pi R^3 V_{tip}^2}$

C_q Rotor sectional torque coefficient around the rotation axis, $C_q = \frac{L_M}{\frac{1}{2}\rho c^2 V_{tip}^2}$

$C_{Q,P}$ Rotor torque coefficient, obtained from the pressure integration only

$C_{Q,v}$ Rotor torque coefficient, obtained from the viscous effects only

C_T Rotor thrust coeffcient, $C_T = \frac{T_r}{\frac{1}{2}\rho\pi R^2 V_{tip}^2}$

C_t Rotor sectional thrust coefficient $C_t = \frac{L_Z}{\frac{1}{2}\rho c V_{tip}^2}$

C_T Thrust coefficient, $C_T = \frac{T}{\frac{1}{2}\rho_\infty \pi R^4 \Omega^2}$

CTA Propeller thrust coeffcient, $CTA = \frac{T_r}{\rho\left(\frac{\Omega}{2\pi}\right)^2 (2R)^4}$

$\tilde{d}$ Length scale used in the DES and DDES turbulence models

D Drag force

d Distance to wall

$\frac{D}{Dt}$ Lagrangian derivative

d_{Fn}, d_{Mn} Sectional bending deflection at the tip of the beam for unit bending force and moment

$d_{outflow}$ Distance of the outflow from the blade when using the Froude boundary condition (see Equation 3.1)

d_t Distance from the field point to the trip for the SA model

$\mathbf{dx}$ Displacement vector of the point $\mathbf{x}$

$\mathbf{dx}_1, \mathbf{dx}_2, \mathbf{dx}_3, \mathbf{dx}_4$ Displacement vectors of the face four corners

E Total energy of fluid

e Specific internal energy

$error$ Convergence criterion of the spring analogy method

$ETAA$ Propeller efficiency, $ETAA = \frac{\mu}{2}\frac{CTA}{CCM}$

E_y Young's modulus

$\mathbf{F}$ Flux vector in the x-direction

$\mathbf{f}$ External forces

f Frequency

F_1, F_2 Blending functions used in the $k-\omega$ BSL and SST models

f_d Blending function in the DDES turbulence models

f_i Body force vector

$\mathbf{F}_{ij}$ Force on the i-th vertex due to the spring between the i-th and j-th vertices

f_i^s Modal forcing for the i-th mode

$\mathbf{F}_i$ Sum of the forces due to the surrounding springs on the i-th vertex

FM Rotor figure of merit $FM = \frac{\sqrt{\sigma}C_T^{\frac{3}{2}}}{2C_Q}$

F_{prop} Propulsive force

$f_{v1}, f_{v2}, f_w, g, r, f_{t2}, f_{t1}, g_t, \chi, c_{w1}$ SA model functions

$\mathbf{G}$ Flux vector in the y-direction

$\mathbf{H}$ Flux vector in the z-direction

I_c, I_f Chordwise and flapwise area moment of inertia

J	Torsional area moment of inertia
$\mathbf{K}$	Stiffness matrix
k	Specific turbulent kinetic energy
k_{ij}	Stiffness of the spring between vertices i and j
k_T	Heat transfer coefficient
L	Lift force
l_{DES}	Length scale used in the DES and DDES approaches
L_M	Rotor moment loading around the blade pitch axis (N or lbf)
l_n	Length of the n-th section of the beam
l_{RANS}	Length scale used in the RANS turbulence models
L_Z	Rotor loading along the span in the thrust direction
$\mathbf{M}$	Mass matrix
m	Linear mass distribution
M_∞	Free-stream Mach number, $M_\infty = \frac{V_\infty}{a_\infty}$
M^2C_m	Mach scaled pitching moment coefficient (around the blade quarter-chord axis)
M^2C_n	Mach scaled normal force coefficient
m_n	Mass at the n-th node
M_{tip}	Tip Mach number, $M_{tip} = \frac{V_{tip}}{a_\infty}$
N	Number of samples/measurements
N_b	Number of blades
$\mathbf{n}_i$	Normal vector to the i-th face of a cell
n_i	Number of vertices linked by a spring to the i-th vertex
n_m	Number of structural modes
P	Non-dimensional pressure $P = \frac{p}{\rho_\infty V_\infty^2}$
p	Pressure
P_∞	Free-stream pressure
P_ω	Dissipation rate specific to k
q_i	(Favre-averaged) Heat flux vector
Q_r	Rotor torque
R	Rotor radius
r	Spanwise location
Re	Reynolds number for an aerofoil, based on the free-stream velocity and the chord length, $Re = \frac{\rho_\infty c V_\infty}{\mu}$

Re_∞ Reynolds number for a rotor, based on the free-stream velocity and the chord length, $Re_\infty = \frac{\rho_\infty c V_\infty}{\mu}$

Re_T Turbulent Reynolds number, $Re_T = \nu_T/\nu$

Re_{tip} Reynolds number for a rotor, based on the tip velocity and the chord length, $Re_{tip} = \frac{\rho_\infty c V_{tip}}{\mu}$

$R_{i,j,k}$ Flux residual

R_ω Constant used in some versions of the $k-\omega$ model in the calculation of α^*, β^* and α

R_ω Turbulent Reynolds number for $k-\omega$ model

$R_{outflow}$ Diameter of the outflow for hovering rotors, when using the Froude boundary condition (see Equation 3.1)

R_t Turbulent Reynolds number for $k-\varepsilon$ model

S Vorticity magnitude

S_1, S_2, S_3 Corners of a structural element

s_1, s_2, s_3, s_4 Stretching functions, defined in Equation 5.13

S_F Sectional force coefficient, $S_F = \frac{L_Z}{\rho_\infty c V_{tip}^2}$

S_{ij} Strain rate tensor of mean flow

Sk Cell skewness

Skr_{max} Max skewness ratio $Skr_{max} = \frac{1-max(Sk_{deformed})}{1-max(Sk_{undeformed})}$

s_n Distance between the shear centre and the elastic axis at the n-th node

S_{NS} Source Term for the Navier-Stokes Equations

St Strouhal number, $St = f\frac{c}{V_\infty}$

T Temperature

t Time

T_{inte} Integration time

T_r Rotor thrust

T_{ref} Reference temperature for Sutherland's law (see Equation 2.8), $T_{ref} = 273.15\,\mathrm{K}$

T_{Suth} Sutherland's temperature, $T_{Suth} = 110.4\,\mathrm{K}$

u_i Velocity vector

u_τ Frictional velocity

U, V, W Velocity components

V Volume

V_∞ Free-stream velocity

v_{Fn}, v_{Mn} Sectional bending angle at the tip of the beam for unit bending force and moment

$\mathcal{V}_{i,j,k}$ Cell volume

V_{loc} Local velocity, $V_{loc} = \left(\mu \sin(\Psi) + \frac{r}{R}\right) V_{tip}$

V_{tip} Blade tip velocity, $V_{tip} = \Omega R$

v_{Tn} Sectional torsion at the tip of the beam for unit torsion moment

$\mathbf{W}$ Vector of conserved variables

$\mathbf{x}_1, \mathbf{x}_2, \mathbf{x}_3, \mathbf{x}_4$ Coordinates of the four face corners

X_b Propulsive force coefficient $X_b = \frac{200F_{prop}}{\rho_\infty \sigma (\pi R)^2 (\Omega R)^2}$

x_i Position vector

$\mathbf{x}(\xi, \eta)$ Coordinates of the point in the local face coordinates

y Distance

y_{el}, z_{el} Elastic chordwise and flapping deflections

y_n Distance to the nearest wall

Z_b Lift force coefficient $Z_b = \frac{200L}{\rho_\infty \sigma (\pi R)^2 (\Omega R)^2}$

Abbreviations

$k-\omega$ BSL Menter's $k-\omega$ baseline turbulence model

$k-\omega$ SST Menter's $k-\omega$ shear-stress transport turbulence model

AFDD Aeroflightdynamics Directorate

BB Baldwin-Barth turbulence model

BILU Block Incomplete Lower-Upper factorisation

BVI Blade-Vortex Interaction

CAMRAD Comprehensive Analytical Model of Rotorcraft Aerodynamics and Dynamics

CFD Computational Fluid Dynamics

CFL Courant-Friedrichs-Lewy number

CPU Central Processing Unit

CSD Computational Structural Dynamics

CVT Constant Volume Tetrahedron method

DDES Delayed Detached-Eddy simulation

DES Detached-Eddy Simulation

DLR Deutschen Zentrums für Luft- und Raumfahrt

DNS Direct Numerical Simulation

elsA Ensemble Logiciel de Simulation en Aérodynamique

FEM Finite-Element Model

FLOWer FLOW solvER

FPR Full Potential Rotor code

FPS Finite Plate Spline

GCG Generalised Conjugate Gradient

HART Higher-harmonic control Aeroacoustic Rotor Test

HIMARCS High Manoeuvrability and Agility Rotor and Control System

HOST Helicopter Overall Simulation Tool

IIM Inverse Isoparametric Method

IPS Infinite Plate Spline

LES Large-Eddy Simulation

LNS Limited Numerical Scales

MQ Multiquadric-Biharmonic

MUSCL Monotone Upstream-centred Schemes for Conservation Laws

NASTRAN NASA STRuctural ANalysis

NTS New Technologies and Services

NUBS Non-Uniform B-Splines

ONERA Office National d'Études et Recherches Aérospatiales

PIV Particle Image Velocimetry

PSD Power Spectral Density

RANS Reynolds-Averaged Navier-Stokes

RBF Radial Basis Functions

RCAS Rotorcraft Comprehensive Analysis System

SA Spalart-Allmaras turbulence model

SALSA Strain-Adaptative Linear Spalart-Allmaras turbulence model

SAM Spring analogy method

SPR Stereo Pattern Recognition

TFI Trans-Finite Interpolation

TPS Thin-Plate Spline

UMARC University of Maryland Advanced Rotorcraft Code

URANS Unsteady Reynolds-Averaged Navier-Stokes

Greek Symbols

$\alpha^*, \beta^*, \alpha, \beta, \sigma_k, \sigma_\omega, S_l$ Model coefficients for $k-\omega$ model

α, β, γ Coefficients used to define the CVT association between fluid nodes and structural elements after the structural deformation

α_i i-th modal amplitude factor

α_{inc} Incidence

α_s Shaft angle of the rotor measured with respect to the Y-axis, positive if the rotor tilts backwards

β_0 Coning angle of the rotor

β_{1c}, β_{1s} Cyclic flap coefficients of the rotor

β_b Bending angle at the root of the beam

β_n Bending angle at the n-th node

γ_L Lock number

Δ Mesh length scale

$\boldsymbol{\delta}_i$ Vector representing the displacement of the i-th block vertex in the spring analogy

δ_{ij} Kronecker delta

$\boldsymbol{\delta}_{i,new}$ Displacement of the i-th block vertex after the iterative update in the spring analogy

$\boldsymbol{\delta}_{i,old}$ Displacement of the i-th block vertex before the iterative update in the spring analogy

$\Delta\Psi$ Azimuth step size

Δt Time step size

δU Difference between velocity at the field point and at the trip

δx Grid spacing along the wall at the trip

Δx, Δy, Δz Cell size length

θ_0 Collective angle of the rotor

θ_{1c}, θ_{1s} Cyclic pitch angle of the rotor

θ_{el} Elastic torsion

θ_n Torsion angle at the n-th node

λ Blade aspect ratio, $\lambda = R/c$

μ Molecular viscosity

μ Rotor advance ratio, $\mu = \frac{V_\infty}{V_{tip}}$

M_b Bending moment at the root of the beam

μ_{ref} Reference viscosity for Sutherland's law (see Equation 2.8, $\mu_{ref} = 1.716 \times 10^{-5}\,\mathrm{kg/ms}$)

μ_T Dynamic eddy viscosity

ν Kinematic molecular viscosity

ν Poisson's coefficient

$\tilde{\nu}$ Working variable

ν_T Kinematik eddy viscosity

Ω Rotor rotational speed

ω	k-specific dissipation rate
ω_i	Eigenpulsation of the i-th mode
Ω_{nom}	Rotor nominal rotational speed
ω_t	Wall vorticity at the trip
ϕ	Deformed blade shape
ϕ_0	Undeformed blade shape
φ	Arbitrary flow quantity
$\overline{\varphi}$	Mean part of a quantity
ϕ'	Fluctuating part of a quantity
ϕ_1^0, ϕ_2^0	Blending functions in the η-direction defined in Equations 5.10 and 5.11
ϕ_i	Blade i-th eigenvector
φ_{tip}	Tip bending angle
Ψ	Azimuth
ψ_1^0, ψ_2^0	Blending functions in the ξ-direction defined in Equations 5.8 and 5.9
ψ_{tip}	Tip torsion angle
ρ	Density
ρ_∞	Free-stream density
σ	Rotor solidity
σ_{Pr}	Turbulent Prandtl number
τ_{ij}	Viscous stress tensor
τ_w	Dynamic wall shear stress
ε	Dissipation rate of k per unit mass of fluid
ξ, η	Local coordinates on the face of a block
ζ_i	Structural damping of the i-th mode

Superscripts

$'$	Fluctuating part
$+$	Non-dimensionalised wall distance
i	Inviscid component
n	Current time-step
$n+1$	Next time-step
R	Reynolds stress

v	Viscous component

Subscripts

b	Basic
i	Index
j	Index
k	Index
t	Current time step
t	Trip
t	Turbulent
$t+1$	Next time step
$t-1$	Previous time step
w	Value at wall

Chapter 1

Introduction

1.1 Motivation

Helicopters are the most versatile flying machines, capable of vertical flight, and for this reason, they have found use in many applications, such as search and rescue missions, police missions, fire fighting, pollution control and even electrical cable maintenance. Their high velocity associated with the ability to hover and land vertically allows for multiple uses which no other mean could perform.

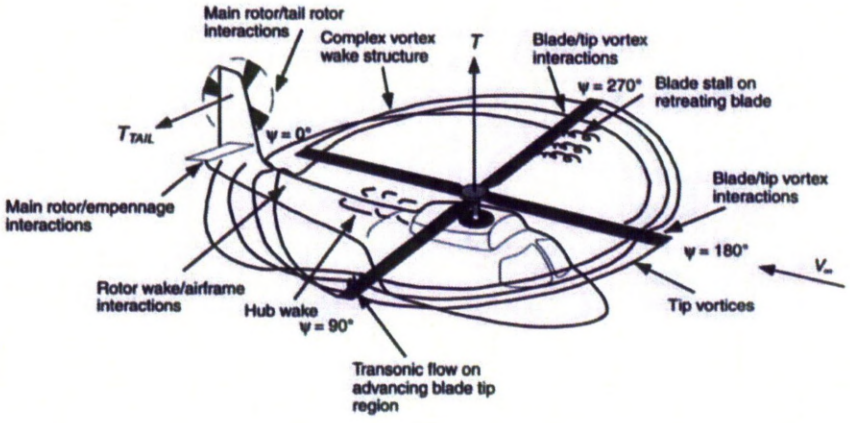

Figure 1.1: Flow structure and aerodynamic problems for a helicopter in forward flight[1].

Their aerodynamics is challenging due to the flow phenomena taking place at the same instant in time. Figure 1.1 shows some of the phenomena happening during a flight. Focusing on the main rotor

only, on the advancing side, the blade tip reaches transonic regime and generates a shock on the upper surface, which may interact with the boundary layer. On the retreating side, at high-speed, the root of the blade sees reversed flow, and stall may happen at the tip of the blade due to the high incidence. Another important phenomenon is the blade-vortex interaction: the vortices created by the blades result in rapid changes of the blade surface pressure when passing close to following blades, increasing vibration and noise levels. The simulation of all these phenomena is a challenge for CFD due to the wide range of conditions encountered by the blades in these particular flows.

The rapid changes in loading on the blade due to the varying conditions imply changes in the blade shape. The blade stiffness, increased by the inertia from the rotational speed is not sufficient to make the blade rigid and the shape variation, particularly in torsion along the blade axis, has a strong influence on the rotor performance. Simulating such interactions is challenging, due to three requirements: accurate flow field has to be obtained from a CFD solver, a good structural model must be able to predict the dynamic deformation of the blade with the unsteady loading, and a good fluid/structure interface must be able to efficiently exchange information between the two solvers. The focus of this thesis is to introduce and demonstrate a rapid information exchange method between the fluid and structural solvers as well as a study of advanced turbulence modelling to increase the frequency content of the CFD predictions in the blade stimulations.

1.2 Literature Survey

This literature survey aims at presenting the current state of aeroelastic coupling for helicopter rotors. It is centred around six points. Firstly, structural blade modelling techniques are presented. Secondly, a description of comprehensive rotor codes is given. Current mesh deformation method for CFD grids are then presented. The current developments in CFD/CSD coupling strategies is then described. Wind-tunnel experiments and flight-test data, used for validation, are then detailed. The limitations of current turbulence modelling for rotorcraft flows are finally exposed.

1.2.1 Structural Dynamics for Composite Beams and Rotor Blades

Hodges *et al.* [2] stated that modelling a structure as a beam usually results in a significant decrease in the number of degrees of freedom, and the structural dynamics of a composite beam such as a helicopter rotor blade may require special consideration owing to the presence of extension-twist and bending-twist couplings along with transverse shear deformation and warping degrees of freedom. A mixed finite element solution for the intrinsic equations of arbitrary deformation in initially curved and twisted composite beams was defined. This approach reduced the problem to the solution of one or more linear, two dimensional problems over the cross section together with a nonlinear one dimensional problem along the beam reference line.

Their modelling technique[2] was compared with analytical and experimental results. Firstly, tip deflections of a cantilever beam as a function of the forces applied at the tip were compared with analytical results and showed a difference smaller than 0.1%. Then, the authors studied aluminium beams with varying tip swept angles at multiple rotational speeds, showing a good correlation with experimental measurements. Finally, four different composite beams were tested at various rotational speeds and compared well with experiments, except some higher frequency modes. A reason provided by the authors was the poor 3-D characterisation of composite blades. However, the new method seemed to improve the results compared to previous numerical methods.

Wilkie *et al.* [3] attempted to calculate the rotating blade frequencies for a generic model, helicopter rotor blade using the MSC/NASTRAN finite element code. Beam elements were used along the reference line. The simulation was done in two steps: firstly, a stiffness matrix was computed using NASTRAN solution 66 (large-displacement static analysis) method, taking into account the inertial effects from the rotation, and then an eigenmode analysis using solution 63 (normal modes analysis) was performed. The standard code was modified so that effects due to the rotation of the blades could be accounted for by allowing the eigenvalue analysis to be performed using the stiffness matrix from solution 66. The results were validated against data obtained experimentally (see Section 1.2.5 for further details about the experiments). The frequencies were obtained for rotating speeds ranging

from 0 to 660RPM. While the lower bending frequencies compared well with the experiments, the torsional frequency showed some noticeable difference (from 8% at 0RPM to 13% at 660RPM). The reason provided by the authors was the influence of the simplified hub model on the torsional eigenmode.

NASTRAN was also applied to the UH-60A rotor blade by Hamade and Kufeld[4]. The rotor used for the flight tests (see Section 1.2.5 for further information about the flight test on the UH-60A rotor) was used as a reference, meaning that two blade models were developed: one for a normal production blade and one for the instrumented blade containing pressure taps, in order to check the similarity of the dynamic behaviour between both blades. The models included 89 beam elements along the reference line. Experimental measurements were obtained for a blade that was hung to the roof using four strings, as shown in Figure 1.2. The strings were modelled as elastic elements. The NASTRAN model also included a model of the shaker that was used during the experiments for determining the natural frequencies. The frequencies predicted by NASTRAN agreed well with the experimental ones, with a maximum difference of 2.4% with experimental measurements. The pressure-instrumented blade frequencies were lower by 2 to 4% compared to the ones of the production blade.

Smith and Chopra[5] modelled composite beams by idealising them as rectangular box-beams. A finite element analysis was performed where the composite beams were modelled with eight elements. Each of these elements had 19 degrees of freedom and was able to undergo flap and lag bending, elastic torsion and transverse shear deformations. The beam was to undergo only small strains and moderate deflections making the formulation suitable for the modelling of hinge-less helicopter blades. As bearing-less blades can undergo large torsional deformations the proposed scheme was deemed unsuitable for their modelling.

The model was tested against experiments and detailed finite element results. For the experiments, graphite/epoxy beams were tested under non-rotating and rotating conditions (up to approximately 1000RPM) in a vacuum chamber. Their natural frequencies and mode shapes were measured for the first two flapping modes and the first lead-lag mode. The finite element analysis was based upon a method by Stemple and Lee[6] and considers the first two flap and lag bending modes together with the

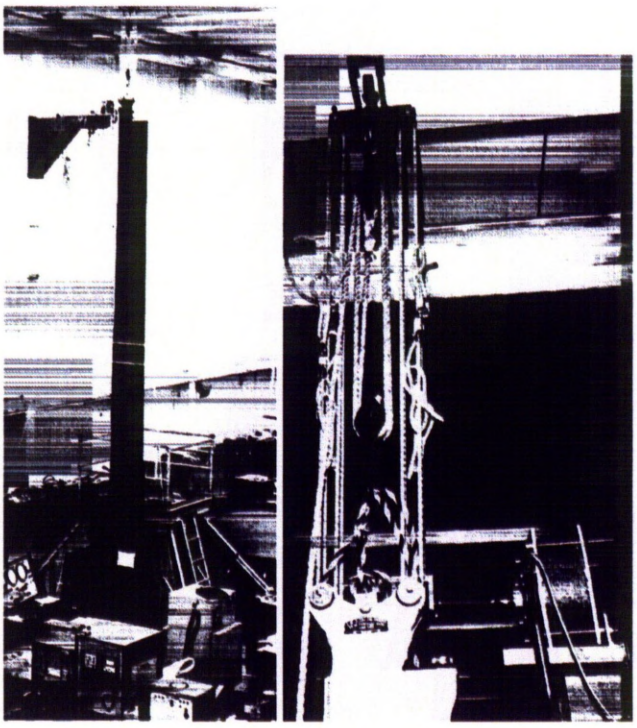

(a) General view (b) Zoom on the shaker

Figure 1.2: Experimental setup for the measurement of the natural frequencies of the UH-60A blade, from [4].

first torsion mode. The analysis used five spanwise elements and four cross-sectional warping elements in each spanwise element.

The results from Smith's analysis compared favourably with the experiments and the detailed finite element results, and errors for the natural frequencies were generally smaller than 10%. Six different configurations of the box beam were tested and it was also found that neglecting the transverse shear couplings resulted in errors of around 20% in the flap and lag frequencies for the 15_6 antisymmetric layup beam (fibres oriented at 15 degrees and fibre volume fraction of 0.6).

Another area of interest for structural modelling is the hub model influence. An example of such work was done by Ho *et al.* [7]. The UH-60A blade was modelled using a beam finite-elements model with 13 beam elements along the span, and the blade was connected to the fixed hub with rigid bars connecting the articulations of the blade. However, the push rod was not kept rigid, but was considered as a spring, and two different stiffness were tested: 364 and 1090 ft.lb/deg (493.5 and 1477.8 Nm/deg, respectively). The blade natural frequencies were obtained with CAMRAD-II and RCAS. The comparison of the frequencies obtained by the structural solvers showed limited differences. On the other hand, the frequency of the first torsional mode increased with the pushrod stiffness (from 3.9/Rev to 4.5/Rev, at the nominal rotor speed).

More recently, 3-D structural models were used in an attempt to account for the blade sectional deformations, the anisotropic behaviour of composite hinge-less and bearing-less blades, and the more complex shapes of rotor blades. Truong[8] developed a 3-D finite-element model in MSC/Marc of the ERATO blade. The ERATO blade has a complex planform, with variable swept angle and chord length along the span. Natural frequencies obtained from MSC/Marc were compared with experimental results for a hanging ERATO blade and showed good agreements: the relative error in frequency was under 5%. The blade modal frequencies were then computed as a function of the rotational speed and compared with a finite-element beam model used in MSC/Marc as well. The comparison between the two simulations appeared to be small for the five modes with the lowest frequencies, but differences occurred between the second lead-lag mode (sixth mode) and the first torsional mode (seventh mode) frequencies. The predicted shape of the third flapping modes by the two simulations were then compared and showed

that while the flapping deflections were both predicted within the experimental measurements margins, the torsional deformation predicted by the beam model was much lower than the one predicted by the 3-D model, which was closer to the experimental results.

Datta and Johnson[9] used brick elements to represent a straight blade with a swept-back tip. A new method based on 3-D brick elements was compared to a finite-element beam model for a hinge-less and an articulated rotors. The comparison of the blade natural frequencies showed limited difference, mainly on the hinge-less rotor for high frequencies.

1.2.2 Comprehensive rotor codes

Yeo *et al.* [10] assessed wake models implemented in CAMRAD-II, aiming at predicting challenging flight conditions: a high-speed cruise flight and a low-speed flight in BVI conditions. A list of their test-cases is shown in Table 1.1. Apart from the SA 349/2 test case, which was modelled as a full aircraft, only the isolated rotor was modelled. All simulations were performed using CAMRAD-II. The rotor non-uniform induced velocity was obtained from a free-wake model. Two models were compared to generate the tip-vortex: a rolled-up model and a multiple-trailer with consolidation model. The trimming method varied with the test case, and the various methods used are shown in Table 1.1.

Table 1.1: Experimental data used for comparison by Yeo[10]

Test Case	Advance-ratio	Model	Trimming Method
H-34	0.129 0.390	Isolated rotor	Matching the experimental thrust, shaft angle and flapping harmonics from experiments
Puma (SA 330)	0.141 0.362	Isolated rotor	
Gazelle (SA 349/2)	0.140 0.361	Full aircraft	No force and moment on the aircraft with a 0degrees slip angle
UH-60A	0.149 0.368	Isolated rotor	Matching the thrust and shaft pitch and roll moments, shaft angle from the experiments
Bo-105	0.150	Isolated rotor	

The comparison between the results from the simulations and the experimental measurements or the flight test data focused on the flap-bending, the chord-bending and the torsional moment measured

at about mid-span. Only the oscillatory part was taken into account, the mean was removed. In most cases, the influence of the tip-vortex model was limited. The agreement of the simulations with the experimental measurements varied, but no general rules could be extracted.

Due to the poor correlation in the chord-bending predictions, arbitrary changes were applied on the lead-lag damper, using the UH-60A rotor test case. The effect of such changes was limited, resulting in no improvements in the predictions. However, when the measured air-loads were applied instead of the free-wake model loads, the predictions improved significantly, suggesting discrepancies from the air-loads predictions using a free-wake model.

Tang and Dowell[11] showed interest in the effect of the coupling between flapping bending, chordwise bending and torsional deformation. A Hodge-Dowell beam model[12] was used to model the blade structure, and two different aerodynamic models were compared. The first model was based on a set of first-order perturbation equations in the state vector which are solved as an eigenvalue problem for a linearisation in the pitch stiffness. The second model was the full non-linear ONERA aerodynamic model. Two different blade flutter test-cases were studied: one of the blade had a clamped root while the other had a root that was excited in pitching. The simulations were compared against experimental results. The first test consisted in a comparison of the static tip deformation, using the clamped blade in order to increase the flutter critical speed. While the results are similar at lower dynamic pressure, at higher dynamic pressure, the use of the full non-linear ONERA aerodynamic model improved the predictions, particularly the tip torsion. This difference mainly occurred when the flow around the blade was stalled.

The second case focused on the dynamic behaviour of the blades, and two major issues were identified. The first of these is the effect of geometric structural non-linearity on the flutter instability and stall response. It was concluded that the effects on both static deflections and dynamic aeroelastic behaviour are significant when the initial blade pitch angle or angle of attack is large or when stall occurs. The second issue is the effect of free-play structural non-linearity on dynamic stall behaviour. It was concluded that the free-play structural non-linearity leads to a bounded oscillation which can be either periodic, aperiodic or chaotic. The initial conditions are a significant factor in this.

Turnour and Celi[13] attempted to couple the flap-lag-torsional dynamics of elastic rotor blades in flight dynamics simulations. For their model, a rigid fuselage was assumed and its motion was described by nine non-linear, rigid body Euler equations. The equations of motion for the main rotor were obtained using an implicit (numerical) approach. Structurally, the rotor blades were modelled as Bernoulli-Euler beams undergoing flap-lag-torsional motion. Quasi steady stall and compressibility effects were included through the use of look up tables for the blade airfoils and the inflow dynamics were modelled with a six state, two harmonic, finite state wake model. Each blade was modelled using four finite elements, the outermost element representing the swept tip. The aircraft modelled was a UH-60A operating at advance ratios of 0.19 and 0.28. These speeds were chosen to match flight test data.

The first five rotating natural frequencies and corresponding mode shapes were calculated. It was shown that the second flap and first torsional modes were coupled containing torsional and flap components. For the case of the second flap mode, the coupling was thought to be caused by the swept tip. Frequency responses were plotted on- and off-axis responses using a range of modes, and these were compared to the flight test data. The correlation of the results with the flight test data was generally quite good for the amplitude and between frequencies in the range of $0.4 - 0.6$ rad/sec to $50 - 55$ rad/sec. However, the inclusion of blade flexibility into the model only had a very small effect on the vehicle dynamics. When looking at the off-axis responses, the phase prediction was poor, often with errors of around 180 degrees. Using higher harmonics in the dynamic inflow model appeared to have very little effect. Above a frequency of 0.8 rad/sec, the two inflow models produced very similar results. The authors concluded by stating that the results from this paper indicate that refining the main rotor model by including blade flexibility and a higher order dynamic inflow model did not improve the prediction of the off-axis response to pilot input or at least not for the helicopter considered in their study.

Tang and Dowell[14] carried out a study of the lead-lag damping predictions. An isolated hingeless 4-bladed rotor model with coupled bending/torsional motion was simulated, using the ONERA full stall models with a free wake model and a Hodges-Dowell beam model[12]. The free oscillations of

the blade were first computed using time-marching simulations, with periodic cyclic pitch oscillations to simulate the swash-plate. The experimental rotor tested for the numerical method validation was trimmed to lower the flapping moment.

Firstly, a lead-lag stimulation was added to the rotor and once steady-state was reached, the forcing was stopped and the resulting oscillations were used to assess the modal damping when the blade was going back to the starting unforced oscillations. The proposed coupling of the ONERA stall model with a Peter and He's wake model improved the damping coefficient predictions compared to more basic inflow models (uniform and Pitt and Peter's 3×3 dynamic inflow model), particularly at higher advance ratios. The steady root flap moments were also found to be closer to experimental measurements. Because of the trim state, the stall-model influence was also found to be minimal. The inclusion of the time variation of the induced inflow influence matrix on the blade lag response was also found minimal, while increasing the computational cost by a factor of 5.

Smith and Chopra[5] implemented their previously described model in the University of Maryland Advanced Rotorcraft Code (UMARC) and applied it to the Bo-105 with a hingeless rotor design. The rotor trim, the aircraft orientation and the blade deformation were solved simultaneously, because the rotor blade deformations modified the rotor loads in an important manner. At each iteration, the blade normal modes were recomputed around the mean blade deflection. A 3×3 dynamic inflow model was used to model the low frequencies of the rotor loads, coupled with quasi-steady aerodynamics for the stability analysis. Five different blade layout were studied: for each blade, the number and orientation of the laminates was modified to assess the influence of such changes. A high advance-ratio $\mu = 0.35$ flight condition was used.

The elastic coupling resulted in significant changes of amplitude and phase for the torsional deflections of the various blades when compared to the baseline case. The flapping and lead-lag deflections were similar. The vibratory constant of the hub loads was also changed, mainly in the yaw moment (from -25% to $+30\%$ compared to the baseline blade). The lag mode damping was also greatly affected by the coupling. The use of a fully unsteady aerodynamic model instead of the quasi-steady one used in the previous study showed amplitude and phase changes for the flapping deformation, but the changes

were smaller for the lag and torsion responses.

In order to overcome the constraints coming from the use of basic aerodynamic models, Beaumier *et al.* [15] studied the use of more advanced techniques used by the ONERA and the AFDD. The 1/5th model of the Boeing Helicopter Vertol 360 rotor[16] was used as a test-case to assess the aerodynamic methods, and the simulations of three hover and three forward-fight cases were validated against experimental measurements done in the DNW wind tunnel. For hovering rotors, ONERA employed the Eulerian flow solver WAVES, and AFDD used the HELIX-I full-potential flow solver. In forward flight, different methods were tested. the ONERA coupled the R85/METAR comprehensive tool with the unsteady full-potential flow solver FP3D. R85/METAR is based on a lifting-line approach using 2D aerofoil tables and a prescribed wake geometry model. In slow forward flight, FP3D was initialised using a free-wake analysis performed with MESIR to improve the BVIs predictions. The AFDD method was based on the use of CAMRAD/JA, which uses a lifting-line theory coupled with a choice of wake models: an uniform inflow, a non-uniform inflow with a prescribed geometry wake or a non-uniform inflow with a free-wake model. CAMRAD/JA was coupled to the FPR potential flow solver.

The hover simulations resulted in a good agreement of the global thrust predictions as a function of the collective, but HELIX-I slightly under-predicted the thrust. However, when looking at the blade loading, WAVES tended to under-predict the loading on the main part of the blade while the loading at the tip was over-predicted. At high collective, WAVES showed a global thrust that was higher than the experimental one, which the authors thought to be the consequence of the lack of viscosity.

In high-speed forward flight, the trim state predictions were first compared. While R85/METAR control angles were in close agreement with the experimental ones, the collective from CAMRAD/JA was higher by 2.5 degrees. The shaft angles from both simulations were also under-estimated by 2 degrees, which could be caused by the lack of correction for the wind tunnel effects. While the blades were expected to be stiff, R85/METAR predicted a tip torsion variation of 3.5 degrees peak to peak, which had a strong influence on the sectional blade loading comparison with experimental measurements at $r/R = 0.95$. The coupling of FP3D with R85/METAR instead of FP3D alone improved the advancing-side predictions of the differential pressure, and, more specifically, the drop around azimuth

80 degrees. When comparing the sectional Mach-scaled loading from the ONERA and AFDD simulations with the experimental measurements, the download around azimuth 140 degrees was well predicted by both methods, however, FPR predicted a strong loading variation around azimuth 290 degrees, which wasn't present in the experiments. This problem was thought to come from a BVI prediction.

Two other forward flight conditions at lower advance-ratios and with BVI occurring at the rear of the disk were also tested. The loads variation due to the BVIs were over-predicted by both simulations by a factor of 2 or 3 compared to experimental measurements. Furthermore, a phase shift appeared between the simulations on the advancing side download, which was the result of different wake convective speeds.

These discrepancies call for advance aerodynamic models which are only reached by CFD. Therefore, in the next part of this literature survey, attention will be paid on the use of CFD for rotorcraft flows and current CFD/CSD coupling techniques.

1.2.3 Mesh Deformation methods

The coupling of CFD and CSD calls for two solvers, one for the structural model, and another one for the fluid flow around the blade. These two solvers need to interact; the aerodynamic solver transferring the loads to the structural solver, and the structural solver transferring the blade shape back to the flow solver. The structural and fluid models of the blade surface tend to have different sizes, with the structural model generally being a beam model with a few nodes along the blade quarter-chord line, while the fluid model contains the whole blade surface with tens of thousands points on it. While a simple load integration allows for the blade loading to be converted to the structural model size, the transfer of the structural shape to the fluid blade surface requires more advanced techniques to interpolate the points displacements. In this section, mesh deformation methods are described. Two parts of the mesh deformations have to be separated: the blade surface mesh deformation, which is extracted from the structural deformation and the mesh deformation propagation through the whole fluid domain.

A common approach in rotor blade grid deformation is to use sectional deformations: all the CFD mesh points are associated with a the beam model on the quarter-chord line and are then deformed

accordingly to the beam movement. The interpolation of the deformation inside a beam is usually performed using splines. This method proved popular in the literature, and can also be used to deform the whole mesh around the blade in the case of overset grids. For example, Wake and Baeder[17] used this technique to deform the UH-60A grid in hover, using a cosine decay function when getting further from the blade surface. A variant of this method was also used by Dietz *et al.* [18] for their aeroelastic simulation of a complete helicopter configuration. The mesh deformation was only applied to the blocks around the blade. The blade surface was first deformed, using the quarter-chord line deformation interpolated from the structural model using Hermite polynomials at each section. Then the blocks around the blade are rigidly moved to match the root-tip secant. The inside of the blocks was then generated using the trans-finite elements interpolation, to reach zero deformation on the outer boundary.

A basic method to deform the mesh after the blade surface is deformed, is the spring-analogy method (SAM), as described by Blom[19]. Springs are connecting each mesh node, having their equilibrium length set to the undeformed mesh length, and the boundary deformations are applied to the boundaries. A new equilibrium position for all nodes is reached using an iterative method. Two methods can be used to compute the spring stiffness constants: in the vertex spring methods, the stiffness is the same for all vertices, while in the segment springs method, the stiffness is set as a function of the inverse of the spring length. However, this method proved costly in terms of CPU-time to deform a whole CFD mesh due to the high number of springs. In order to lower the CPU-time cost, Dugeai[20], in elsA, packed the cells (from 2 to 5 in each direction) and then applied the spring-analogy to the cell groups instead of the numerical cell themselves. The inner nodes were then interpolated inside each macro-cell. This method was applied to rotors by Ortun *et al.* [21], and the blade deformation in the grid surface was obtained by using the quarter-chord line deformation.

Smith *et al.* [22] carried out a study of six different models to deform a surface from a structural model deflection. The models were then assessed for various test cases.

The Inverse Isoparametric Method (IIM) interpolates the fluid grid deformation using shape

functions. The fluid mesh nodes position can be assessed as follows:

$$\mathbf{x} = \sum_{i=1}^{N_S} S_i(\boldsymbol{\chi})\mathbf{x}_i^e \tag{1.1}$$

were $\boldsymbol{\chi} = (\chi, \eta)$ are the local Cartesian plane coordinates, $\mathbf{x} = (x,y)$ are the global Cartesian plane coordinates and S_i are the shape functions. N_S is the number of structural nodes and $\mathbf{x}_i^e$ the structural nodes location.

The Finite Plate Spline (FPS) is applying a matrix transformation to the fluid mesh displacement vector $\mathbf{q_a}$ as a function of the structural mesh displacement vector $\mathbf{q_s}$:

$$\mathbf{q_a} = \boldsymbol{\Psi}_\mathbf{a}\left(\mathbf{A}^{-1}\mathbf{K} + \boldsymbol{\Psi}_\mathbf{s}^T\boldsymbol{\Psi}_\mathbf{s}\right)^{-1}\boldsymbol{\Psi}_\mathbf{s}^T\mathbf{q_s} \tag{1.2}$$

where $\mathbf{K}$ is the stiffness matrix, $\mathbf{A}$ is the diagonal matric of the weighting constants, and $\boldsymbol{\Psi}_\mathbf{s}$ and $\boldsymbol{\Psi}_\mathbf{a}$ are the assembled matrices for the local shape functions evaluated at the structural and fluid nodes respectively.

The Infinite Plate Spline (IPS) methods is based on the superposition of the solutions for the partial differential equations of equilibrium for an infinite flat plate. Based on the deflection of N_S points in a planar surface, the vertical deflection $H(\mathbf{x})$ of a fluid grid point can be expressed as:

$$H(\mathbf{x}) = \sum_{i=1}^{N_S}\left[A_i + B_i\|\mathbf{x} - \mathbf{x}_i^e\|^2 + F_i\|\mathbf{x} - \mathbf{x}_i^e\|^2 \ln\|\mathbf{x} - \mathbf{x}_i^e\|^2\right] \tag{1.3}$$

A_i, B_i and F_i are undetermined coefficients. This method is not restricted to rectangular arrays, but requires non-coincident points. The numerical error tend to increase with the number of points in the structural model.

The Multiquadric-Biharmonic (MQ) method can be used to represent irregular surfaces:

$$H(\mathbf{x}) = \sum_{i=1}^{N_S} a_i\left[\|\mathbf{x} - \mathbf{x}_i^e\|^2 + r^2\right]^{1/2} \tag{1.4}$$

r is a user-defined parameter: large r values give flat sheet-like functions, while small r values give a cone-like function. r can even be set to vary among the basis functions. It can be used with overlapping domains.

The Thin-Plate Spline (TPS) method characterises an irregular surface by minimising an energy functional, and is similar to the MQ method. It is expressed as:

$$H(\mathbf{x}) = \sum_{i=1}^{N_S} a_i \left[\|\mathbf{x} - \mathbf{x}_i^c\|^2 \log \|\mathbf{x} - \mathbf{x}_i^c\| \right] \tag{1.5}$$

This deformation is invariant with rotation and translation.

The Non-Uniform B-Splines (NUBS) uses a tensor product of two splines to represent the surface. Generally, B-splines are used because rational splines create poles that deteriorate the numerical stability. It can be expressed as:

$$S_{kl}(\mathbf{x}) = \sum_{i=1}^{m-1} \sum_{j=1}^{n-1} P_{ij} B_{ik}(x) B_{jt}(y) \tag{1.6}$$

where S_{kl} is the surface deflection at any $\mathbf{x}$, P_{ij} are the coefficients multiplying the splines to fit the data, and B_{ik} and B_{jl} are the B-splines functions in the x and y directions.

Taking the IPS method as a reference, the resources required by each method were then compared. The MQ, TPS, NUBS and IIM methods proved much less time- and memory-consuming (2% to 3% of the IPS time and 3% to 20% of the memory used by IPS). The four methods in focus (MQ, TPS, NUBS and IIM) were applied to five test cases: the AGARD wing, an engine liner, a generic hypersonic vehicle, a wing strake configuration and a F-16 flexible wing with a rigid body. Furthermore, the flow-field around the wing and body in the last test case was simulated for the various methods. All methods were able to deal with all problems with the exception of the MQ which gave a folded mesh for the engine liner, for any value of the r parameter. The accuracy of the interpolation varied with the method and the test case, and all method had difficulties to deal with discontinuities in the structural model, which tend to be shifted when applied to the fluid grid. However, no comparison included aeroelastic coupling results, which would have allowed to compared the influence of the method on the fluid forces on the surface and the resulting deformation.

A study of the Radial Basis Functions was carried out by Rendall and Allen[23]. The structural nodes displacements were interpolated as:

$$H(\mathbf{x}) = \sum_{i=1}^{N_S} a_i \phi \left(\|\mathbf{x} - \mathbf{x}_i^c\| \right) + p(\mathbf{x}) \tag{1.7}$$

where ϕ is the form of function adopted, a_i are coefficients recovered by an exact match at the structural locations, and p contains polynomial terms. The norm can be set to the euclidian norm, however, it can also be adapted in order to increase or decrease the influence of one direction. For example, this property can be used for wing cases so that the nodes displacement is mainly influenced by the structural nodes located on the same section and less influenced by the structural nodes located at other spanwise locations.

Multiple forms ϕ of functions were compared, and the proposed mesh deformation methods were applied to multiple test cases. After a demonstration of the mesh deformation using a fuselage and a deforming wing with pylons and nacelle, a study was carried out on a wing with a static deformation along the span. The deformation amplitude was obtained by coupling a structural model based on the modal approach with a in-house CFD solver. The blade natural modes were obtained from the UNSI EU, FP4 project. The wing incidence was trimmed to match the lift coefficient. The vertical tip wing deflections varied between $0.069s$ and $0.089s$, with s the wing span, for an euclidian norm and a support radius of 200. Variations of the norm coefficient and support radius introduced heavy changes in the tip deflections which then varied between $0.069s$ and $0.129s$. The simulation was then switched to unsteady, with the wing freely oscillating. The resulting oscillations in the lift coefficient happened at the same frequency. However, the amplitudes of the oscillation varied: while some methods predicted decreasing oscillations, other predicted an increase. Equivalent variations in the behaviour were observed when modifying the norm or the support radius. The authors assumed that this was related to the behaviour of the shock on the wing surface.

For the DLR Tau solver, Gerhold and Neumann[24] developed a method adapted to the use of unstructured grids. the spring analogy or linear elasticity analogy methods were too costly in CPU-time, therefore an algebraic method was used. The mesh surface is deformed using RBFs. All the points in the mesh were sorted according to their distance from the deformed surface. The mesh points are then moved, starting with the nearest points to the mesh surface and increasing progressively the distance from it. The new displacement of a point is computed as a scaled average of the displacements of the neighbours that are closer to the deformed surface and whose position has already been updated. The

average of the displacement was weighted by the length of the connecting edges to the contributing neighbours as:

$$D_i = \frac{\sum_{j=1}^{N_{ne}} W_j D_j}{\sum_{j=1}^{N_{ne}} W_j} \tag{1.8}$$

where D_i is the current node displacement, D_j is the neighbour node displacement and N_{ne} is the number of neighbours that are closer to the deformed surface. The weight W_j is set as the invert of the edge length $W_j = L_j^{-1}$. The scale is a function of the ratio between the local displacement and the cell sizes around the point: when the point displacement is smaller than a fraction K ($K = 0.1$ was used in this work), the displacement was scaled by $D = D/KL$. For a parallel computation, this process was applied in each partition of the domain, and at the end of an inner loop in the partition, the displacements at the boundaries were exchanged between processors, and this process was repeated between 20 and 50 times. Furthermore, a repair method was implemented for collapsed cells to allow bigger deformations to be used, using a volume spline interpolation in the collapsed volumes surrounded by valid cells.

The proposed method was then applied to aeroelastic simulations of the AMP wing using an unstructured grid, a generic wing/flap configuration using a Chimera grid, and a generic aeroelastic simulation of the X31 aircraft during manoeuvres using an unstructured grid. The method proved to be able to deal with the high wing deformation levels and the normal deformations of the full aircraft configuration.

For the Fun3D solver, which uses unstructured grids, Biedron and Lee-Rausch[25] used the linear elasticity equations, which is based on a Young's modulus and a Poisson's ratio. The Poisson's ratio was set to 0. Two methods can be used to compute the Young's modulus: it can be proportional to either the inverse of the closest wall, either the dual-cell volume. The latter method was chosen by Biedron and Lee-Rausch. The elasticity equations were solved at each time-step as a steady-state problem. The blade surface was deformed following the sectional quarter-chord line deformation, which were interpolated from the structural beam modes using splines. If overset grids were used, the linear elasticity problem was applied to the whole domain, and the points that should not be moved were marked and their deformation was not applied. This method was tested on the HART-II rotor in forward-flight, and results are described in the next section.

A last possible approach consists in using Delaunay graphs as shown by Yoon *et al.* [26]. This deformation method was described in the work of Liu *et al.* [27]. The mesh deformation consists in four steps. The first step generates the Delaunay graph from the selected points on the domain boundaries. The selected points must allow the whole domain to be covered with the Delaunay graph. The second step computes the relative surface/volume coefficients that are used to associate the mesh points with the Delaunay graph. This implies that all points in the domain are located within one element of the Delaunay graph. Each node is associated with the element it lies in. For a 2D grid, each triangular element is divided into 3 triangles using the mesh point and the three element vertices, while a tetrahedron element in 3D is divided in four tetrahedra, using the mesh point. The share of the triangle surfaces or tetrahedra volumes is kept constant before and after the deformation. The boundaries are then moved to the deformed position in the Delaunay graph. A limitation arises from this movement: the surface/volume of each element has to stay positive, limiting the amplitudes of the displacements. The mesh points are then moved, ensuring that the ratio of the triangles/tetrahedron formed from the Delaunay graph and the grid points stay constant.

The method was applied to unstructured grids for various cases: a pitching multi-element aerofoil, a multi-element aerofoil with large dynamic deployments, movements of a deformable sphere in a cube and deformation of a flexible 3D wing. It showed the ability of the method to cope with large displacements. However, large movements had to be decomposed into smaller segments and the Delaunay graph was recomputed at each step in order to limit the applied deformation in one step and thus avoid negative volumes in the Delaunay graph. These steps are however bigger than what would be required for a CFD simulation. For a 20% artificial bending at the tip of the wing, no intermediate step was required to generate the deformed mesh and only one Delaunay graph could be used for the whole simulation. It showed as well that the Delaunay graph did not maintain the surface integrity. The proposed method was also compared to spring-analogy for a wing-body simulation. The Delaunay graph proved 10 times faster but consumed 50% more memory.

1.2.4 Previous Attempts to Couple CFD and CSD Codes

The coupling of a computational fluid dynamics (CFD) code with a computational structural dynamics (CSD) code is not a simple task. This is evident from the relatively small number of researchers who have successfully demonstrated this coupling in practical rotor calculations.

Research conducted in France

In 2001, Servera *et al.* [28] conducted a study, coupling the CFD code WAVES with the dynamics code HOST. A weak coupling strategy was used. HOST was used to supply the trim state, based on 2D-aerofoil look-up tables, and the blade deformation from the aerodynamic loads. The blade was represented as a set of rigid blade elements linked by fictive articulations, and a modal approach was chosen to compute the blade in-flight deformation. WAVES solved Euler's equations on multi-block grids.

A weak coupling procedure was used: at the end of each revolution, the rotor trim state was recomputed by HOST based on the error between the current global loads and the target ones, and the deformations were recomputed from sectional loads obtained from the CFD solver. This process was repeated until convergence of the loads and deformation. A comparison of the effect of the various loads was also carried out: the sectional loads transferred from the CFD solver to the CSD solver first only contained the normal force component, then the sectional pitching moment was included, and finally the sectional drag was also transferred.

The coupling method was applied to the ONERA 7A rotor in forward flight. The chosen test case was a high advance-ratio flight ($\mu = 0.4$, $M_{tip} = 0.646$). This particular conditions were tested as part of the HELISHAPE program, allowing a validation of the simulation against experimental measurements (see Section 1.2.5 for more details). First, the use of HOST alone was compared to weakly coupled simulations. The difference between the two coupled simulations lied in the transfer of the sectional forces from CFD to CSD: in the first one, only the normal forces were transferred, while in the second one, the pitching moments were included as well. Four iterations allowed the first coupled simulation to converge. The addition of the pitching moments in the transfer allowed for predictions of the control

angles that were closer to experimental measurements. Sectional loads at $r/R = 0.975$ were compared to experimental measurements. While the difference between HOST predictions and the first coupled simulation were limited, the inclusion of the pitching moment in the force transfer allowed only for a slight improvement of the normal force prediction. Also, large improvements were noticed in the sectional moment, with the down-peak on the advancing side being predicted at the right azimuth and its amplitude being slightly under-predicted. The improvement was also noticeable on the retreating side. The tip torsion was also extracted and compared to experimental measurements. The general shape of the twist variation with the azimuth was captured, but the strong 5/Rev component in the experimental measurements had a lower amplitude in the simulation, and its phase was also offset.

A new simulation was run, adding the drag force in the force transfer between CFD and CSD. The only noticeable difference in the sectional loads at $r/R = 0.975$ appeared on the drag force, with a lower drag coefficient on the back of the disk as a result. The lack of experimental results did however not allow to assess the possible improvements from this difference.

The ONERA 7AD rotor was also tested at the same flight conditions, using the three components of the sectional forces in the force transfer, and compared to the HOST uncoupled simulation as well as experimental measurements. The normal force predictions were not improved and the amplitude of the down-peak in the normal force was reduced compared to the uncoupled simulation, while both simulations predict a lower amplitude and a different phase compared to experiments. While the predictions of the sectional moments were improved by the coupled simulation, the azimuth of the down-peak was offset by 45 degrees. The tip torsion showed some improvements in amplitude, but the 5/Rev component was sill under-predicted and had a phase offset. To conclude, improvements were expected to come from the use of a Navier-Stokes solver, mainly due to the better ability of this model to predict sectional loads.

Table 1.2: Hovering flight conditions used by Beaumier *et al.* [29].

Rotor	Re_{tip}	M_{tip}	Collective (degrees)
ONERA 7A	1.9×10^6	0.617	5.97, 7.46, 8.94
Bo-105	4.5×10^6	0.641	3.3, 6.2, 8.0, 9.4

Beaumier *et al.* [29] carried out a study on hovering rotors, and compared the predictions from two CFD solvers: CANARI and FLOWer, with both solving the Navier-Stokes equations. FLOWer used the Baldwin-Lomax turbulence model, and CANARI Michel's algebraic turbulence model. Two rotors were chosen for this comparison: the ONERA 7A, a fully articulated rotor, and the Bo-105, a hingeless rotor. The flight conditions are summarised in Table 1.2.

A first comparison was carried out between FLOWer and CANARI using a rigid ONERA 7A rotor at a collective of $\theta_0 = 5.97$ degrees. The integrated loads predictions agreed well, the difference between the thrust predictions was limited to 2% and between the figures of merit 0.01. The loading distribution along the span predicted by CANARI was higher at the root and lower at the tip compared to FLOWer. The vortex from the preceeding blade also showed higher vorticity in CANARI, which probably came from a lower numerical dissipation in the employed numerical scheme. Compared to experimental measurements, the thrust was overestimated by 18% but the error on the figure of merit was minimal (less than 0.01).

A second comparison was carried out to assess the effect of the structural deformations. These were obtained from a simulation from R85, based on the lifting line theory. The ONERA 7A rotor was first considered. The lift and torque coefficients at a given collective were lowered by the blade deformation, getting in closer agreement with experimental measurements. However, the figure of merit was under-estimated in both cases by 0.05 for FLOWer simulations and 0.03 for CANARI simulations. Similar results were obtained for the Bo-105 rotor. The over-estimation of the lift coefficient was divided by 5 when including aeroelastic deformation. The tip torsion for the ONERA 7A reached -0.45 degrees at $\theta_0 = 5.97$ degrees, which was small but was expected due to the stiffness of the model rotor blade. However, in the Bo-105 case, the tip torsion reached -2 degrees at $\theta_0 = 6.2$ degrees, explaining the higher difference between the thrust and torque coefficients from the rigid and elastic blades at a given collective. The effect of transition was also investigated on the ONERA 7A rotor, showing little difference in thrust, but lowering the torque coefficient, allowing for better figure of merit predictions compared to experimental measurements.

In 2008, Ortun *et al.* [21] were interested in coupling a more complex 3D-FEM structural model

developed for the ERATO blade by Truong[8] and described in Section 1.2.1. The CFD solver elsA was coupled to HOST to obtain the rotor trim and MSC.Marc to compute the structural deformations. elsA solved the Navier-Stokes equations, using the algebraic turbulence model from Michel. An azimuthal step of $\Delta\Psi = 1.2$ degrees was used, with a strong coupling approach. A first validation of the coupling strategy was carried out using the ONERA 7A rotor at an advance-ratio $\mu = 0.4$, from the HELISHAPE database, that was used previously by Servera *et al.* [28]. A grid of 2 million nodes was used, and the 7A blade was modelled using a Timoshenko beam. The elsA/MSC.Marc/HOST coupling method was compared to a elsA/HOST coupling, where HOST was also computing the blade structural deformations. Nine revolutions were performed to reach convergence: the first three were performed by HOST alone to initialise the deformations, followed by six with the proposed coupled solvers. The blade deformation and sectional loading agreed well between the two simulations, demonstrating the ability of the new approach to perform aeroelastic calculations. The agreement of the sectional loads with experimental measurements was fair on the retreating side, but poor on the advancing side. The coarse grid was reported as the reason for these discrepancies.

The assessment of the coupling approach then moved to the ERATO blade, which has a complex geometry. A demonstration of the method was performed, using a very coarse CFD grid containing 0.58 million nodes. The flow field was solved around the rotor flying at a high advance-ratio $\mu = 0.423$. A 3D-FEM structural model, described by Truong[8] was used. While the comparison of sectional loads with experimental measurements proved poor, this paper was only aiming at presenting the coupling method, using a 3D-FEM model. The CFD grid was extremely coarse, which did not allow for the main features of the flow (shock and stall) to be properly resolved.

Research conducted in Germany

In 2002, Altmikus *et al.* [30] compared weak and strong coupling approaches. Their study was performed using HOST to trim the solution and compute the structural deformations, and the FLOWer and WAVES CFD solvers were compared, both using Euler's equations. The blade eigenmodes were obtained using a quasi-1D Euler-Bernoulli beam model, and were used by HOST to compute the blade deformations

using a modal approach.

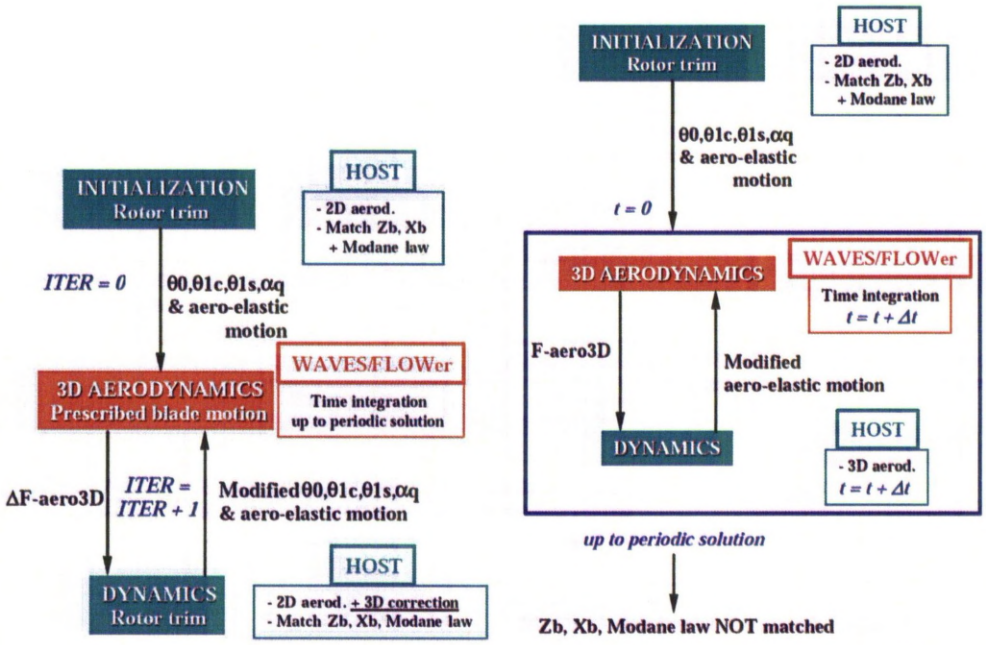

(a) Weak coupling strategy, from [30]

(b) Strong coupling strategy, from [30]

Figure 1.3: Strong and weak coupling strategies used by Altmikus *et al.* [30], from [30].

The weak coupling strategy is shown in Figure 1.3a. The control angles and blade deformation were first initialised using the HOST lifting line model. The flow field was then computed using the CFD solver, and the resulting loads extracted. HOST updated the blade deformations using these new loads, and a new trim state was also determined to achieve the required integral loads. The CFD flow was then updated with the new blade shape and control angles. This iterative process was repeated until convergence of the loads, control angles and blade deformations.

The strong coupling strategy is shown in Figure 1.3b. The structure and fluid solvers are offset by half a time step. A second-order Adams-Bashford-Moulton predictor-corrector scheme was used. The simulation was initialised using a HOST simulation based on the 2D-lifting line model. Modifying the control angles to trim the rotor was however more complex. Two trimming procedure were assessed: the *manual* and the *automatic* methods. The *manual* method involved linearising the relationship between the control inputs and the trim condition. At the end of the coupling scheme, new control angles were estimated from the present control vector and the desired control vector which was defined by the trim

conditions. This is shown in equation 1.9 where **J** represents the Jacobian matrix of the trimming. With the new updated commands, a new aerodynamic integration takes place to give a periodic solution. If the new solution is still not trimmed then the process is repeated.

$$\begin{bmatrix} \theta_0 \\ \alpha_S \\ \theta_{1c} \\ \theta_{1s} \end{bmatrix}_{new} = \begin{bmatrix} \theta_0 \\ \alpha_S \\ \theta_{1c} \\ \theta_{1s} \end{bmatrix}_{old} + \mathbf{J} \cdot \left(\begin{bmatrix} Z_b \\ X_b \\ \beta_{ls} \\ \beta_{lc} + \theta_{ls} \end{bmatrix}_{new} - \begin{bmatrix} Z_b \\ X_b \\ \beta_{ls} \\ \beta_{lc} + \theta_{ls} \end{bmatrix}_{old} \right) \tag{1.9}$$

The *automatic* method is a combination of both weak and strong coupling. The sectional aerodynamic loads are stored at each time step. After convergence was obtained for the original control inputs, the stored aerodynamic loads were harmonically decomposed and served as input for a new trim computation using the weak coupling approach. This means that a new data set of control inputs were obtained followed by a strongly coupled simulation until the aeroelastic system had freely developed periodicity. The weak/strong coupling procedure was repeated until a global trim was achieved.

Table 1.3: Properties of the flight simulations by Altmikus *et al.* [30].

Rotor	μ	Re_∞	M_{tip}	X_b	Z_b
ONERA 7A	0.4	0.856×10^5	0.646	1.6	12.5

Table 1.4: Flight conditions used by Altmikus *et al.* [30].

CFD code	$\Delta\Psi$ (degrees)	Grid size
WAVES	0.06	0.7×10^6
FLOWer	1	2.0×10^6

The ONERA 7A rotor in high-speed forward flight ($\mu = 0.4$) was used to validate the strong coupling approach with both FLOWer and WAVES, and compare the effectiveness of the two trimming procedures. The flight conditions for the CFD simulations are summarised in Table 1.3 and the properties of the simulations in Table 1.4. The small azimuthal steps used by WAVES were justified by the lack of dual time stepping in its numerical scheme. A first assessment of the two CFD solvers was first performed without trimming the rotors, using control angles from HOST simulations. The resulting

lift predicted by FLOWer was lower than the one from WAVES. This difference is also visible in the sectional loads, but the variations of the loads are equivalent in the two simulations. The elastic torsion at the tip of the blade was similar between the two simulations, but the down-peak at $\Psi = 130$ degrees was not predicted, and the variations were generally smaller than in the experiments. The trim methods were then tested. The *automatic* trim method, used in the FLOWer simulation, needed 4 iterations and 16 revolutions to reach convergence. On the other hand, the *manual* trim method, used in the WAVES simulation, needed 3 iterations and 23 revolutions to reach convergence. The difference in the sectional loads and tip torsion between the two trimmed simulations was low.

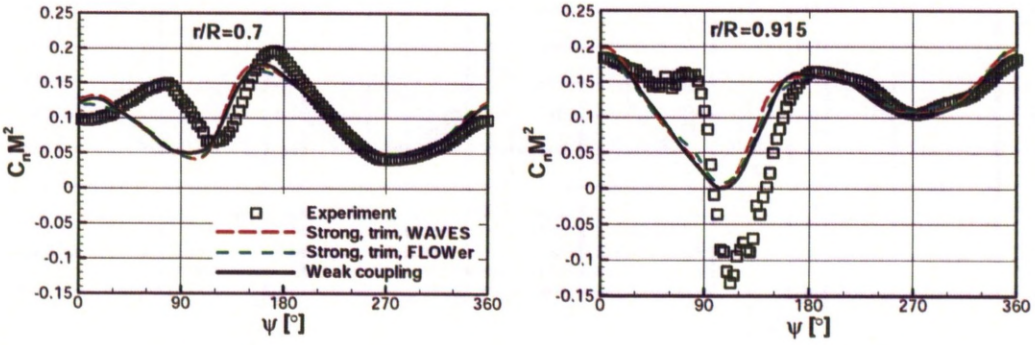

(a) $r/R = 0.7$ (b) $r/R = 0.915$

Figure 1.4: Predicted Mach-scaled sectional normal force on the ONERA 7A blade in forward flight ($\mu = 0.4$) by Altmikus *et al.* [28], compared to experimental measurements.

A simulation of the same case using the weak coupling approach was performed using WAVES and HOST. Five iterations allowed the rotor trim and blade deformations to converge. The resulting trim state was very similar to the one obtained using the strong coupling strategy. The main difference in the sectional loads appeared around $\Psi = 0$ degree and $\Psi = 180$ degrees. However, this difference was limited and appeared to be linked to the difference in longitudinal cyclic between the two simulations. The comparison of the sectional loads with experimental measurements showed that the amplitude and the phase of the strong down-peak of the normal force on the advancing side were not predicted accurately as shown in Figure 1.4. The sectional moments amplitude was also under-predicted on the advancing side. The tip torsion also showed major differences: the peak-to-peak amplitude was lower when using the strong coupling (1.25 degrees compared to 1.75 degrees), but more importantly lower than the exper-

imental measurements (2.4 degrees). The amplitude of the 5/rev content was under-estimated, and the phase was offset. The strong coupling approach, despite being more costly (about 2.5 times the CPU cost of a weak coupling), did not improve the predictions. However, the poor prediction of the moments and therefore of the tip torsion, was expected by the authors due to the use of Euler's equations.

A weak coupling procedure has been documented by Pahlke and Van der Wall[31]. The aim of this paper was to present a weak fluid-structure coupling technique between the CFD solver FLOWer, which uses RANS equations, with the DLR rotor simulation code S4. For the turbulence model, the algebraic Baldwin-Lomax model with a modification by Degani and Schiff together with two versions of the 2-equation $k-\omega$ model ($k-\omega$[32] and $k-\omega$ LEA[33] with Kok's modification for vortices) were compared. The coupling methodology between the two codes was as follows. The S4 code using simplified aerodynamics calculated the trim state. This gave the elastic blade motion based upon blade element theory. Next the CFD code was applied with the previously calculated blade motion acting as prescribed boundary conditions. This provided a field of aerodynamic forces and moments for every blade element and azimuthal position. The difference between the aerodynamics computed by CFD and the S4 code was then calculated and added to the S4 aerodynamic model in terms of normal forces, tangential forces and pitching moments for the next iteration as a non-variable offset. A new trim state was then obtained, and the procedure was repeated until the blade motion between two consecutive iterations was within a specified tolerance. This approach was tested by using the ONERA 7A rotor in high-speed forward flight used previously by Servera *et al.* [28] and Altmikus *et al.* [30]. A first set of simulations were performed using the range of turbulence models, using a single-bladed rotor to save on the computational time. It was concluded that for the moderate loading, high speed forward flight configuration in question the differences between the Baldwin-Lomax model and the more sophisticated models were not significant. All computations were, therefore, completed using the Baldwin-Lomax model as this saved approximately 50 percent of the computational time compared to the more sophisticated turbulence models.

The 7A rotor results showed that five iterations were required to obtain a converged trim for the control angles. However, there was a 2.5 degrees difference in collective between the experimental and

computed values. The cyclic and rotor shaft angles showed a slight improvement with differences ranging from 2 degrees to 0.1 degrees. The authors acknowledged this as only a fair agreement but stated that the differences could probably be explained by the simulation of an isolated rotor and did not include the nacelle or the wind tunnel walls. Comparisons of the results from the coupled FLOWer/S4 codes, and the uncoupled S4 code with the experimental data showed an improvement in the normal force distributions with the coupled code. The major improvement was in the phase matching of the tip torsion with experimental results. The coupled code also produced less overshoots than the uncoupled version. Comparisons of the elastic torsion at the blade tip showed that both coupled and uncoupled codes predicted the maximum torsion at the tip well, although the phase agreement was slightly improved for the coupled methods. The experimental results showed a 5/Rev effect in the blade tip torsion. This was captured by the uncoupled method but almost entirely damped out by the coupled methods.

The results from the 7AD rotor showed that the trim procedure was slightly faster for this rotor, requiring only four iterations to converge. The differences between the experimental and computed control angles were also slightly improved. Comparison of the coupled code with the experimental data for the normal force distributions only showed a fair agreement. When comparing the pitching moment distributions the coupled code also failed to predict the double peak character of the experimental data around $\Psi = 90$ degrees. As with the 7A rotor blade, the coupled code did not predict the 5/Rev content in the torsion at the blade tip. It was found that for predicting the power consumption of the rotor, the agreement between the experimental and computed values was improved by the use of the coupled codes. Overall, the weakly coupled procedure gave an improvement in the solution when compared to experimental data.

A study by Pomin and Wagner[34] used both a strongly coupled procedure along with a viscous flow solver. The Navier-Stokes solver INROT was coupled with the finite element structural dynamics code DYNROT and both hover and forward flight configurations were modelled. DYNROT modelled the blades as quasi-one-dimensional, geometrically linear, Timoshenko beams. INROT computed the flow field, using structured Chimera grids. Euler's equations were solved in the background grid while the RANS equations were solved in the near-blade mesh, using the Baldwin-Lomax turbulence model,

to save on the memory and CPU time. The location of the transition from laminar to turbulent was forced, using experimental measurements.

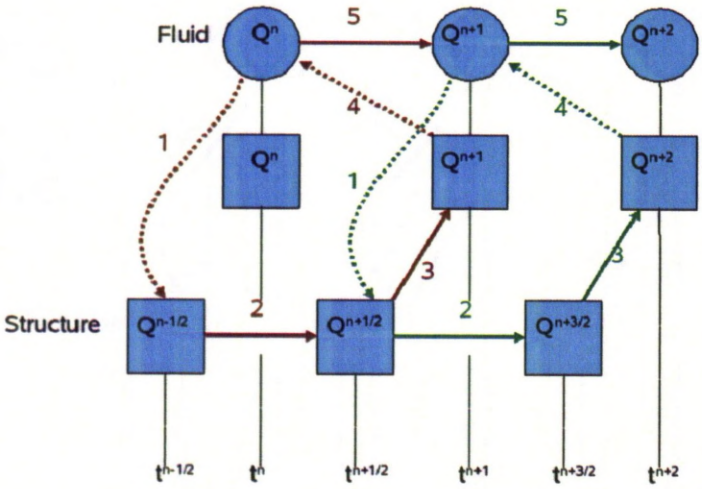

Figure 1.5: Implicit-implicit coupling scheme used by Pomin and Wagner[35], from [35].

The coupling between the flow and structural codes was defined as strong with information exchanged throughout the computation along the surface of the rotor blade. The coupling followed an implicit-implicit scheme shown in Figure 1.5. Firstly the aerodynamic loads from time step t^n were transferred to the structural code. Time integration using the mid-point rule was performed taking the structural state from $t^{n-1/2}$ to $t^{n+1/2}$. A predictor step then determined the surface co-ordinates at t^{n+1}, which were transferred back to the CFD solver. The grid was then deformed for the new time level of t^{n+1}.

The coupling strategy was first tested for a hovering ONERA 7A rotor. The flight conditions were equivalent to the ones used by Beaumier *et al.* [29] shown in Table 1.2. The CFD grid contained approximately 15.8 million nodes. The simulation was run as an unsteady simulation for the full rotor, and the azimuthal increment was set to $\Delta\Psi = 1$ degree. The global rotor coefficients presented in the results have been averaged over the final four revolutions. The computed values of thrust for coupled calculations and the pure Euler calculations correlated well with the experimental values. The effect of the inclusion of the laminar-turbulent transition was small. The inclusion of the laminar-turbulent

transition did, however, have an effect on the prediction of the torque coefficient as predictions were reduced by 7.7%, presumably coming from the 30% reduction in skin-friction-induced rotor torque. The inclusion of coupling reduced the predicted torque coefficient by 5.5% from the uncoupled results. Predictions of the rotor figure of merit were very similar between the coupled and uncoupled computations with both values agreeing fairly well with the experimental data. The inclusion of the laminar-turbulent transition caused a significant over estimation of the figure of merit, which was thought to come from the lack of hub or an error in the supplied location of the transition. Plots of the pressure distribution for the coupled Navier-Stokes computations correlated well with the experimental data with the only significant differences being deviations in the rear portion of the suction side at $r/R = 0.50$ and an over estimation of the suction peak at the tip.

The strong coupling method was then tested on the ONERA 7A rotor in high-speed forward flight ($\mu = 0.4$) presented previously. It was found that the rotor thrust predicted by the coupled Navier-Stokes analysis correlated far better with the experimental values than the uncoupled predictions did. It was also noted that the results from both viscous and inviscid calculations were very similar for the uncoupled codes, while for the coupled codes there was almost 9% difference between viscous and inviscid computations. This indicates that significant differences exist in the calculation of the blade motion and deformation between the Euler and Navier-Stokes codes. The authors[29] stated that the coupled analysis underestimated the experimental drag and attributed this to not including the rotor head in the computations. The coupled Navier-Stokes analysis predicted the coefficient of torque to within 3% of the experimental value. Plots of the normal force coefficients over the entire azimuth for a range of blade radial locations showed that the data from the coupled analysis correlated reasonably well with experimental data. There was a slight phase shift between the data sets and the dip in the tip region of the blade at $\Psi = 120$ degrees was underestimated. The local normal force maximum that preceded this characteristic dip was predicted as a trend only. Comparison of the pitching moment distributions showed that both viscous and inviscid computations predicted the pitching moment well towards the blade tip although there were slight improvements when using the Navier-Stokes model. At $r/R = 0.7$ the Navier-Stokes computation significantly under predicted the negative pitching moment on the ad-

vancing rotor. However, the Euler calculation returned a positive value for the pitching moment for the first quarter of the azimuth. The correlation of the chordwise pressure distributions at the tip between experimental and coupled analyses was generally good, especially on the retreating blade side. The high advance ratio meant that a strong shock built up on the advancing blade and the most significant discrepancies appeared when the shock weakened and vanished. Further inboard, the correlation between computed and experimental results worsened on the retreating side owing to the region of reverse flow and low dynamic pressure which had to be dealt with by the compressible flow solver. The eddy viscosity model was also unable to predict accurately the dynamic stall on the retreating blade, which was needed to accurately predict the blade loads.

Finally, the authors stated that the correlation between the experimental and computed results could be further improved, albeit at a very high computational cost, by incorporating a trim capability in the aeroelastic analysis with the rotor trim provided by HOST used as the initial solution.

Dietz *et al.* [18] were interested in the aeroelastic deformation of the main rotor of a full helicopter configuration using the GOAHEAD[36] project configuration. FLOWer was used to compute the flow field using the RANS equations coupled with a $k-\omega$ turbulence model[32], and HOST was used for the trim and the structural deformations, based on a quasi-1D Bernoulli-Euler beam model. A weak coupling approach was chosen. Only the main rotor was undergoing elastic deformations. The azimuthal steps were set to $\Delta\Psi = 2$ degrees and the simulation was performed on a 14.2 million nodes grid. Low advance ratio flight conditions were chosen ($\mu = 0.0956$). In order to save CPU time, as a first step, the rotor was trimmed and deformed using the main rotor only, and this trim state and deformations were then used to initialise the simulation on the full helicopter configuration. Five iterations were needed to reach convergence of the loads and deformations on the isolated rotor, and an additional five iterations were then required to reach convergence on the full helicopter configuration. The effect of the fuselage on the flapping deformation proved limited: only the peak-to-peak amplitude was increased by 15%. However, the tip torsion saw a increase in the amplitude of the 4/Rev component by 50%. The phase of the torsion was kept similar.

Research conducted in the USA

Potsdam *et al.* [37] attempted to couple CFD with CSD using a weak coupling strategy. OVERFLOW-D was used for the CFD computations and the comprehensive code CAMRAD-II handled the the CSD analysis as well as the rotor trim. Four different flight conditions were simulated: high speed with advancing blade negative lift (flight counter 8534), low speed with BVIs (flight counter 8513) and high thrust with dynamic stall (flight counter 9017). The flight conditions modelled were chosen to match the flight test data from the flight testing of the UH-60A. Comparisons were also made against the comprehensive code CAMRAD-II with the addition of a multiple trailer consolidation wake model and an ONERA EDLIN dynamic stall model for the high thrust case.

The weak coupling procedure started with CAMRAD-II initialising the process using lifting line aerodynamics to trim the rotor. Quarter chord blade motions were then transferred to OVERFLOW-D. After $360/N_b$ degrees of azimuth were simulated by the CFD solver, the normal force, pitching moment and chord force were passed to CAMRAD-II. CAMRAD-II calculated the difference between the aerodynamic forces and moments it yielded from lifting line theory and those obtained using CFD and this corrected value was used in the next iteration to continue to trim the rotor. This process was continued until convergence.

A mesh of 26.5 million nodes was used in OVERFLOW-D, with blade azimuth steps of $\Delta\Psi = 0.05$ degrees. The coupling procedure performed well, with convergence being achieved for all of the flight conditions in ten iterations. In general, the addition of a coupled analysis gave a much improved comparison with the flight test data than the uncoupled comprehensive analysis. The most significant improvement evident from this analysis was the reduction in the phase lag in the air loads which tends to persistently cause problems. In the high-speed and high-thrust flights a clear improvement of the stall predictions was noticed.

The effect of the grid coarseness was also studied. Removing approximately every other point from the original base line grid yielded large computational savings as it reduced the required time to approximately 1/8th of the original. This increase in the grid coarseness had little effect on the predicted

air loads apart from at the high thrust condition. However, this was expected as stall prediction using CFD is already known to be highly grid dependent.

Sitaraman and Roget[38] simulated a pull-up manoeuvre of the UH-60A helicopter. The DYMORE structural code was coupled with the UMTURNS CFD solver, using strong coupling. The flow around the airfoil was calculated through the URANS equations with a Spalart-Allmaras turbulence model, and the wake was calculated through vorticity transport equations allowing for a cheaper calculation. The DYMORE code used beam elements. In this simulation, the blade deformation was updated at the end of each time step, using the history of the blade aerodynamic loading. This new shape was used for the computation of the next time step flow field. This method degraded the accuracy of the results and was unstable for high time step values. Furthermore, due to the strong coupling, the lifting line theory was firstly used alone instead of the CFD and then progressively mixed with the CFD during the first revolution to avoid instabilities at the beginning of the calculation. Thereafter only the CFD code was used.

The fuselage and tail rotor effects were not included in this simulation, therefore the lift was underestimated. During the pull-up, the nose quickly went up during the 16 first revolutions, and after this first phase, the angle of attack rapidly decreased due to the increased vertical speed and the pitch angle gradually decreased. The shape of the lift curve was well captured, apart from the end of the manoeuvre where the calculated lift was too high. The magnitude of the stalls was under-predicted, and the separation, re-attachment and shock-boundary layer interaction were not well captured due to the URANS model. The structural deformations were well captured, apart from the edgewise bending at $r/R = 0.5$. The authors also suggested that some progress could come from a better turbulence modelling as well as the full integration with flight dynamic.

Biedron and Lee-Rausch[25] coupled the RANS solver FUN3D with CAMRAD-II using a weak coupling approach. FUN3D is an unstructured solver, able to use overset grids. The coupling procedure was based on a first run of three revolutions to initialise the flow field, and thereafter, the blade shape was updated every $2 \times 360/N_b$ degrees of azimuth. The HART-II test case, described in Section 1.2.5, was used to assess the efficiency of the coupling method. First, a grid convergence study using prescribed

blade deformation from the AFDD was carried out. Grids of 3.6, 6.9 and 13.6 million nodes were used, and showed that the BVIs were sharply captured by the finest grid only. The medium grid was however deemed interesting: while not predicting the high frequencies in the loads, their lower frequency content was equivalent to the one from the fine grid. Stating that the high frequencies do not influence the blade deformations, the authors decided to carry out the coupled simulation on the medium grid to save CPU time.

In the coupled simulation, an azimuthal time step of $\Delta\Psi = 1$ degree was used. Eight iterations allowed to reach convergence on the loads. The deformations were converged after four iterations, the subsequent ones mainly updated the trim state. The tip torsion agreed with experimental measurements, but the peak-to-peak amplitude was lower. The resulting deformations from this simulations were then applied to the finer grid. The sectional loads at $r/R = 0.87$ were compared with experiments: the vibratory part agreed well, but the mean normal force and pitching moment amplitudes were under-predicted and over-predicted, respectively.

This study was completed in [39] with a study of the UH-60A rotor in forward flight, using flight test measurements to validate the simulations. The sensitivity of the coupled simulation to multiple parameters was assessed. The studied test cases were a high-speed flight (flight counter 8534) and a high-thrust flight (flight counter 9020). The sectional loads from simulations using azimuthal time steps of $\Delta\Psi = 1$ degrees and $\Delta\Psi = 0.5$ degrees were compared and showed no difference in the high-speed case and slightly modified the high frequency variations when recovering from the first stall (the amplitude was increased for the smaller time step) in the high thrust case. The addition of a fuselage only modified the loads on the innermost stations ($r/R < 0.5$), showing improvements when compared to flight test measurements. However, the mean air loads were not affected by this parameter. Finally, a turbulence model dependency was carried out, using the 1-equation SA model[40], the 2-equations $k-\omega$ SST model[41] and the hybrid RANS-LES HRLES model[42]. The former model was expected to improve the results, but in the high-speed case, with an azimuthal time step $\Delta\Psi = 1$ degrees, no difference was noticed between the sectional loads predicted by the three models. For the high-thrust case, an azimuthal time step $\Delta\Psi = 0.5$ degrees was used, and the only loads difference appeared on the

second stall at $\Psi = 330$ degrees, as shown in Figure 1.6. Surprisingly, while the $k-\omega$ SST and SA models were able to predict this stall, the HRLES model did not. The authors thought that the reasons for the limited differences between the loads came from either a too coarse grid or too big time steps.

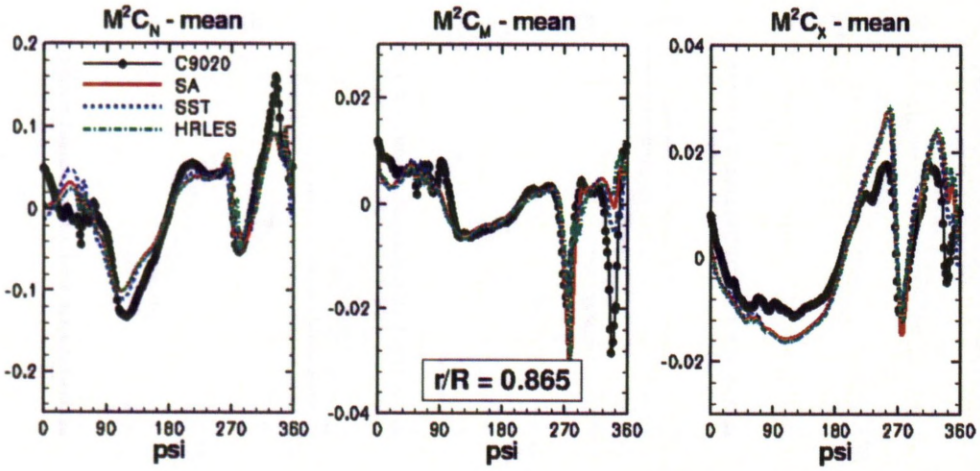

Figure 1.6: Predicted sectional loadings on the UH-60A blade in fight counter 9020 by Biedron and Lee-Rausch[39].

A summary of all presented coupling methods is given in Table 1.5.

Table 1.5: CFD/CSD coupling methods in the literature

Authors	**Coupling Strategy**	**CFD Code**	**CSD Code**	**Fluid model**	**Test case**
Servera *et al.* [28], 2001	Weak	WAVES	HOST	Euler	ONERA 7A and 7AD rotors ($\mu = 0.4$)
Beaumier *et al.* [29], 2001	Weak	CANARI, FLOWer	R85	RANS	Hovering ONERA 7A and Bo-105 rotors
Ortun *et al.* [21], 2008	Strong	elsA	MSC.Marc	RANS	ONERA 7A ($\mu = 0.4$) and ERATO ($\mu = 0.423$) rotors
Altmikus *et al.* [30], 2002	Weak, Strong	WAVES, FLOWer	HOST	Euler	ONERA 7A rotor ($\mu = 0.4$)
Pomin and Wagner[34], 2004	Strong	INROT	DYNROT	Hybrid RANS-Euler	ONERA 7A rotor (hover and $\mu = 0.4$)
Pahlke and Van der Wall[31], 2005	Weak	FLOWer	S4	RANS	ONERA 7A and 7AD rotors ($\mu = 0.4$)
Dietz *et al.* [18]	Weak	FLOWer	HOST	RANS	GOAHEAD helicopter configuration ($\mu = 0.0956$)
Potsdam *et al.* [37], 2004	Weak	OVERFLOW-D	CAMRAD II	RANS	UH-60A rotor (flight counters 8534, 8513 and 9017)
Sitaraman and Roget[38], 2009	Strong	UMTURNS	DYMORE	RANS, Vorticity transport	UH-60A rotor (pull-up manoeuvre flight counter 11029)
Biedron and Lee-Rausch[25,39], 2008, 2011	Weak	FUN3D	RANS	CAMRAD-II	HART-II ($\mu = 0.1509$) and UH-60A (flight counters 8534 and 9020) rotors

1.2.5 Experimental Data

There are limited experimental data in existence which can be used to validate computational results for aeroelastic rotors. Flight tests proved difficult to carry out: pilot inputs are constantly corrected to maintain the flight conditions and wind gusts or wind velocity changes in the atmosphere will alter the conditions. Flight testing is particularly difficult in hover where pilots tend to maintain a fixed position, countering the wind effect, and also keep correcting the helicopter unstable behaviour. Additionally, measurements in the flow field are hard to carry out. A way to overcome these limits is the use of a wind tunnel. However, wind tunnels tend to have a limited test section size and this creates other constraints linked to the use of a model rotor that are described in the following sub-section.

The Problems with Aeroelastic Scaling

Singleton and Yeager[43] studied the effect of three varying parameters when scaling rotor blades: the Reynolds number, the blade lock number and the blade elasticity. Several problems linked with scaling rotors were highlighted. To duplicate compressibility effects, the blade tip Mach number must be matched on the scaled and full-scale rotors, which also minimised the reduction in the Reynolds number limited by the chord size that can be employed at model scale. Considering that many rotor aerofoils are selected owing to the relatively high Mach numbers encountered by the advancing blade, matching the tip Mach number was deemed important. As the model is geometrically smaller, a much higher rotor speed is required to generate the same tip Mach numbers, leading to higher centrifugal loads on the model, which, in turn, affect the structural dynamics. However, modifying the elasticity of the blade had little effect on a scale model, compared to the lock number and Reynolds number effects. Therefore, Mach-scaling was recommended, along with a similar lock number. The Reynolds number should be kept as high as possible, possibly through the use of a heavy gas environment.

Friedmann[44] also carried out research into scaling for rotary wing aircraft, particularly focusing on scaling for aeroelasticity testing. Friedmann recognised that classical aeroelastic scaling laws are inadequate for use in modern applications, because they do not allow for the presence of a control system. Non-linearities coming from the control system (saturation, free-play and friction) as well as

aerodynamic non-linearities from the Euler or Navier-Stokes equations are not taken into account. A new approach to aeroelastic scaling was presented, combining the classical approach with a computer simulation of the problem. The computer simulation works by presenting a range of numerical similarity solutions that can replace the analytical solutions. By combining the two sets of requirements based upon the classical approach and the computer simulation, a refined set of scaling parameters was obtained. Keeping the original tip Mach number and Froude number was shown to be only possible if a full-scale rotor was tested. Therefore, only one of the two parameters could be maintained. The Froude scaling was recommended by Friedmann for aeroelastic stability test on isolated rotors and aeromechanical stability tests on full helicopter configuration, otherwise a Mach-scaling should be used.

Wind Tunnel Experiments

The validation of Tang and Dowell's[11] effort to include the ONERA code with Hodges and Dowell's non linear structural dynamics equations was achieved in the Duke University low speed wind tunnel. The model consisted of a blade section with a root support mechanism. The blade was constructed from an aluminium alloy spar with uniform mass per unit length. Styrofoam fairing elements covered the blade to give the aerodynamic contour of the blade. The blade was rectangular, untwisted, and flexible in flap, lag and torsion. The root mechanism was mounted to a very heavy support frame attached to the ground which allowed the blade to have a pitch motion degree of freedom with no flap or lag motion at the root. Stimulation in pitch was provided through an electric motor with variable speed through a cam. This enabled the driving frequency and amplitude to be adjusted. Strain gauges were glued to the spar to measure the bending-torsional deflections of the blade tip. The pitch angular displacement was measured through a rotational velocity/displacement transducer. This also measured the pitch and lateral displacement driving frequency and amplitude which are also partly measured by an accelerometer which was also mounted to the root mechanism.

As part of the HELISHAPE program, experimental data were obtained from the ONERA S1 wind tunnel, using the fully articulated, 4 bladed ONERA 7A and 7AD rotors described in Section 3.3.3. Forward flying rotors were tested. This high-speed forward flight proved popular for validating CFD/CSD

coupling strategies, as shown previously[21,28,30,31,34]. The flight conditions were previously summarised in Table 1.3. The rotor was trimmed using the Modane law, meaning that the non dimensional lift and propulsive forces had to match whilst setting the longitudinal flapping angle to zero and the lateral flapping angle to the longitudinal pitch angle.

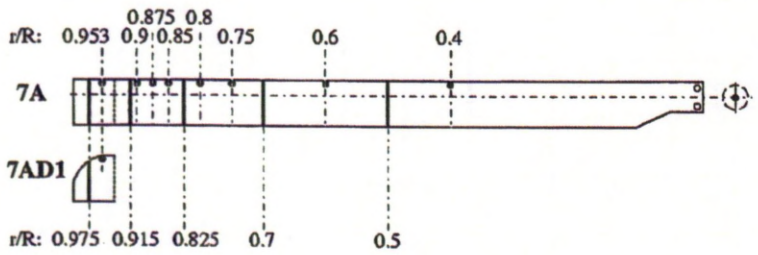

Figure 1.7: Location of the pressure taps on the ONERA 7A and 7AD rotors, from Schultz *et al.* [45].

Chordwise pressure distributions were measured at spanwise locations given by $0.5R$, $0.7R$, $0.825R$, $0.915R$ and $0.975R$, as shown in Figure 1.7. These pressures were integrated and the data was corrected so as to isolate the hub forces and rotor stub forces from the total force in order to obtain the normal force coefficients and pitching moments at these locations.

These rotors were also later tested in the DNW wind tunnel by Schultz *et al.* [45]. The experimental setup is shown in Figure 1.8. The rotors were tested in three flight conditions: in hover, in descent flight with BVIs ($\mu = 0.155$) and in moderate high-speed level flight ($\mu = 0.336$). The pressure distribution on the blade surface was measured at the same location as in the HELISHAPE program, but noise levels were also measured in a horizontal plane located under the rotor.

Wong *et al.* [46] recently conducted a proof of concept study into using pressure sensitive paint (PSP) for measuring the pressure distributions on a hovering rotor. The aim of using PSP was to better understand the pressure distribution at the blade tip and hence better understand the fundamental physics of the rotor blade tip. Instrumenting the blades with additional transducers to increase the spatial resolution quickly becomes prohibitive owing to the cost and practicality of fitting a large number of sensors into a small area. It was hoped that PSP will yield a significant increase in spatial resolution together with a cost saving over discrete transducers. PSP contains luminophores which react optically

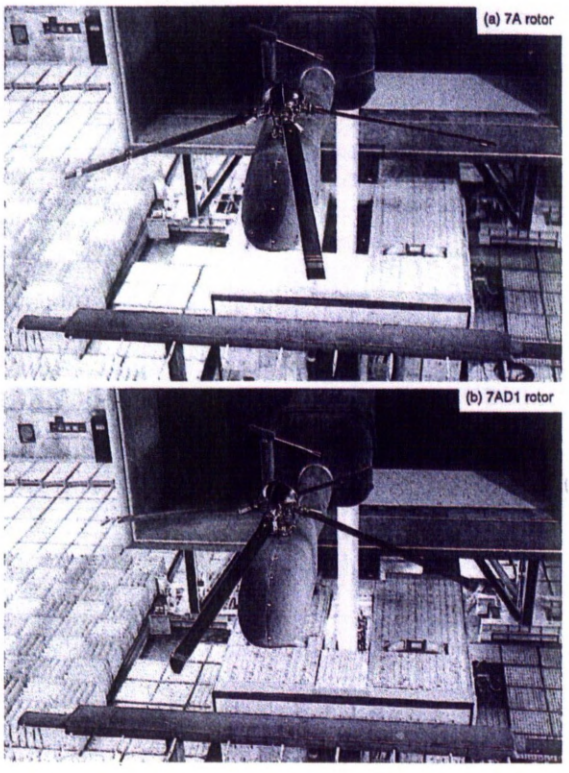

Figure 1.8: Experimental setup for the ONERA 7A and 7AD rotors experiments, from Schultz *et al.* [45].

to the presence of oxygen. The presence of oxygen inhibits the luminophores ability to luminesce. The variation in luminesce over an area relates directly to the local oxygen concentration and this leads to the pressure distribution. The experimental setup consisted of a five bladed fully articulated hub with one cuff of the hub instrumented to measure the lead-lag and flapping. The hub was mounted on the US Army 2-metre Rotor Test Stand (2MRTS). The rotor blades had constant chord out to the tip where they become swept and tapered. The testing was conducted in the Rotor Test Cell (RTC) at the NASA Langley Research Centre Subsonic Tunnel. The model was tested in hover for low to moderate thrust conditions. Results from use of the PSP indicated a low pressure region forming with increasing thrust at the leading edge. This data compared favourably with aerofoil data obtained by Flemming[47] and suggested that the observed low pressure region was the suction peak of the blade. The authors experienced several problems during the testing but believed that the approach was very promising and recommended further research.

Noonan *et al.* [48] conducted an investigation in a wind tunnel using a model helicopter rotor blade with slotted aerofoils at the tip. It has been recognised that to improve the lift and drag characteristics of an advanced single element aerofoil further, so called unconventional technology must be used. One such technology under investigation by the U.S. Army was the use of slotted aerofoils. Two dimensional aerodynamics suggested that the performance advantage from the use of slotted aerofoils was favourable. However, it was unknown whether the performance advantages would still be present in a three dimensional, unsteady, rotating environment as would be experienced in actual flight. For this reason a model rotor with slotted aerofoils was developed for experimental investigation.

The testing took place in the Langley Transonic Dynamics Tunnel (TDT). Freon 12 was used as the test medium, because its properties aided in the matching of the model Reynolds and Mach numbers with the full scale values. A further advantage of using Freon 12 was that its higher density allowed a heavier, less efficient structural design to be used whilst still having the required stiffness characteristics. The aeroelastic scaling of the model was representative of a full scale blade. The HIMARCS (High Manoeuvrability and Agility Rotor and Control System) rotor is described in Appendix A.1. Four different configurations were tested. The first (and baseline configuration) was a conventional blade with

no flaps or slats. The second and third blades were forward slotted aerofoils with -6 and -10 degrees slats respectively. The fourth blade used an aft-slotted aerofoil with a 3 degrees flap (trailing edge down). The blades were tested using the aeroelastic rotor experimental system (ARES) test bed, consisting in a streamlined fuselage shape which houses the rotor controls and drive system. The ARES is shown in Figure 1.9. This investigation made use of a four-bladed articulated hub with coincident lead-lag and flapping hinges and the pitch-flap coupling ratio was 0.5.

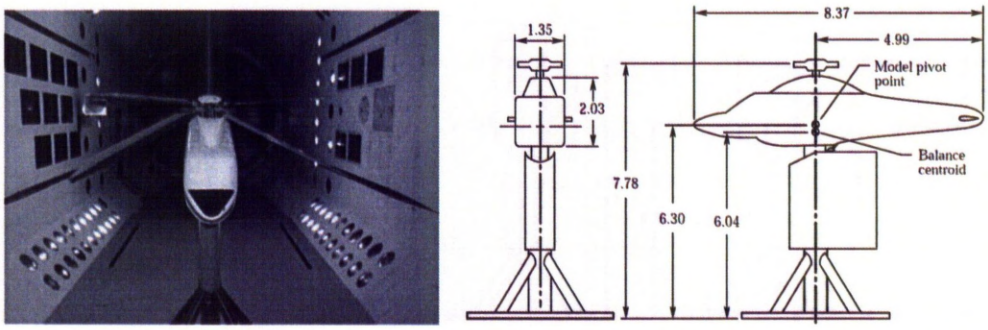

(a) ARES test bed, from [48]

(b) Schematic of the ARES test bed (dimensions in feet), from [48]

Figure 1.9: Experimental setup of the HIMARCS rotor.

The instrumentation on the model consisted of a strain gauge on one pitch link to measure the pitch link tension and compression loads. Rotary potentiometers mounted on the rotor hub measured the rotor blade flap and lag motions. A magnetic sensor determined the rotor shaft speed. A six component strain gauge balance mounted beneath the pylon and drive system measured the rotor forces and moments.

The four different blade configurations were all tested with the same values of advance ratio, hover tip Mach number, rotor shaft angle of attack and rotor blade collective pitch. In forward flight, data was obtained at advance ratios from $\mu = 0.15$ to 0.45. The blade tip Mach number was $M_{tip} = 0.627$. During hover, the height of the hub from the wind tunnel floor was $1.66R$, placing the rotor in ground effect. At each test point, rotor cyclic pitch was used to remove the first harmonic flapping with respect to the rotor shaft. This reduced the blade loads and made data acquisition simpler.

The results for the blade performance generally indicate that the 6 degree slat configuration has

benefits over the three other rotor configurations at higher lift coefficients. In the hover, it can be seen that for lift coefficients greater than 0.007, the rotor with the −6 degrees slat configuration has the lowest value of torque coefficient and the highest figure of merit. For lift coefficients lower than 0.007, the base line rotor configuration has the highest figure of merit and lowest torque coefficient. In forward flight the general trend appeared to be that the −6 degrees slat configuration had the lowest value of torque coefficient at higher lift coefficients with the baseline configuration having the lowest torque coefficients at lower lift coefficients. As the advance ratio increased the cross over point between the −6 degrees slat and the base line configuration occurred at lower values of lift coefficient. The results for the rotor blade loads also seem to indicate an advantage with using the −6 degrees slat configuration over the other three configurations.

Wilkie *et al.* [3] determined experimentally the rotating blade frequencies of a model generic helicopter blade mounted on an articulated hub. The blade properties are shown in Section 4.3.1. The experiment was conducted in the Langley Helicopter Hover Facility (HHF). The tests were conducted at sea level atmospheric conditions. The rotor blade geometry together with a photo of the experimental setup is shown in Figure 1.10. Results were obtained through strain gauges mounted in the flapwise, chordwise and torsional directions on one blade. These results were used to validate the results obtained using a finite element computer code, as shown in Figure 1.11.

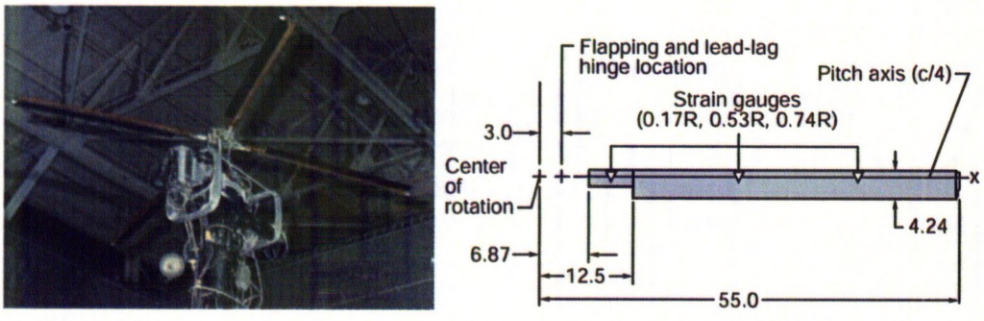

(a) Rotor blades mounted on the ARES test bed, from [3]

(b) Rotor Blade Geometry Used in the Rotating Shake Test Experiment, from [3]

Figure 1.10: Experimental setup for the rotating shake test experiment of Wilkie *et al.* [3].

A 1/5th scale model of the Boeing Helicopter Model 360 rotor was tested in the Duits Nederlandse Windtunnel (DNW)[15]. The rotor blades were instrumented with pressure transducers and strain

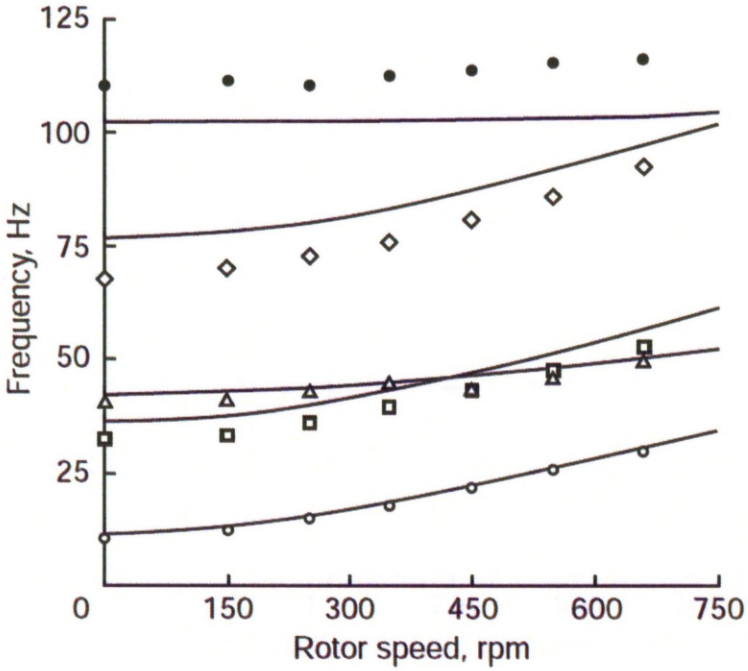

Figure 1.11: Comparison of the evolution of experimental and computed frequencies evolution with the rotor speed for Wilkie *et al.* 's[3] rotor, from [3].

gauges and data was obtained from two different flight tests. The first test varied the speed from a hover condition to an advance ratio of 0.36. the second test increased the advance ratio up to 0.46.

Table 1.6: Properties of the model rotor used in the HART-II test[49]

Property	Value
Number of blades (N_b)	4
Radius (R)	2 m
Root cutout	0.44 m
Blade chord (c)	0.121 m
Rotor solidity (σ)	0.077
Aerofoil section	NACA23012
Tab length	5 mm
Linear twist	-8 degrees$/R$
Precone	2.5 degrees

In 1994, the HART program was setup to investigate the effects of higher harmonic control (HHC) on rotor aerodynamics and noise radiation [49]. HHC consisted in adding a 3/Rev component to the blade cyclic. The main conclusion was that HHC reduces noise by increasing the blade vortex miss distance. HHC seemed to increase the strength of the vortices, yet the miss distance between the vortex

Table 1.7: Basic conditions in the HART-II test[49]

Variable	Nominal Value
Velocity (V_∞)	33 m/s
Rotational speed (Ω)	1041 RPM = 109 rad/s
Advance ratio (μ)	0.1508
Tip Mach number (M_{tip})	0.641
Thrust coefficient (C_T)	0.00886
Pitching and Rolling Moment	0.0
Shaft angle(α_s)	5.3 degrees

and the blade resulted in reduced noise. It was concluded that to effectively simulate noise reduction, it is essential to be able to simulate the wake accurately. HART-II was subsequently setup focused on the rotor wake. Details regarding the model blade and basic trim conditions are given in Tables 1.6 and 1.7. The experimental setup is shown in Figure 1.12.

The test was split in to four different parts, each requiring a different set of measuring equipment. The four parts were noise radiation, particle image velocimetry (PIV) of the advancing and retreating sides and blade position. The same test rig was used for each part.

The setup of the test rig was as follows. The rotor shaft was instrumented with a torque meter for measuring the drive moment and the power and measured strains were transmitted inductively to the non-rotating part. The balance upper plate was connected to the test rig base via seven force transducers (four in the vertical, two in the lateral and one in the horizontal direction). Swashplate actuators were mounted on top of the balance upper plate. These consisted of a lower electrical actuator for the collective and cyclic control. The HHC system tuned for 4/Rev dynamic motion was mounted on top of the lower electric actuators. It was decided to only make use of 3/Rev control for the test.

All of the rotor blades were equipped with six strain gauge pairs at the root (three for flap, two for lead-lag and one for torsion). Two of the blades were implemented with blade pitch sensors and two of the blades were implemented with a total of 51 absolute pressure transducers, enabling the leading edge pressure distribution to be measured between $r/R = 0.40$ and $r/R = 0.97$. At $r/R = 0.87$ a chord wise distribution of 17 Kulites enabled the computation of the sectional aerodynamic loading. The distribution of the blade instrumentation can be seen in Figure1.12e. Two strain gauge pairs were

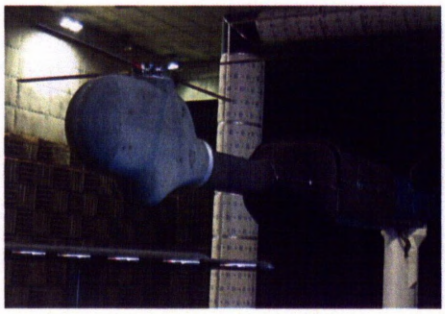

(a) General setup[49]

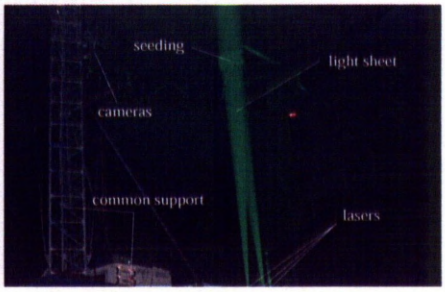

(b) PIV measurements setup[49]

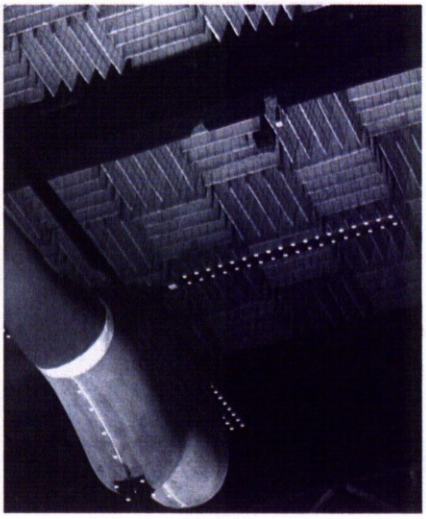

(c) SPR measurements setup[49]

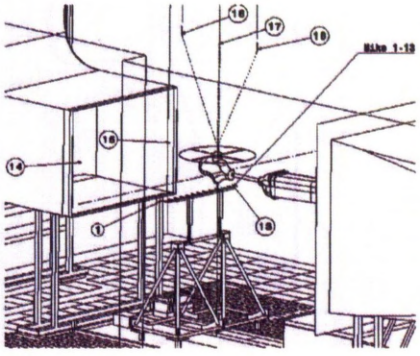

(d) Noise measurements setup[49]

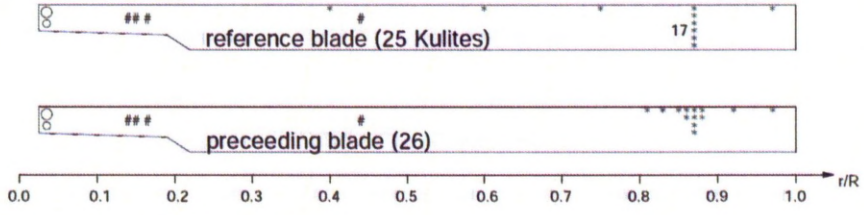

(e) Location of Instrumentation on the HART-II Rotor Blade[49]

Figure 1.12: HART-II experimental setup[49]

mounted on the shaft to measure the bending moments in the rotating frame.

The setup for the measurement of noise consisted of 13 microphones mounted laterally on a traverse, which was located under the rotor and swept along the helicopter flight direction. A further two microphones were mounted in the nozzle exit and three more beneath the ceiling. The measurements covered background noise, an angle of attack sweep from 6 degrees in climb to 6 degrees in descent, a complete sweep of 3/rev HHC phase angles in increments of 30 degrees in phase angle.

The PIV setup consisted of directing the beams from the lasers vertically into the flow at a predetermined test matrix of positions. The cameras were positioned with two looking from above the observation area and two looking from beneath. The cameras were focused on the predicted vertical range of vortex locations.

For the stereo pattern recognition (SPR) measurements, the blades were painted black and equipped with 18 pairs of white markers on the leading and trailing edges of the lower blade side. The markers were spaced equally between $r/R = 0.223$ and 0.997. The setup consisted of four widely spaced cameras on the ground, on pair focusing on the advancing disk and one the other pair focusing on the retreating disk. Two more cameras focused on the blade tips at 90 and 135 degrees of azimuth. These cameras captured the lead-lag, flap and torsional deflections of the tip relative to its non-rotating position at the same azimuths. The SPR data was recorded at increments of 15 degrees in azimuth with 50 to 100 data sets taken at each location.

The data set from the HART-II is very detailed providing information on blade motion, aerodynamics, and flow data to name but a few.

Flight Test Experiment

Flight test data were measured for the UH-60A in a level flight condition[51] and for transient manoeuvres[52]. The database provides details of aerodynamic pressures, control positions, rotor forces and moments and structural loads. The aircraft was fitted with a Rotating Data Acquisition System[51] with 242 pressure transducers, 50 temperature sensors, 25 strain gauges and 12 accelerometers, shown in Figure 1.13. Over 200 different flight conditions were flown, from hovering to high-speed forward flying rotors.

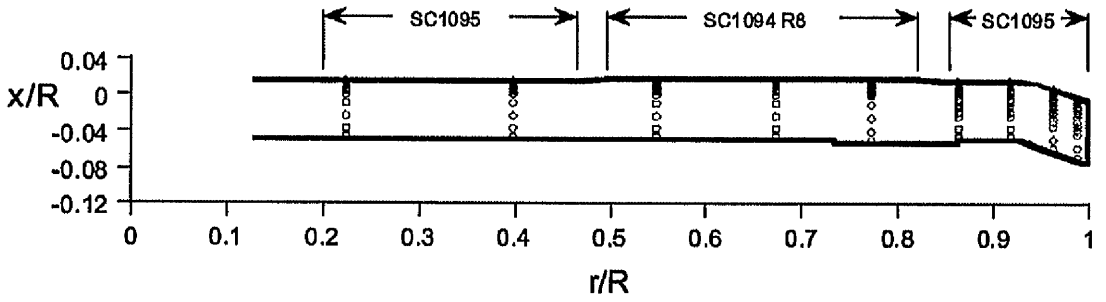

Figure 1.13: Planform of the UH-60A rotor blade, showing the location of pressure transducers located at $r/R = 0.225$, 0.400, 0.550, 0.675, 0.7750, 0.865, 0.920, 0.965 and 0.990[50].

Figure 1.14 shows various tested flight test conditions.

Summary of the Available Experimental Data

A summary of the available experimental data is shown in Table 1.8.

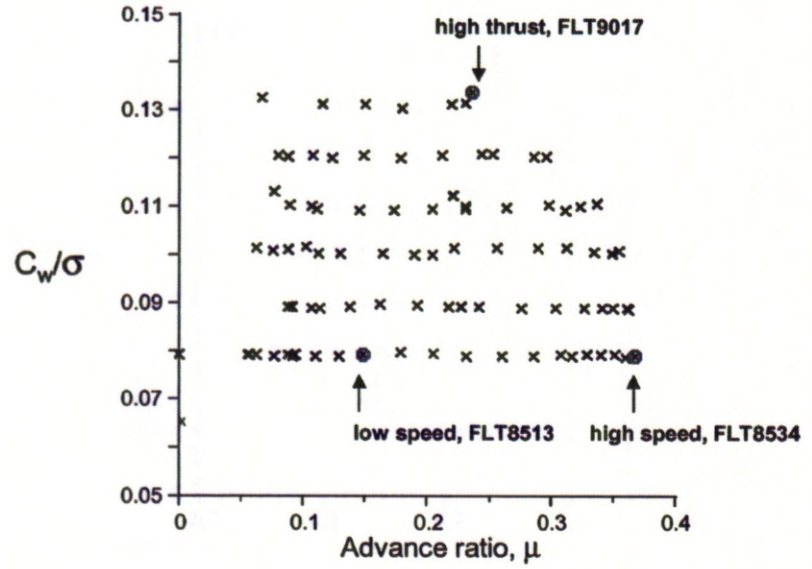

(a) Level flights[37]

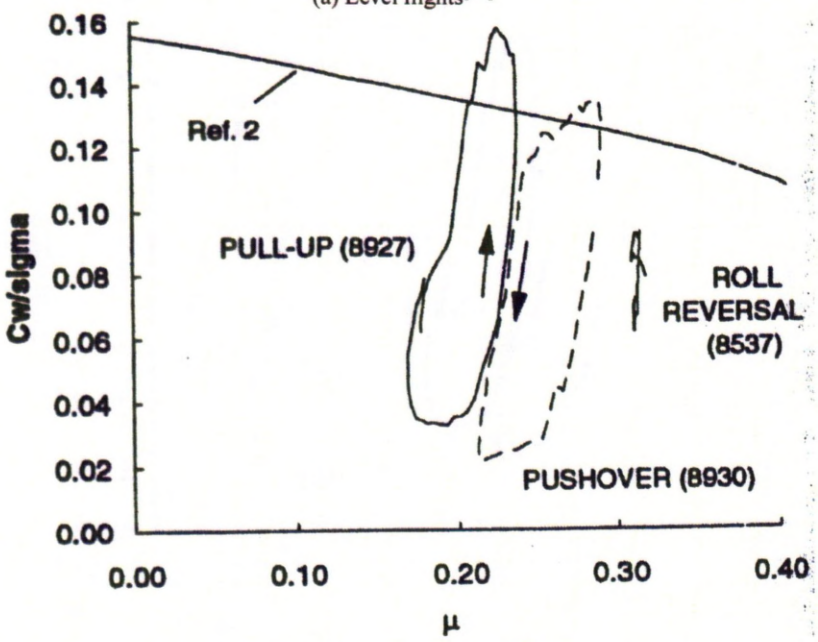

(b) Manoeuvring flights[52]

Figure 1.14: UH-60A flight test conditions[50]

Table 1.8: Summary of the wind tunnel (WT) and flight tests (FT) presented in the literature survey.

Test case	**WT/FT**	Re_{tip}	M_{tip}	μ	**Measurements**
HIMARCS	WT	4.12×10^6	0.627	$0-0.45$	Pitch Link Loads, C_L, C_D, C_Q
UH-60A	FT	6.813×10^6	0.642	$0-0.368$	Sectional loads, Integrated loads
HART-II	WT	1.91×10^6	0.641	0.1509	Sectional loads at $r/R = 0.87$, noise levels, PIV planes, blade deformation
Wilkie's rotor[3]	WT	$2.11 - 9.28 \times 10^6$	$0.065-0.284$	0	Blade natural frequencies
ONERA 7A and 7AD	WT	1.92×10^6	0.646, 0.641	$0-0.4$	Integrated loads, sectional loads, sections pressure coefficients
Boeing Vertol 360	WT	2.03×10^6	$0.635-0.637$	$0-0.356$	Sectional pressure distributions, flapping and torsional moments

1.2.6 Current turbulence models for rotor flows

Rotor CFD calculations are complex and turbulent due to the high Reynolds number. These flows contain many vortical structures interacting with the blades, and dynamic stall may also occur. Table 1.9 summarises turbulence models currently in use in the rotorcraft domain, and as shown these are dominated by the URANS 2-equation model $k-\omega$[32] and its derivatives. However these models show

Table 1.9: Comparison of the turbulence models used by several research institutes.

Author	CFD Solver	Turbulence Model	Test Case	Institute
Pahlke *et al.* [31]	FLOWer	BL, $k-\omega$[53], $k-\omega$ LEA[33,54]	7A/7AD	DLR
Dietz *et al.* [55]	FLOWer	$k-\omega$	BK-117 rotor and full helicopter	Eurocopter
Borie *et al.* [56]	elsA	$k-\omega$	NH-90	Eurocopter
Potsdam *et al.* [57]	OVERFLOW	SA[40] (near body) and inviscid	Dauphin 365N	AMRDEC
Khier *et al.* [58]	FLOWer	$k-\omega$	NH-90	DLR
Renaud *et al.* [59]	elsA	SA, $k-l$, $k-\omega$	Dauphin 365N	ONERA
Sitaraman *et al.* [38]	UMTURNS	SA and wake model	UH-60A	National Institute of Aerospace
Min *et al.* [60]	GENECAS	SA DES[61] and wake model	Bo-105 rotor	Georgia Tech
Steijl *et al.* [62]	HMB	$k-\omega$	Georgia Tech Teetering-Rotor, ROBIN and GOAHEAD	University of Liverpool
Smith *et al.* [63]	OVERFLOW	SA, $k-\omega$ SST[41], HRLES-SGS[42]	NACA0012 and SC1095 at high incidence or in reverse flow	Georgia Tech

deficiencies in several aspects of rotorcraft flows: in particular, the cutoff frequency of URANS is at about 500Hz, which could be too low to predict all the phenomena occurring in rotorcraft flow, with blades usually rotating at 300RPM and within a vortical wake. Other limitations come from the Boussinesq approximation. Boussinesq-based models tend to predict a turbulent stagnation, under predicted stall and over-predicted eddy viscosity at the core of vortices[64]. These problems can be partly solved by adding non-linear terms, however, the lack of numerical stability of such models make them impractical in the case of rotorcraft flows. Therefore, more advanced turbulence models could be used to improve

the predictions.

Direct Numerical Simulation

Direct Numerical Simulation (DNS) is the best possible fluids simulation. However, it is very expensive as every structure of the turbulence has to be resolved, which implies very fine grids, particularly close to a wall. Capturing small time scales also requires substantial computer resources. Therefore a DNS simulation can only be realised for low-Reynolds flows.

Rotor flows are high Reynolds number flows, and the geometry can be complex. Therefore, DNS is un-affordable now and in the next years. Spalart[65] assessed the order of magnitude of the computational cost for simulating a full airliner or a car. While the Reynolds number are slightly higher than in helicopter rotor cases, this case did not include the complexity of moving bodies and could provide an estimate for helicopter flows. Using DNS increased the required grid size from 10^7 to 10^{16} and the number of steps from $10^{3.5}$ to $10^{7.7}$, making it un-affordable with the current computational capabilities and for another 70 years.

Large Eddy Simulation

The Large-Eddy simulation (LES) uses the Kolmogorov theory in order to reduce the DNS CPU requirements. The theory of Kolmogorov says that the smaller scales of the turbulence are homogenous and isotropic, therefore the slope of the energy logarithm repartition in this scales is constant and equals $-\frac{5}{3}$. This part of the turbulence spectrum can easily be modelled and allows coarser grids compared to the DNS.

Two types of LES exist. The Quasi Direct Navier-Stokes Simulation models the small scales and calculates the anisotropic ones in the whole flow while the Wall-Modelled LES (WMLES) uses a model close to the wall, in order to reduce the cost of the simulation. The QDNS is almost as expensive as DNS and thus can not be used for rotor flows, while WMLES is cheaper and nowadays affordable at a high Reynolds number for usual basic flows like the flow around an aerofoil or in a channel. However, this simulation method is still not affordable for complex flows like rotor flows.

Another problem with LES is the generation of a turbulent inflow. A randomly generated turbulence would not be structured enough and would be dissipated early. A solution of this problem is the calculation of a flow where the turbulence can develop, and use the output of this calculation as the input of the new calculation. However this method is long and requires some heavy calculations. Therefore other inlet turbulence generation methods were developed. One of them is synthetic turbulence, like the model proposed in [66].

In summary, only empirical simulation methods are left to predict the turbulence: the URANS methods and the hybrid ones. In the case of a lightly loaded hovering rotor, URANS methods work well and give good prediction of the flow properties. However if a blade stalls during the revolution or if BVI phenomena appear, then the URANS prediction may not be good and other methods have to be used.

Detached-Eddy Simulation

The hybrid methods like Detached-Eddy Simulation (DES) have shown some improvements in highly detached flows like the one around bluff bodies, as shown for instance in [67]. These methods calculate a broader part of the frequencies and flow scales around a blade, allowing perhaps for aero-acoustic studies.

The original idea of DES was postulated by Spalart *et al.* [61]. The RANS equations with a modified length scale are used in the whole domain. This length scale is now also depending on the mesh length scale. In the RANS areas, the usual RANS length scale will be used, but in the LES zones, the length scale will now depend on the mesh length scale, forcing the turbulence model to behave like a LES simulation. DES does not need an interface between the RANS and LES part.

A similar idea put forward by Batten *et al.*[68] is called LNS: Limited Numerical Scales and has several advantages compared to the original DES. For instance, LNS claims to be 'automatic' by detecting the areas of application of the RANS and LES without *a priori* knowledge of the location of walls or wall-distances. Furthermore, LNS approaches DNS as $\Delta \rightarrow 0$ and reverts back to RANS at the far-field of the flow if the grid there is coarse. Ref. [69] describes how to implement LNS. LNS is so far adopted by few authors.

The DES can have some problems handling the transition between the LES and RANS zones. In the case of a coarse mesh around the wall, the DES will work as expected with a transition outside the boundary layer. If the mesh is very fine ($\Delta = \delta/20$, with δ the boundary layer thickness and Δ the chosen grid length scale), then the simulation will behave like a Wall-Modelled LES (LES with a wall model, RANS in this case). The problem appears for mesh size in between these two cases. The transition takes place at about the first third of the boundary layer, and the two upper thirds of the boundary layer will then be in LES mode. This will reduce the turbulent viscosity and therefore the Reynolds strains. Therefore, Spalart[70] developed the Delayed Detached-Eddy simulation. A limiter will force the transition between RANS and LES outside of the boundary layer.

Recently, Deck[71] worked on the turbulent inflow for Detached Eddy Simulation. The problem is caused by the calculated structures of turbulence that are not created at the inlet. If this turbulence is not structured enough (which is the result for example if we apply a randomly generated fluctuation of speed at each point and time step) then the energy that will go to the smaller structures will be more important and it will dissipate this turbulence too quickly. Therefore, a model to generate structured turbulence on the inlet is proposed.

On another hand, Shur[72] worked on the transition between RANS and LES in the case of the DDES. The position of the transition in the logarithmic region create a mismatch between the slope in the RANS and LES part of this layer. This mismatch lower the friction coefficient of about 15 to 20%, which is not acceptable. A blending function is added to make the two part match, and the model is calibrated for a channel flow.

Interest for hybrid turbulence models is starting to appear for rotorcraft flows. Smith *et al.* [63] studied the behaviour of a hybrid RANS-LES model HRLES-SGS[42] at predicting the flow field around the NACA0012 and SC1095 aerofoils at high incidence (between -180 degrees and 180 degrees). The simulation was validated against experimental results and proved able to predict the lift, drag and moment coefficients within the experimental margin. A high grid dependence was however shown in reverse flow condition when switching from a C- to an O-topology, showing an increase in lift coefficient of 25%. The ability of hybrid turbulence models to improve the predictions at high angle of attacks

or in reverse flows was highlighted. An improvement of rotorcraft flows predictions, particularly in high-speed forward flight, was therefore expected by the authors.

1.3 List of the test cases in this thesis

Considering data availability, restrictions on geometries and popularity of test cases in the literature, a summary of the test cases used in this work is shown in Table 1.10.

Table 1.10: List of test cases used in this thesis.

Test Case	Available data	Interest
HART-II	Experiments	comprehensive dataset available, including PIV measurements, pressure transducers, structural data, blade deformation, noise levels
UH-60A	Flight Tests	Only flight test data available, containing pressure transducers and strain gauges
SO-1	Experiments	Rotor developed by Westland in order to test structural modelling techniques, integrated loads from tunnel testing
PM3-PM4	Experiments	BERP tip rotor, integrated loads from tunnel testing
7A-7AD	Experiments	Very popular in the rotorcraft research
Caradonna-Tung rotor	Experiments	Pressure measurements available for various tip Mach numbers
HIMARC	Experiments	Comprehensive structural dataset
Model main rotors	none	High aspect ratio rotors
Tilt-Rotors	Experiments	Low aspect ratio rotors, and high rotation speed, data obtained as part of the NICETRIP project

1.4 Objectives

Based on the literature survey, the objectives of this work include:

- the development of a mesh deformation method suitable for rotor blade analysis,
- the coupling of the mesh deformation method with blade structural dynamics,
- the evaluation of DES for rotor flows.

1.5 Novelty of the current research

A hybrid mesh deformation method was developed for cases with the large displacements encountered by the rotor blades. The method can be used for multi-block structured grids and parallel computations. It proved able to cope with strong rotor blade deformations and preserves the mesh quality of the original grid. Furthermore, the ability of DES to be used with rotors in forward flight and deforming grids was demonstrated.

1.6 Thesis outline

In the next chapter, the HMB CFD solver will be introduced, followed by a description of the meshing techniques used for rotor blades. The structural modelling technique is then described in Chapter 4 and applied to rotor cases. The mesh deformation method description and assessment as well as the coupling strategy follow in Chapter 5. The assessment of various DES-based turbulence models is then shown on a stalled NACA0021 aerofoil in Chapter 6. The mesh deformation method is then used and validated for a hovering UH-60A rotor using steady-state calculations in Chapter 7. The coupling methodology is then assessed on a forward-flying UH-60A rotor before the method is tested on the HART-II rotor coupled with the use of a DES turbulence model in Chapter 8.

Chapter 2

Mathematical Models for Rotor Flow Simulations

2.1 The Helicopter Multi-Block CFD Solver

All computations were performed using the Helicopter Multi-Block (HMB) flow solver developed at the University of Liverpool. The flow solver has been revised and updated over a number of years and has been successfully applied to a variety of problems including cavity flows, dynamic stall, rotors, wind turbines and full helicopter configurations amongst others. HMB is a 3D multi-block structured solver for the Navier-Stokes equations in the 3D Cartesian frames of reference. The Navier-Stokes equations consist of Partial Differential Equations (PDEs) describing the laws of conservation for:

- mass (continuity equation),
- momentum (Newton's 2nd Law), and
- energy (1st Law of Thermodynamics).

The continuity equation simply states that the mass must be conserved. In Cartesian coordinates, x_i, this is written as

$$\frac{\partial \rho}{\partial t} + \frac{\partial (\rho u_i)}{\partial x_i} = 0 \tag{2.1}$$

where ρ is the density of the fluid, t is the time and u_i is the velocity vector. In the above, Einstein's notation is used, which implies summation for repeated indices.

The second conservation principle states that momentum must be conserved. It is written in Cartesian coordinates as

$$\frac{\partial (\rho u_i)}{\partial t} + \frac{\partial (\rho u_i u_j)}{\partial x_j} = \rho f_i - \frac{\partial p}{\partial x_i} + \frac{\partial \tau_{ij}}{\partial x_j} \tag{2.2}$$

where f_i represents body forces, p the pressure and τ_{ij} the Newtonian stress tensor, which is defined as

$$\tau_{ij} = \mu \left[\left(\frac{\partial u_i}{\partial x_j} + \frac{\partial u_j}{\partial x_i} \right) - \frac{2}{3} \delta_{ij} \frac{\partial u_k}{\partial x_k} \right] \quad , \tag{2.3}$$

with μ the molecular viscosity and δ_{ij} the Kronecker delta, defined as

$$\delta_{ij} = \begin{cases} 1 & \text{if i=j} \\ 0 & \text{otherwise} \end{cases} \tag{2.4}$$

The third principle can be written in Cartesian coordinates as

$$\frac{\partial \rho E}{\partial t} + \frac{\partial}{\partial x_j} [u_i (\rho E + p)] - \frac{\partial}{\partial x_j} (u_i \tau_{ij} - q_j) = 0. \tag{2.5}$$

where E is the total energy of the fluid per unit volume, defined as

$$E = \left[e + \frac{1}{2} u_i u_i \right] \tag{2.6}$$

and e is the specific internal energy with $u_i u_i$ representing the kinetic energy.

The heat flux vector, q_i, is calculated using Fourier's Law

$$q_i = -k_T \frac{\partial T}{\partial x_i} \tag{2.7}$$

where k_T is the heat transfer coefficient and T is the temperature of the fluid.

An ideal gas approximation is used, and the adiabatic index is set to $\gamma = 1.4$. Sutherland's law is used to calculate the viscosity:

$$\mu = \mu_{ref} \left(\frac{T}{T_{ref}} \right)^{\frac{3}{2}} \frac{T_{ref} + T_{Suth}}{T + T_{Suth}} \tag{2.8}$$

2.1.1 Vector Form of the Conservation Laws

These three laws of conservation can be combined and written in the equation shown below, which is referred to as the Navier-Stokes equation of viscous flow. For brevity, vector notation is used

$$\frac{\partial \mathbf{W}}{\partial t} + \frac{\partial \left(\mathbf{F}^i + \mathbf{F}^v\right)}{\partial x} + \frac{\partial \left(\mathbf{G}^i + \mathbf{G}^v\right)}{\partial y} + \frac{\partial \left(\mathbf{H}^i + \mathbf{H}^v\right)}{\partial z} = S_{NS} \tag{2.9}$$

where $\mathbf{W}$ is the vector of conserved variables and is defined by

$$\mathbf{W} = (\rho, \rho u, \rho v, \rho w, \rho E)^T \tag{2.10}$$

with the variables ρ, u, v, w, p and E having their usual meaning of density, the three components of velocity, pressure and total energy, respectively. The superscripts i and v in Equation 2.9 denote the inviscid and viscid components of the flux vectors $\mathbf{F}$ (in the x-direction), $\mathbf{G}$ (in the y-direction) and $\mathbf{H}$ (in the z-direction). The inviscid flux vectors, $\mathbf{F}^i$, $\mathbf{G}^i$ and $\mathbf{H}^i$, are given by

$$\begin{aligned}
\mathbf{F}^i &= \left(\rho u, \rho u^2 + p, \rho uv, \rho uw, u(\rho E + p)\right)^T \quad , \\
\mathbf{G}^i &= \left(\rho v, \rho uv, \rho v^2 + p, \rho vw, v(\rho E + p)\right)^T \quad , \\
\mathbf{H}^i &= \left(\rho w, \rho uw, \rho vw, \rho w^2 + p, w(\rho E + p)\right)^T \quad ,
\end{aligned} \tag{2.11}$$

while the viscous flux vectors, $\mathbf{F}^v$, $\mathbf{G}^v$ and $\mathbf{H}^v$, contain terms for the heat flux and viscous forces exerted on the body and can be represented by

$$\begin{aligned}
\mathbf{F}^v &= \frac{1}{\mathrm{Re}} \left(0, \tau_{xx}, \tau_{xy}, \tau_{xz}, u\tau_{xx} + v\tau_{xy} + w\tau_{xz} + q_x\right)^T \quad , \\
\mathbf{G}^v &= \frac{1}{\mathrm{Re}} \left(0, \tau_{xy}, \tau_{yy}, \tau_{yz}, u\tau_{xy} + v\tau_{yy} + w\tau_{yz} + q_y\right)^T \quad , \\
\mathbf{H}^v &= \frac{1}{\mathrm{Re}} \left(0, \tau_{xz}, \tau_{yz}, \tau_{zz}, u\tau_{xz} + v\tau_{yz} + w\tau_{zz} + q_z\right)^T \quad .
\end{aligned} \tag{2.12}$$

S_{NS} represents source terms. In most calculations, these terms are set to 0, however, for hovering rotors, a fixed grid approach is used and a source term is then added:

$$S_{NS} = [0, -\rho \vec{\omega} \times \vec{u_h}, 0]^T \tag{2.13}$$

where $\vec{u_h}$ is the local velocity field in the rotor-fixed frame of reference.

Although the Navier-Stokes equations completely describe turbulent flows, the large number of temporal and spatial turbulent scales associated with high Reynolds numbers make it difficult to

resolve all the turbulent scales computationally[65]. In such circumstances, the number of turbulent scales are reduced by time averaging the Navier-Stokes equations to give the Reynolds-Averaged Navier-Stokes equations (RANS). This results in additional unknowns (called Reynolds stresses) which must be modelled[73]. The fluid stress tensor mentioned in Equation 2.12 is then approximated by the Boussinesq hypothesis[74], more description of which is provided in the following sections.

2.1.2 Numerical Methods

The HMB solver uses a cell-centred finite volume approach combined with an implicit dual-time method. In this manner, the solution marches in pseudo-time for each real time-step to achieve fast convergence. According to the finite volume method, the RANS equations can be discretised for each cell by

$$\frac{d}{dt}\left(\mathbf{W}_{i,j,k}\mathcal{V}_{i,j,k}\right)+\mathbf{R}_{i,j,k}=0. \tag{2.14}$$

where $\mathcal{V}_{i,j,k}$ denotes the cell volume and $\mathbf{R}_{i,j,k}$ represents the flux residual.

The implicit dual-time method proposed by Jameson[75] is used for time-accurate calculations. The residual is redefined to obtain a steady state equation which can be solved using acceleration techniques. The following system of equations are solved in the implicit scheme during the time integration process

$$\frac{\Delta V\mathbf{W}^{m+1}_{i,j,k}-\Delta V\mathbf{W}^{m}_{i,j,k}}{\Delta V\Delta\tau}+\frac{\Delta V\mathbf{W}^{n+1}_{i,j,k}-\Delta V\mathbf{W}^{n}_{i,j,k}}{\Delta V\Delta t}=\mathbf{R}^{n+1}_{i,j,k} \tag{2.15}$$

where ΔV is the change in cell volume, $\Delta\tau$ is the pseudo time-step increment and Δt is the real time-step increment. The flux residual $\mathbf{R}^{n+1}_{i,j,k}$ is approximately defined by

$$\mathbf{R}^{n+1}_{i,j,k}\approx\mathbf{R}^{n}_{i,j,k}+\frac{\partial\mathbf{R}^{n}_{i,j,k}}{\partial\mathbf{W}^{n}_{i,j,k}}\left(\mathbf{W}^{n+1}_{i,j,k}-\mathbf{W}^{n}_{i,j,k}\right) \tag{2.16}$$

By substituting Equation 2.16 into Equation 2.15, the resulting linear system can be written as

$$\left(\frac{1}{\Delta t}+\left(\frac{\partial\mathbf{R}}{\partial\mathbf{W}}\right)^{n}\right)\Delta\mathbf{W}=-\mathbf{R}^{n} \tag{2.17}$$

where the subscripts i,j,k have been dropped for clarity and ΔW is used for $\left(\mathbf{W}^{n+1}_{i,j,k}-\mathbf{W}^{n}_{i,j,k}\right)$.

Osher's upwind scheme [76] is used to resolve the convective fluxes although Roe's flux-splitting scheme [77] is also available. The Monotone Upstream-centred Schemes for Conservation Laws (MUSCL)

variable extrapolation method[78] is employed in conjunction to formally provide second-order accuracy. The Van Albada limiter is also applied to remove any spurious oscillations across shock waves. The central differencing spatial discretisation method is used to solve the viscous terms. The non-linear system of equations that is generated as a result of the linearisation is then solved by integration in pseudo-time using a first-order backward difference. A Generalised Conjugate Gradient (GCG)[79] method is then used in conjunction with a Block Incomplete Lower-Upper (BILU)[79] factorisation as a pre-conditioner to solve the linear system of equations, which is obtained from a linearisation in pseudo-time.

The flow solver can be used in serial or parallel mode. To obtain an efficient parallel method based on domain decomposition, different methods are applied to the flow solver [80]. An approximate form of the flux Jacobian resulting from the linearisation in pseudo-time is used which reduces the overall size of the linear system by reducing the number of non-zero entries. Between the blocks of the grid, the BILU factorisation is also decoupled thereby reducing the communication between processors. Each processor is also allocated a vector that contains all the halo cells for all the blocks in the grid. Message Passing Interface (MPI) is used for the communication between the processors in parallel. Most computations undertaken in this work have been performed on the Beowulf Pentium 4 130-processor workstations of the CFD Laboratory at the University of Liverpool. For very large grids, however, calculations were conducted on different supercomputing clusters such as HECToR[81] in Edinburgh, UK, and the necessary porting of the code onto these facilities performed. HECToR is based on the Cray XE6 system and comprises 3712 12-core AMD Opteron 2.1GHz Magny Cours processors in 1856 XE6 compute nodes, delivering a peak-performance of 373 Teraflops.

A number of linear and non-linear statistical turbulence models have been implemented into HMB. The one-equation SA turbulence model[40] to realise the turbulent properties for DES computations, and the DDES approach as well as the SALSA modification of the SA turbulence model were implemented for this project. Options for DES with two-equation Wilcox $k-\omega$[53] and Menter's $k-\omega$ Shear-Stress Transport (SST)[41] turbulence models are also available. All these turbulence models and indeed the simulation techniques are described in greater detail in the following sections.

2.2 General Description of Turbulence and its Modelling

Turbulent flows contain structures which show rapid fluctuations in time and space. A broad range of scales are observed to exist at high Reynolds numbers where turbulence develops as an instability of the laminar flow. Starting with the laminar flow, fluid layers slide smoothly past each other and the molecular viscosity dampens any high-frequency small-scale instability. At high Reynolds number, the flow reaches a periodic state. The character of the flow also changes and becomes more diffusive and dissipative. This flow has increased mixing friction, heat transfer rate and spreading rate. Boundary layers consequently become thicker and less susceptible to separation[82].

The non-linearity of the Navier-Stokes equations leads to various interactions between the turbulent fluctuations of different wavelengths and directions. Wavelengths extend from a maximum comparable to the width of the flow to a minimum fixed by viscous dissipation of energy. A key process that spreads the motion over wide range of wavelengths is called vortex stretching[82]. Turbulent structures in the flow gain energy if the vortex elements are primarily orientated in a direction which allow the mean velocity gradients to stretch them. This mechanism is called production of turbulence. The kinetic energy of the turbulent structures is then convected, diffused and dissipated.

Most of the energy is carried by the large scale structures, the orientation of which is sensitive to the mean flow. The large eddies cascade energy to the smaller ones via stretching. Small eddies have less pronounced preference in their orientation and statistically appear to be isotropic. For the shortest wavelengths, energy is dissipated by viscosity. This description corresponds to what is known as isotropic turbulence. For this flow, the ratio of the largest to smaller scale increases with Reynolds number[82].

If the unsteady Navier-Stokes equations are used to calculate the flow, a vast range of length and time scales would have to be computed. This would require a very fine grid and a very high resolution in time. This approach known as Direct Numerical Simulation of turbulence (DNS) is by today's computing speeds applicable only to flows at very low Reynolds number. One technique called Large-Eddy Simulation explicitly resolves the scales away from the wall and exploits modelling in

the near-wall regions. A sub-grid scale (SGS) model is used to model the smaller scales which are assumed to be more isotropic. Although less computationally intensive than DNS, this is still expensive, especially for higher Reynolds number flows.

A turbulence model therefore needs to account for some part of the fluctuating motion in order to keep the computing cost down. The optimum model should therefore be simple to implement, general and derived out of the flow physics. It is equally important that the model is computationally stable and co-ordinate invariant. These statistical turbulence models are applied to a special form of the equations of motion called the Reynolds-Averaged Navier-Stokes (RANS) equations. These are obtained by Reynolds averaging the Navier-Stokes equations.

2.3 Reynolds Averaging

In a turbulent flow, the fields of pressure, velocity, temperature and density vary randomly in time. Reynolds' approach involves separating the flow quantities into stationary and random parts. The quantities are then presented as a sum of the mean flow value and the fluctuating part[82]:

$$\varphi = \overline{\varphi} + \varphi' \tag{2.18}$$

This formulation is then inserted into the conservation equations and a process known as Reynolds averaging is performed. Three averaging methods are possible:

- time averaging,
- spatial averaging,
- ensemble averaging.

2.3.1 Time Averaging

Time averaging is the most common averaging method. It can be used only for statistically stationary turbulent flows, i.e. flows not varying with time on the average. For such flows, the mean flow value is

defined as

$$\overline{u_i(x)} = \lim_{T\to\infty} \frac{1}{T_{inte}} \int_t^{t+T_{inte}} u_i(x,t)\,\mathrm{d}t \tag{2.19}$$

In practice, $T_{inte} \to \infty$ means that the integration time T_{inte} needs to be long enough relative to the maximum period of the assumed fluctuations.

2.3.2 Spatial Averaging

Spatial averaging can be applied to homogeneous turbulence, which is a type of turbulent flow that is uniform in all directions, on average. In this case, a parameter is averaged over all the spatial directions by performing a volume integral. The mean flow value is then defined as

$$\overline{u_i(t)} = \lim_{V\to\infty} \frac{1}{V} \int\int\int_V u_i(x,t)\,\mathrm{d}t \tag{2.20}$$

where V represents the volume of the domain.

2.3.3 Ensemble Averaging

The most general type of averaging is called ensemble averaging and is applicable to flows that decay in time, for instance. This method of averaging is similar to time-averaging but rather than dividing by the integration time, T_{inte}, the mean flow value is obtained by taking a sum over all the measurements or samples, N, and is defined by

$$\overline{u_i(x)} = \lim_{N\to\infty} \frac{1}{N} \sum_{n=1}^{N} u_i(x,t) \tag{2.21}$$

For turbulent flows that are both stationary and homogeneous, all the three types of averages mentioned above are assumed to be equal. This assumption is referred to as the ergodic hypothesis[82].

By time-averaging the mass, momentum and energy equations, the Reynolds-Averaged Navier-Stokes (RANS) equations are obtained. The continuity equation remains the same since it is linear with respect to velocity. However, extra terms appear in the momentum and energy equations due to the non-linearity of the convection term. These extra terms are called the Reynolds Stresses, τ_{ij}^R, and are defined in tensor notation as being equivalent to $-\rho\overline{u_i'u_j'}$. The time-averaged momentum equation then

takes the form

$$\frac{\partial(\rho u_i)}{\partial t}+\frac{\partial(\rho u_i u_j)}{\partial x_i}=\rho f_i-\frac{\partial p}{\partial x_i}+\frac{\partial}{\partial x_j}\left(\tau_{ij}+\tau_{ij}^R\right) \tag{2.22}$$

where the overbar has been dropped from the mean values for clarity. A similar result is obtained for the energy equation (Equation 2.23):

$$\frac{\partial \rho E}{\partial t}+\frac{\partial}{\partial x_j}\left[u_i(\rho E+p)\right]-\frac{\partial}{\partial x_j}\left(u_i\left(\tau_{ij}+\tau_{ij}^R\right)-q_j^R\right)=0. \tag{2.23}$$

where q_j^R is the turbulent heat flux. The main problem in turbulence modelling involves calculating the Reynolds stresses, from the known mean quantities. One common approach is based on Boussinesq's approximation.

2.4 Boussinesq-Based Models

The Boussinesq approximation is based on an analogy between viscous and Reynolds stresses and expresses the Reynolds stresses as a product of the eddy viscosity (μ_T) and the velocity gradient. Boussinesq's eddy viscosity hypothesis states that

$$-\rho\overline{u_i'u_j'}=\mu_T\left[\left(\frac{\partial u_i}{\partial x_j}+\frac{\partial u_j}{\partial x_i}\right)-\frac{2}{3}\delta_{ij}\frac{\partial u_k}{\partial x_k}\right]-\frac{2}{3}\rho\delta_{ij}k \tag{2.24}$$

where k represents the specific kinetic energy of the fluctuations and is given by

$$k\equiv\frac{\overline{u_i'u_i'}}{2} \tag{2.25}$$

The key idea behind Boussinesq's hypothesis is that the Reynolds stresses can be calculated as a product of the dynamic eddy-viscosity, μ_T, and the strain-rate tensor of the mean flow, i.e.

$$-\rho\overline{u_i'u_j'}=2\mu_T S_{ij}-\frac{2}{3}\delta_{ij}k \tag{2.26}$$

where

$$S_{ij}=\frac{1}{2}\left(\frac{\partial u_i}{\partial x_j}+\frac{\partial u_j}{\partial x_i}-\frac{2}{3}\delta_{ij}\frac{\partial u_k}{\partial x_k}\right) \tag{2.27}$$

The eddy viscosity, μ_T, is a scalar and consequently the Reynolds stress components are linearly proportional to the mean strain-rate tensor. What is also implied here is that compressibility plays a secondary

rate in the development of the turbulent flow-field. According to Morkovin's hypothesis [83], compressibility affects turbulence only at hypersonic speeds.

To compute μ_T, further modelling is required and it is at this point that turbulence models come into play. Turbulence models are classified into categories based on the number of transport equations required to calculate μ_T. According to the number of transport equations needed for the calculation of the eddy viscosity, the Boussinesq-based models are classified as:

- algebraic or zero-equation models, such as the Cebeci-Smith[84] and Baldwin-Lomax[85] models,
- one-equation models, such as the Spalart-Allmaras (SA)[40] and Baldwin-Barth (BB)[86] models.
- two-equation models, such as the $k-\omega$[53], $k-\varepsilon$[87], $k-\omega$ baseline (BSL) and shear-stress transport (SST)[41] and $k-g$[88] models.
- multi-equation models: three-equation[89–91], four-equation[92], five-equation [93] and multiple time-scale [94–96] models.

An additional family of models solves equations for all components of the Reynolds stress tensor. These are also known as Reynolds Stress Models (RSM), second-order closures or second-moment closures.

2.5 Viscosity-Dependent Parameters

Non-dimensionalised wall distances for turbulent flow, y^*, and non-turbulent flow, y^+, are defined by the following

$$y^* \equiv \frac{y_n k^{1/2}}{\nu}, \qquad y^+ \equiv \frac{y_n u_\tau}{\nu}, \tag{2.28}$$

where y_n is the distance from the nearest wall, $u_\tau \equiv \sqrt{\tau_w/\rho}$ is the friction velocity and τ_w represents the dynamic wall shear stress. Turbulent Reynolds numbers for the $k-\varepsilon$ model (denoted by R_t) and for the $k-\omega$ model (denoted by R_ω) are given by the following equation

$$R_t \equiv \frac{k^2}{\nu\varepsilon}, \qquad R_\omega \equiv \frac{k}{\nu\omega} \quad , \tag{2.29}$$

which represents the importance of the eddy over molecular viscosity.

2.6 One-Equation Models

This type of turbulence model was designed to improve the ability of algebraic models to account for the convection and diffusion of turbulence. This was accomplished by employing an additional transport equation, usually for the realisation of the kinetic energy of turbulence, k. The general form of this transport equation takes the following form

$$\frac{\partial k}{\partial t} + u_j \frac{\partial k}{\partial x_j} = \tau_{ij} \frac{\partial u_i}{\partial x_j} - \varepsilon + \frac{\partial}{\partial x_j} \left[\frac{\mu}{\rho} \frac{\partial k}{\partial x_j} - \frac{1}{2} \overline{u_i' u_i' u_j'} - \frac{1}{\rho} \overline{p' u_j'} \right] \tag{2.30}$$

The first term in Right-Hand Side (RHS) $\left(\tau_{ij} \frac{\partial u_i}{\partial x_j}\right)$ represents the production of turbulence. From the terms in the square brackets, the first $\left(\frac{\mu}{\rho} \frac{\partial k}{\partial x_j}\right)$ is the molecular diffusion term, the second $\left(\overline{u_i' u_i' u_j'}\right)$ is the turbulent flux of the turbulent kinetic energy, modelled as a function of the gradient of the turbulent kinetic energy, and the third $\left(\frac{1}{\rho} \overline{p' u_j'}\right)$ is the pressure diffusion term, which is usually neglected due to its small contribution. The term ε is the dissipation rate of k per unit mass of fluid, and is usually defined by

$$\varepsilon = \frac{\mu}{\rho} \overline{\frac{\partial u_i'}{\partial x_k} \frac{\partial u_i'}{\partial x_k}} \tag{2.31}$$

Eddy viscosity for one-equation turbulence models is usually calculated by

$$\mu_T = \rho C_\mu l_{mlx} \sqrt{k} \tag{2.32}$$

where C_μ is a coefficient specific to the model.

BB[86] and SA[40] are the most common types of one-equation models. History effects of the turbulent kinetic energy profile are better accounted for in one-equation models due to the additional differential equation. Specifically tuned for aerodynamic flows with adverse pressure gradients and transonic flow conditions, one-equation models also work well for flow regions where the mean velocity gradient is zero. Better prediction of near-wall effects and transition, for instance, can simply be integrated into the model's formulation by adding extra relevant terms because of its modular design. For these reasons, one-equation models have gained much popularity in aerospace applications. The disadvantage of one-equation models is that no mechanism for the computation of the length scale, l, is included, making the prediction of highly turbulent flows (with a broad range of length scales) difficult.

In that respect, one-equation models are still similar to algebraic models[82].

Many modifications have been undertaken to one-equation turbulence models, especially to the SA model, with the view of extending their range of applications. Extensions to compressible supersonic flows over complex configurations have been addressed by Deck[97] while rotational and curvature effects to account for the change on turbulent shear stress have been addressed by Spalart and Shur[61]. The SA model has also been modified to be used in DES computations[98].

2.6.1 Spalart-Allmaras Model

The one-equation SA turbulence model [40] solves a transport equation for the undamped eddy viscosity directly. The kinematic eddy viscosity, (ν_t), in the SA model is calculated by

$$\nu_t = \tilde{\nu} \cdot f_{v1} \tag{2.33}$$

where

$$f_{v1} = \frac{\chi^3}{\chi^3 + c_{v1}^3} \qquad \text{and} \qquad \chi = \frac{\tilde{\nu}}{\nu} \tag{2.34}$$

In the above equations, and hereafter, the term f refers to a function, c refers to a constant, ν is the molecular viscosity and $\tilde{\nu}$ is the undamped eddy viscosity that obeys the following transport equation

$$\begin{aligned} \frac{D\tilde{\nu}}{Dt} &= c_{b1}(1 - f_{t2})\tilde{S}\tilde{\nu} + \frac{1}{\sigma_{Pr}}\left(\nabla \cdot ((\nu + \tilde{\nu})\nabla\tilde{\nu}) + c_{b2}(\nabla\tilde{\nu})^2\right) \\ &\quad - \left(c_{w1} f_w - \frac{c_{b1}}{\kappa^2} f_{t2}\right)\left(\frac{\tilde{\nu}}{d}\right)^2 + f_{t1}\Delta U^2 \end{aligned} \tag{2.35}$$

The first term on the right-hand side is the production term, the second is the diffusion term and the third is the near-wall term. The last term models transition downstream of tripping. The subscript b stands for basic, w for wall and t for trip. The parameter σ_{Pr} represents the turbulent Prandtl number and d is the wall-distance.

The term $\tilde{S}$ in Equation (2.35) is defined by the following equation, where S is the magnitude of vorticity

$$\tilde{S} = S + \frac{\tilde{\nu}}{k^2 d^2} f_{v2}, \qquad f_{v2} = 1 - \frac{\chi}{1 + \chi f_{v1}} \tag{2.36}$$

The function f_w in Equation (2.35) is given by

$$f_w = g\left(\frac{1+c_{w3}^6}{g^6+c_{w3}^6}\right)^{1/6}, \qquad g = r + c_{w2}\left(r^6 - r\right), \qquad r = \frac{\tilde{\nu}}{\tilde{S}k^2d^2} \tag{2.37}$$

For large r, the function f_w approaches a constant value. Values for r where this occurs can be truncated to approximately 10. The wall boundary condition is satisfied where $\tilde{\nu} = 0$. In the free-stream, 0 is the best value to use for the working variable ($\tilde{\nu}$), provided that numerical errors do not push $\tilde{\nu}$ to negative values near the edge of the boundary layer (the exact solution cannot go negative). Values below $\nu/10$ are also acceptable. The same applies to the initial condition. The f_{t2} function is defined by

$$f_{t2} = c_{t3} \cdot e^{-c_{t4}\cdot\chi^2} \tag{2.38}$$

The trip function f_{t1} is defined as

$$f_{t1} = c_{t1}g_t \cdot e^{-c_{t2}\frac{\omega_t^2}{\Delta U^2}\left(d^2 + g_t^2 d_t^2\right)} \tag{2.39}$$

where d_t is the distance from the field point to the trip, ω_t is the wall vorticity at the trip, ΔU is the difference between the velocity at the field point and that at the trip and $g_t = \min(0.1, \Delta U/\omega_t \Delta x)$, in which Δx is the grid spacing along the wall at the trip.

Values used in HMB for the SA turbulence model constants are given in Table 2.1.

Table 2.1: Closure coefficients for the SA model

Coefficient	c_{b1}	σ_{Pr}	c_{b2}	κ	c_{w2}	c_{w3}	c_{v1}	c_{t1}	c_{t2}	c_{t3}	c_{t4}
Value	0.1355	2/3	0.622	0.41	0.3	2	7.1	1	2	1.1	2

The constant c_{w1} is defined as

$$c_{w1} = \frac{c_{b1}}{k^2} + \frac{(1+c_{b2})}{\sigma_{Pr}} = 3.2391. \tag{2.40}$$

A value of 2/3 has been used for the turbulent Prandtl number, σ_{Pr}.

2.6.2 Strain-Adaptive Linear Spalart-Allmaras

The SA model showed deficiencies in the predictions of the vortex cores. These are predicted as extremely turbulent which is not physical. Therefore, a limiter was added to the production term by Rung

in [99] and the new model called Strain-Adaptive Linear Spalart-Allmaras (SALSA). The production term was consequently modified in order to limit the turbulence production. The new production term is defined as a product of a shear-stress function, the undamped viscosity and an adaptation factor C_{b1}:

$$P_{\tilde{\nu}_t} = \tilde{\nu}\tilde{S}C_{b1} \tag{2.41}$$

The new coefficient C_{b1} is defined as:

$$C_{b1} = 0.1355\sqrt{\Gamma} \tag{2.42}$$

with $\Gamma = \min[1.25, \max(\gamma, 0.75)]$, $\gamma = \max(\alpha_1, \alpha_2)$, $\alpha_1 = \left[1.01\left(\tilde{\nu}/\kappa^2 d^2 S^*\right)\right]^{0.65}$, $\alpha_2 = \max[0, 1 - \tanh(\chi/68)]^{0.65}$ where $S^* = \sqrt{2S_{ij}S_{ij}}$.

The α_1 term allows the damping of the excessive production in high strains, while the α_2 term avoids unwanted wall damping.

2.7 Two-Equation Models

By far the most popular type of turbulence model used is of the two-equation type. Two-equation models are 'complete', i.e. can be used to predict properties of a given flow with no prior knowledge of the turbulence structure or flow geometry. Two transport equations are used for the calculation of the turbulent kinetic energy, k, and turbulence length scale, l, or a function of it. The choice of the 2nd variable is arbitrary and many proposals have been presented. The most popular involves using:

- ε — specific dissipation rate of turbulence.
- ω — k-specific dissipation rate.
- τ — turbulent time-scale.

A description of the different types of two-equation models is provided in Table 2.2 below. As well as indicating the variable used for the second transport equation, Table 2.2 includes the equation used to calculate the eddy viscosity.

Table 2.2: Different types of two-equation turbulence models and the corresponding second variable.

Two-Equation Model	Equation	2nd Variable Used
Kolmogorov (c. 1942) [100]	$k^{1/2}l^{-1}$	ω (Frequency Length Scale)
Rotta (c. 1950)	l	
Harlow-Nakayama (1967) [101]	$k^{3/2}l^{-1}$	ε (Energy Dissipation Rate)
Spalding (1969) [102]	kl^{-2}	ω'^2 (Vorticity fluctuations squared)
Speziale (1992) [103]	$lk^{-1/2}$	τ (Time-Scale)
Nee	kl	kl (k times length scale)
Harlow-Nakayama	$lk^{-1/2}$	ν_t (Eddy viscosity)

One of the most widely used two-equation turbulence models is the $k-\varepsilon$ model. One of the original versions of this model was developed by Jones and Launder [87] in 1972. The turbulent scale in the $k-\varepsilon$ model is calculated using a second transport equation for the turbulent dissipation rate, ε. The eddy viscosity for the $k-\varepsilon$ model is typically derived from

$$\mu_T = C_\mu \rho \frac{k^2}{\varepsilon} \tag{2.43}$$

where C_μ is the model coefficient. The advantage of the $k-\varepsilon$ model is that it performs well for attached flows with thin shear layers and jets but fails to predict the correct flow behaviour in many flows with adverse pressure gradients, extended separated flow regions, swirl, buoyancy, curvature secondary flows and unsteady flows.

The other class of two-equation turbulence models that is widely used is the $k-\omega$ model. In 1988, Wilcox[53] developed the famous $k-\omega$ model originally conceived by Kolmogorov. The $k-\omega$ model is similar to the $k-\varepsilon$ model but instead uses the k-specific dissipation rate as a second variable to compute the turbulent length scale. The eddy viscosity is obtained by

$$\mu_T = \rho \frac{k}{\omega} \tag{2.44}$$

Although the $k-\omega$ model provides better performance in adverse pressure gradient flows, it suffers largely from the same problems as the $k-\varepsilon$ model. Hybrid versions of the $k-\omega$ and $k-\varepsilon$ models called the $k-\omega$ baseline (BSL) and $k-\omega$ shear-stress transport (SST) models were later introduced by Menter[41]. These, in particular the $k-\omega$ SST version, perform well in separated flows. The idea behind the $k-\omega$ BSL model is to exploit the robust and accurate formulation of the $k-\omega$ model near

the wall but to also take advantage of the lack of sensitivity to free-stream values of the $k-\varepsilon$ model away from the wall. Menter[41] achieved this by transforming the $k-\varepsilon$ model into the same format as the $k-\omega$ formulation. This process generated an additional cross-diffusion parameter in the ω transport equation. For the SST model[41], the idea was to improve the $k-\omega$ BSL model by including terms to account for the transport of the principal shear stress. This term is incorporated in Reynolds Stress Models (RSM) and was also applied in the Johnson-King model[104]. Its importance was realised based on the significantly improved results for adverse pressure gradient flows[41].

2.7.1 Model Equations: Linear $k-\omega$ Model

Mathematical formulations of the different types of the linear $k-\omega$ two-equation turbulence models discussed in the previous sections are described here. More information on the $k-\varepsilon$ and $k-g$ models can be obtained from [69].

Since the introduction of the linear $k-\omega$ model by Wilcox in 1988[53], the other notable modification to the $k-\omega$ model came from Menter in 1994[41] who proposed the hybridisation of the $k-\omega$ model with the $k-\varepsilon$ model, as described previously. Table 2.3 lists the four notable versions of the $k-\omega$ models and further describes if they include parameters to compute the low Reynolds number properties.

Table 2.3: Different types of linear $k-\omega$ turbulence models

Type of Model	Low-Re
Wilcox (1988)[53]	Yes
Wilcox (1994)[32]	Yes
Menter (1994)[41] — (i) BSL Model	Yes
Menter (1994)[41] — (ii) SST Model	Yes

Turbulence transport equations used in the formulation of the $k-\omega$ models are given by the following:

$$\frac{\partial}{\partial t}(\rho k)+\frac{\partial}{\partial x_j}(\rho U_j k)=\frac{\partial}{\partial x_j}\left[\left(\mu+\frac{\mu_T}{\sigma_k}\right)\frac{\partial k}{\partial x_j}\right]+\rho\left(P_k-\beta^*\omega k\right) \tag{2.45}$$

$$\frac{\partial}{\partial t}(\rho\omega)+\frac{\partial}{\partial x_j}(\rho U_j\omega)=\frac{\partial}{\partial x_j}\left[\left(\mu+\frac{\mu_T}{\sigma_\omega}\right)\frac{\partial \omega}{\partial x_j}\right]+\rho\left(\frac{\alpha}{\nu_t}P_\omega-\frac{\beta}{\beta^*\omega^2}\right)+\rho S_l \tag{2.46}$$

In the transport equation for k and ω above, the production of turbulence, P, and the dissipation rate specific to k, P_ω, is defined by

$$P_k = \tau_{ij}^R \frac{\partial u_i}{\partial x_j}, \qquad P_\omega = \rho \frac{\alpha}{\nu_t} P_k. \tag{2.47}$$

Values for the coefficients used in all the four types of linear $k-\omega$ models discussed here are given in the Table 2.4.

Table 2.4: Values of constants used in linear $k-\omega$ models.

Type of Model	α^*	β^*	α	β
Wilcox (1988)[53]	1	$\frac{9}{100}$	$\frac{5}{9}$	$\frac{3}{40}$
Wilcox (1994)[32]	$\frac{\frac{1}{40}+\frac{R_\omega}{6}}{1+\frac{R_\omega}{6}}$	$\frac{9}{100}\frac{\frac{5}{18}+\left(\frac{R_\omega}{8}\right)^4}{1+\left(\frac{R_\omega}{8}\right)^4}$	$\frac{5}{9}\frac{\frac{1}{10}+\frac{R_\omega}{2.7}}{1+\frac{R_\omega}{2.7}}$	$\frac{3}{40}$
Menter (1994)[41] ***(BSL)***[1]	1	0.09	$B\begin{pmatrix}0.553\\0.440\end{pmatrix}$	$B\begin{pmatrix}0.075\\0.083\end{pmatrix}$
Menter (1994)[41] ***(SST)***[2]	$\min\left(1, \frac{0.31}{F_2}\frac{\omega}{w}\right)$	0.09	$B\begin{pmatrix}0.553\\0.440\end{pmatrix}$	$B\begin{pmatrix}0.075\\0.083\end{pmatrix}$

Type of Model	σ_k	σ_ω	S_l
Wilcox (1988)[53]	2	2	0
Wilcox (1994)[32]	2	2	0
Menter (1994)[41] ***(BSL)***[1]	$\frac{1}{B\begin{pmatrix}0.5\\1.0\end{pmatrix}}$	$\frac{1}{B\begin{pmatrix}0.5\\0.856\end{pmatrix}}$	$B\begin{pmatrix}0\\\frac{1.71}{\omega}\nabla k\cdot\nabla\omega\end{pmatrix}$
Menter (1994)[41] ***(SST)***[2]	$\frac{1}{B\begin{pmatrix}0.85\\1.0\end{pmatrix}}$	$\frac{1}{B\begin{pmatrix}0.5\\0.856\end{pmatrix}}$	$B\begin{pmatrix}0\\\frac{1.71}{\omega}\nabla k\cdot\nabla\omega\end{pmatrix}$

Menter's models[41] are constructed as a 'blend' of the $k-\omega$ and $k-\varepsilon$ models. Here the $k-\varepsilon$ model is phrased in the same form as the $k-\omega$ model so as to exploit its independence of free-stream values. Blending of the $k-\varepsilon$ and $k-\omega$ model values for α, β, σ_k^{-1} and σ_ω^{-1} is (in this notation) given by the following equation

$$B\begin{pmatrix}a\\b\end{pmatrix} \equiv F_1 a + (1-F_1)\, b. \tag{2.48}$$

The blending function is defined by

$$F_1 = \tanh\left(\arg_1^4\right), \tag{2.49}$$

where

$$arg_1 = \min\left[\max\left(\frac{k^{1/2}}{\beta^*\omega y}, \frac{500\nu}{y_n^2\omega}\right), \frac{2k\omega}{y_n^2 \max(\nabla k \cdot \nabla\omega, 0.0)}\right]. \tag{2.50}$$

The $k-\omega$ SST model places an additional vorticity-dependent limiter on the shear-stress

$$F_2 = \tanh\left(arg_2^2\right), \qquad arg_2 = \max\left(\frac{2k^{1/2}}{\beta^*\omega y}, \frac{500\nu}{y^2\omega}\right). \tag{2.51}$$

Note that this model also uses a slightly different value of σ_k.

For low-Reynolds number versions of the $k-\omega$ model and Menter's $k-\omega$ BSL and SST models, the following boundary conditions are assumed for a direct integration to the wall

$$\text{For } k: \quad k_w = 0, \qquad flux(k)_w = 0 \quad , \tag{2.52}$$

$$\text{For } \omega: \quad \omega = 0, \qquad flux(\omega)_w = -\nu\nabla\omega \quad . \tag{2.53}$$

where the subscript w denotes the value *at* the wall.

2.8 Detached-Eddy Simulation

2.8.1 Original Detached-Eddy Simulation

Despite its potential, the need of fine grids close to the wall does not allow the use of LES in complex flows. Therefore, some hybrid simulations have been developed, including Detached-Eddy Simulation (DES). The main principle of these models is the use of RANS close to the walls and LES further.

The original idea of DES was postulated by Spalart *et al.* [61]. The RANS equations with a modified length scale are used in the whole domain. This length scale is now also depending on the mesh length scale. In the RANS areas, the usual RANS length scale will be used, but in the LES zones, the length scale will now depend on the mesh length scale, forcing the turbulence model to behave like LES. This concept is called Detached-Eddy Simulation (DES). DES does not need an interface between the RANS and LES part.

Spalart introduced the mesh length scale Δ as a function of the cell size following the three axis

Δ_x, Δ_y and Δ_z:

$$\Delta = \max(\Delta_x, \Delta_y, \Delta_z) \quad . \tag{2.54}$$

The new length scale for DES is then:

$$l_{DES} = \min(l_{RANS}, C_{DES}\Delta) \quad , \tag{2.55}$$

where C_{DES} is an arbitrary constant. For example, in the case of the Spalart-Allmaras model, the scale length d is the wall distance. In the new DES model, the length scale $\tilde{d}$ is defined as:

$$\tilde{d} = \min(d, C_{DES}\Delta) \quad . \tag{2.56}$$

Therefore, when close enough to the wall, the model will use the RANS equations, and, further from the wall, the length scale will switch to the grid length scale and the model will behave like LES.

This modification aims at increasing the dissipation term of the turbulent kinetic energy and thus decrease the production term. The dissipation term is now equal to:

$$-C_{w1} f_{w1} \left(\frac{\tilde{\nu}}{\tilde{d}}\right)^2 \quad . \tag{2.57}$$

This process can be generalised to other RANS models, like the $k-\omega$ ones as described by Strelets[105]. In this case, the length scale is changed from $\frac{\sqrt{k}}{\omega\beta}$ to:

$$l_{DES} = \min\left(\frac{\sqrt{k}}{\omega\beta}, C_{DES}\Delta\right) \quad . \tag{2.58}$$

A similar idea put forward by Batten *et al.* [68] is called LNS: Limited Numerical Scales and has several advantages compared to the original DES. For instance, LNS claims to be 'automatic' by detecting the areas of application of the RANS and LES without *a priori* knowledge of the location of walls or wall-distances. Furthermore, LNS approaches DNS as $\Delta \rightarrow 0$ and reverts back to RANS at the far-field of the flow if the grid there is coarse. Ref. [69] describes how to implement LNS.

For DES with the two-equation $k-\omega$ model, the only modification, as with the one-equation Spalart-Allmaras DES variant, is in the dissipation term

$$-\beta^* \rho \omega k \tag{2.59}$$

The turbulent length scale is defined by

$$l = \frac{k^{1/2}}{\beta^* \omega} \tag{2.60}$$

Re-arranging for $\beta^*\omega$ and substituting into equation 2.59 gives

$$-\rho \frac{k^{3/2}}{l_{DES}} \tag{2.61}$$

where l_{DES} is given by

$$l_{DES} = \min(l, C_{DES}\Delta). \tag{2.62}$$

C_{DES} is set to 0.78 and Δ is as before.

2.8.2 Delayed Detached-Eddy Simulation (DDES)

The DES can have some problems to handle the transition between the LES and RANS zones. In the case of coarse mesh around the wall, the DES will work as expected with a transition outside the boundary layer. If the mesh is very fine ($\Delta = \delta/20$, with δ the boundary layer thickness), then the simulation will behave like a Wall-Modelled LES (LES with a wall model, RANS in this case). The problem appears for mesh size in between these two cases. The transitions takes place at about the first third of the boundary layer , and the two upper thirds of the boundary layer will then be in LES mode. This will reduce the turbulent viscosity and therefore the Reynolds strains.

Therefore, Spalart [70] developed the Delayed Detached-Eddy Simulation (DDES). The DDES introduces a limiter in the length scale ($\frac{\sqrt{k}}{\omega}$ in the $k-\omega$ model) that ensures that the transition will not take place in the boundary layer. In the Spalart-Allmaras model, this limiter modifies the parameter r (root of the ratio between the length scale and the wall distance):

$$r_d = \frac{\nu_t + \nu}{\sqrt{\frac{\partial U_i}{\partial x_j}\frac{\partial U_i}{\partial x_j}\kappa^2 d^2}} \tag{2.63}$$

with κ the Kàrmàn constant. The term $\nu_t + \nu$ can be replaced with $\tilde{\nu}$ in the Spalart-Allmaras model. Now r_d equals 1 in the logarithmic part of the boundary layer and equals 0 outside the boundary layer. ν avoids this term to tend to 0 very close to the wall. A new function f_d is defined as:

$$f_d = 1 - \tanh\left([8r_d]^3\right) \tag{2.64}$$

f_d equals 1 in the LES zones and 0 elsewhere. The "8"and "3"values are arbitrary and set the shape of f_d. These value were chosen in order to obtain good results for a planar wall flow.

The new value of the length scale un the Spalart-Allmaras model is now set at:

$$\tilde{d} = d - f_d \max(0, d - C_{DES}\Delta). \tag{2.65}$$

The RANS zone is defined by $f_d = 0$ and the LES zone by $f_d = 1$. In the case of highly detached flows, the detached zone is calculated in LES mode and the transition is quicker, allowing a smaller grey zone.

2.9 Summary of the Turbulence Models Used in this Thesis

A list of the turbulence models used in this paper and the acronyms used to designate them is shown in Table 2.5.

Table 2.5: Summary of the turbulence model used in this thesis, as well as their acronyms.

Acronym	**Description**
SA	Spalart-Allamaras model[40]
SALSA	Strain-Adaptative Linear Spalart-Allmaras[99]
DES	Detached-Eddy Simulation[61]
DES SALSA	Detached-Eddy Simulation[61]n with the Strain-Adaptative Linear Spalart-Allmaras[99] production term modification
DDES	Delayed Detached-Eddy Simulation[70]
DDES SALSA	Delayed Detached-Eddy Simulation[70] with the Strain-Adaptative Linear Spalart-Allmaras[99] production term modification
$k-\omega$	Wilcox's $k-\omega$ (1994) model[32]
$k-\omega$ BSL	Menter's $k-\omega$ Baseline model[41]
$k-\omega$ SST	Menter's $k-\omega$ Shear-Stress Transport model[41]

Chapter 3

Fluid Domain Modelling Strategy

The use of the HMB solver requires a CFD domain with boundaries far from the rotor. This domain is discretised using multi-block structured grids. A meshing method compatible with HMB, and adapted to rotor flows, has been used in this work. It uses multi-block topologies, which allow for easy sharing of the computational load over multiple processors and can also account for complex geometries. This method is described in this chapter followed by the description of the geometric properties of the rotors used in this work. The mesh generation was done using ICEM from Ansys.

3.1 Meshing Technique

3.1.1 Computational Domain Geometry

The computational domain is defined as a cylinder around the rotor. The cylinder's height and radius are set between 5 and 10 rotor radii, and 3 to 10 radii respectively, depending on the flight profile, as explained in the the following paragraphs.The origin of the reference frame is located on the rotor centre. The first blade is located at the positive X-axis, which corresponds to an azimuthal position of $\Psi = 0$ degrees and the rotation is about the Z-axis. For forward flying rotors, the wake will be concentrated near the rotor disk plane, and this allows for a narrower domain in the Z-direction. However, a wider

domain is needed (with respect to a hovering rotor) to accurately capture the wake structure. An example of such a domain is shown in Figure 3.1a. The blade is shown in blue, the far field in green and the hub in red. The mesh around one blade is first generated and then copied N_b times to create the complete computational domain. A flattened sphere is used to model the hub, limiting the interference with the flow field while still generating a wake and interacting with the flow field. The hub is not connected to the blades to allow for easy modification of the control angles of the rotor and account for some of the vorticity shed near the rotor hub. The hub can be modified to better approximate a real rotor head for test cases like the simulation of a complete helicopter. An example of hub shape is shown in Figure 3.2.

For hovering rotors, only a part of the rotor is modelled and higher wake resolution below the rotor plane is needed to predict the rotor performance. Since the wake tends to contract below the rotor disc, the far field boundary on this side of the domain can be located closer to the rotor (about 3 or $4R$). High quality wake predictions require the boundary under the blade to be moved down at about 5 to $7R$ away from the disk[106]. The spatial flow periodicity allows to compute the flow around one blade only, and periodic conditions are used on the planes $\Psi = \frac{180}{N_b}$ degrees and $\Psi = -\frac{180}{N_b}$ degrees. The fluid domain is then reduced to an angle of $\frac{360}{N_b}$ degrees as shown in Figure 3.1b, with the periodicity planes shown in green. The rotor hub is modelled in hover flight by a simple cylinder along the full height of the domain. Furthermore, a Froude boundary condition[107] shown in orange and purple is used instead of a far field boundary condition to bring the domain boundaries closer to the blade and thus decrease the computational cost[106]. This boundary condition shown in Figure 3.3 is based on the momentum theory and the outflow boundary is located on the lower surface of the cylinder. The velocity on this boundary depends on the thrust coefficient and the radius of the outflow part is set as:

$$\frac{R_{outflow}}{R} = 0.78 + 0.22 \exp\left(\frac{d_{outflow}}{R}\right) \tag{3.1}$$

with the notations shown in Figure 3.3.

In order to apply the control angles, the blade is rigidly moved to its new position. This approximation is acceptable since the blade is already missing all the actuators and the exact geometry of the hub, which would be too CPU-costly to represent and analyse. Their effect is also expected to

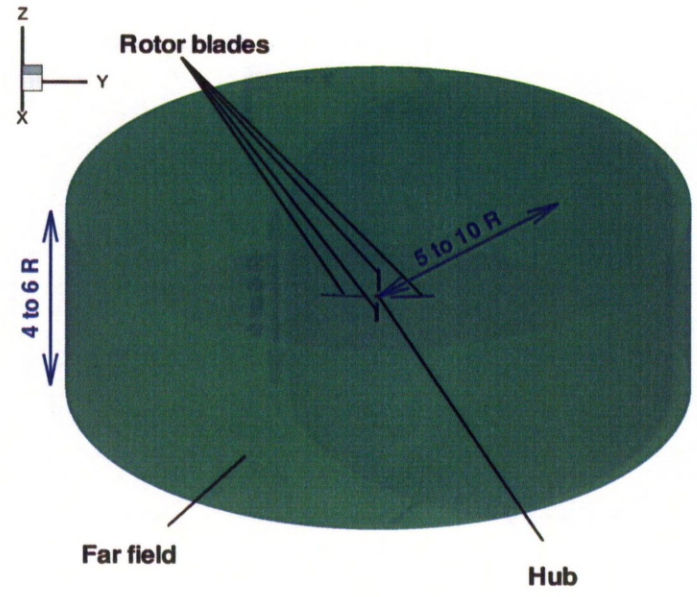

(a) Forward flight

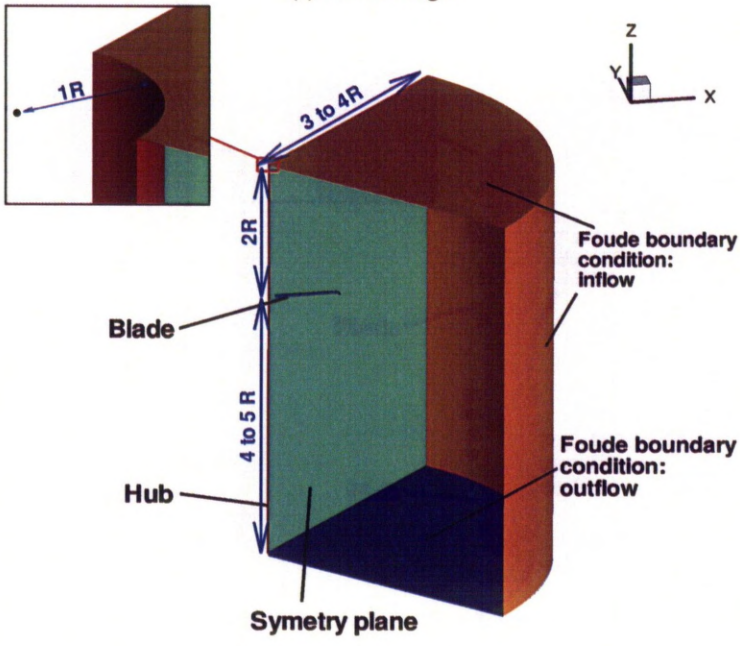

(b) Hover for a four bladed rotor

Figure 3.1: Computational domain geometry for forward flight and hover simulations.

(a) Basic rotor hub geometry

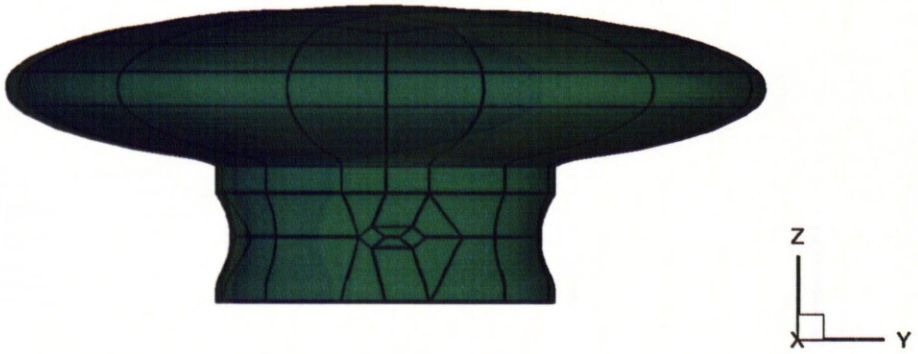

(b) More realistic rotor hub geometry

Figure 3.2: Hub geometries for forward flight cases.

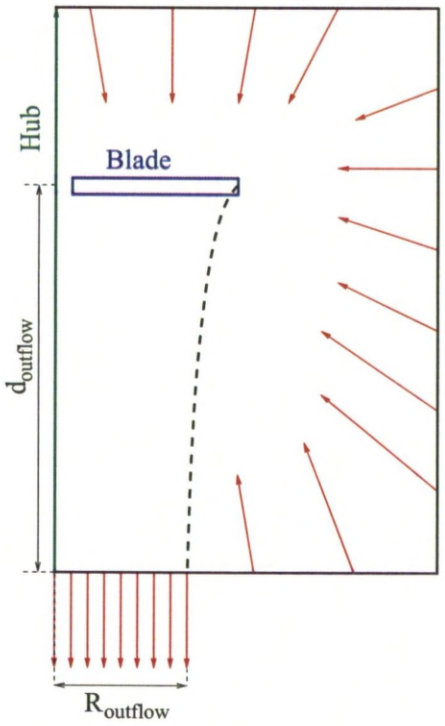

Figure 3.3: Description of the Froude boundary condition.

be secondary since near the centre of rotation the flow speed is substantially reduced and the resulting dynamic head is low.

The geometrical and computational differences are summarised in Table 3.1.

3.1.2 Blade Topology

The rotor multi-block topology was developed in a step-by-step fashion. The starting topology is a C-topology around a 2D aerofoil grid as shown in Figure 3.4a. A C-topology allows an adapted mesh to fit an aerofoil, following the properties of most sections: a smooth rounded leading edge and a truncated or sharp trailing edge. This grid is extruded in order to obtain the mesh around an infinite wing as shown in Figure 3.4b. However, to mesh a finite wing with a blunt tip, a structure is required to fit the void present in the C-topology from the wing tip to the far field. A double-A topology shown in Figure 3.4c is therefore inserted in the hole and projected on the wing tip as shown.

This wing topology is then generalised for rotor blades. The C-topology is embedded in an H-

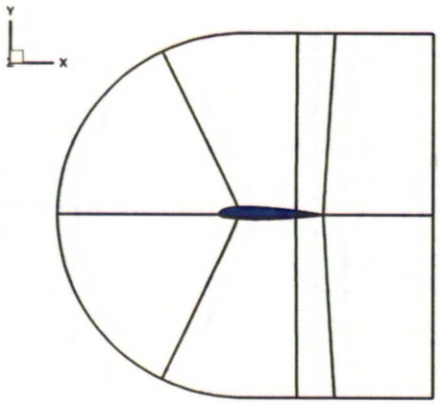

(a) 2D Aerofoil Section

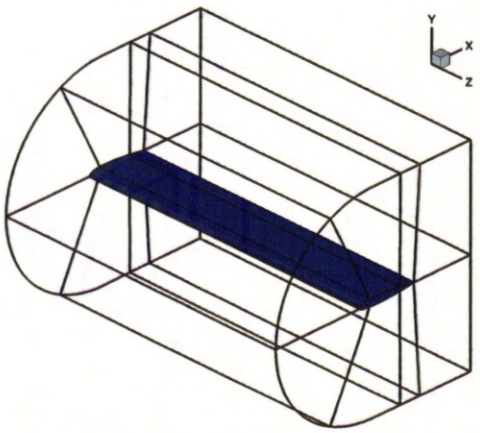

(b) 3D Infinite Wing

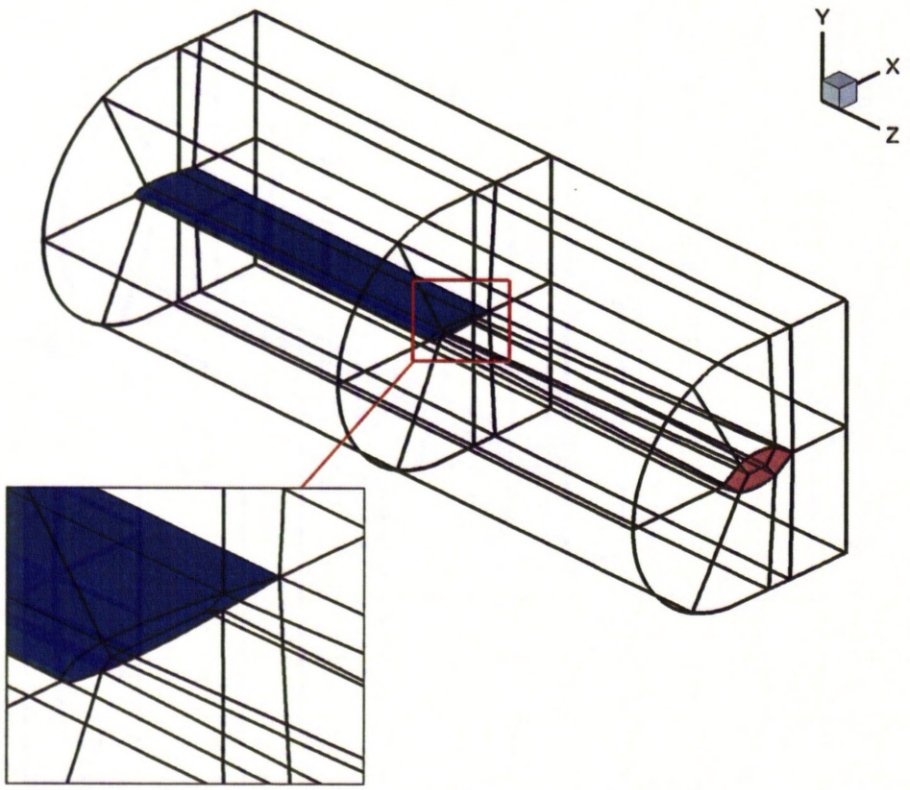

(c) 3D Finite Wing, with a zoom on the double-A topology

Figure 3.4: Multi-block topology for 2D-aerofoils and wings.

Table 3.1: Comparison of geometry and the computational methods for hovering and forward flying rotors.

Flight Type	Inflow Height	Outflow Height	Far Field Distance	Hub Geometry
Hover	$2R$	$-4R$ to $-5R$	$3R$ to $4R$	cylinder
Forward	$2R$	$-2R$ to $-3R$	$5R$ to $10R$	sphere

Flight Type	Calculation Type	Boundary Condition	Number of Blades in the Domain	Inertial Forces
Hover	steady	Froude	1	Source term/fixed term
Forward	unsteady	Far field	N_b	Moving mesh

O-block structure in order to fill the computational domain. The O-topology is used around the rotor rotation axis. Due to the blade-to-blade periodicity of the rotor geometry, the topology around a blade is first created and the full grid is then obtained by copying and rotating the grid by $360/N_b$ degrees $(N_b - 1)$ times.

An example of hover topology is shown in Figure 3.5. The four bladed ONERA 7A rotor is chosen here. The tip blocks are projected on the far field as shown in Figure 3.5a with the C-part of the mesh in blue. Due to the blunt tip of the blade, a double A-blocking is used from the blade tip to the far field. The H-O blocks embedding the C-blocks and filling in the computational domain are shown in white. When looking at slices perpendicular to the blade axis in Figure 3.5b, the C-part is also shown in blue and the blade surface in red. The projection of the double A-part (shown in detail in Figure 3.4c) on the blade tip is shown, as well as the use of this double-A topology between the root and the hub in green.

In the case of sharp blade tips like the ones used on the BERP-tip blade, the block topology was modified so that only one block, located on the leading edge of the blade, is added near the tip. This block is then extended to the far field. The rear of the C-part is then merged with the sharp trailing edge in order to avoid holes in the computational domain. The additional block is needed to keep the quality to a reasonable level and this quality could not be reached by just merging the C-blocks located around the leading-edge. The modified mesh topology is shown in Figure 3.6. An O-topology can also

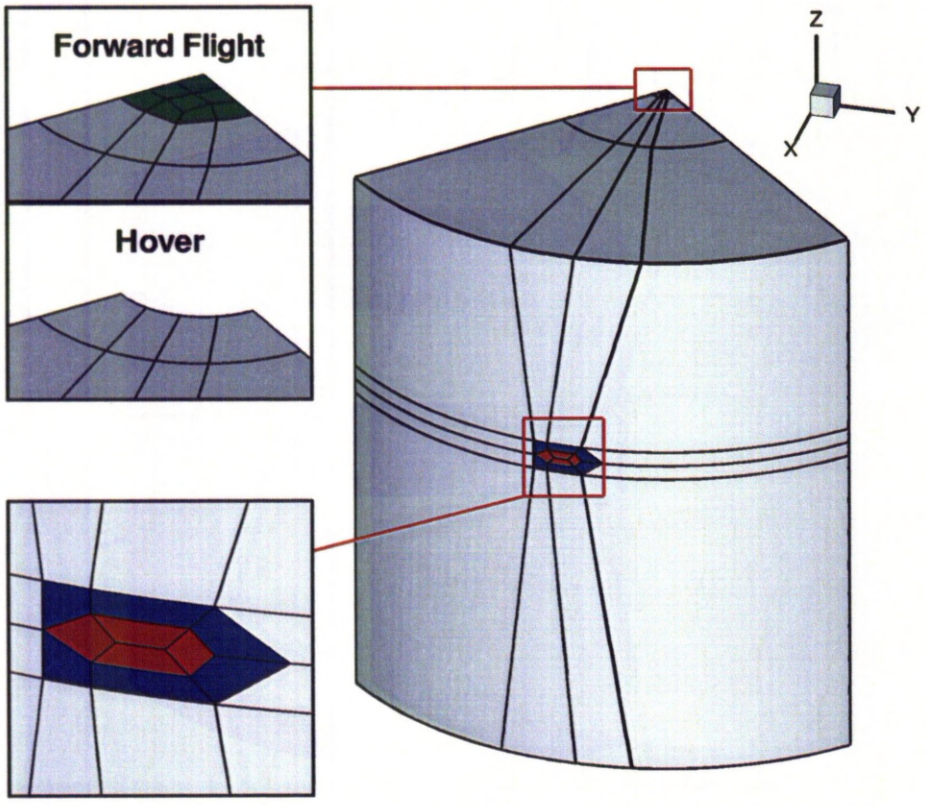

(a) Projection of the block edges on the far field

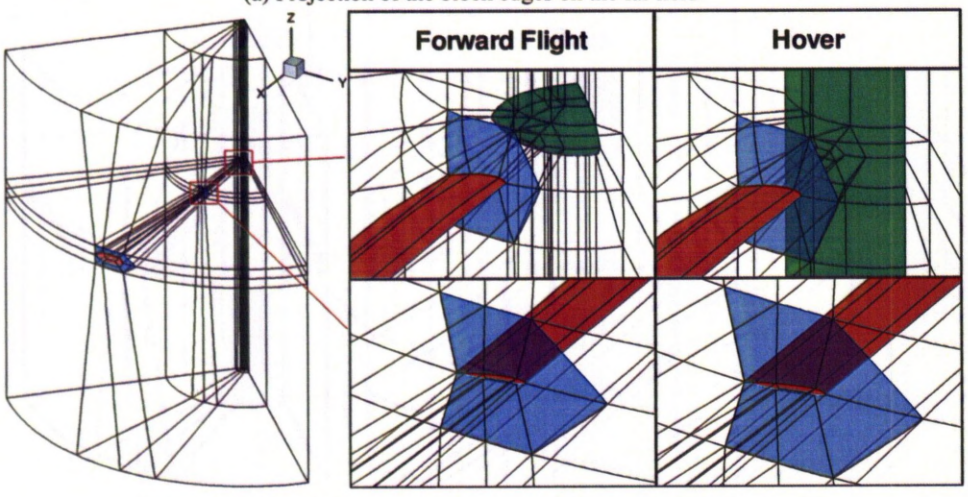

(b) Highlighted multi-block topology near the tip and hub of the rotor

Figure 3.5: Multi-block topology for hovering and forward flying rotors.

be added inside the leading-edge block at the tip as shown in Figure 3.6c. This addition increases the computational cost but allows a better quality of the cells located at the leading edge. This topology is used, for example, with DES turbulence models due to their high-quality mesh requirements.

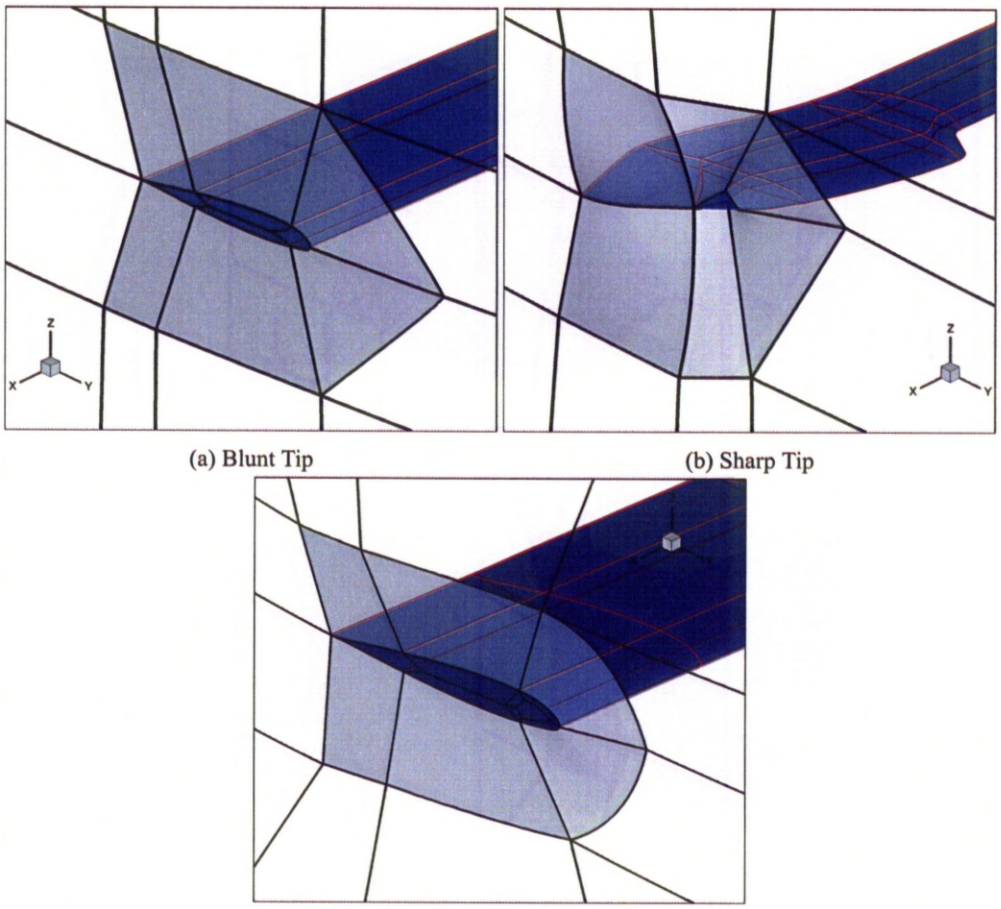

(a) Blunt Tip (b) Sharp Tip

(c) Blunt Tip with O-blocking at the Leading Edge

Figure 3.6: Multi-block topologies for several blade tips.

In forward flight, the main differences in topology are located close to the hub, with the rest of the computational domain unchanged. The new O-H-part over the hub is shown in green in Figure 3.5a. The double A-part from the blade root is now projected on the hub as shown in Figure 3.5b. The projection of the O-topology on the top surfaces of the hub is also shown. An O-topology can also be added around the hub to deal with more complex hub shapes as the one shown in Figure 3.2b.

3.1.3 Blade Meshing

The various blocks are then meshed. ICEM offers a choice of laws for distributing the nodes along an edge. For rotorcraft meshes, four laws are mainly used. L_1 denotes the spacing at the first end, L_2 the spacing at the other end, r_1 and r_2 the growth ratios at the first and second end of the edge respectively, S_i the curvilinear abscissa of the i-th node, N is the number of nodes and i the index of the current node. The law is described for an edge with a length of 1.

Exponential law This law distributes the nodes along the edge using the first spacing. The nodes location is defined by $S_i = L_1 ie^{[R(i-1)]}$. The R coefficient is set as $R = \frac{-\log[(N-1)L_1]}{N-2}$. This law allows for an appropriate nodes distribution in the logarithmic part of a viscous boundary layer.

Bigeometric law This law distributes the nodes based on the spacings and the growth ratios at both ends. The ratios are applied to the spacing until saturation is reached. If the growth ratios are too small to reach saturation, a hyperbolic law is applied instead.

Hyperbolic law This law computes the distribution of the nodes using a hyperbole law and by specifying the spacings at both ends. The nodes position is computed as $S_i = \frac{U_i}{2A+(1-A)U_i}$ with $U_i = 1 + \frac{\tanh(bR_i)}{\tanh(\frac{b}{2})}$, $R_i = \frac{i-1}{N-1} - \frac{1}{2}$, $A = \sqrt{\frac{L_1}{L_2}}$ and b is obtained by solving $\sinh b = \frac{b}{(N-1)\sqrt{L_1 L_2}}$.

Half-cosine law The spacing pattern follows a half cycle of a cosine function. The spacings can be set at both ends, however due to a possible high growth ratio at the second end, it is recommended not to enter any spacing at the second end (spacing set at 0.0). This law is mainly used for clustering the nodes around the stagnation point and the trailing edge.

The preceeding laws were applied to an edge with an unit length with 20 nodes, using a length of 0.01 and a growth ratio of 1.3 at both ends were applicable and the resulting nodes distributions are shown in Figure 3.7.

Most of the spacings are defined using the chord length c on the main part of the blade as the reference length. The most important spacing is the first wall-distance: this has to be low enough to allow capturing the blade geometry and have enough resolution in the boundary layer for viscous

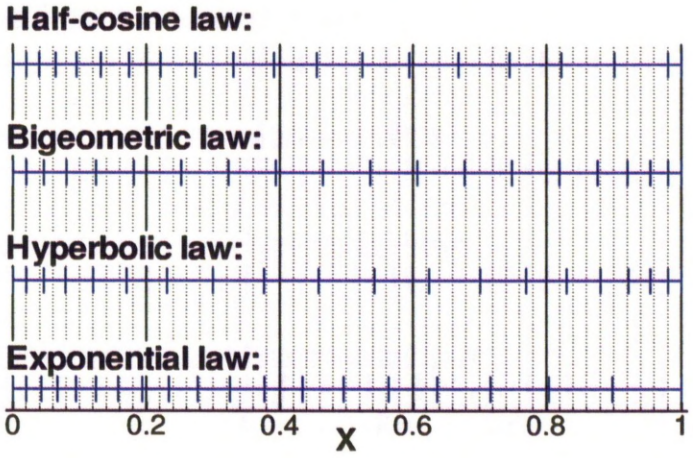

Figure 3.7: Nodes distribution laws in ICEM.

calculations, while being large enough to keep the computational cost at a reasonable level. Experience at Liverpool shows that wall spacing of $10^{-3}c$ for inviscid flows and $10^{-5}c$ gives enough resolution in the boundary layer and allows for $y^+ < 1$ in the first layer of cell for viscous flows, while keeping the cost of the calculation affordable. An exponential law perpendicular to the wall is used. On a blade section, at the leading and trailing edges, a half-cosine law is used in order to refine the grid close to the stagnation point and the trailing edge. The spacing used for this law is between $10^{-4}c$ and $10^{-3}c$ depending on how refined the grid is and if the flow is viscous or not. The mesh is also refined in the span-wise direction near the tip and the root. Spacings of $10^{-3}c$ for inviscid cases and $10^{-4}c$ for viscous cases are used with a bigeometric law at moderate coefficients between 1.5 and 1.7, if the target grid size allows. A hyperbolic law is used perpendicular to the hub with equivalents wall spacing compared to the blade. The use of a hyperbolic law allows smaller spacings at the other end of the edge but the spacing increase on the wall side will be high. This allows for the creation of a wake which will interact with the flow field around the blade at the back of the disk. Because of the high growth ratios perpendicular to the hub surface that the hyperbolic law may result in, the boundary layer may not be well capture, however the simulation is not aiming at accurately predicting the flow field and forces on the hub, therefore this approximation is acceptable.

The spacings are then smoothed inside the grid: the spacings at block boundaries are matched between adjacent blocks and the spacings are set on the edges using bigeometric laws with low ratios, near 1.3 if affordable. The ratios have to be increased behind the trailing edge with the increase of the radius due to the small spacings on the trailing edge side, and due to the need of a good quality grid coupled with the O-topology, which requires the cell edges to be almost parallel to planes at constant azimuth.

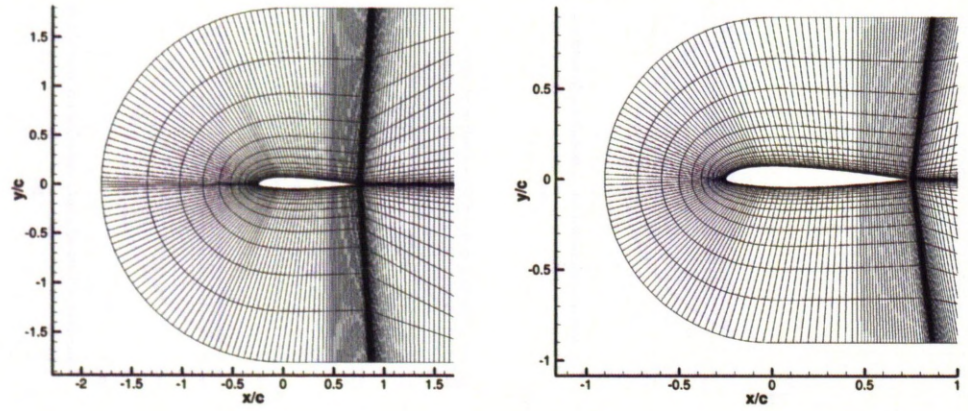

(a) $d_C = 1.8c$, $L_{max} = 0.52c$

(b) $d_C = 0.9c$, $L_{max} = 0.23c$

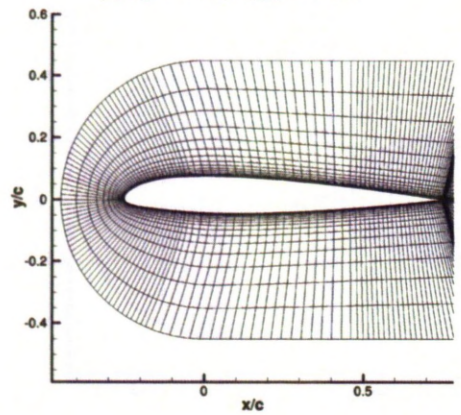

(c) $d_C = 0.45c$, $L_{max} = 0.12c$

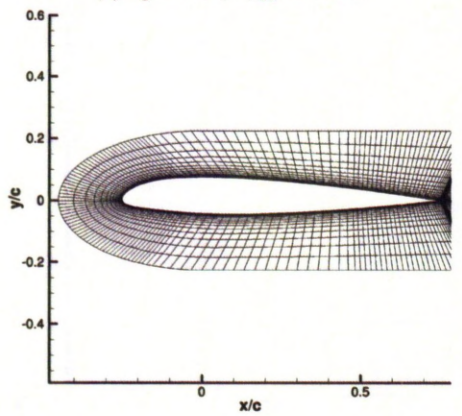

(d) $d_C = 0.225c$, $L_{max} = 0.06c$

Figure 3.8: Effect of an exponential distribution perpendicular to a wall with varying edge length, using a typical number of nodes along the edge. d_C is the height of the far field and L_{max} longest spacing in the exponential law.

Care is also needed when locating the face opposite to the blade surface for the blocks in contact with the blade. These should be located close to the blade surface to avoid long spacings at the top of it due to the exponential distribution, as shown in Figure 3.8. However, it needs to be high enough in order

to accommodate the blade structural deformations as will be explained in Section 5.1. A recommended distance would be between $0.25c$ and $0.5c$ and the number of points perpendicular to the blade is set so that the spacings due to the exponential law preferably don't exceed $0.1c$.

The requested flow definition also has to be taken into account: the grid has to be fine where resolution is needed. In hovering cases, the grid density has to be high along the path of the tip vortex in order to give a good resolution of the wake and thus of the rotor performance. The grid must be fine enough to accurately capture the tip vortex shed from the preceeding blade without too much dissipation. Preferably several vortices should be captured. In forward flight, the propagation of the tip vortices must be accurately predicted around the rotor disk due to the strong influence of the wake to the rotor. The field outer from the blade tip should also be refined in order to avoid too strong dissipation of vortices that may come back in the rotor disk area and influence the flow.

The mesh technique has been applied to multiple rotors and proved flexible enough to deal with a whole range of rotors available in the literature. A summary of the rotor grids developed using this technique is shown in Table 3.2.

Table 3.2: List of rotors meshed using the multi-block grid techniques of Section 3.1.2.

Rotor	Type	Blades	Tip Geometry
HART-II	model	4	blunt
ONERA 7A/7AD	model	4	blunt
UH-60A	main	4	blunt
Tilt-rotor, ADYNE blade	propeller	4	blunt
Tilt-rotor, TILTAERO blade	propeller	4	blunt
HIMARCS	model	4	blunt
SO-1	model	4	blunt
PM-3/4	model	4	sharp
Model main rotor 1	main	5	blunt
Model main rotor 2	main	5	sharp
Tail rotor model 1	tail	2	sharp
Caradonna-Tung	model	2	blunt

3.2 Mesh Topology for the Tilt-rotor Test Case

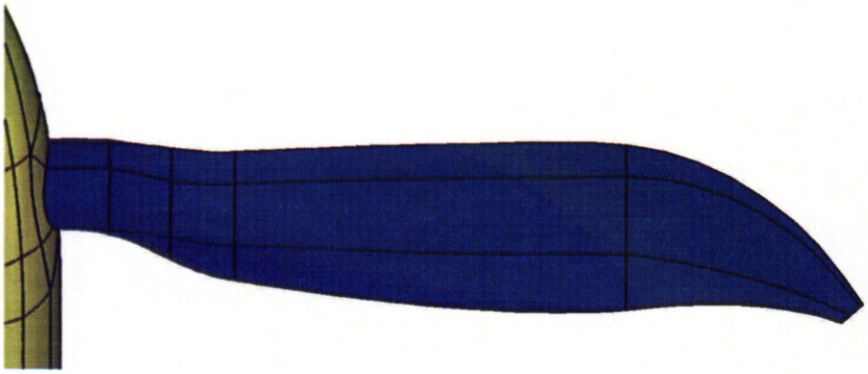

(a) TILTAERO Blade

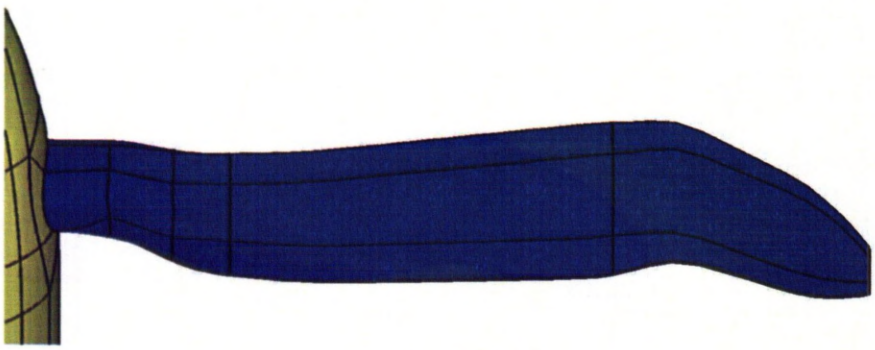

(b) ADYNE Blade

Figure 3.9: Comparison of the TILTAERO and ADYNE blade planform shapes.

To further demonstrate the flexibility of multi-block grids, the meshing technique developed in Section 3.1 was also used to create the mesh around tilt-rotor blades.The tilt rotor grids have to allow for large collective settings when used in propeller mode and therefore, the technique had to be adapted. The TILTAERO and ADYNE blades were used in this work. The ADYNE blade geometry was obtained out of an optimisation process by Beaumier *et al.*[108]. The blade planforms are compared in Figure 3.9.

Due to the configuration of the blades of the tilt rotor and the input direction of the flow, the block topology had to be adapted. The C-blocks were turned by 90 degrees around the blade axis on the far field and now face the top of the cylinder. This allows better mesh quality at high pitch angles in propeller mode. The topology can be seen in Figure 3.10. Furthermore, a spinner connected to the blades has been added. Without sliding plane[62], HMB can not rigidly rotate the blade to change the

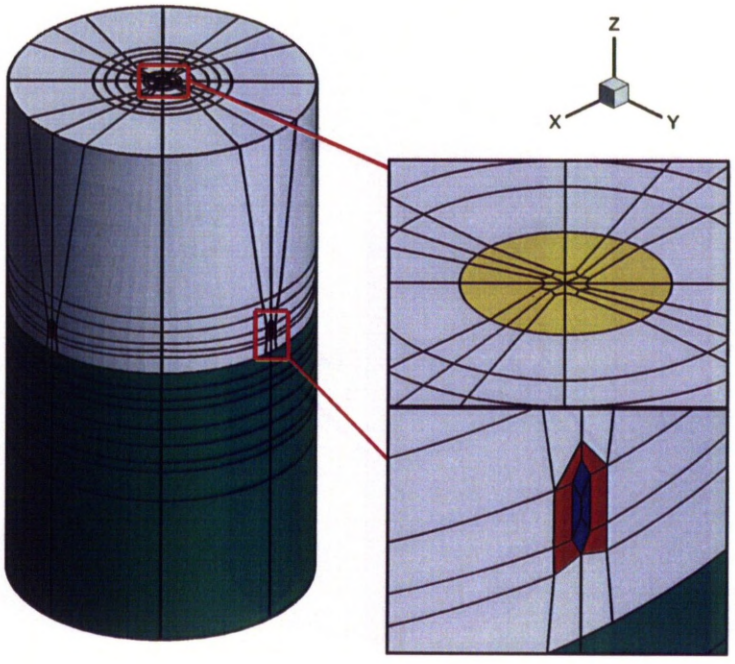

Figure 3.10: Edge projection on the far-field for a tilt rotor with nacelle. The non-rotating blocks around the nacelle are shown in green, the double-A structure from the blade tip in blue, the C-blocks around the blade in red and the blocks on top of the spinner in yellow. For the case without nacelle, the projection of the blocks is similar.

collective of the blade and this has to be done when the mesh around the blade is created in ICEM. The spinner starts with a conical shape as shown in Figure 3.11a and the cylinder at the bottom of the rotors goes along the spinning axis all the way to the far-field. On top of the spinner, the same block structure as the one used in forward flight was used.

A nacelle was later added using the sliding plane method available in HMB. The nacelle shape was representative of the geometry used in the experiments[109]. The geometry of the nacelle is shown in Figure 3.11b. The sliding surface is located very close to the rotor blade due to the proximity of the nacelle's thick upper part with the spinner of the rotor and the root of the blades. The sliding plane location can be seen in Figure 3.12.

The new topology was tested for both tilt rotor blades geometries (TILTAERO and ADYNE blades) without and with nacelle. Appendix C shows some CFD results for this case.

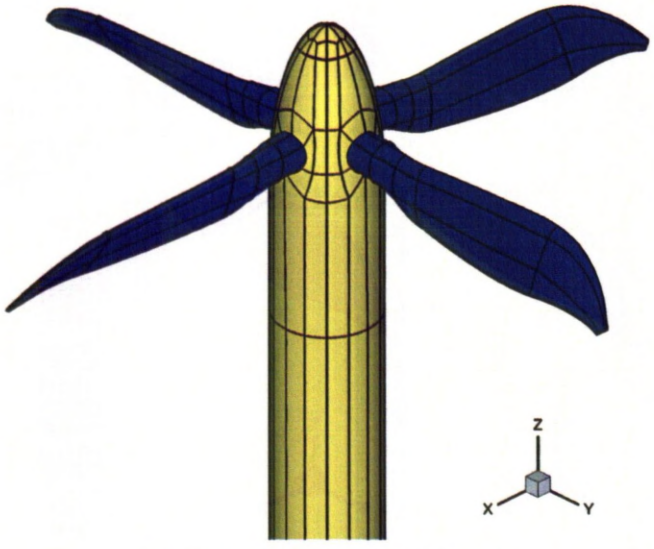

(a) Blades and spinner without Nacelle

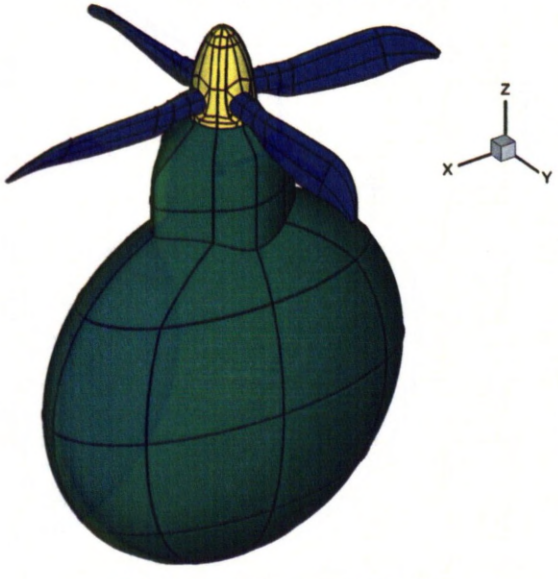

(b) Blade and spinner with Nacelle

Figure 3.11: Geometry used for the TILTAERO rotor in the case with and without nacelle. The blade is shown in blue, the (rotating) spinner in yellow and the (non-rotating) nacelle in green.

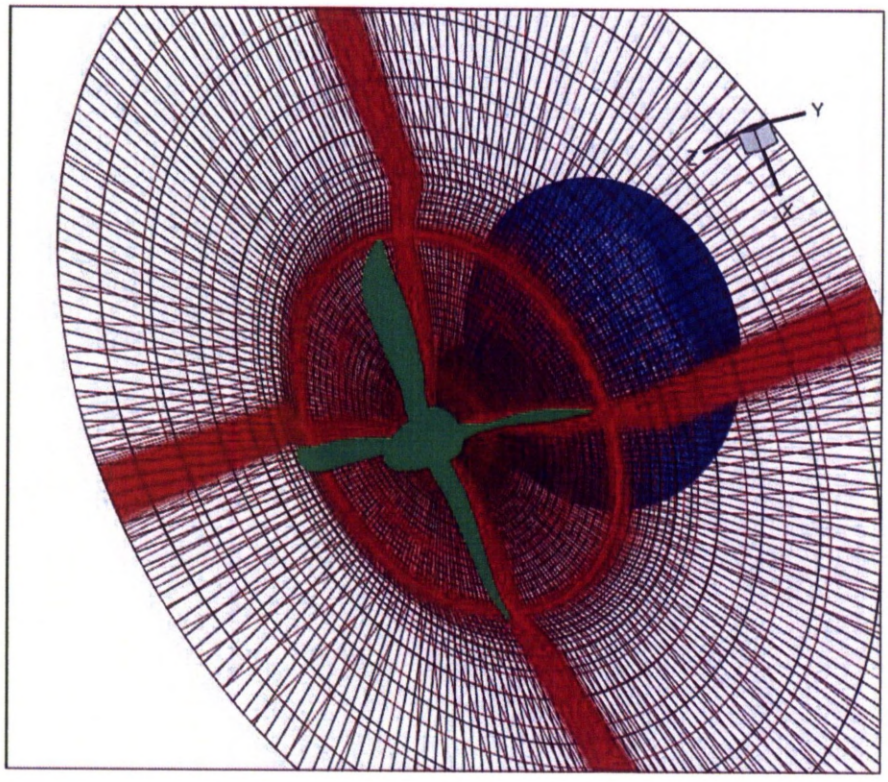

Figure 3.12: Location of the sliding plane in the grid around the TILTAERO rotor, with the mesh around the blade, the nacelle and the sliding plane. The rotor is in green, the nacelle in blue and the sliding plane in red (rotor side) and black (nacelle side).

3.3 Rotor Blade Geometries

3.3.1 The HART-II rotor

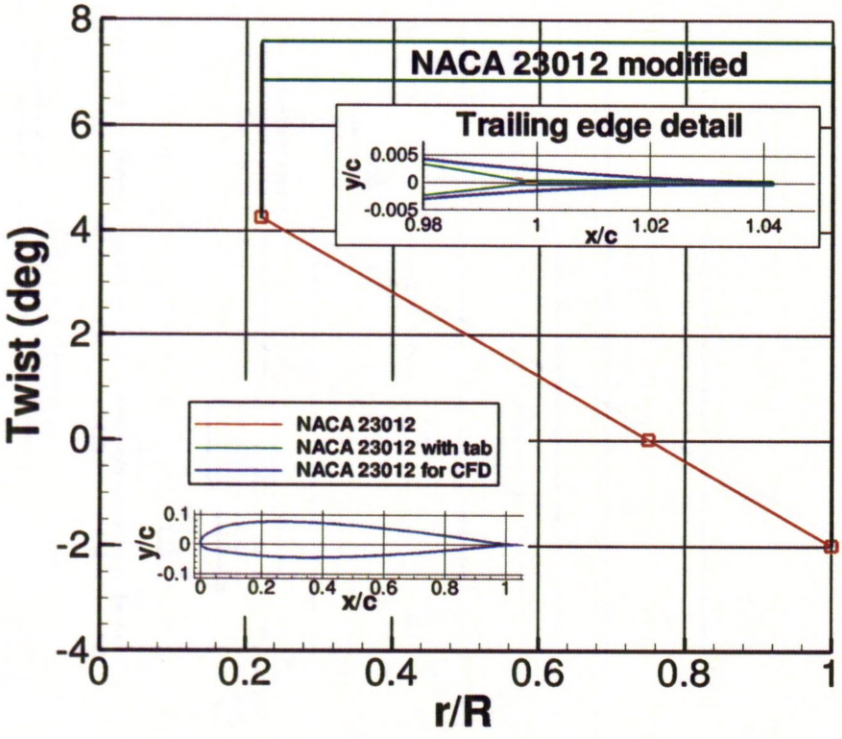

Figure 3.13: HART-II blade properties.

The HART-II[49] rotor consists of 4 rectangular blades with a 2 m radius and a chord of 0.121 m. The blade properties are shown in Figure 3.13. The blades have a built-in twist of -8 degrees/radius. A NACA23012 section is used along the span, and a 5 mm long tab is added at the tip of the blade. The shape of the aerofoil as well as the blade planform are described in Figure 3.13. In order to simplify the blocking topology, the blunt tip was made sharp. The root cut-out is located at $r/R = 0.22$.

3.3.2 The UH-60A rotor

The UH-60A[110] rotor has 4 rectangular blades with a swept-back tip. It has a radius of 28.63 ft (8.73 m) and a chord of 1.735 ft (0.529 m). The blade properties are shown in Figure 3.14. The tip of the blade

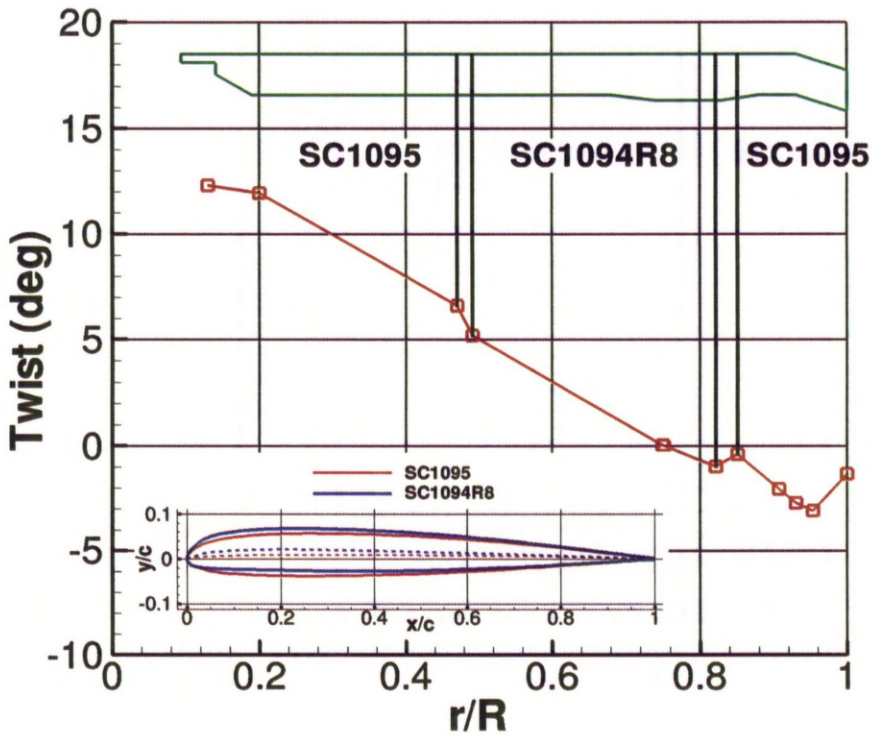

Figure 3.14: UH-60A blade properties.

is swept back at 20 degrees from $r/R = 0.93$. Two aerofoil sections are used, with linear transitions in between: the SC1095 from $r/R = 0.1925$ to $r/R = 0.4658$ and from $r/R = 0.8540$ to the tip, and the SC1094R8 from $r/R = 0.4969$ to $r/R = 0.8230$. The blade twist is shown in Figure 3.14.

3.3.3 The ONERA 7A and 7AD rotors

The ONERA 7A and ONERA 7AD[45] rotors are 4-bladed with a diameter of 4.2m and a chord of 0.14m. The 7A blade has a rectangular planform with a square tip, while the 7AD blade has a swept-back parabolic tip with a small anhedral from $r/R = 0.925$. Blade planforms and properties are shown in Figure 3.15. Both rotors use the same aerofoil distributions based on the OA213 from the root to $0.75R$ and the OA209 from $0.90R$ to the tip. Linear blending is used between the two sections. The twist distribution of this rotor is shown in Figure 3.15.

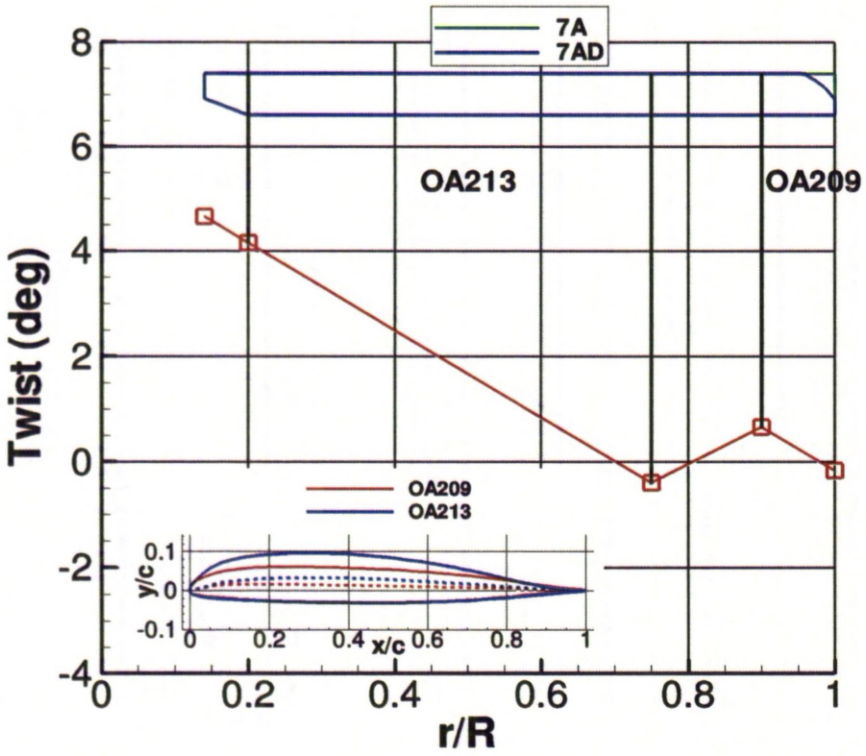

Figure 3.15: ONERA 7A and ONERA 7AD blade properties.

3.3.4 Summary of the rotor properties

The main properties of the various rotors used in this work are shown in Table 3.3. The properties of the other rotors meshed using the technique explained in this Chapter are described in Appendix A.

Table 3.3: Comparison of the geometrical properties of the rotors used in this work.

Rotor	Blades Number	Aspect Ratio	Aerofoil Sections	Linear Twist
HART-II	4	16.528	NACA23012 with tab	-8deg/R
UH-60A	4	15.476	SC1095 and SC1094R8	-20deg/R
ONERA 7A/7AD	4	15	OA209 and OA213	-8deg/R

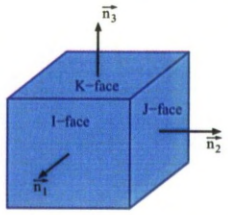

Figure 3.16: Notation for cell skewness definition.

3.4 Mesh Quality Assessment

The mesh quality has then to be assessed. Two criteria were used: the cell volume and the cell skewness, defined as:

$$Sk = \max\left(\mathbf{n}_i \cdot \mathbf{n}_j\right) , \qquad i \neq j \quad , \tag{3.2}$$

where $\mathbf{n}_i$ is the normal of the i-th face with the notations shown in Figure 3.16. The cell volumes are checked as all being positive. The skewness also has to be kept within reasonable levels.

The quality is demonstrated for a UH-60A rotor blade mesh in Figures 3.17 and 3.18. The grid is adapted for hover flight, with a cylindrical hub and a refined area under the blade. The grid contains 8.6 million nodes. The refinement under the blade tip area is clearly visible in the cell volumes plot. Despite a high increase of the cell volume being expected at increasing radii due to the O-topology, the cell volume is still set at a rather low level, allowing for a lower numerical diffusion of the tip vortex. The skewness shows that highly skewed cells tend to be out of the C-part of the mesh where a high quality is needed in order to accurately predict the flow field around the aerofoil and the tips. The skewness on the leading edge is one of the main problems linked to this grid topology due to the high suction that appears on the blade tip leading edge when the blade tip is blunt. If the quality of the mesh needs to be increased, an O-grid can be introduced in the block at the leading edge, allowing a smoother grid at the leading edge while increasing the computational cost and introducing constraints on the mesh in other parts as shown in Figure 3.6c.

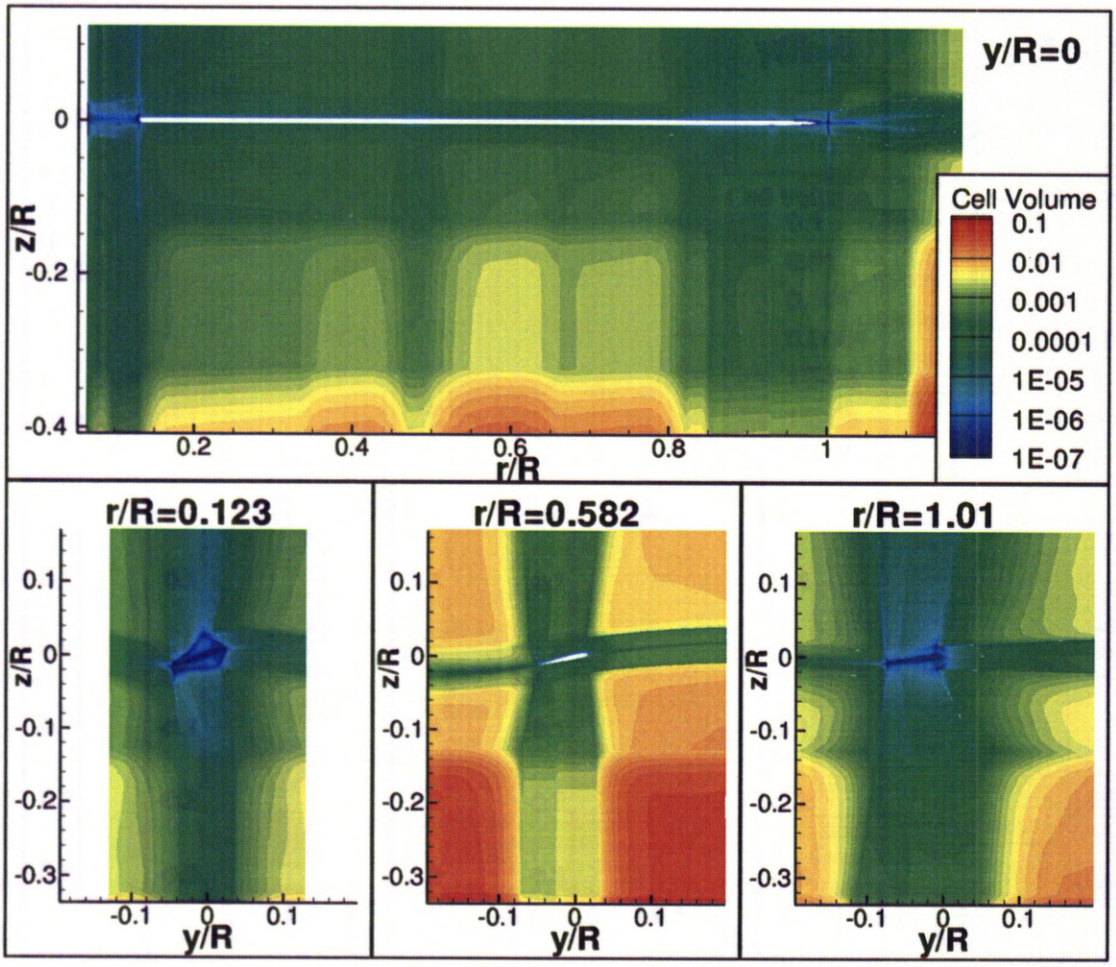

Figure 3.17: Mesh quality assessment on a UH-60A rotor grid for hover — Cell volume.

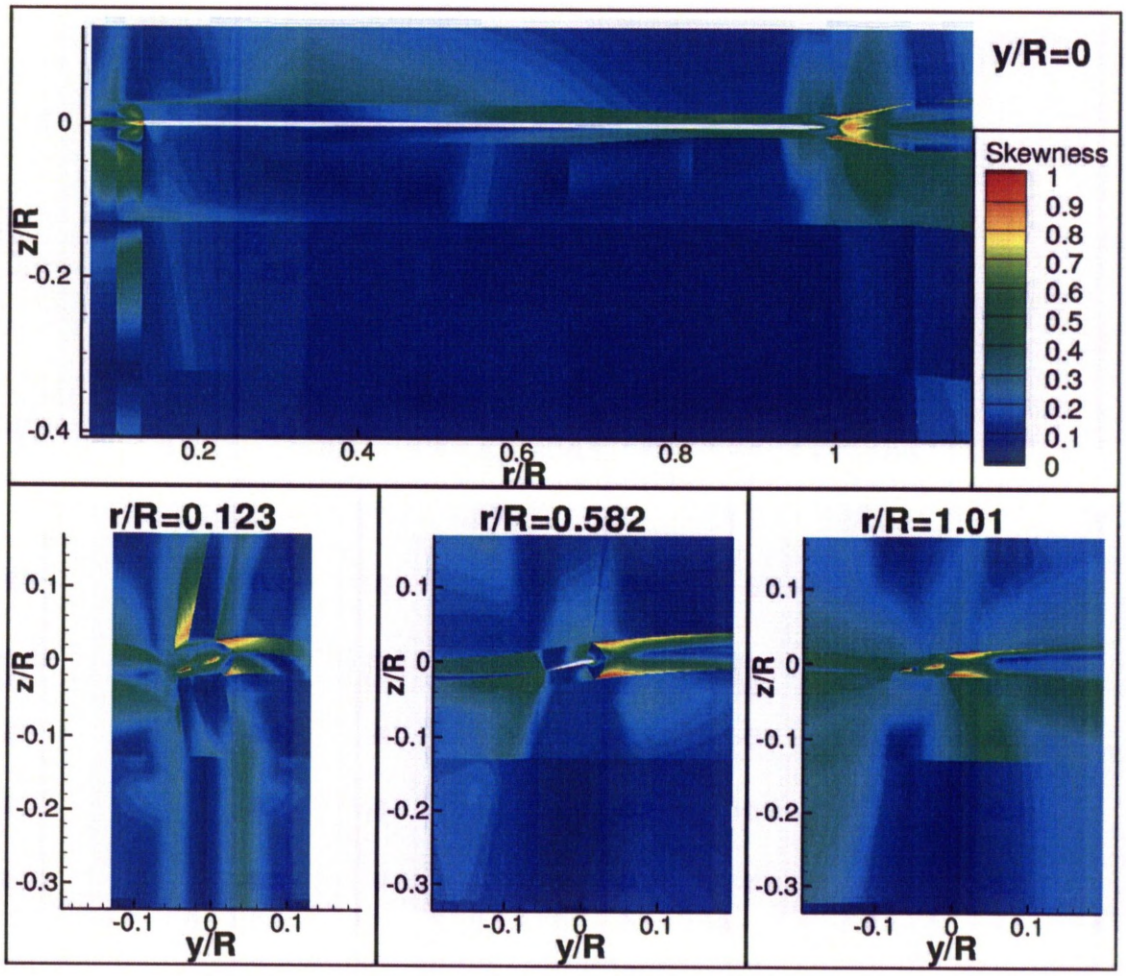

Figure 3.18: Mesh quality assessment on a UH-60A rotor grid for hover — Cell skewness.

Chapter 4

Blade Structural Modelling Methods

Blade structures are often modelled as beams, since their properties are mainly distrubuted in the span-wise direction and 1-D Finite element models (FEM) can be used. In this work, the beam modelling approach has been chosen, as it is also well adapted to the blade geometry: the blade span tends to be much larger than the chord and the aerofoil thickness.

4.1 Modal Approach

For forward flying rotors, the modal approach is used to lower the cost of computing the blade deformations. It expresses the blade deformation as a function of the blade eigenmodes. The blade shape ϕ is then described as a sum of eigenvectors ϕ_i representing the blade displacements for each eigenmode multiplied by the coefficient α_i:

$$\phi = \phi_0 + \sum_{i=1}^{n_m} \alpha_i \phi_i \tag{4.1}$$

where ϕ_0 is the undeformed eigenvector. The problems is then reduced to solving for the coefficients α_i.

In the modal approach, the coefficients can be obtained by solving the following differential equation:

$$\frac{\partial^2 \alpha_i}{\partial t^2} + 2\zeta_i \omega_i \frac{\partial \alpha_i}{\partial t} + \omega_i^2 \alpha_i = \mathbf{f} \cdot \phi_i \tag{4.2}$$

where **f** are the external forces applied to the blade projected at each structural node, ω_i is the eigenpulsation and ζ_i the structural damping coefficient, which tends to be small.

For hovering rotors, a static deformation under a prescribed loading was found more adapted to the steadiness of the problem and therefore used.

4.2 Structural Models: Finite Element Models

In order to solve the blade eigenmodes, a finite element model is used due to the complexity of getting analytical solutions for problem with the complex blade properties. Two methods were compared: the Myklestad's method described in Appendix B and a finite-element model using NASTRAN[111]. Myklestad's method is simple and allows for quick evaluation of the eigenmodes and natural frequencies, however, the numerical stability of the method induces limitations on the rotational speed range and the range of natural frequencies. Therefore NASTRAN was used in this work to extract the blade natural frequencies and vectors.

4.2.1 Structural Model Design

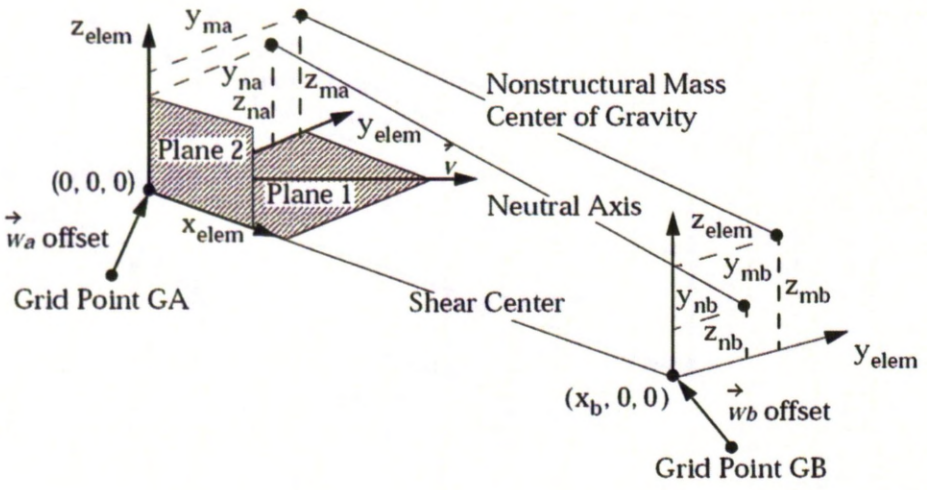

Figure 4.1: CBEAM/PBEAM element properties, from [111].

In NASTRAN, the blades are modelled using CBEAM elements with a set of PBEAM properties. CBEAM/PBEAM element properties are shown in Figure 4.1. These elements allow the use of the following properties:

- **chordwise and flapwise area moment of inertia** (I_c, I_f) defined at each end of the beam with a linear variation, intermediate values can be added,
- **torsional stiffness** (J) defined at each end of the beam with a linear variation, intermediate values can be added,
- **linear mass distribution**(dm) defined at each end of the beam with a linear variation, intermediate values can be added,
- **location of the shear centre compared to the actual node location** ($\vec{w}_a$, $\vec{w}_b$) allows for the structural model to be located on the quarter chord line,
- **mass centre position relative to the shear centre** (y_{ma}, z_{ma}, y_{mb}, z_{mb}) defined at each end of the beam with a linear variation,
- **neutral axis relative to the shear centre** (y_{na}, z_{na}, y_{nb}, z_{nb}) defined at each end of the beam with a linear variation,
- **radius of gyration** defined at each end of the beam with a linear variation.

Inertial forces and an arbitrary loading can be introduced using RFORCE and PLOAD entries respectively.

The blade properties are usually spread on 25 to 100 CBEAM elements along the blade span. This number of elements is shown to be sufficient for the modal analysis (see Section 4.3.3) and gave a fine enough base for the interpolation on the fluid grid. The interpolation of the structural movements to a group of triangular elements covering the blade surface perpendicular to the vertical axis was helped by the use of CBARS connected to the CBEAM nodes and going in the chordwise direction. A typical rotor blade model is shown in Figure 4.9.

4.2.2 Eigenmodes Extraction

The blade eigenmodes are extracted using SOL 106 of NASTRAN with the Modified GIVens (MGIV) Method. The SOL 106 is a non-linear simulation, allowing to extract both the static deformation under a prescribed loading and the structure eigenmodes. The centrifugal forces are taken into account in the stiffness matrix by recomputing them after each iteration to update their orientation in the local beam element frame. The eigenvectors are then extracted with the modified Givens (MGIV) method[111].

The MGIV method first rearranges the matrix of the eigenvalue problem using a Cholesky decomposition of the positive definite matrix:

$$\mathbf{K}+\lambda_s\mathbf{M}=\mathbf{L}\mathbf{L}^T \tag{4.3}$$

where $\lambda_s > 0$ is selected by the program.

The eigenvector equation is then written as:

$$\left[\bar{\mathbf{J}}-\bar{\lambda}\mathbf{I}\right]\bar{\mathbf{w}}=\mathbf{0}, \begin{cases} \bar{\lambda}=\frac{1}{\lambda+\lambda_s} \\ \bar{J}=\mathbf{L}^{-1}\mathbf{M}\mathbf{L} \end{cases} . \tag{4.4}$$

The $\bar{\mathbf{J}}$ matrix is then converted to a tridiagonal matrix using Givens' method. The eigenvalues of this tridiagonal matrix are then extracted using a modified QR algorithm[112]. The eigenvectors are computed over the specified range. The physical eigenvectors are then recovered as:

$$\mathbf{u}=\mathbf{L}^{T,-1}\bar{\mathbf{w}}, \tag{4.5}$$

the modal matrix is calculated using:

$$\mathbf{M}_{modal}=\mathbf{\Phi}^T\mathbf{M}\mathbf{\Phi}. \tag{4.6}$$

$\mathbf{M}_{modal}$ is then decomposed following

$$\mathbf{M}_{modal}=\mathbf{L}^T\mathbf{L}, \tag{4.7}$$

and the refined eigenvectors $\bar{\mathbf{\Phi}}^T$ are found by a forward pass on the equation:

$$\mathbf{L}\bar{\mathbf{\Phi}}^T=\mathbf{\Phi}^T. \tag{4.8}$$

4.3 Blade Eigenmodes Demonstration and Validation

NASTRAN analyses were compared to experimental results for several test cases including Wilkie's blade[3], the UH-60A blade[110] and the HART-II blade[49].

4.3.1 Wilkie's Blade Validation

The first validation was realised on Wilkie's blade[3]. This blade was experimentally tested and the natural frequencies were extracted. The main blade properties were also measured and are shown in Figure 4.2. The blade natural frequencies were tested for non-rotating and rotating rotors with the rotational speed varying between 150 and 660RPM. This rotor was chosen to assess both NASTRAN and the Myklestad's method.

The blade was divided into 51 CBEAM elements along the quarter chord line. The attachment on the hub consisted of a lead-lag damper, modelled as a perfect elastic CELAS2 element and the blade root was rigidly attached to the hub in translation, and no torsion was allowed on the hub attachment. The blade model is shown in Figure 4.3 comparison between the experimental measurements and the simulation results is shown in Figure 4.4.

The Myklestad's method showed very strong limitations on the frequency range of both the natural frequencies and rotational speed due to numerical stability issues. The results however proved accurate when in the non-rotating test-case. However, for a rotating blade, the frequency are over-predicted. Therefore, it was decided to only use the NASTRAN finite element for the rest of this work. The test case is entered in NASTRAN as shown in Table 4.1. The included *nasamodel* file contains the blade structural model data as MAT, GRID, CBEAM and PBEAM entries, as shown in Table 4.2. The amplitude can be scaled either to a unit mass or a unit maximum displacement (in translation or rotation). The default scaling is the mass one.

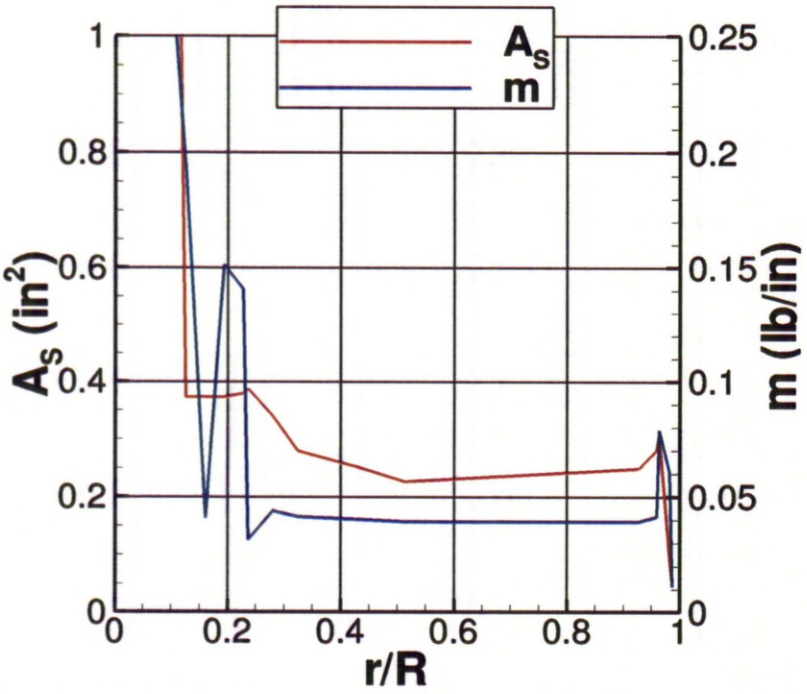

(a) Sectional area and linear mass distribution ($1\,\text{in}^2 = 6.45 \times 10^{-4}\,\text{m}^2$ and $1\,\text{lb/in} = 17.86\,\text{kg/m}$)

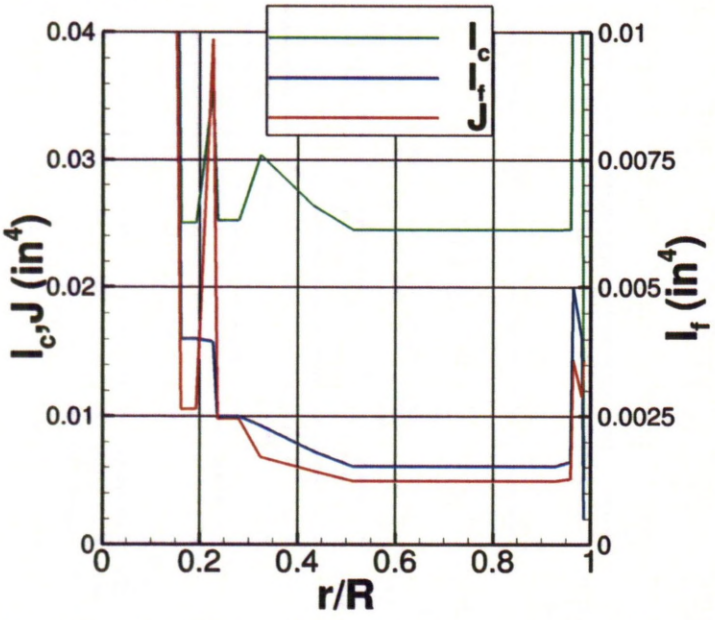

(b) Chordwise, flapwise and torsional area moments of inertia ($1\,\text{in}^4 = 4.16 \times 10^{-7}\,\text{m}^4$)

Figure 4.2: Main properties of Wilkie's blade.

Table 4.1: NASTRAN input file for Wilkie's blade case.

	Instruction	Description
1	PROJ='WILKIE'	Project name
2	ID NASA ROTOR	Project ID
3	SOL 106	Solution number
4	TIME 20	Maximum computational time
5	CEND	End of execution control section
6	TITLE=NASA SHAKE TEST ROTOR	Case name
7	LABEL=CF LOAD 11 HZ ROTATION	Case label
8	SUBTITLE= NORMAL MODES RESTART SOL 106	Case sub-name
9	ECHO=BOTH	Print sorted and unsorted bulk data in the output
10	DISP=ALL	Generate the displacements of all grids
11		
12	OLOAD=ALL	Print the applied loads in the output
13	SEALL=ALL	All superelements matric need to be generated and assembled
14	LOAD=1	Loading ID
15	NLPARM=100	Non-linear parameters ID
15	METHOD=10	eigenvalue extraction method ID
16		
17	BEGIN BULK	Start the bulk data cards
18	PARAM, TINY, 0.999	Do not display elements with small energy
19	PARAM, GRDPNT, 0	Reference GRID point for the weight generation, 0=(0.,0.,0.)
20	PARAM, MAXRATIO,1.+13	Min. eigenvalue ratio for the matrix to be considered as singular
21	PARAM, COUPMASS,1	Use coupled masses
22	PARAM, WTMASS, 0.00259	Scale the masses if using a non-consistent unit system
23	PARAM, AUTOSPC,YES	Remove very small degrees of freedom
24	PARAM, LGDISP, 1	Enable the large displacement capability
25	PARAM, NMLOOP, 1	Compute the normal modes with the update nonlinear stiffness
26	NLPARM, 100, 2, , ITER, 1	Non-linear calculation entry
27	PARAM, TESTNEG, 1	Continue if negative terms are encountered on the factor diagonal
28	EIGR, 10, MGIV, 0., 100.	Eigenvalue extraction method
29	RFORCE, 1, 0, , 11., 0., 0., 1., 2	Inertial forces
30	INCLUDE 'nasamodel'	Include the entries from the 'nasamodel' file
31	ENDDATA	End of the input file

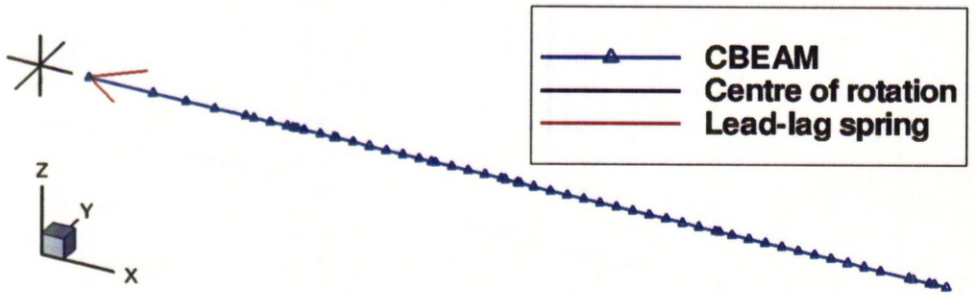

Figure 4.3: Wilkie's rotor blade model in NASTRAN.

Table 4.2: NASTRAN input file for Wilkie's blade properties.

	Instruction	Description
1	`MAT1, 1000, 1.0+7, , 0.3`	MAT1, ID, E, G, Poisson's coefficient.
2	`GRID, 200, , 3.00, 0.0, 0.0, , 1234`	GRID, ID, , X, Y, Z, , Boundary condition.
3	`CBEAM, 200, 200, 200, 201, 0.0, 1.0, 0.0`	CBEAM, ID, PBEAM ID, End1 GRID ID, End2 GRID ID, Xorientation, Yorientation, Zorientation
3	`CBEAM, 200, 200, 200, 201, 0.0, 1.0, 0.0`	CBEAM, ID, PBEAM ID, End1 GRID ID, End2 GRID ID, orientation vector (X,Y,Z)
4	`PBEAM, 200, 1000, 5.500, 0.5000, 0.5000, , , 0.2632, 0.42511,+P2001`	PBEAM, ID, $A_s, I_c, I_f, I_{cross}, J, m_A$
5	`+P2001, , , , , , , , , +P2002`	
6	`+P2002, , , , , 2.200-1`	m_B
7		
8		

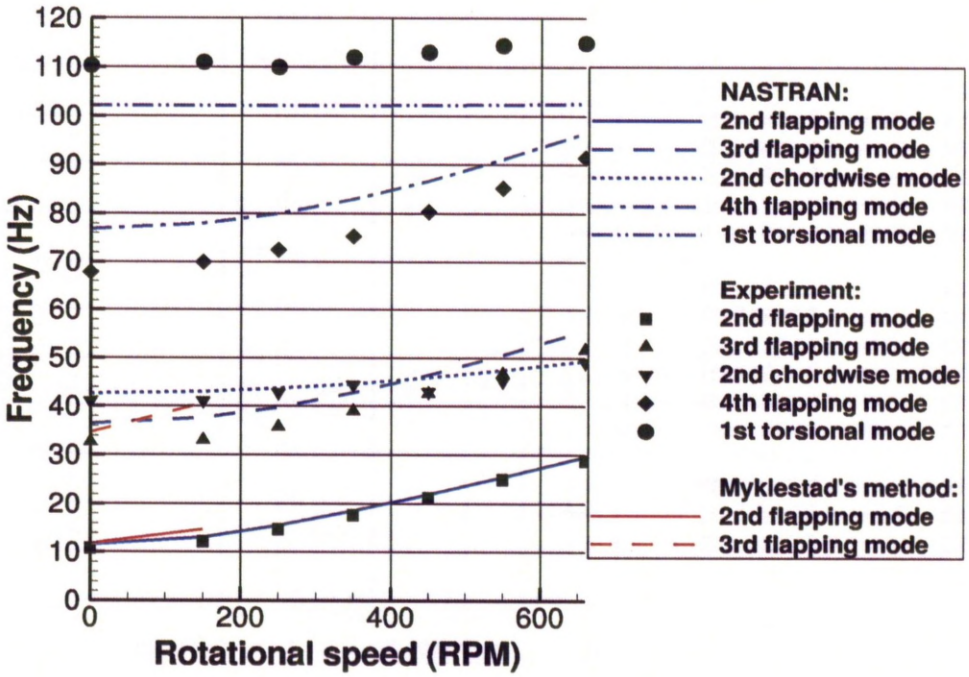

Figure 4.4: Comparison of the natural frequencies on Wilkie's blade predicted by NASTRAN and the Myklestad's method with experimental results.

The output file, with a *.f06* ending, contains both the natural frequencies and displacements. The output file contains first the natural frequencies for every mode, which are presented as shown:

```
                                    R E A L   E I G E N V A L U E S

MODE   EXTRACTION   EIGENVALUE       RADIANS        CYCLES       GENERALIZED     GENERALIZED
 NO.      ORDER                                                      MASS          STIFFNESS
   1          1   -3.523759E-08  1.877168E-04  2.987605E-05  1.000000E+00  -3.523759E-08
```

The *CYCLE* field contains the natural frequencies and the *GENERALIZED MASS* field contains the mass (here the mode was mass scaled, meaning that the amplitude was scaled so that the mode scale reached one). The mode shape is then described for each eigenvalue:

```
  CYCLES =  2.987605E-05     R E A L   E I G E N V E C T O R   N O .      1

POINT ID.  TYPE       T1            T2            T3            R1            R2            R3
     200     G  0.0           0.0           0.0           0.0           4.470830E-01  2.683275E-29
(...)
    1051     G  3.734695E-08  2.332878E+01 -5.448011E-06  2.607854E-09  4.200116E-07  4.524987E-01
```

For each grid node (identified by its ID in the first row), the displacements along the X-, Y- and Z-axis (T1, T2 and T3) are presented followed by the rotation around the X-, Y- and Z-axis (R1, R2 and R3).

NASTRAN predictions were relatively close to the experimental results, however, the error increased with the frequency, and the first torsional frequency is under-predicted by about 10Hz. Wilkie[3] had the same error and point out the link between the rotor head and the blade not being modelled but being replaced by a rigid link between the two in the analysis.

A more detailed description can be found in the HMB Technical Note TN09-002.

4.3.2 UH-60A Blade Validation

The second validation of the NASTRAN structural modelling technique was done on the UH-60A rotor blade. The UH-60A blade properties are shown in Figure 4.5 and were obtained from Hamade *et al.*[4]. The blade natural frequencies were measured by Kufeld *et al.*[113]. The experiment was done for a blade suspended to the roof by four elastic strings. The experiment aimed at reproducing a free-free condition

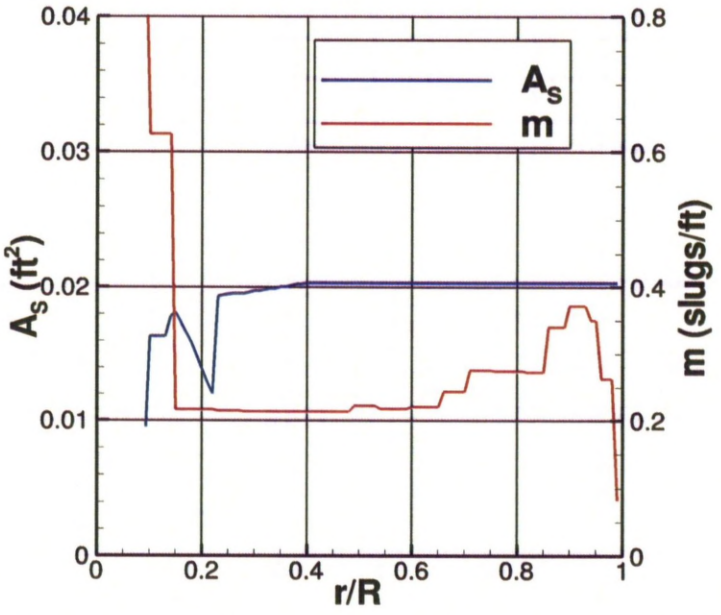

(a) Sectional area and linear mass distribution ($1\,\text{ft}^2 = 0.0929\,\text{m}^2$ and $1\,\text{slug/ft} = 47.88\,\text{kg/m}$

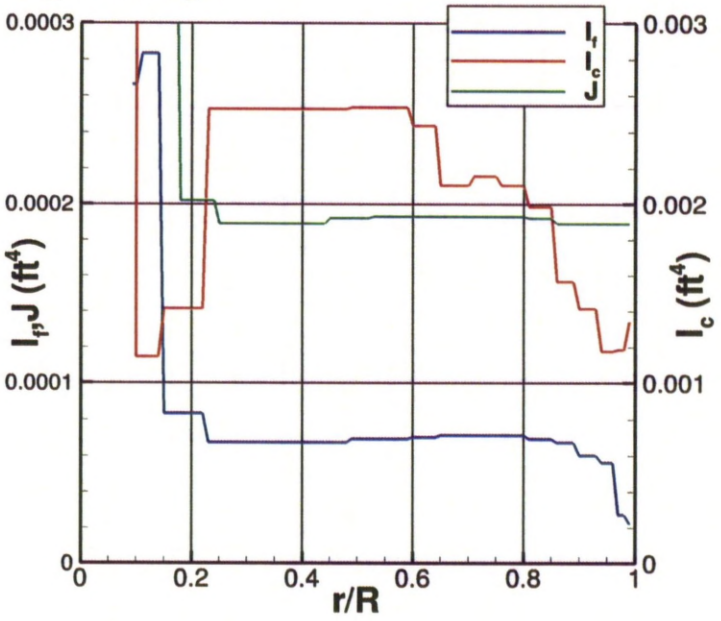

(b) Chordwise, flapwise and torsional area moments of inertia ($1\,\text{ft}^4 = 0.00863\,\text{m}^4$)

Figure 4.5: Main properties of the UH-60A rotor blade.

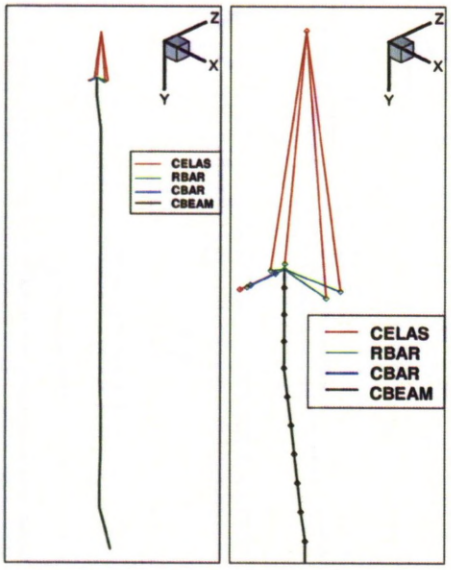

(a) General view (b) Zoom on the root

Figure 4.6: Hanging UH-60A blade model in NASTRAN.

for the test. The blade model is shown in Figure 4.6 and contains 89 CBEAM elements along the quarter chord line, with the nodes being spaced by $.01R$. The four attachment strings are modelled as elastic elements and the shaker is modelled as CBAR elements. The main difference in the NASTRAN deck, apart from the FEM model is the loading: the inertial forces entry (RFORCE) has been replaced with a gravity entry, set to $32.174\,\mathrm{ft/s^2}$ ($9.807\,\mathrm{m/s^2}$):

```
GRAV,21,0,32.174,0.0,-1.0,0.0
```

The natural frequencies obtained from the NASTRAN model compared well with experimental measurements, as shown in Figure 4.7. The eigenmode shapes are shown in Figure 4.8.

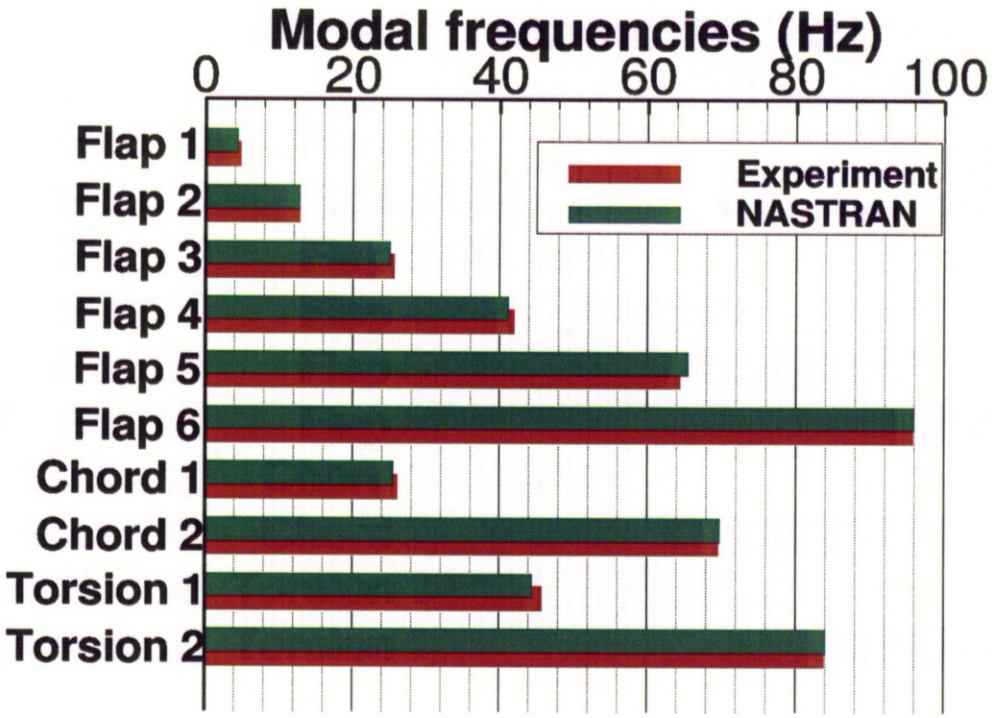

Figure 4.7: Comparison of the natural frequencies obtained by NASTRAN for a hanging UH-60A blade with experimental measurements from Kufeld *et al.*[113].

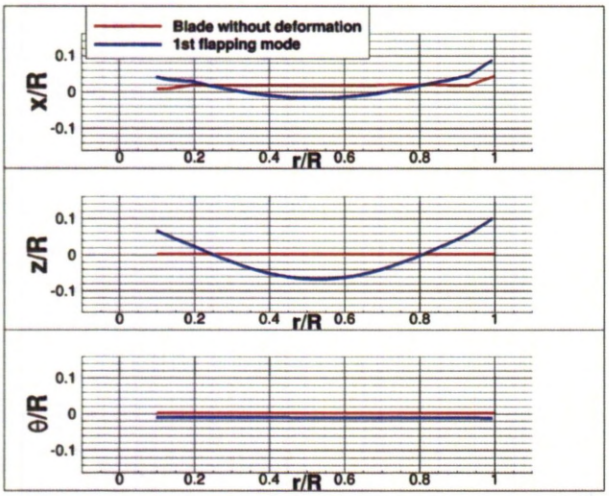

(a) First flapping mode at 4.36Hz

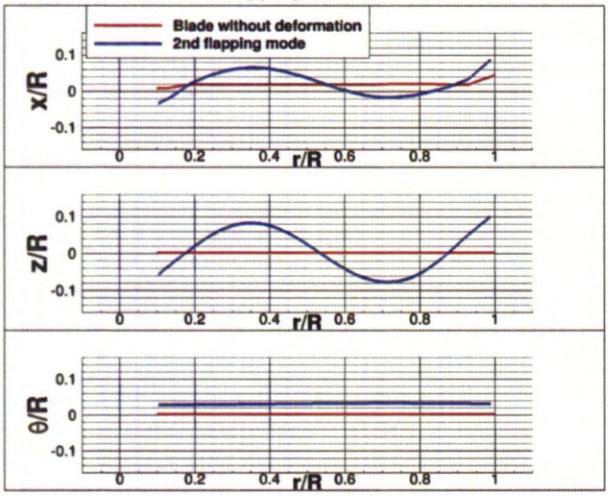

(b) Second flapping mode at 12.81Hz

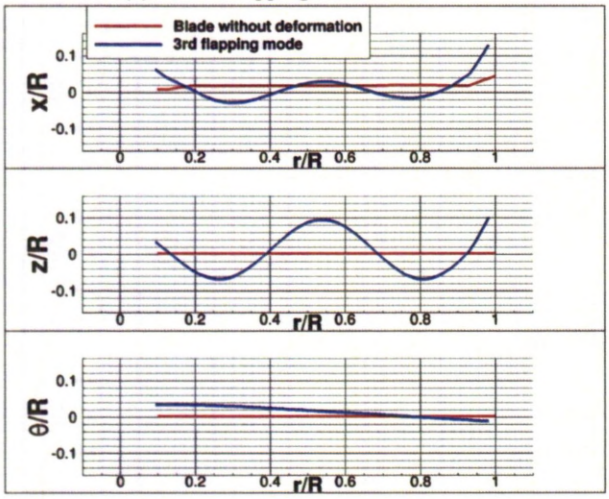

(c) Second flapping mode at 25.09Hz

Figure 4.8: Eigenmodes of a non-rotating UH-60A blade. Continued.

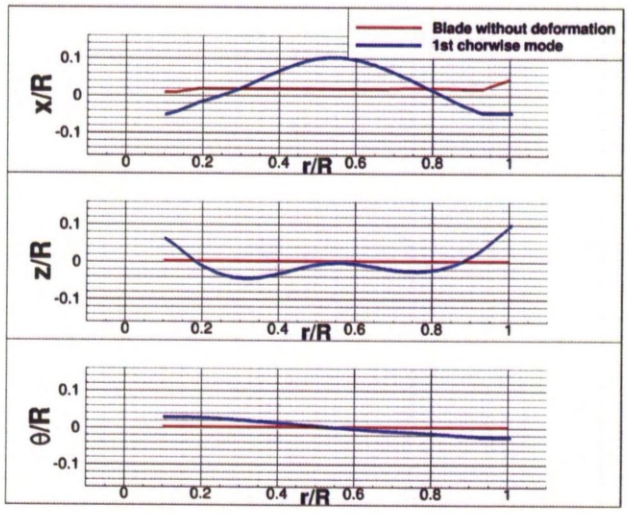

(d) First chordwise mode at 25.55Hz

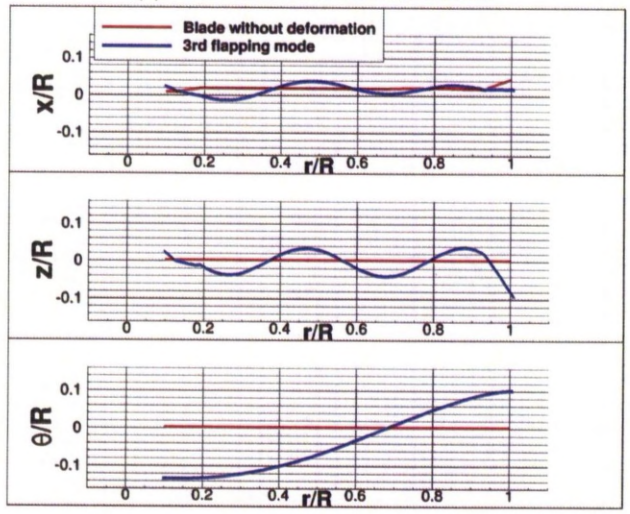

(e) Forth flapping mode at 41.17Hz

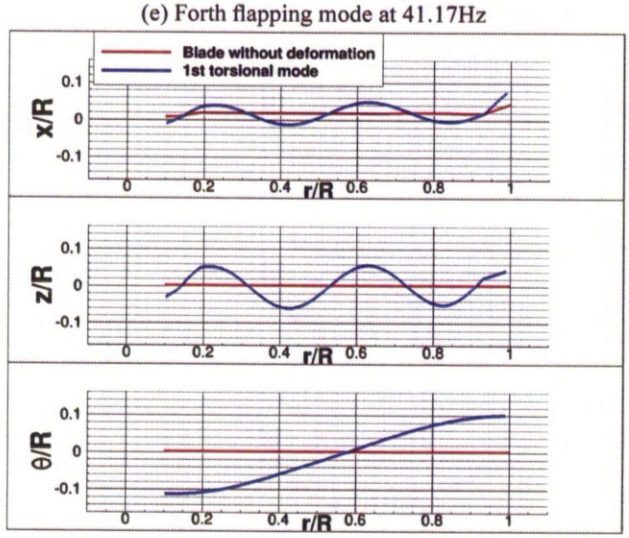

(f) First torsional mode at 84.05Hz

Figure 4.8: Eigenmodes of a non-rotating UH-60A blade. Concluded.

Evolution of the Eigenmode Shapes with the Rotational Speed

The blade was later modelled as part of a full rotating rotor. In order to simulate the blade attachment to the rotor, the blade root was fixed in translation as well as in rotation around the X-axis which represents the blade pitch axis. This corresponds to a blade root that is fixed in space and can only rotate about the flap and lead-lag planes. The approximation of a fixed rotation around the span axis in order to simulate the collective setting command was deemed acceptable to model the usually complex rotor head. A lead-lag damper is added as a linear elastic element creating a moment that is a function of the lead-lag angle. Its strength was set at 353 lbf.ft/rad (478.6 Nm/rad). A flapping spring with the same strength was also added for computational stability. The new blade model is shown in Figure 4.9.

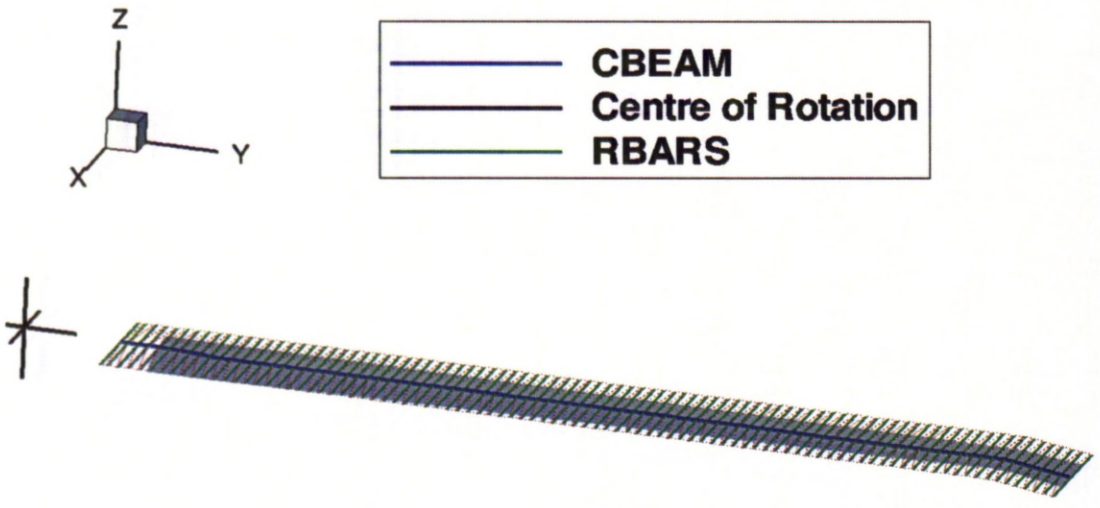

Figure 4.9: Rotating UH-60A blade model.

The evolution of the eigenmodes and natural frequencies with the rotational speed was analysed in NASTRAN. The rotational speed tested were between 0 and 300 RPM with the rotor nominal rotational speed being 258 RPM. The natural frequencies evolution with the rotational speed is shown in Figure 4.10. Due to the increased stiffness of the blade from the rotation, the natural frequencies tend to increase at variable speeds. The most stable natural frequencies are the torsional natural frequencies. Some natural frequencies cross and some interact as also shown by Bramwell[114].

The effect of the increased stiffness is also visible on the eigenmodes shape evolution shown in

Figure 4.11. The increase in the rotational speed moved the peaks of the eigenmodes further outward.

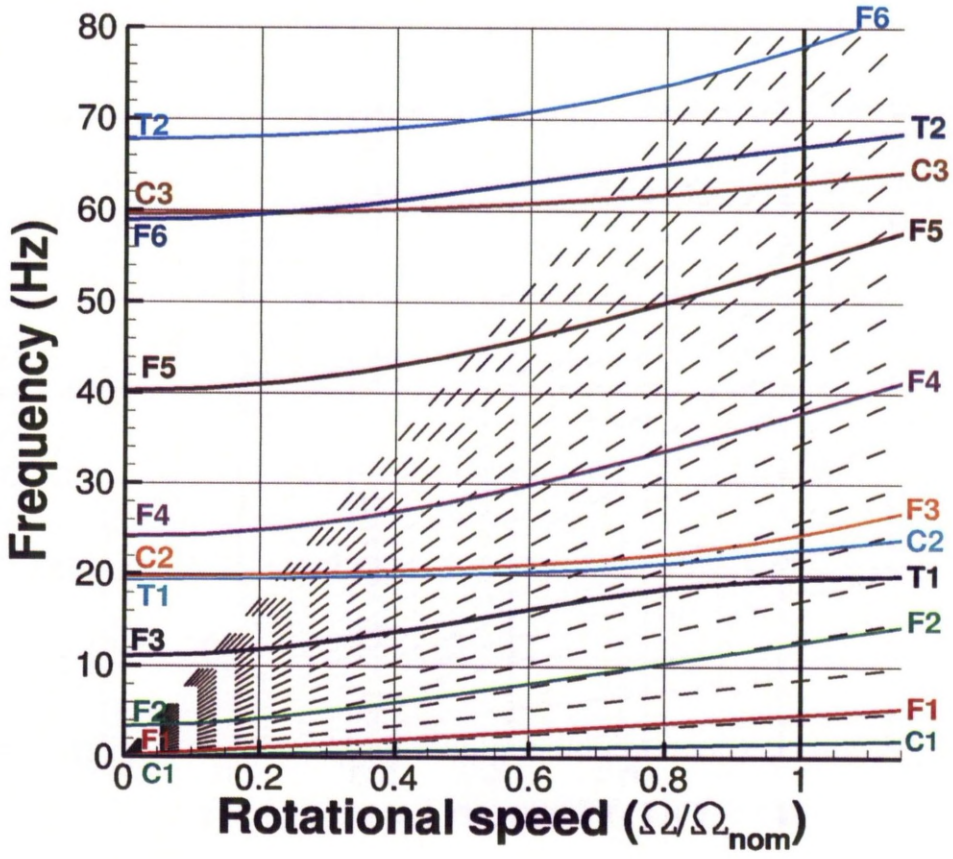

Figure 4.10: Evolution of the frequency of the various modes of the UH-60A blade with the rotational speed of the rotor. $\Omega_{nom} = 258$RPM. F denotes a flapping mode, C a chordwise mode and T a torsional mode.

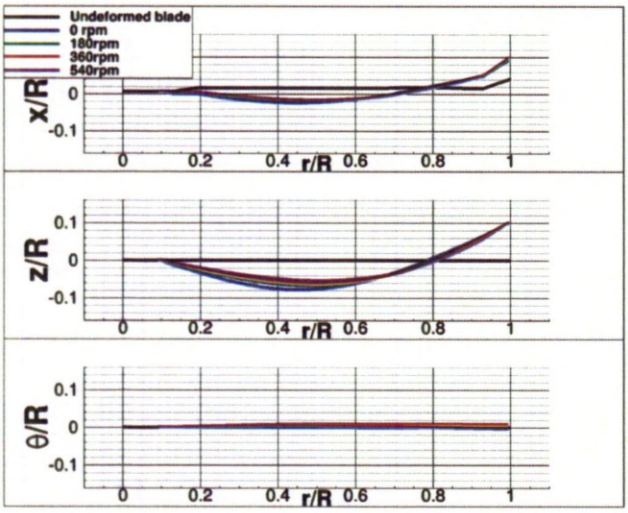

(a) Second flapping mode

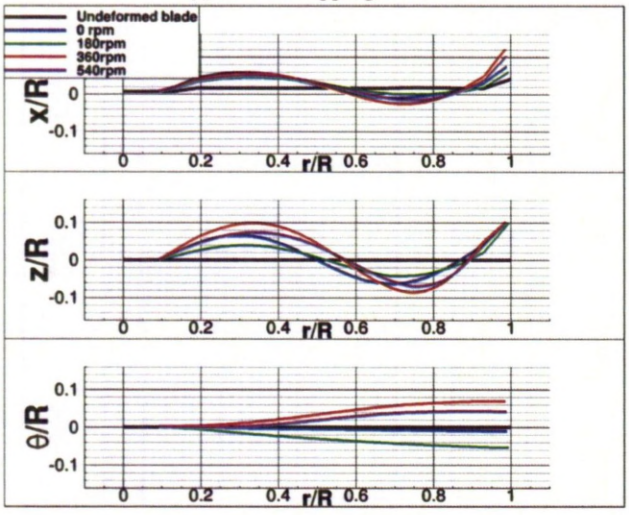

(b) Third flapping mode

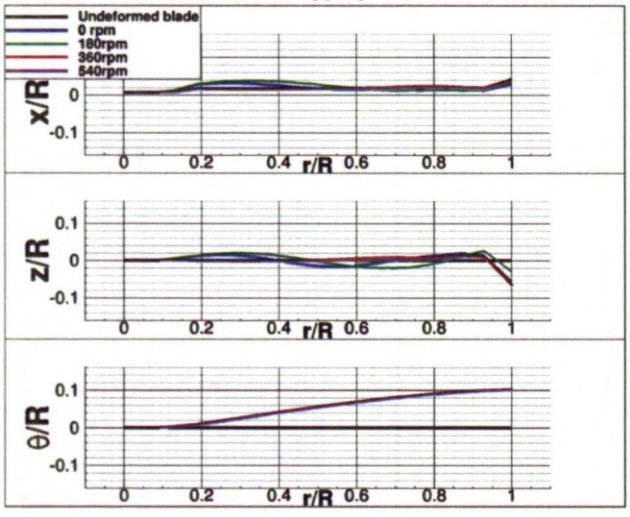

(c) First torsional mode

Figure 4.11: Evolution of the UH-60A eigenmode shapes with the rotational speed. Continued.

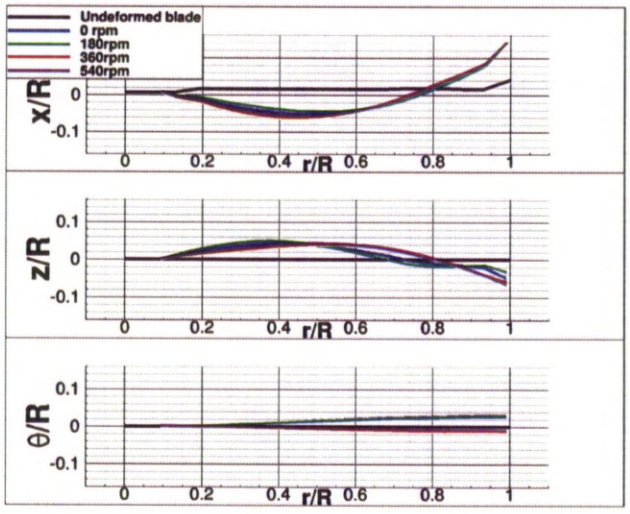

(d) Second chordwise mode

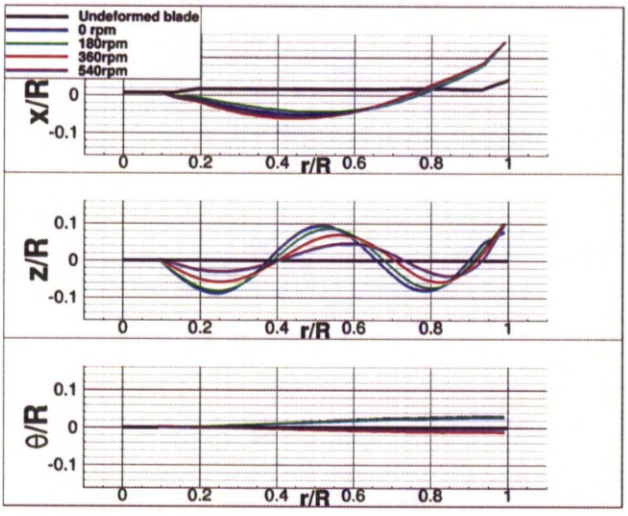

(e) Forth flapping mode

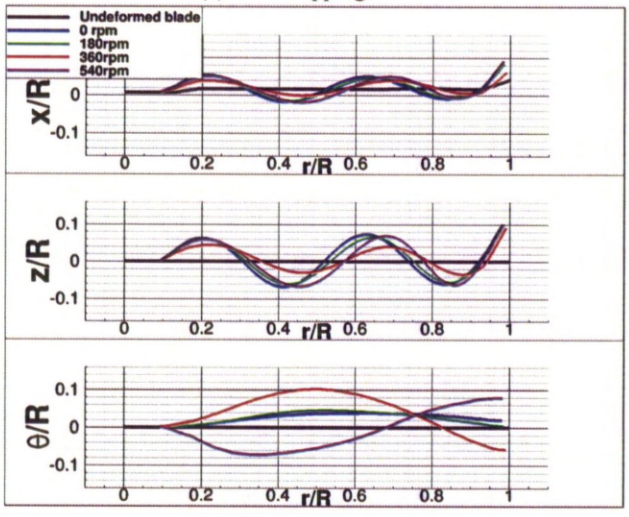

(f) Fifth flapping mode

Figure 4.11: Evolution of the UH-60A eigenmode shapes with the rotational speed. Concluded.

4.3.3 HART-II Blade Demonstration

Assessment of the Influence of the Number of Elements

A structural model for the HART-II was also developed. The blade properties were obtained in [115] and are shown in Figure 4.12.

The HART-II rotor has been chosen to assess the dependency of the results to the model size. For this test, the number of elements was modified in the main part of the blade with constant properties but kept unchanged in the root area were the properties are varying. The blade is linked to the hub by not allowing any translation of the root or around the blade axis, but rotation around the Y- and Z-axis (flap and lead-lag motions respectively) are free. Lead-lag and flap dampers with stiffnesses of 253 N/rad each were added. The coarser model contained 13 elements, and the finer grid was obtained by dividing each element on the main part of the blade in two, leading to model sizes of 17, 25, 40 and 71 elements. The natural frequencies obtained with the various models are shown in Figure 4.13. The frequencies were well converged from 25 elements. The higher number of elements tended to mainly modify the frequencies of the higher natural frequency modes. For the rest of this work, the blade model containing 40 elements will be used and is shown in Figure 4.14.

Validation of the Structural Model Against FEM Analysis of DLR

DLR published in [115] the HART-II eigenmodes shape and frequencies obtained through an in-house finite-element code. These results were used to validate the present structural model for NASTRAN. For the HART-II experimental setup presented in Section 8.4, the blade was clamped to the hub to match the experimental measurements. The comparison of the natural frequencies predicted by NASTRAN with the ones from the DLR is shown in Figure 4.15. NASTRAN predictions compare well with the DLR ones, except for the first torsional mode at low rotational speed where NASTRAN predicts lower frequencies. However, the predictions are equivalent at the nominal rotational speed (1040RPM). The blade shape predictions at the nominal rotational speed are compared in Figure 4.16. Two main differences appear between the predictions. Firstly the maximum of the flapping modes are more outward

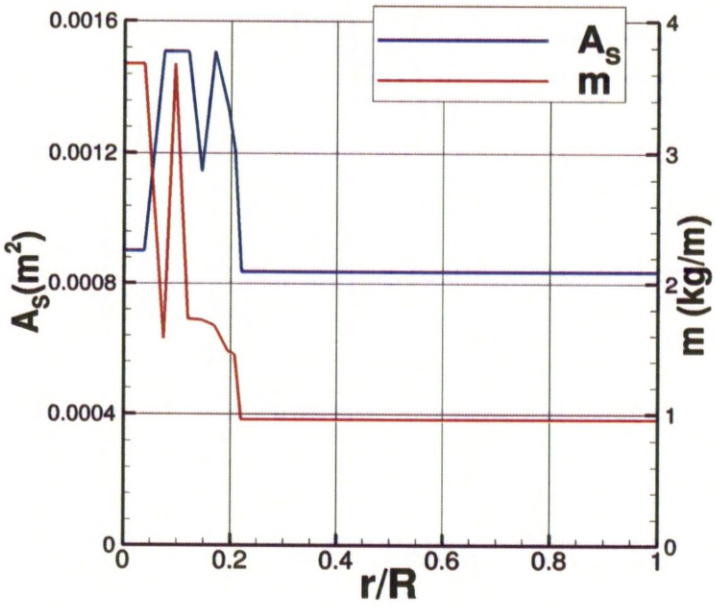

(a) Sectional area and linear mass distribution

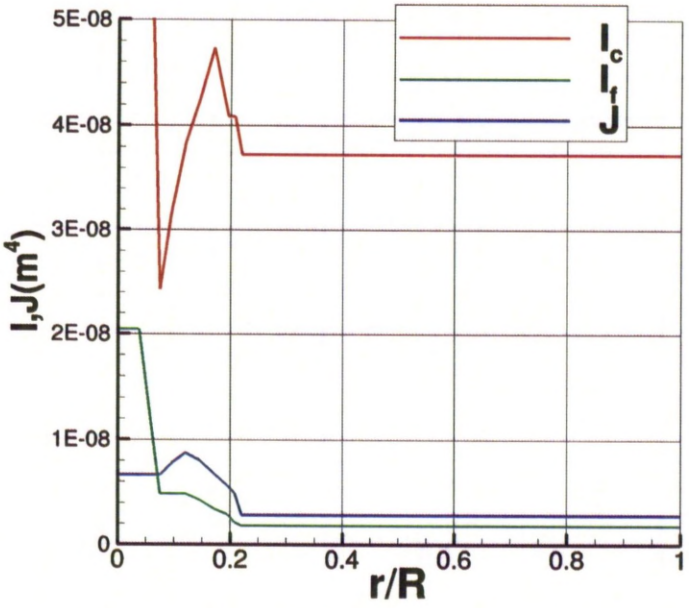

(b) Chordwise, flapwise and torsional area moments of inertia

Figure 4.12: Main properties of the HART-II rotor blade.

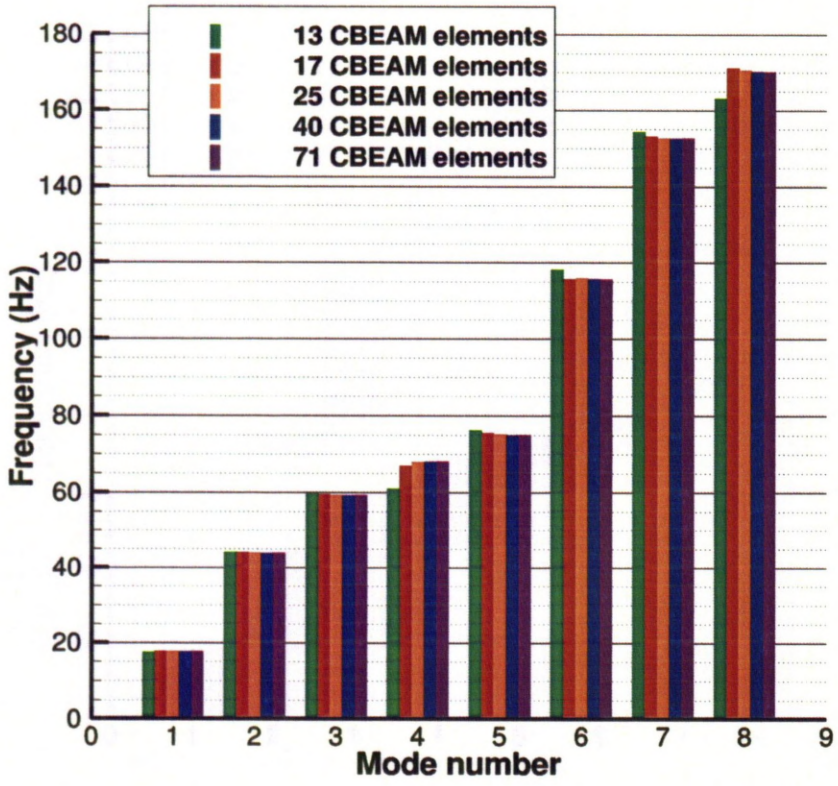

Figure 4.13: Evolution of the natural frequencies of the HART-II blade with the number of elements on the structural model, at the nominal rotational speed.

in the NASTRAN predictions and tend to have a higher amplitude relatively to the tip displacement. Secondly, the boundary condition at the root of the blade seems to be different: the tangent of the blade is fixed in the NASTRAN predictions while it seems to have some rotational freedom in the DLR model. This might explain the difference in location for the peaks of the eigenmodes. The difference in boundary condition created a large difference in torsion at the root of the blade for the torsional mode: the torsion was set to zero in NASTRAN while it had some freedom in the DLR model. The shape of the eigenmode is however the same if this offset is not taken into account.

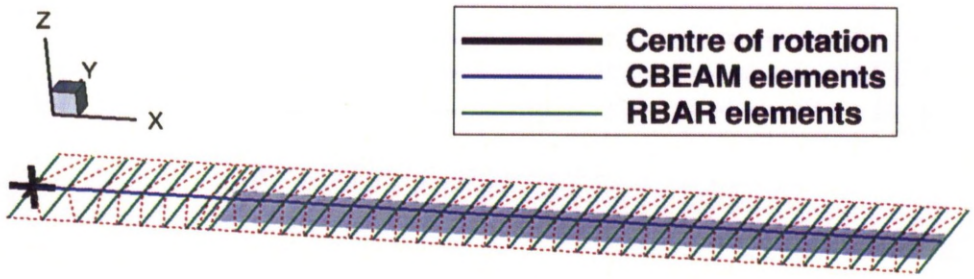

Figure 4.14: HART-II blade structural model.

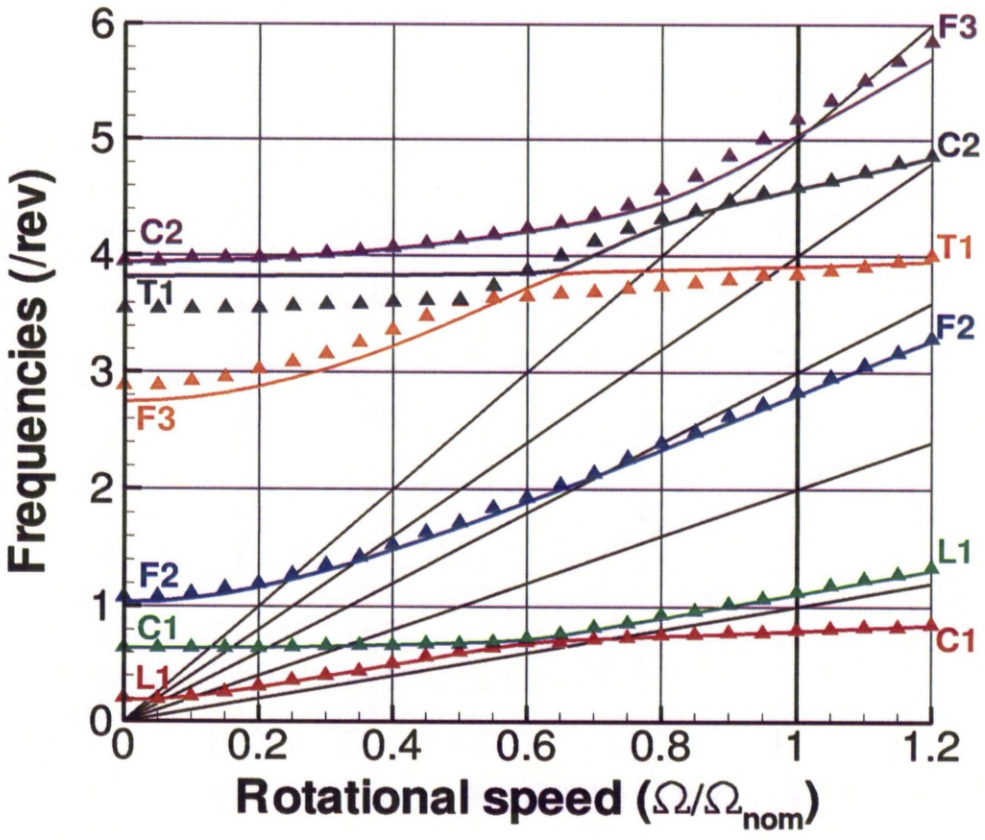

Figure 4.15: HART-II blade natural frequencies evolution with the rotational speed: comparison of the NASTRAN predictions (solid lines) with the DLR[115] ones (symbols). $\Omega_{nom} = 1040\,\text{RPM}$. F denotes a flapping mode, C a chordwise mode and T a torsional mode.

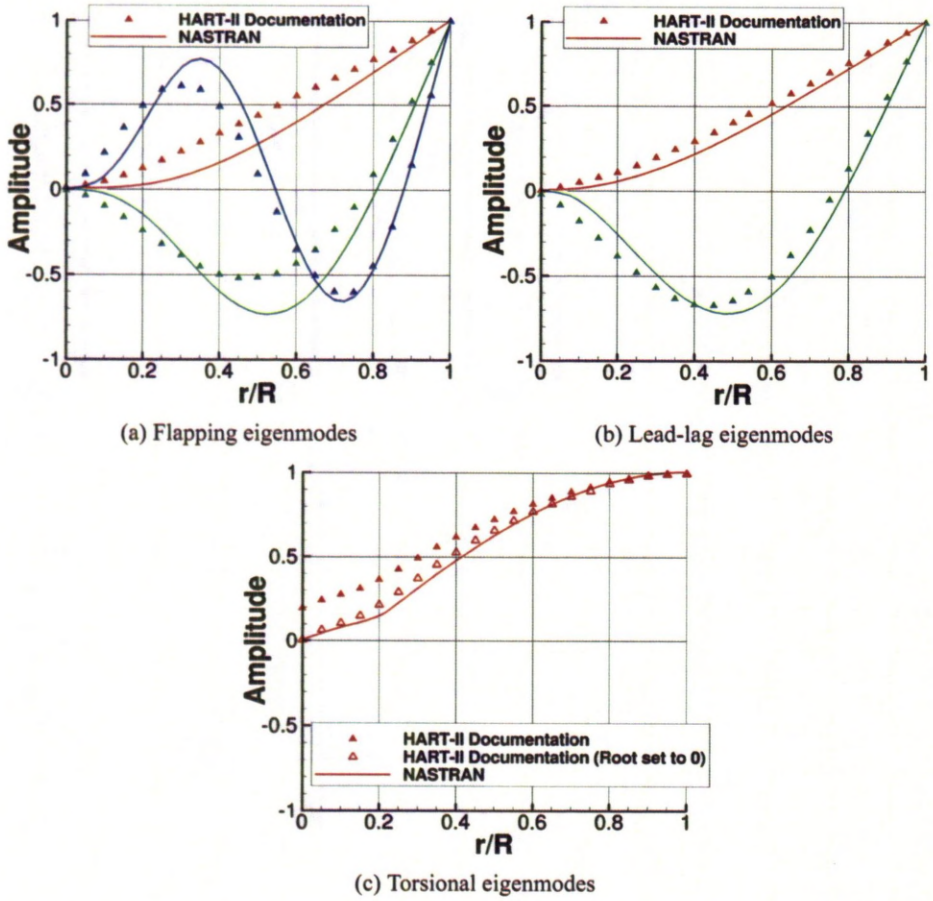

(a) Flapping eigenmodes

(b) Lead-lag eigenmodes

(c) Torsional eigenmodes

Figure 4.16: Comparison of the eigenmode shapes prediction from NASTRAN (solid lines) and the DLR (symbols) at the nominal rotational speed.

Chapter 5

Aeroelastic Coupling Method for Rotors

The aeroelastic coupling can be divided in three repeated steps:

- transfer of the fluid loads to the structural model,
- computation of the blade shape,
- transfer of the blade structural deformation back to the fluid grid.

The main problem associated with the information transfer comes with the size difference between the blade surface in the fluid mesh (typically more than 10000 nodes) and the structural beam model (typically 50 nodes). Therefore an interpolation method is needed. To transfer the fluid loads from the CFD simulation to the structural model, a simple addition of the forces from the cells on the blade surface is sufficient to obtain a sufficient level of accuracy for the forces. The transfer of the structural deformation to the fluid mesh requires an advanced interpolation able to deal with the strong deformations a rotor can undergo during its flight. A new method developed for HMB has been developed and is introduced in this chapter before presenting the aeroelastic coupling method.

5.1 Mesh Deformation Method for Rotor Blades

The deformation of the fluid mesh is done in three main steps. Firstly, the constant volume tetrahedron (CVT) method is used to interpolate the deformed shape of the blade surface. Secondly, the block vertices are moved accordingly to the spring analogy method (SAM). Finally, the full mesh is regenerated with a trans-finite interpolation (TFI).

5.1.1 Constant Volume Tetrahedron

Method Description

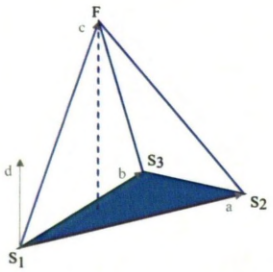

Figure 5.1: Notations for the projection of a point from the fluid grid (F) with a structural element (S_1, S_2, S_3)

The Constant Volume Tetrahedron (CVT) method was developed by Goura[116]. This method projects each fluid node to the nearest structural triangular element and moves it linearly with the element.

The first step in order to calculate the transformation is to find the nearest triangular element (S_1, S_2, S_3) to each fluid point (F) as shown in Figure 5.1. Then, the location of the fluid element can be expressed as follows:

$$\mathbf{c} = \alpha\mathbf{a} + \beta\mathbf{b} + \gamma\mathbf{d} \tag{5.1}$$

where $\mathbf{a} = \overrightarrow{S_1S_2}$, $\mathbf{b} = \overrightarrow{S_1S_3}$, $\mathbf{c} = \overrightarrow{S_1F}$ and $\mathbf{d} = \mathbf{a} \wedge \mathbf{b}$. The coefficients α, β and γ can then be expressed as:

$$\alpha = \frac{(\mathbf{a}\cdot\mathbf{c})\,\|\mathbf{b}\|^2 - (\mathbf{a}\cdot\mathbf{b})\,(\mathbf{b}\cdot\mathbf{c})}{\|\mathbf{a}\|^2\|\mathbf{b}\|^2 - (\mathbf{a}\cdot\mathbf{b})^2} \tag{5.2}$$

$$\beta = \frac{(\mathbf{b}\cdot\mathbf{c})\,\|\mathbf{a}\|^2 - (\mathbf{a}\cdot\mathbf{b})\,(\mathbf{a}\cdot\mathbf{c})}{\|\mathbf{a}\|^2\|\mathbf{b}\|^2 - (\mathbf{a}\cdot\mathbf{b})^2} \tag{5.3}$$

$$\gamma = \frac{(\mathbf{c}\cdot\mathbf{d})}{\|\mathbf{a}\|^2\|\mathbf{b}\|^2 - (\mathbf{a}\cdot\mathbf{b})^2}. \tag{5.4}$$

The new position of the deformed blade fluid point is obtained by calculating:

$$\mathbf{c}' = \alpha\mathbf{a}' + \beta\mathbf{b}' + \gamma\mathbf{d}', \tag{5.5}$$

where $\mathbf{a}'$, $\mathbf{b}'$, $\mathbf{c}'$ and $\mathbf{d}'$ are the same vectors after the structural deformation.

Demonstration of the CVT for Rotor Blades

Two test cases representative of the various geometries for rotor blade have been chosen to validate the blade deformation method. The HART-II and its rectangular geometry is representative of the most basic geometries, while the UH-60A blade is used to demonstrate the method for more advanced tip shapes. CVT was applied to the blade surface and the general smoothness of the blade surface was then assessed.

Example on a rectangular blade: the HART-II blade The HART-II blade was described in 3.3.1. A grid adapted for a hovering rotor was used, with a size of $8.9M$ nodes. CVT was first applied to the blade surface and the surface was inspected for discrepancies. A deformed surface with a mild deformation typical of an in-flight deformation is shown in Figure 5.2. The second flapping mode with an amplitude of $0.1c$ at the tip and the first torsional mode with an amplitude of -5 degrees at the tip were applied to the blade surface. CVT coped well with this deformation keeping a smooth surface on the whole blade and equivalent spacings. This is particularly visible at the tip of the blade where the surface quality has to be kept due to the high suction on the blunt tip and the vortex formation.

CVT was then used to apply a strong deformation to the blade. The amplitude of the second flapping mode was increased to $1c$ at the tip and the amplitude of the first torsional mode to -10 degrees. The blade surface is shown in Figure 5.3. Despite the strong deformation, the blade surface is still good enough for a fluid computation, and the grid at the tip remained properly fine as needed to predict the vortex formation.

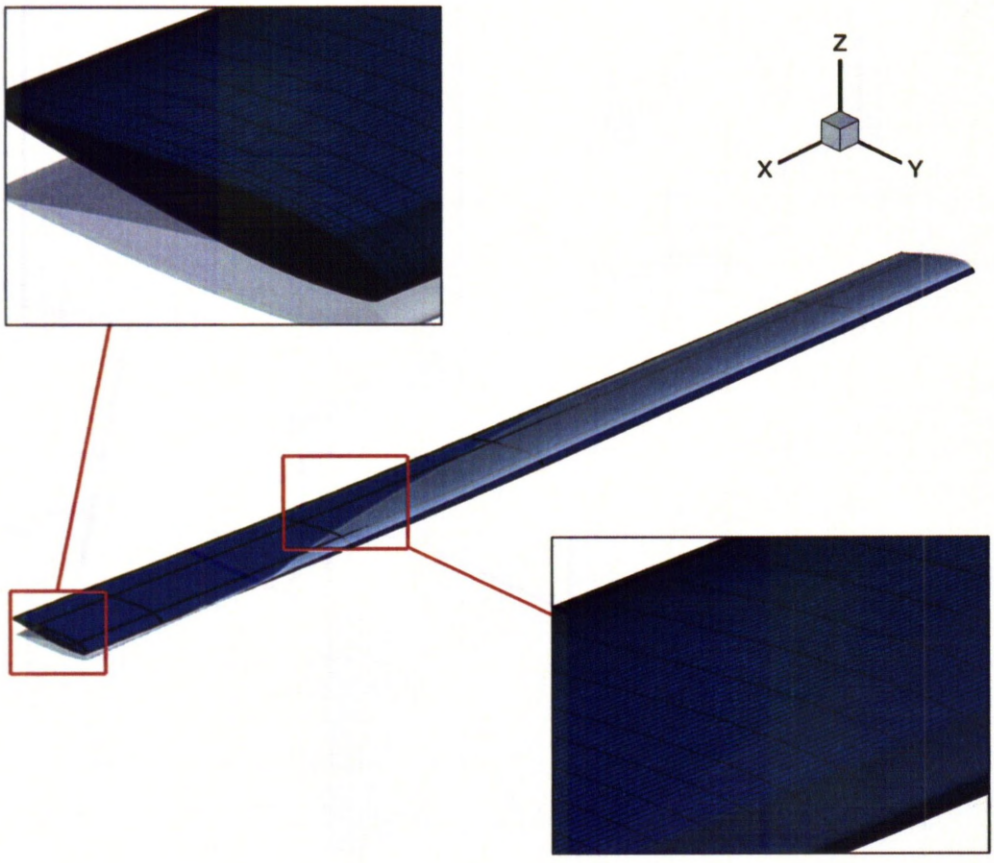

Figure 5.2: HART-II blade surface deformation obtained by CVT when applying the second flapping mode with an amplitude of $0.1c$ at the tip and the first torsional mode with an amplitude of -5 degrees at the tip. The undeformed blade is in grey and the deformed one in blue.

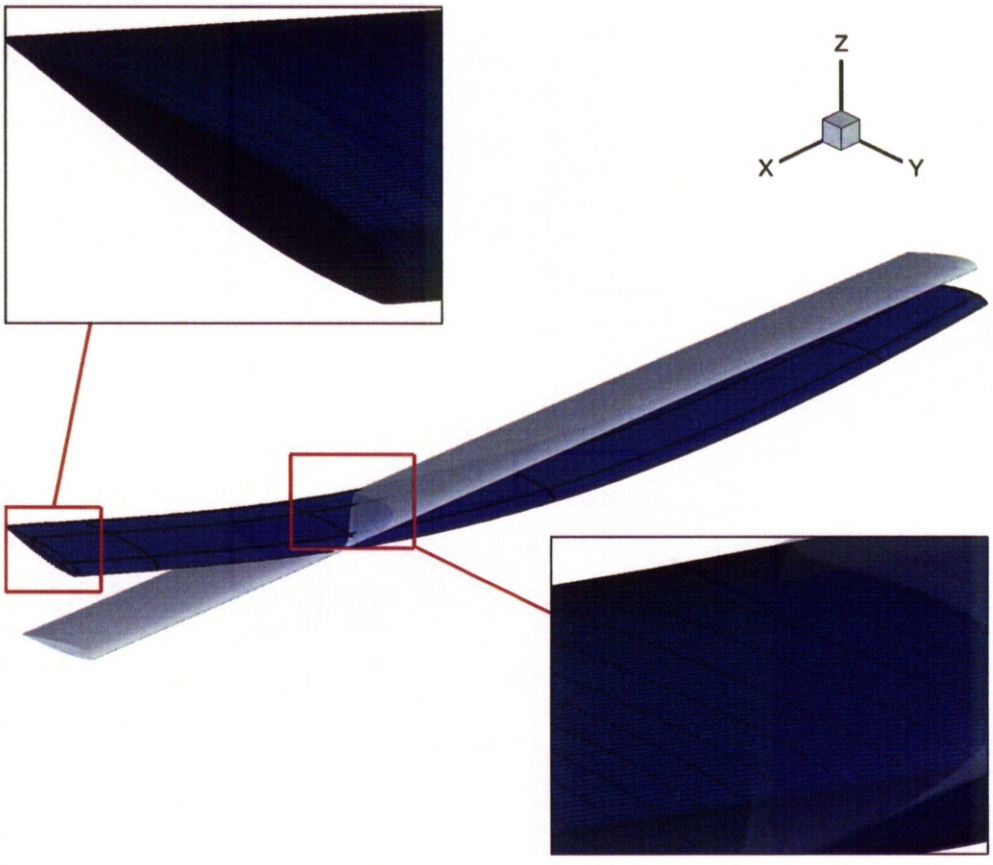

Figure 5.3: HART-II blade surface deformation obtained by CVT when applying the second flapping mode with an amplitude of $1c$ at the tip and the first torsional mode with an amplitude of -10 degrees at the tip. The undeformed blade is in grey and the deformed one in blue.

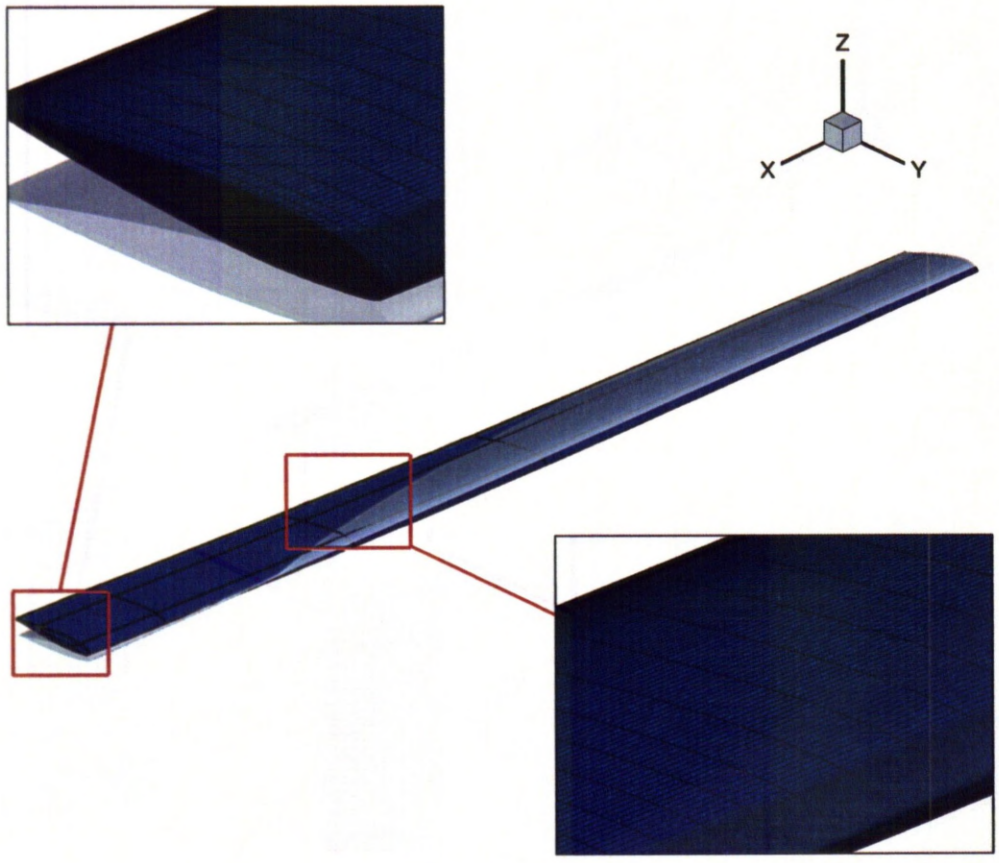

Figure 5.4: UH-60A blade surface deformation obtained by CVT when applying the second flapping mode with an amplitude of $0.1c$ at the tip and the first torsional mode with an amplitude of -5 degrees at the tip. The undeformed blade is in grey and the deformed one in blue.

Example on a blade with swept-back tip: the UH-60A blade The previous encouraging results lead to the test of a different rotor geometry. The UH-60A rotor blade described in section 3.3.2 was used to test the method compatibility with a swept-back tip. The grid was designed for a hovering rotor and had a size of $8.9M$ nodes. The same mild deformation was first used: the second flapping mode was used with an amplitude of $0.1c$ upward at the tip and the first torsional mode was used with an amplitude of -5 degrees at the tip. The surface deformation is shown in Figure 5.4. The blade surface proved smooth once again after deformation, and the tip area kept the high quality mesh on the blade surface.

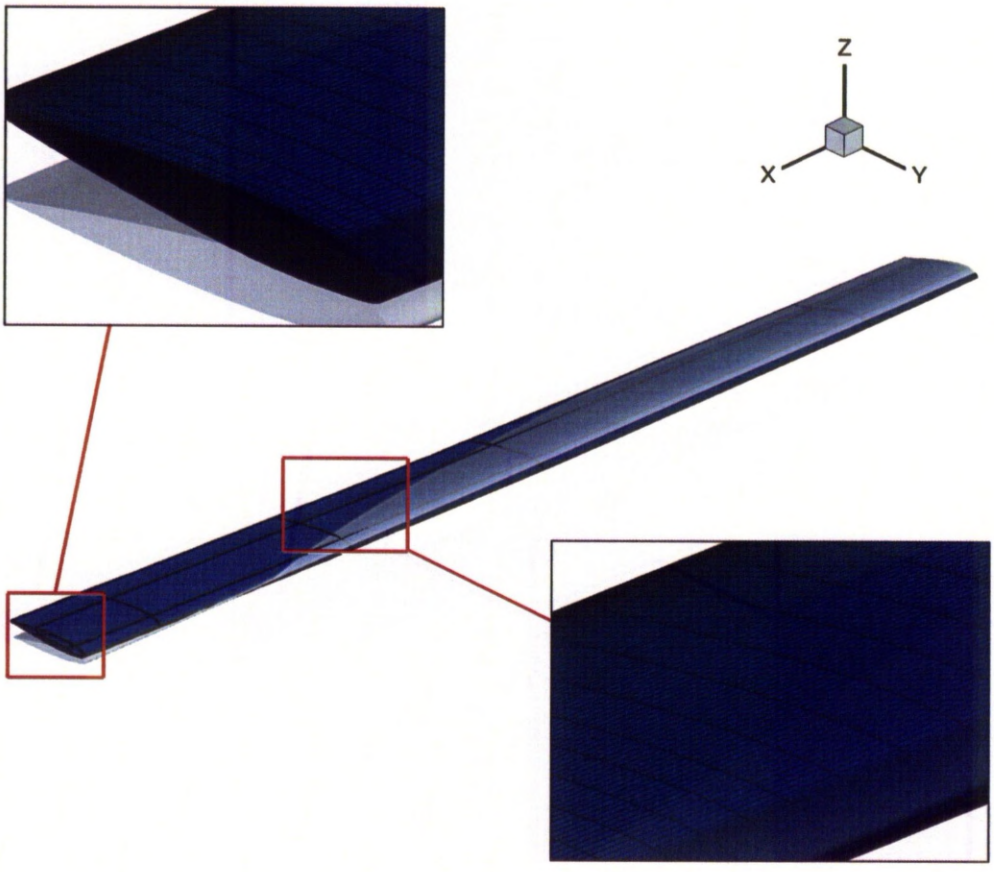

Figure 5.5: UH-60A blade surface deformation obtained by CVT when applying the second flapping mode with an amplitude of $1c$ at the tip and the first torsional mode with an amplitude of -10 degrees at the tip. The undeformed blade is in grey and the deformed one in blue.

A stronger deformation using the second flapping mode with an amplitude of $1c$ upward and the first torsional mode with an amplitude of -10 degrees at the tip were then applied. The deformed blade surface is shown in Figure 5.5. The flapping amplitude at the tip is increased due to the offset between

the quarter chord line at the tip and the blade main axis. This strong deformation did not introduce surface discrepancies.

No in-flight measurements of the blade deformation were carried out, and model rotors tend to be stiffer than real blades. However, Datta *et al.* [117] predicted for the UH-60A rotor a deformation up to -9 degrees in torsion, using the air-loads to assess the actual blade shape. This deformation was obtained for a high-speed flight, and is considered as extreme. Therefore, the proposed method appears to be able to cope with large rotor blade deformations in flight.

CVT Limitations

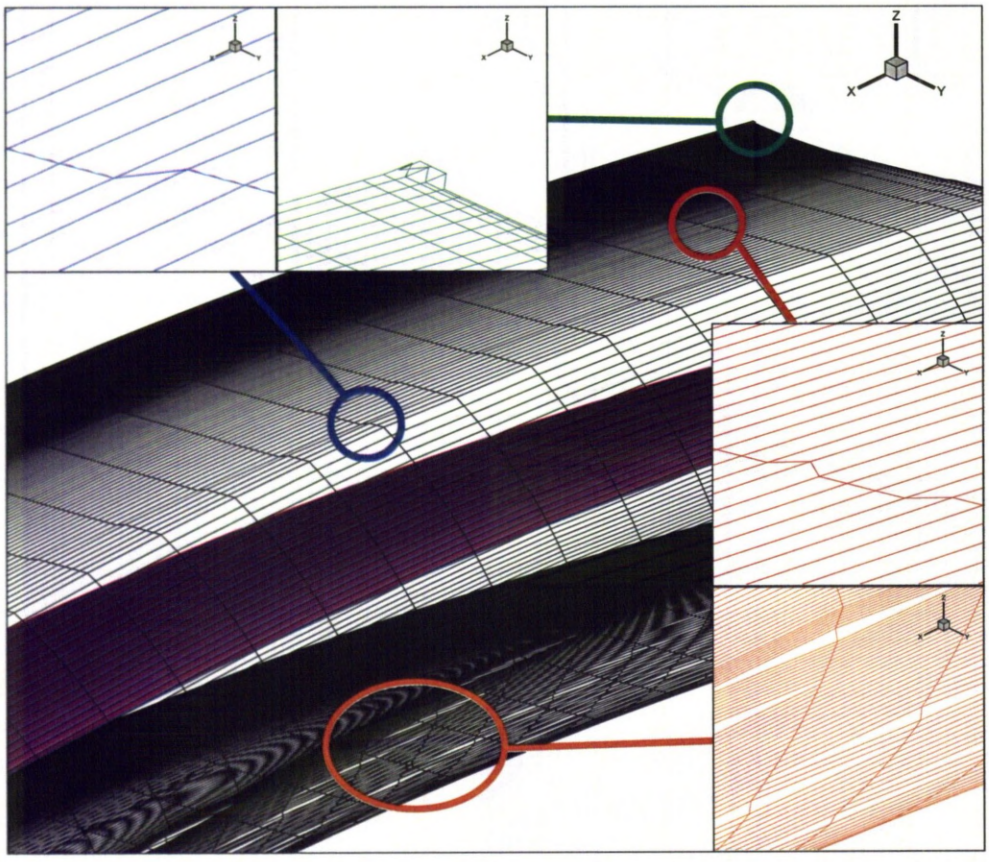

Figure 5.6: Discontinuities in the mesh obtained by the use of CVT in the blocks in contact with the blade surface.

CVT is an efficient deformation method, however, it showed limitations when used further from the blade surface. This is visible in Figure 5.6, showing the mesh deformation when the CVT is applied

to the full blocks in contact with the blade. Strong discontinuities in the mesh appear on the block surfaces opposite to the blade, and the resulting cell skewness does not allow for a CFD calculation to be carried out on this mesh.

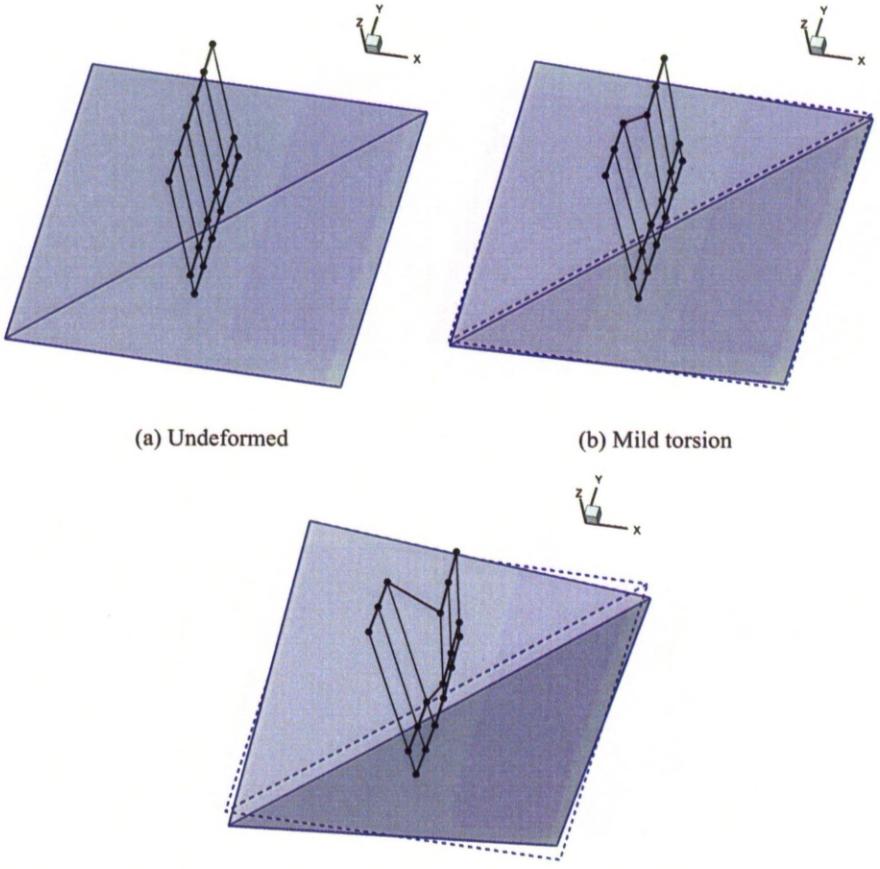

(a) Undeformed

(b) Mild torsion

(c) Strong torsion

Figure 5.7: Deformation of three mesh lines (black) at various height from the structural model (blue) with a torsional deformation. The undeformed structural shape is shown in dashed lines.

The linear association with the triangular structural elements can create discontinuities between two nodes close to each other, but associated with two different structural elements. If two of these fluid nodes are associated with two different neighbour elements which are angled in the deformed shape, the linear association means that they will move according to their corresponding elements, and the distance between the two nodes will be increased with the node height. This is shown in Figure 5.7, and also available as an animation in the CD attached to this thesis. A torsional difference was applied between the extremities of the structural elements in blue at both ends, the first one being small and the second

one strong. Three lines of nodes projected on the triangular elements are represented: the first one on the structural model surface, the second one at a height of $0.1l$ and the third one at a height of $0.6l$ with l the side length of the structural model. The mild torsional deformation is well coped with for the two first lines, however on the top line, the junction between the nodes projected on each element already shows a high level of deformation. When the structural deformation becomes strong, this line deforms at a very high level and might create cells with negative volumes on a blade mesh. The two lower lines however showed reasonable deformations for such a strong deformation.

Therefore the mesh deformation away from the blade surface has to be performed with a different method. A transfinite interpolation (TFI) of the mesh was therefore introduced in the C-part of the mesh.

5.1.2 Trans-Finite Interpolation

Due to the CVT limitations further from the blade surface, it was decided to interpolate the mesh for blocks in direct contact with the blade. The Trans-Finite Interpolation (TFI) is used in order to re-interpolate the cells inside these blocks.

Method Description

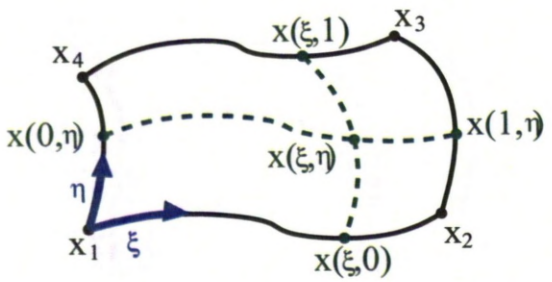

Figure 5.8: Notation for the TFI application on a block face.

The Trans-Finite Interpolation (TFI), described by Dubuc *et al.*[118], is used for interpolating the block face deformation from the edge deformations and then the full block deformation from the deformation of the block faces.

The mesh deformation uses a weighted approach to interpolate a face/block from the boundary

vertices/surfaces respectively. The weight depends on the curvilinear coordinate divided by the length of the curve. The notation used here is shown in Figure 5.8. The generation of the mesh on a block face $(\mathbf{x}_1, \mathbf{x}_2, \mathbf{x}_3, \mathbf{x}_4)$ can be expressed as:

$$\mathbf{dx}(\xi,\eta) = \mathbf{f}_1(\xi,\eta) + \phi_1^0(\eta)[\mathbf{dx}_1(\xi) - \mathbf{f}_1(\xi,0)] + \phi_2^0(\eta)[\mathbf{dx}_3(\xi) - \mathbf{f}_1(\xi,1)], \tag{5.6}$$

where $\mathbf{f}_1$ is defined as:

$$\mathbf{f}_1(\xi,\eta) = \psi_1^0(\xi)\mathbf{dx}_4(\eta) + \psi_2^0(\xi)\mathbf{dx}_2(\eta), \tag{5.7}$$

with $\mathbf{dx}_1$, $\mathbf{dx}_2$, $\mathbf{dx}_3$ and $\mathbf{dx}_4$ representing the displacements of the four faces corners and ϕ and ψ representing the blending functions in the η and ξ directions. The blending functions are expressed as a function of the stretching functions s_1, s_2, s_3 and s_4:

$$\psi_1^0(\xi) = 1 - s_1(\xi) \tag{5.8}$$

$$\psi_2^0(\xi) = s_3(\xi) \tag{5.9}$$

$$\phi_1^0(\eta) = 1 - s_4(\eta) \tag{5.10}$$

$$\phi_2^0(\eta) = s_2(\eta). \tag{5.11}$$

$$\tag{5.12}$$

The stretching function s_1 is defined by:

$$s_1(\xi) = \frac{\widehat{\mathbf{x}_1\mathbf{x}(\xi,0)}}{\widehat{\mathbf{x}_1\mathbf{x}_2}}, \tag{5.13}$$

where $\widehat{\mathbf{x}_1\mathbf{x}_2}$ is the curvilinear length between $\mathbf{x}_1$ and $\mathbf{x}_2$. s_2, s_3 and s_4 are defined in a similar way for the curves x_2x_3, x_3x_4 and x_4x_1 respectively. The interpolation of the inside of the block from the shape of the block faces follows the same method.

Demonstration of the TFI with CVT for Rotor Blades

This interpolation was introduced in the blade-adjacent blocks after having moved the blade surface using CVT giving good results in terms of mesh quality. The same test cases and the same grids were used as in the previous section.

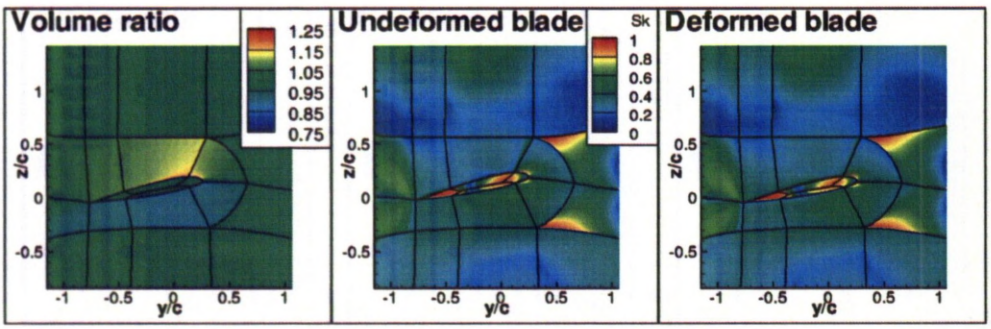

(a) Root section

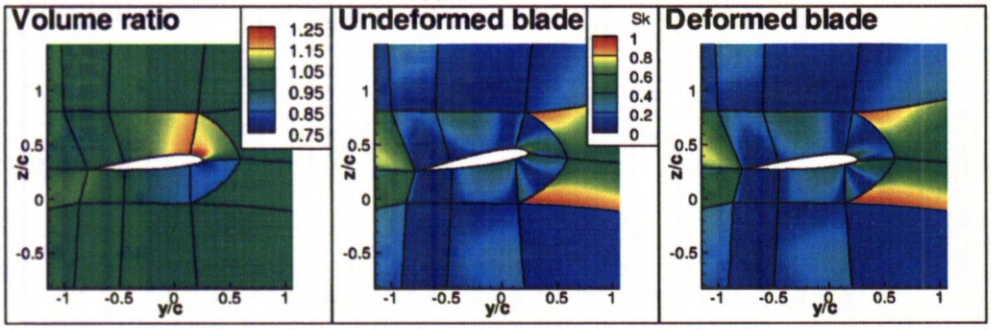

(b) Mid-span section

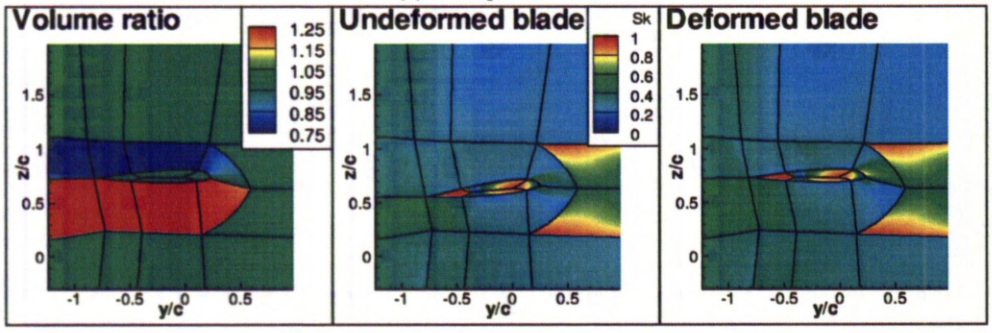

(c) Tip section

Figure 5.9: Evolution of the mesh quality for the HART-II blade in sections perpendicular to the blade: the surface deformation was applied with CVT and the blocks around the blade were computed with TFI. The second flapping mode with an amplitude of $0.1c$ at the tip and the first torsional mode with an amplitude of -5 degrees at the tip were used.

Example on a rectangular blade: the HART-II blade The CVT was first applied on the blade surface, and TFI was used to recreate the mesh inside the blocks in direct contact with the blade. The second flapping mode with an amplitude of $0.1c$ at the tip and the first torsional mode with an amplitude of -5 degrees at the tip were applied to the blade. The blade quality evolution due to the changes in three sections perpendicular to the blade is shown in Figure 5.9. Two criteria were used: the volume ratio $V_R = \frac{V_{new}}{V_{old}}$ and the grid skewness described in Section 3.4. The volume and quality changes are limited to the blocks around the blade. Despite the strong modification of the volumes at the tip due to the blade movement (more than 50%), the grid skewness was kept within reasonable values. The main skewness increase is however located at the leading edge at the tip, which is critical due to the importance of keeping a high quality in this area.

Example on a rectangular blade with a swept-back tip: the UH-60A blade The same criteria were used at four sections perpendicular to the UH-60A blade. Those are shown in Figure 5.10. The blade was deformed following the second flapping mode with an amplitude of $0.05c$ at the tip and the first torsional mode with an amplitude of -2.5 degrees at the tip. Due to the swept-back tip coupled to the torsional deformation and the close location of the block boundaries from the blade surface, the changes could not be increased without an unacceptable loss of quality for the mesh. The volume changes were very high at the tip of the blade. The skewness was also increased above the surface of the blade at the tip, and this is probably just acceptable.

Limitations of CVT on the blade surface with TFI

TFI is not able to move the block edges if the vortices are not moved. Therefore, if the blade deformation amplitude brings the blade close to the C-part boundary, TFI will not be able to generate a good quality mesh around the blade. However, the C-part of the mesh can be located no further than $0.25c$ from the blade, which is not acceptable for the high deformations the blade might undergo. Figure 5.11 shows what happens if a deformation with a higher amplitude than the distance of the C-part of the mesh is added to the blade. The CVT moves the blade to its final position, and the TFI generates a mesh that

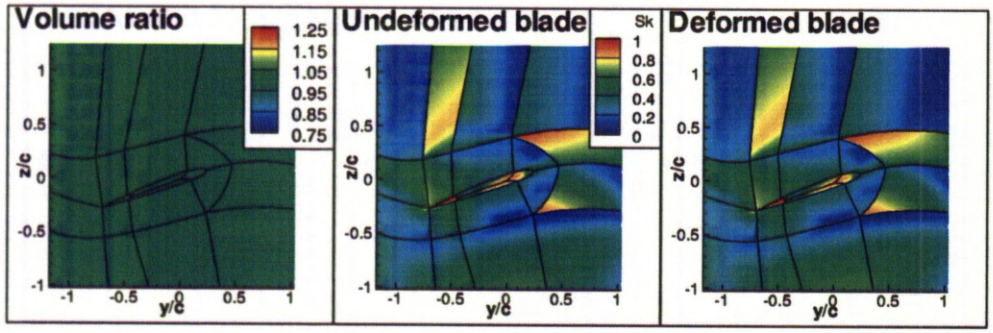

(a) Root section

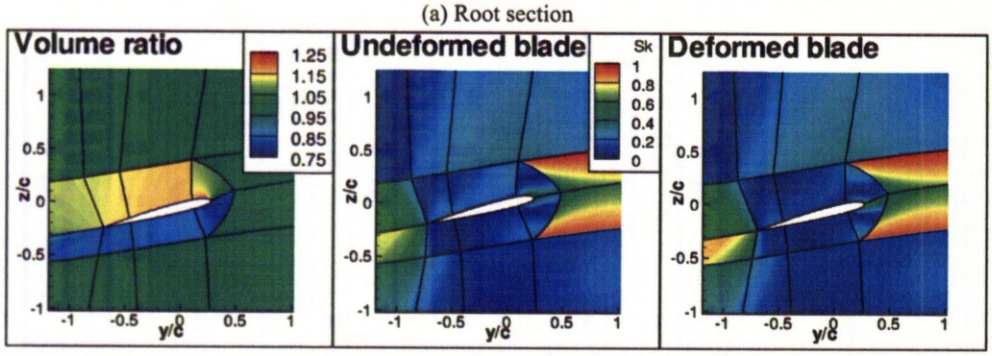

(b) Mid-span section

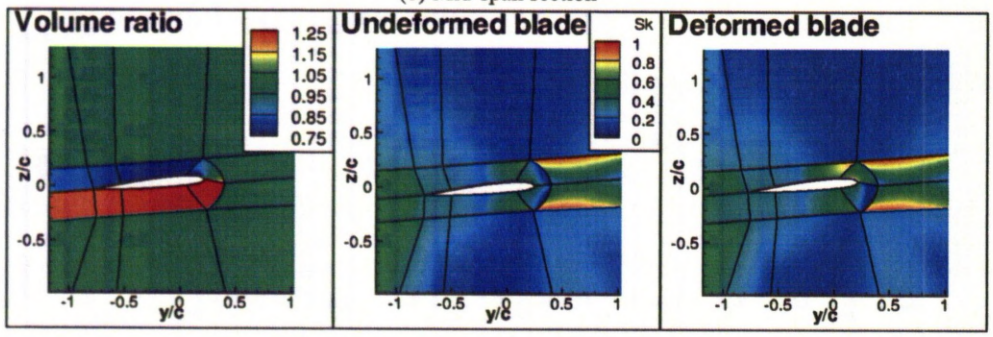

(c) Sweep-back start section

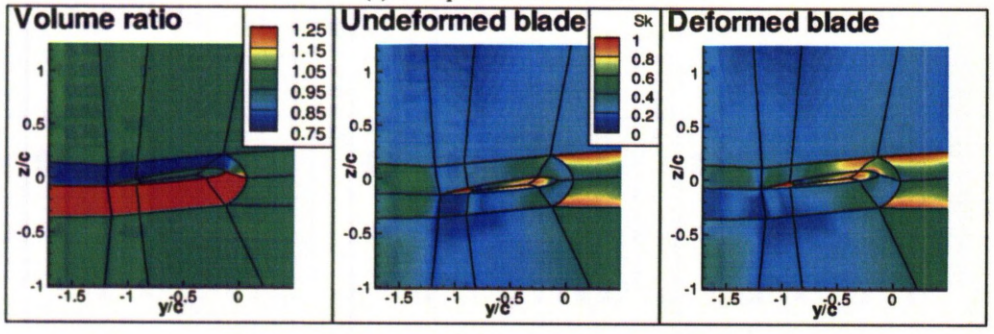

(d) Tip section

Figure 5.10: Evolution of the mesh quality for the UH-60A blade in sections perpendicular to the blade: the surface deformation was applied with CVT and the blocks around the blade were computed with TFI. The second flapping mode with an amplitude of $0.05c$ at the tip and the first torsional mode with an amplitude of -2.5 degrees at the tip were used.

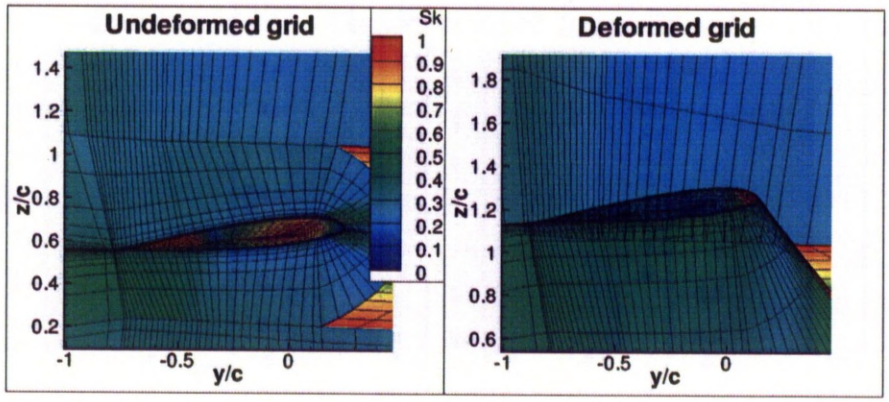

Figure 5.11: Limitations on the displacement amplitude due to the use of CVT and TFI. The blade tip was moved vertically with an amplitude of $0.6c$. Contours of the cell skewness are represented with every third mesh line shown.

is not usable for CFD. To overcome this limit, the boundaries of the blocks around the blades also have to be moved according to the blade deformation, and damping must be introduced when getting further from the blade to get no deformation at the calculation boundaries. Particular attention must also be paid to the mesh quality close to the blade as CFD calculations are extremely sensitive to a loss of quality in the refined mesh parts close to the blade.

5.1.3 Spring Analogy Method

The method developed for HMB first deforms the blade surface using CVT, then obtains the updated block vertex positions via spring analogy method (SAM) and finally generates the full mesh via TFI. The TFI first interpolates the block edges and faces from their new vertex positions and then interpolates the full mesh from the surfaces. This method uses the properties of multi-block meshes and maintains efficiency as the number of blocks increases, particularly in the spanwise blade direction. The use of spring analogy on the block vertices only allows for efficient calculation, large deformations of the blade and good mesh quality.

The SAM [19] consists of adding springs on each surface side and diagonal of the mesh, as shown in Figure 5.12. The springs along the sides of the surfaces tend to avoid large compression or dilatation of the block surfaces and the ones on the diagonals tend to limit skewness, which is critical in some

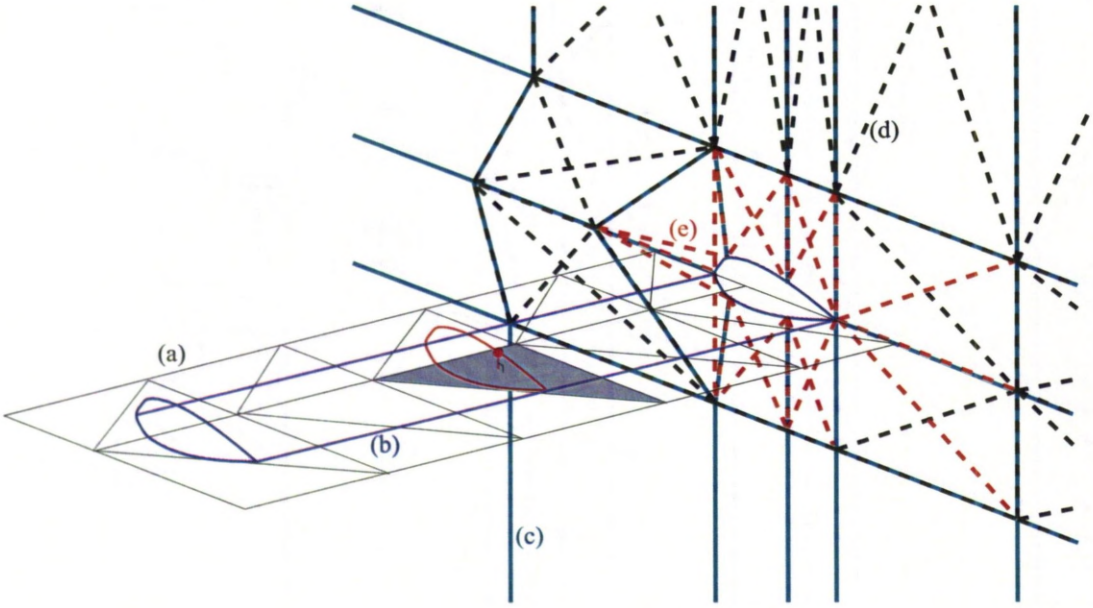

Figure 5.12: Projection of the fluid grid on the structural model through CVT. (a) Blade structural model, (b) Blade shape, (c) Fluid mesh block boundaries, (d) springs for the spring analogy not in contact of the blade and (e) springs for the spring analogy in contact of the blade

parts of the mesh like the tip of the blade where the cells are usually skewed.

The strength of the springs is set as the inverse of their length and the springs in contact with the blade are usually made stiffer in order to make the blocks close to the blade surface extremely rigid. An example of spring location and stiffness for a C-mesh around an airfoil is shown in Figure 5.12, where the springs on two faces are shown with black and red dashed lines. The black lines represent the normal springs inside the computational domain and the red ones are in contact with the blade and are therefore made stiffer. The force on each vertex is calculated as the sum of the forces due to the neighbouring springs:

$$\mathbf{F}_i = \sum_{j=1}^{n_i} k_{ij} \left(\boldsymbol{\delta}_j - \boldsymbol{\delta}_i \right), \tag{5.14}$$

where k_{ij} is the stiffness of the spring between the i-th and j-th nodes, $\boldsymbol{\delta}_i$ is the displacement vector of the i-th node and n_i the number of vertices linked by springs to the i-th one. A segmented spring method uses the nodes displacement in order to compute the force on each node, and was preferred to the vertex spring method which uses the original nodes location instead. The former method was judged more suitable for our meshes as the displacements could be significant close to the blade and the C-part of the

mesh has to be kept as near as possible to the undeformed blade.

The displacement of the nodes on the blade surface is forced and a new equilibrium is reached. The nodes on the blade and the far-field are fixed, and the new equilibrium position of the interior nodes is obtained by solving, for each node, the equation:

$$\sum_{j=1}^{n_l} \mathbf{F}_{ij} = \mathbf{0}, \tag{5.15}$$

where $\mathbf{F}_{ij}$ is the force exerted on the i-th node by the spring between the i-th and j-th nodes and is defined by $\mathbf{F}_{ij} = k_{ij}(\boldsymbol{\delta}_j - \boldsymbol{\delta}_i)$. Equation 5.15 can then be written as:

$$\sum_{j=1}^{n_l} k_{ij}(\boldsymbol{\delta}_j - \boldsymbol{\delta}_i) = \mathbf{0}. \tag{5.16}$$

The above system of equations can also be written for each δ_i as:

$$\boldsymbol{\delta}_i = \frac{\sum_{j=1}^{n_l} k_{ij}\boldsymbol{\delta}_j}{\sum_{j=1}^{n_l} k_{ij}} \tag{5.17}$$

and solved iteratively, by using the algorithm:

$$\boldsymbol{\delta}_{i,new} = \frac{\sum_{j=1}^{n_l} k_{ij}\boldsymbol{\delta}_{j,old}}{\sum_{j=1}^{n_l} k_{ij}}. \tag{5.18}$$

The process is initialised with the vertices located in the original grid except for vertices on the blade surface which are moved to the deformed position. This iterative process is repeated about 1,000 times, which was enough to reach a convergence of less than 10^{-15} even on meshes with a large number (about 3000) of vertices. The convergence criterion employed is:

$$error = \sqrt{\sum_{i=1}^{n_v} \|\boldsymbol{\delta}_{i,new} - \boldsymbol{\delta}_{i,old}\|^2}, \tag{5.19}$$

where n_v is the total number of vertices.

One of the drawbacks of the TFI method is that it does not modify the shape of the edges. Therefore, several cuts in the block topology along the blade span have to be added when creating the blade. These cuts allow the surface opposite to the blade blocks to conform more closely to the new blade shape. Larger deformation amplitudes can thus be used without having the blade surfaces becoming too close to the flat block outer surface. The more cuts along the blade span are added to the topology, the easier it is for the mesh to conform to the blade deformation.

Method Assessment

The same two examples as in the previous section are used here to demonstrate the method.

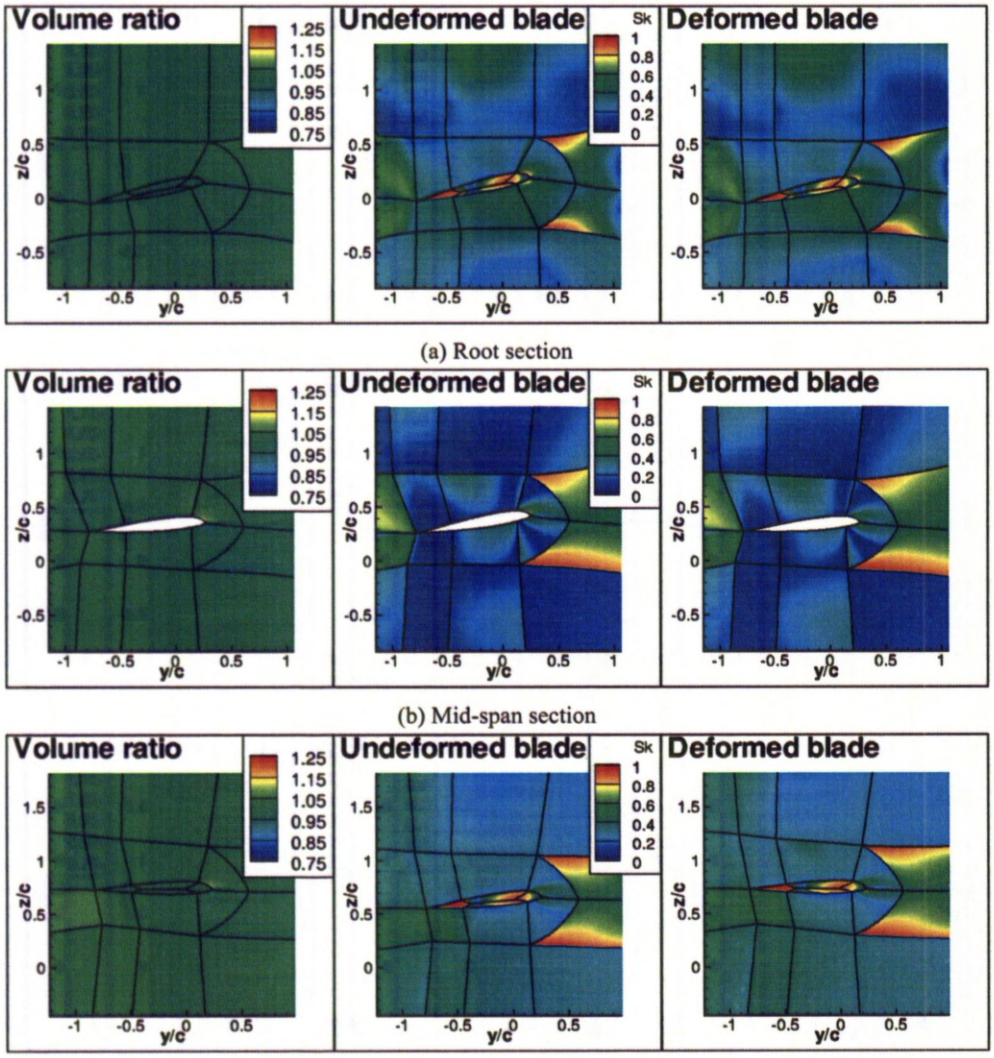

(a) Root section

(b) Mid-span section

(c) Tip section

Figure 5.13: Evolution of the mesh quality for the HART-II blade in sections perpendicular to the blade: the deformation was applied using the full hybrid mesh deformation method. The second flapping mode with an amplitude of $0.1c$ at the tip and the first torsional mode with an amplitude of -5 degrees at the tip were used.

HART-II Blade Mesh Deformation A mild deformation was first applied to the blade using the second flapping mode with an amplitude of $0.1c$ at the blade tip and the first torsional mode with an amplitude of -5 degrees. The grid quality is shown in Figure 5.13. The use of SAM allowed the volume

changes to be limited at very low values (less than 15%) and the cell skewness is kept similar. Only a slight increase of skewness in the blocks in contact with the blade can be noticed on top of the aerofoil section, but the skewness is kept within reasonable levels.

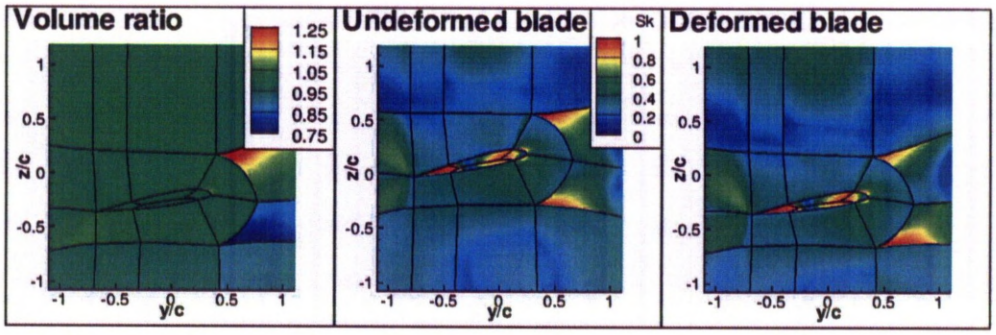

(a) Root section

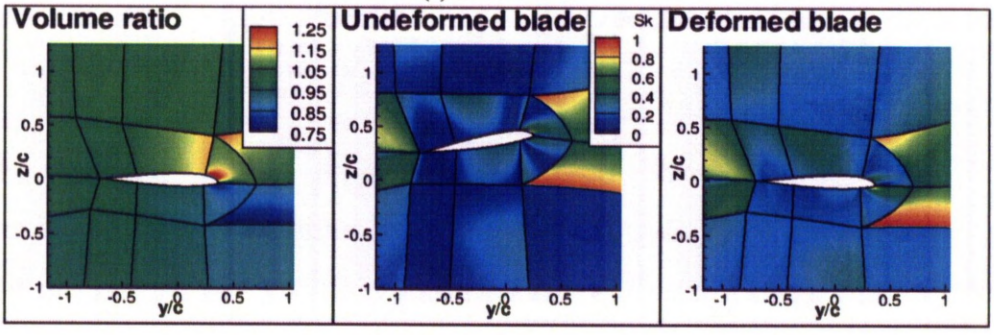

(b) Mid-span section

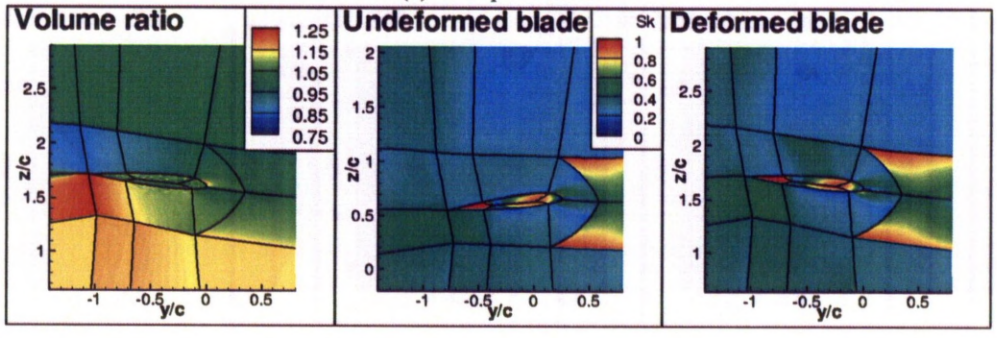

(c) Tip section

Figure 5.14: Evolution of the mesh quality for the HART-II blade in sections perpendicular to the blade: the deformation was applied using the full hybrid mesh deformation method. The second flapping mode with an amplitude of $1c$ at the tip and the first torsional mode with an amplitude of -10 degrees at the tip were used.

A stronger deformation was then applied to the blade with amplitudes increased to $1c$ and -10 degrees at the tip for the second flapping and the first torsional modes, respectively. The grid quality is shown in Figure 5.14. This deformation is stronger than what would be expected to happen on

a flying rotor. The deformation method spreads the cell volume changes on the surrounding blocks and the cell volume changes at the tip do not exceed 25%. While the skewness is increased at the tip, the overall skewness levels are kept similar. The largest modification happens at a mid-span station, where the volume changes are high near the leading edge. The skewness is also increased, but due to the very low skewness of the initial undeformed grid, the new skewness levels are acceptable for HMB.

UH-60A Blade Mesh Deformation The same deformations were applied to the UH-60A grid. This test case is more challenging, not only due to the sweep back at the tip which creates strong flapping displacements with the torsional deformation, but also by the small height of the blocks in contact with the blade. Therefore, the method has to force most of the mesh deformation outside the blocks in contact with the blade, or the grid quality will become unacceptable.

The grid quality for the mild deformation at four sections perpendicular to the blade is shown in Figure 5.15. Once again, the volume changes are limited in the blocks in contact with the blade, not exceeding 15%. The skewness is also kept at equivalent levels.

The strong deformation was then applied. The grid quality at four sections perpendicular to the blade is shown in Figure 5.16. Due to the strong deformation, large volume changes appears at the tip of the blade. However, this volume changes also spread to the surrounding blocks. At mid-span, the volume did not change much in the blocks in contact with the blade (less than 5%). The cell skewness in the block in contact with the blade is reasonable, despite some noticeable increase close to the tip and particularly at the start of the sweep-back. However, the maximum level reached by the skewness still allows for efficient HMB simulations.

The grid quality was also tested for deformations following the second flapping mode with various tip deflection amplitudes. The results are presented in Table 5.1. The maximum skewness in the blocks near the blade $Skr_{max} = \frac{1-max(Sk_{deformed})}{1-max(Sk_{undeformed})}$ is used. The volume ratio was also used to determine the maximum acceptable deformation. In order to preserve the grid properties (e.g. wall spacings for the boundary layer), the volume ratio was better kept between 0.5 and 2. The requested deformation amplitude was limited to $1.2c$. The location of the max cell volume change is around the main part

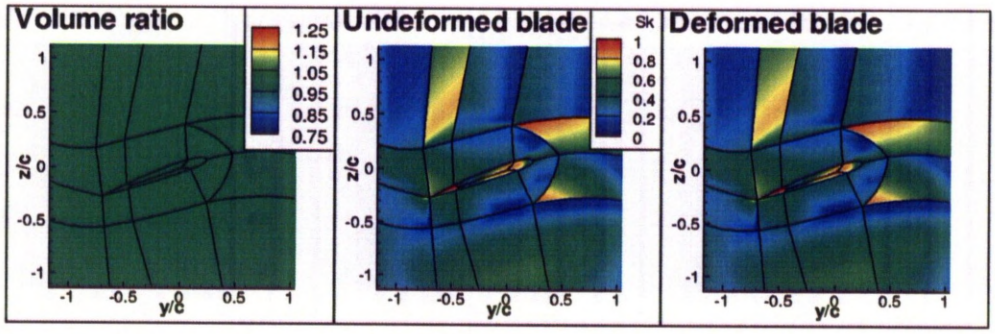

(a) Root section

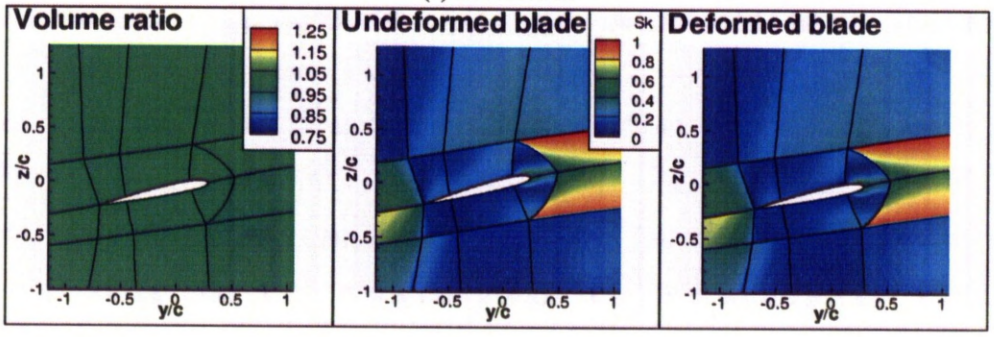

(b) Mid-span section

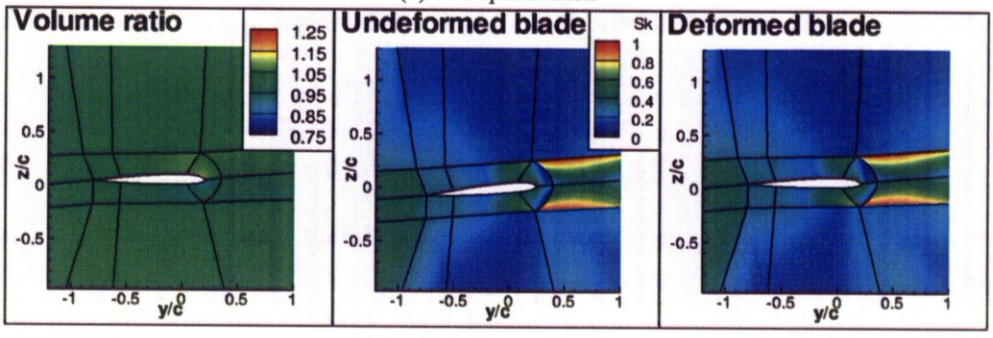

(c) Sweep-back start section

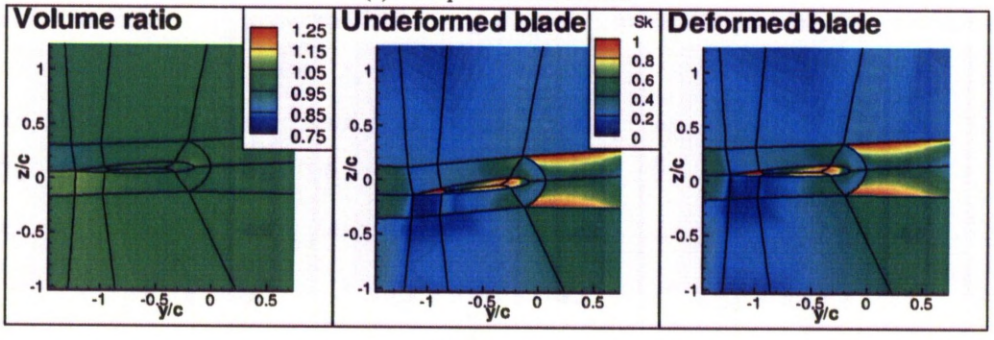

(d) Tip section

Figure 5.15: Evolution of the mesh quality for the UH-60A blade in sections perpendicular to the blade: the deformation was applied using the full hybrid mesh deformation method. The second flapping mode with an amplitude of $0.1c$ at the tip and the first torsional mode with an amplitude of -5 degrees at the tip were used.

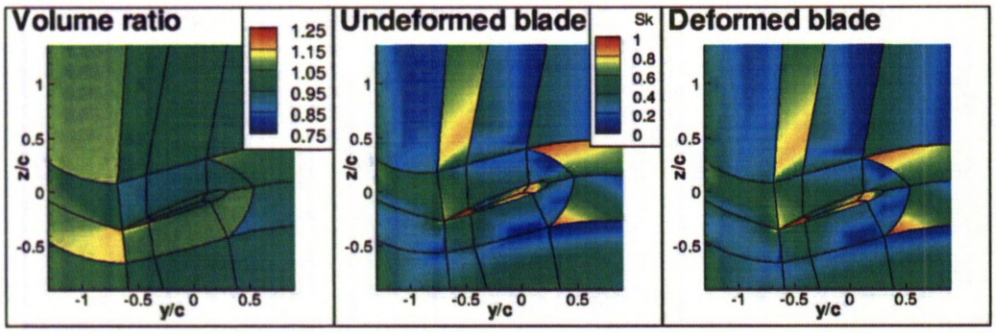

(a) Root section

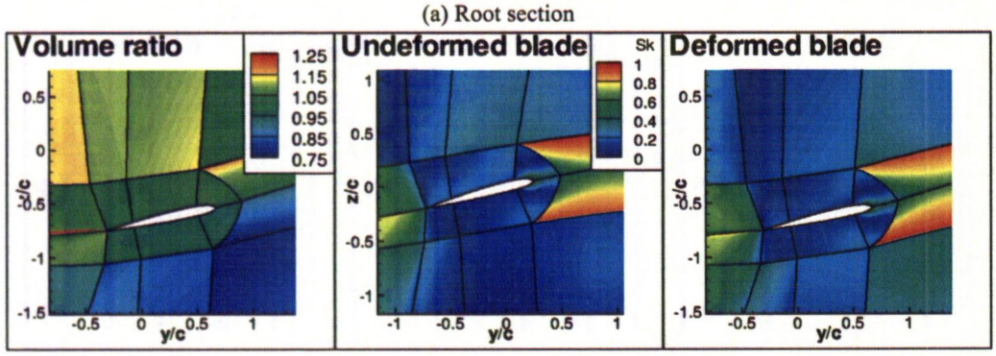

(b) Mid-span section

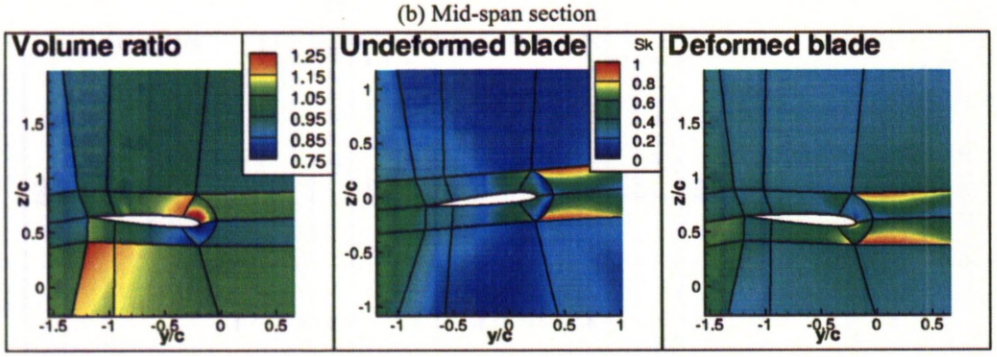

(c) Sweep-back start section

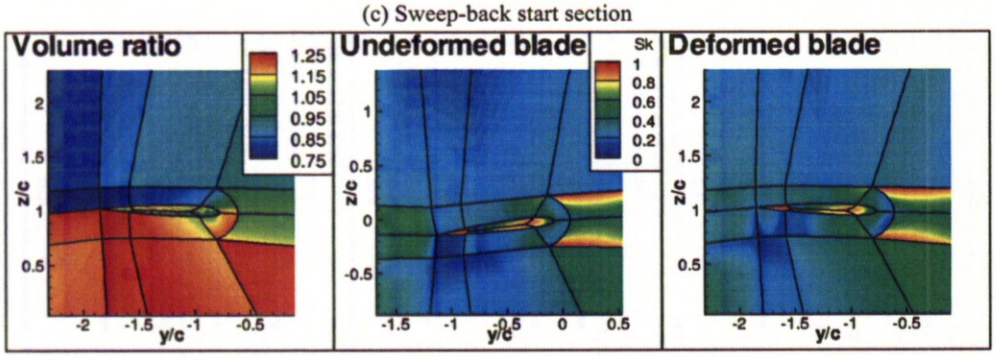

(d) Tip section

Figure 5.16: Evolution of the mesh quality for the UH-60A blade in sections perpendicular to the blade: the deformation was applied using the full hybrid mesh deformation method. The second flapping mode with an amplitude of $1c$ at the tip and the first torsional mode with an amplitude of -10 degrees at the tip were used.

of the blade which was allocated to in a single block in the span-wise direction. Had this block been divided in two, the spring analogy would move the block boundaries according to the blade movements and would further improve further the grid quality.

Table 5.1: Evolution of the grid quality with the increase of the blade deflection.

Tip deflection	**Volume ratio min (near blade)**	**Volume ratio max (near blade)**	Skr_{max} **(near blade)**	**Volume ratio min (full grid)**	**Volume ratio max (full grid)**
$0.3c$	0.8555	1.1423	0.9856	0.8555	1.1939
$0.6c$	0.7494	1.2654	0.9724	0.7494	1.3879
$0.9c$	0.6250	1.3343	0.9688	0.6250	1.5820
$1.2c$	0.5000	1.4322	0.9616	0.5000	1.7762
$1.5c$	0.3745	1.5437	0.9652	0.3745	1.9705
$1.8c$	0.2489	1.6572	0.9292	0.2489	2.1649
$2.1c$	0.1237	1.7724	0.9232	0.1237	2.3595

PM-4 Blade Mesh Deformation The ability of the proposed mesh deformation method to cope with complex blade shape was also shown for the PM-4 blade, that features an advanced BERP tip. The blade geometry and properties are summarised in Appendix A.3. The test included only the first torsional mode, that mainly alters the blade surface. A tip torsion of -11 degrees was applied at the tip of the blade. The grid quality at four sections perpendicular to the blade is shown in Figure 5.17. The grid deformation created important volume changes at the leading edge at the end of the transition as well as at the tip, however, the cell skewness was kept reasonable.

Method Limitations

A summary of the method containing the advantages and drawbacks of each step is shown in Table 5.2. One of the drawbacks of this method is due to the TFI: as this interpolation does not deform the edges, and in order to avoid mesh quality problems after a strong deformation, the mesh needs to contain a sufficient number of block layers along the blade, as these will be giving the shape of the outer C-part of the mesh. The blade cuts along the blade need to be almost equally spaced in order to capture the shape of the blade. Usually splitting blocks to improve the load-balance leads to blocks with roughly the same number of nodes in the direction of the blade chord. Due to the refined mesh at the tip to predict

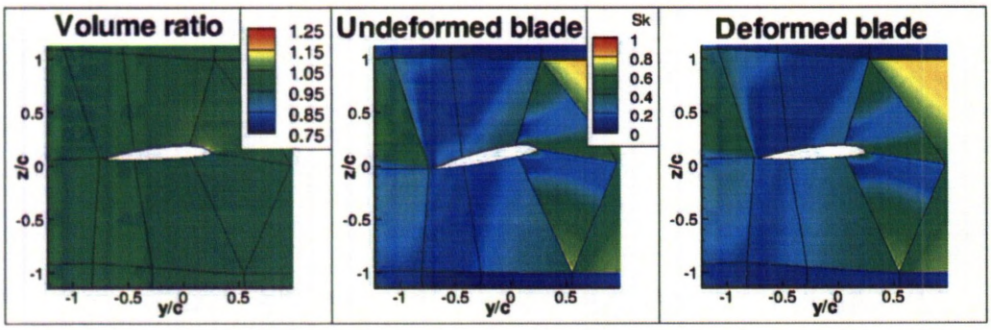

(a) Mid-span section

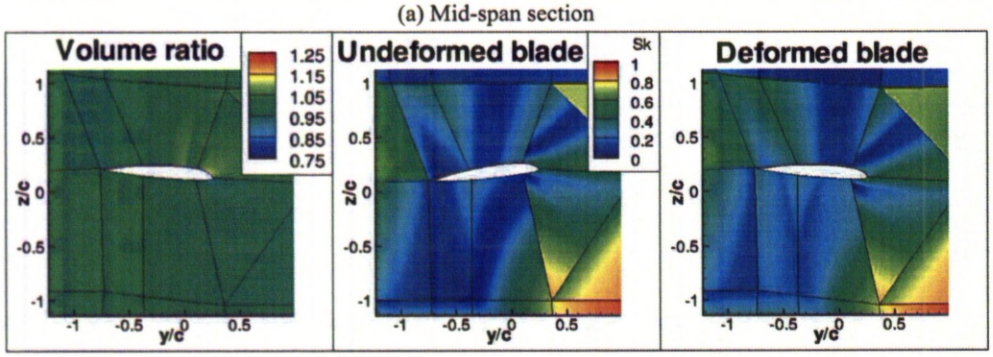

(b) Beginning of the transition to the BERP tip

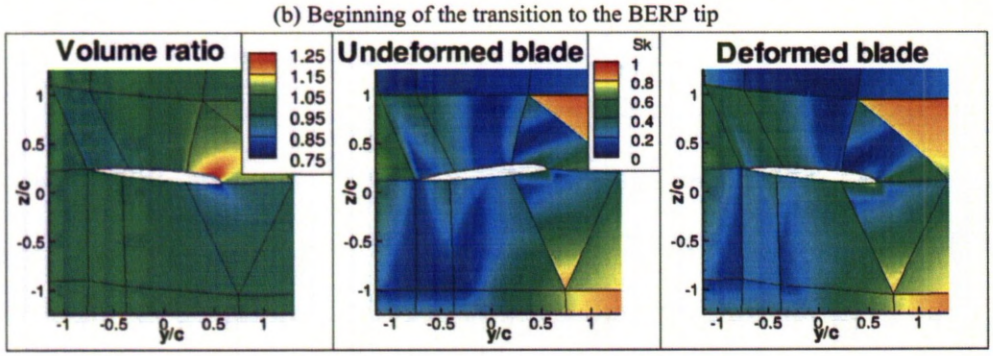

(c) End of the transition to the BERP tip

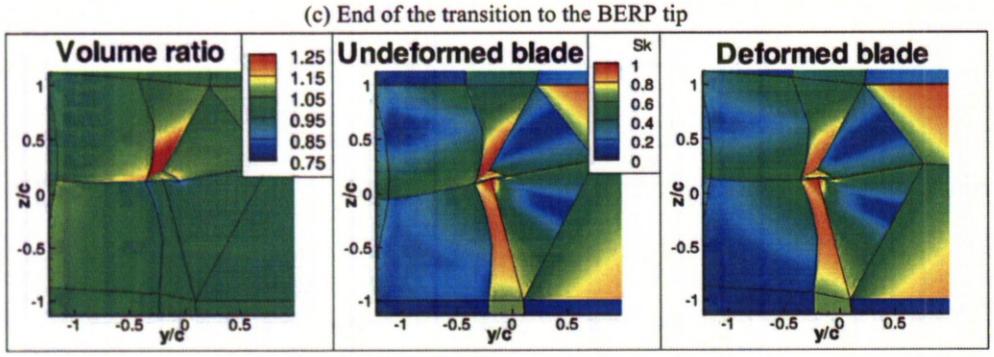

(d) Tip section

Figure 5.17: Evolution of the mesh quality for the PM-4 blade in sections perpendicular to the blade: the deformation was applied using the full hybrid mesh deformation method. The first torsional mode was applied with an amplitude of -11 degrees at the tip.

Table 5.2: Summary of the methods used in the proposed hybrid mesh deformation method.

Method	Domain of application	Advantages	Drawbacks
CVT	On the blade surface	Quick and memory-saving	Discrepancies far from the structural model
TFI	Inside the blocks	Quick	Not able to move the block boundaries
SAM	Between the vertices	Efficient at propagating a deformation, flexible to choose were most of the deformation is applied	CPU-time and memory

the vortex rolling process, this would mean narrower blocks at the tips in order to get equivalent block sizes. Therefore, a compromise has to be found for the location of the cuts along the span between the load-balance and the structural deformation method. A solution is to highly increase the number of cuts along the span, generating many blocks and allowing for both a good load-balance and an efficient grid deformation.

Method Implementation in HMB

In HMB, the mesh deformation was adapted to the settings of the solver. The method had to be able to cope with parallel simulations, as well as being repeated often, meaning that the computational cost had to be reduced as much as possible. Each processor of a parallel computation only stores a part of the full grid, containing only the locally solved blocks. In the preprocessing of the calculation, the blocks are visited, and only the two first layers of blocks around each blade are selected to be deformed. Blocks that will not be deformed are just revolving in forward flight calculations, which decreases the size of the SAM problems to be solved as well as the number of blocks were TFI needs to be applied. For each grid deformation step, the blade surface is deformed following the structural deformation using CVT, and then, the SAM is applied. The location of all the vertices for the SAM in the grid is known by all the processors to allow a reduced number of communications between the processors at this step. The deformed blocks are then recomputed using TFI.

5.2 Aeroelastic Coupling Methods for Rotors

5.2.1 Hovering Rotor Coupling Procedure

Coupling is realised using an iterative method, shown in Figure 5.18. NASTRAN is used as the structural solver, using SOL106 to solve the blade shape. A static computation is used, and no modal analysis

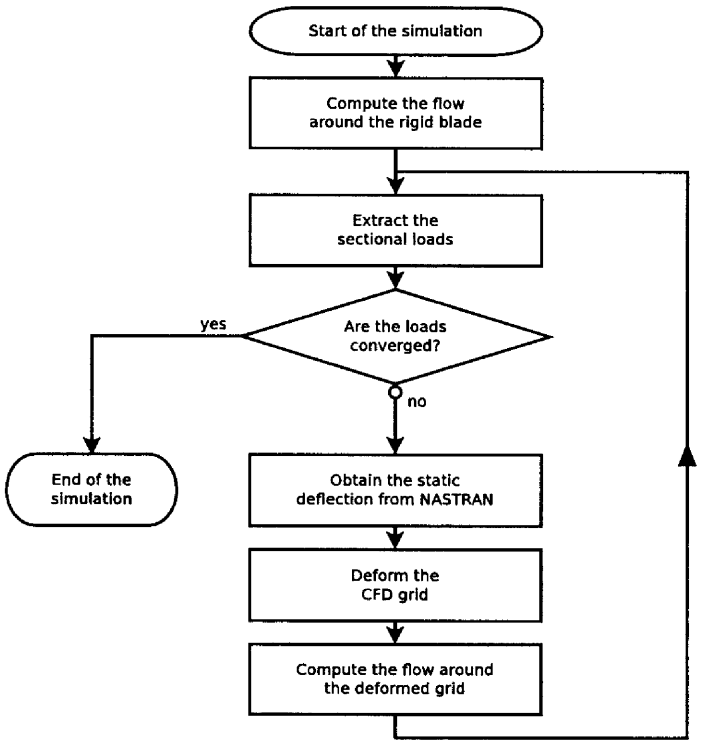

Figure 5.18: Aeroelastic coupling strategy for a hovering rotor.

is performed in this case. The loading is first extracted from the fluid grid, using a sectional pressure integration. NASTRAN is then used to compute the deformed shape of the blade with the loads introduced as *PLOAD* elements (linear loading between both ends of the element) and this new shape is applied to the fluid grid using the previously described mesh deformation method. This iterative process is repeated until a load convergence is reached. This convergence appeared rather quickly: in the test case of the UH-60A rotor described in Section 7.2, only 3 iterations were needed to obtain the final deformed shape.

5.2.2 Forward Flying Rotors Coupling Procedure

A strong coupling approach was chosen due to its flexibility and ability to predict complex manoeuvres for rotors. The modal approach was selected to allow for the eigenmodes to be computed before the fluid simulation.

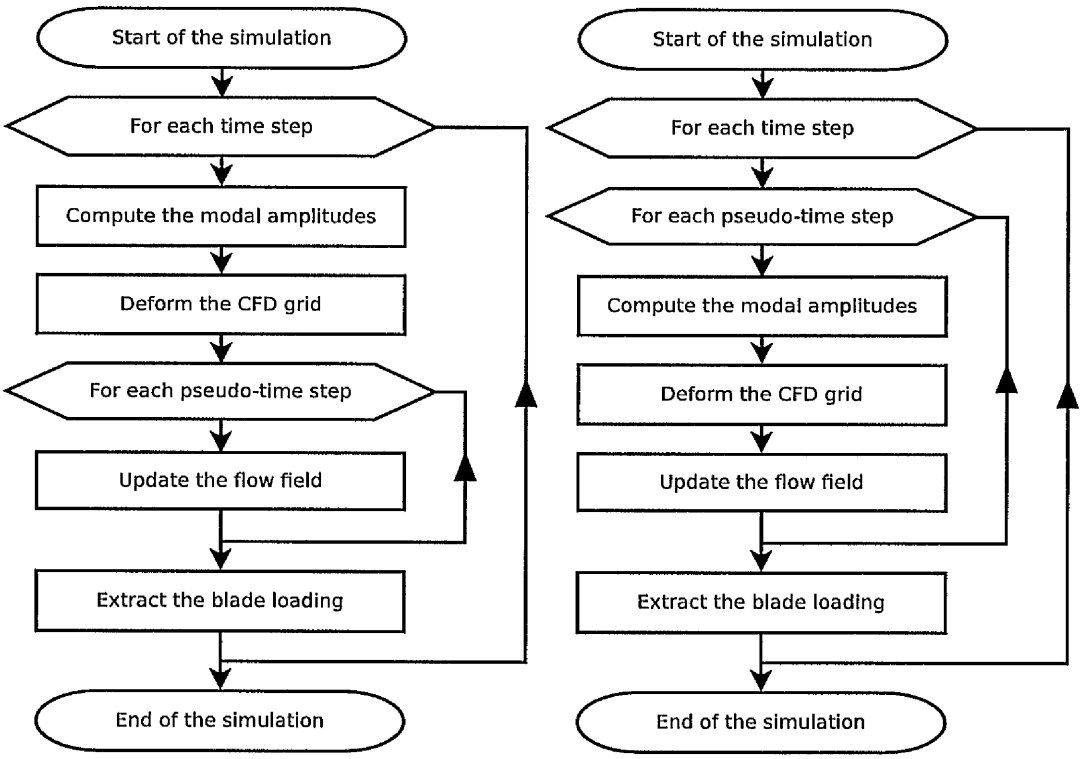

(a) Leap-frog method (b) Implicit method

Figure 5.19: Aeroelastic coupling strategies tested for a forward-flying rotor.

As described in Section 4.1, the blade shape ϕ is expressed following the eigenmode shapes as follows:

$$\phi = \phi_0 + \sum_{i=1}^{n_m} \alpha_i \phi_i \quad . \tag{5.20}$$

The differential equation on the modal amplitude is solved at each time step:

$$\frac{\partial^2 \alpha_i}{\partial t^2} + 2\zeta_i \omega_i \frac{\partial \alpha_i}{\partial t} + \omega_i^2 \alpha_i = \mathbf{f} \cdot \phi_i \quad . \tag{5.21}$$

For stability purposes, the analysis is started with a strong damping level of $\zeta_i = 0.7$ for each mode. The high starting damping in the equation is used to damp the oscillations created by the step that appear

at the beginning of the simulation, due to the sudden change in the forcing applied to a second order system. Once the blade reaches an acceptable level of deformation, usually after half of a revolution, the damping is then brought back to a smaller value of $\zeta_i = 0.3$ for each mode to allow the system to start oscillating. When convergence is reached, the damping can be lowered to its final value.

Two approaches were tested and compared: a leap-frog method computed the modes amplitudes between each time step, and an implicit method computed the mode shape amplitudes between each pseudo-time step. A flow chart showing the different steps for each method is shown in Figure 5.19.

The Leap-Frog Method

Equation 4.2 is solved at the end of each time step, as shown in Figure 5.19b. The i-th mode forcing is extracted from the computed time step t as:

$$f_i^s = \mathbf{f} \cdot \phi_i \tag{5.22}$$

The i-th amplitude α_i is then assessed for time step $t+1$ as:

$$[\alpha_i]_{t+1} = [\alpha_i]_t + \left[\frac{\partial \alpha_i}{\partial t}\right]_t \Delta t + \frac{1}{2}\left[\frac{\partial^2 \alpha_i}{\partial t^2}\right]_t \Delta t^2 \tag{5.23}$$

The time derivative of the amplitudes are then computed as:

$$\left[\frac{\partial^2 \alpha_i}{\partial t^2}\right]_{t+1} = [f_i^s]_t - \omega_i^2 [\alpha_i]_t - 2\zeta_i \omega_i \left[\frac{\partial \alpha_i}{\partial t}\right]_t \tag{5.24}$$

$$\left[\frac{\partial \alpha_i}{\partial t}\right]_t = \frac{1}{2}\left(\left[\frac{\partial^2 \alpha_i}{\partial t^2}\right]_t + \left[\frac{\partial^2 \alpha_i}{\partial t^2}\right]_{t+1}\right) \Delta t \tag{5.25}$$

using the non-updated amplitudes derivatives estimates from the previous time step t.

The Implicit Method

The discretisation of the derivatives of the modal amplitudes is expressed as follows:

$$\left[\frac{\partial \alpha_i}{\partial t}\right]_t = \left[\frac{\partial \alpha_i}{\partial t}\right]_{t-1} + \Delta t \left[\frac{\partial^2 \alpha_i}{\partial t^2}\right]_{t-1} \tag{5.26}$$

$$= \frac{[\alpha_i]_t - [\alpha_i]_{t-2}}{2\Delta t} + \frac{[\alpha_i]_t - 2[\alpha_i]_{t-1} + [\alpha_i]_{t-2}}{\Delta t} \tag{5.27}$$

$$= \frac{3[\alpha_i]_t - 4[\alpha_i]_{t-1} + [\alpha_i]_{t-2}}{2\Delta t} \tag{5.28}$$

which, if applied to the modal amplitudes and their time derivatives, gives:

$$\left[\frac{\partial \alpha_i}{\partial t}\right]_t = \frac{3[\alpha_i]_t - 4[\alpha_i]_{t-1} + [\alpha_i]_{t-2}}{2\Delta t} \tag{5.29}$$

$$\left[\frac{\partial^2 \alpha_i}{\partial t^2}\right]_t = \frac{3\left[\frac{\partial \alpha_i}{\partial t}\right]_t - 4\left[\frac{\partial \alpha_i}{\partial t}\right]_{t-1} + \left[\frac{\partial \alpha_i}{\partial t}\right]_{t-2}}{2\Delta t} \quad . \tag{5.30}$$

Equation 4.2 is discretised as:

$$\begin{bmatrix} 2\zeta_i\omega_i + \frac{3}{2\Delta t} & \omega_i^2 \\ -1 & \frac{3}{2\Delta t} \end{bmatrix} \begin{pmatrix} \left[\frac{\partial \alpha_i}{\partial t}\right]_t \\ [\alpha_i]_t \end{pmatrix} = \begin{pmatrix} [f_i^s]_t + \frac{4\left[\frac{\partial \alpha_i}{\partial t}\right]_{t-1} - \left[\frac{\partial \alpha_i}{\partial t}\right]_{t-2}}{2\Delta t} \\ \frac{4[\alpha_i]_{t-1} - [\alpha_i]_{t-2}}{2\Delta t} \end{pmatrix} \tag{5.31}$$

and solved at the end of each time step. The matrix is inverted using Cramer's rule and the modal amplitudes coefficient updated for the following pseudo-time step. This method implies the computation of the new grid at each pseudo-time step, as shown in Figure 5.19b, compared to each time step for the leap-frog method, but was deemed more robust.

Chapter 6

Results and Discussion — NACA0021 Test Case

The NACA0021 aerofoil has a substantial thickness and at a high incidence of $\alpha_{inc} = 60$ degrees behaves like a bluff body, with a Kármán way created in its wake. This test case involving a lifting body with a highly detached flow was deemed interesting as a test of the implementation of hybrid turbulence models and for assessing their performance. This highly stalled flow was also seen as interesting for rotorcraft flows, because deep stalls can occur on the retreating side, when the blade reaches cross flow conditions, and flow separation also occurs along helicopter fuselages behind the rear ramp or the dog house and hub region.

6.1 Test Case Description

The NACA0021 aerofoil shown in Figure 6.1 was tested in the post-stall regime by Swalwell *et al.* in [119].

The experiment covered angles of attack from 20 to 90 degrees. The wing model had a span of 7.2 chords and was spanning the wind tunnel test section in order to get an airflow equivalent to an

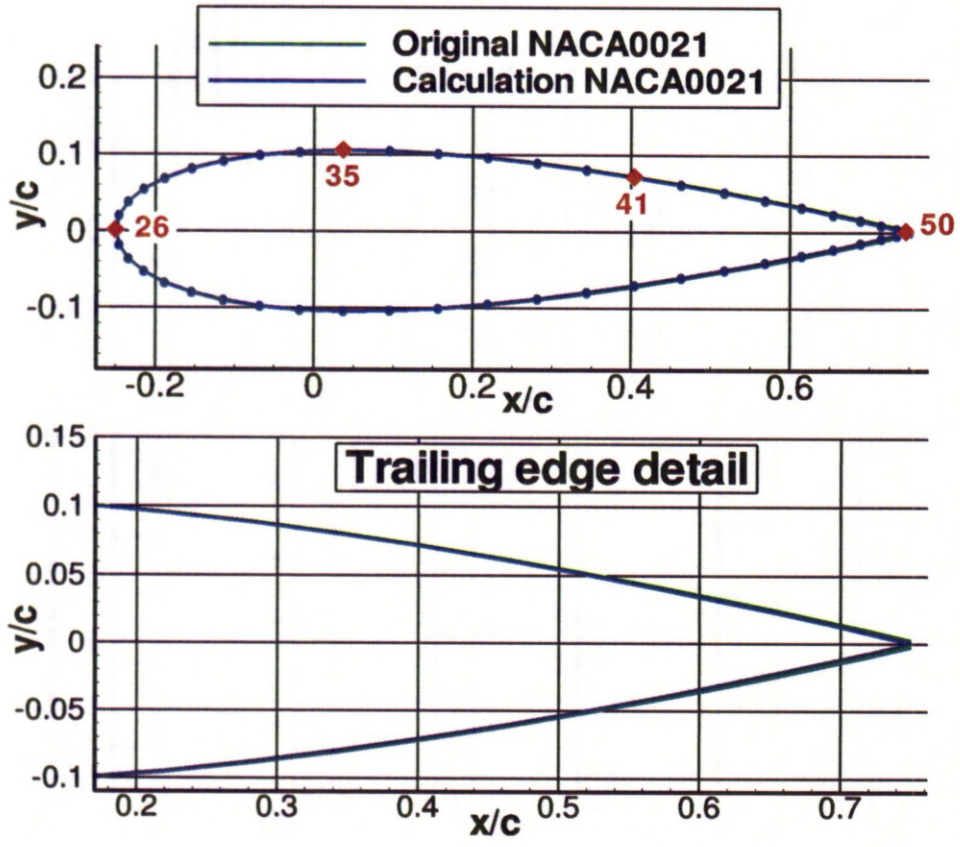

Figure 6.1: Shape of the NACA0021 aerofoil used by Swalwell *et al.* [119]. The shape of the aerofoil used in the HMB simulation as well as the probe locations are also shown.

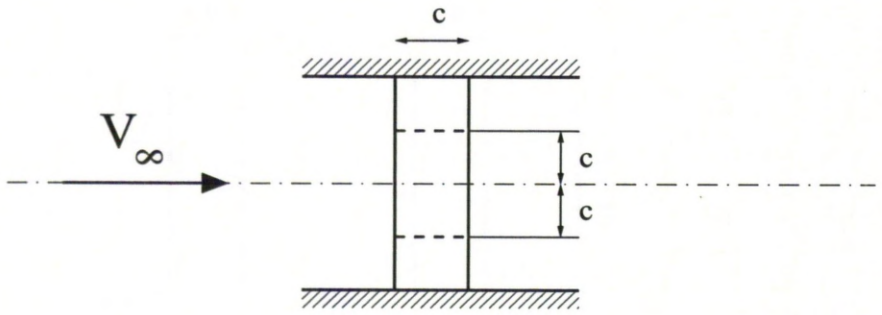

(a) Experimental setup

Figure 6.2: Experimental setup used for the NACA0021 with the location of the sections where measurements were taken at.

infinite wing in most of the wing flow. Pressure measurements were taken at two stations each one chord away from the wing mid-span as shown in Figure 6.2a. The mean values of the lift and drag coefficients were computed from these pressure measurements. A short part of the signals can be seen in Figure 6.3. The authors were also interested in measuring the frequency content of these coefficients.

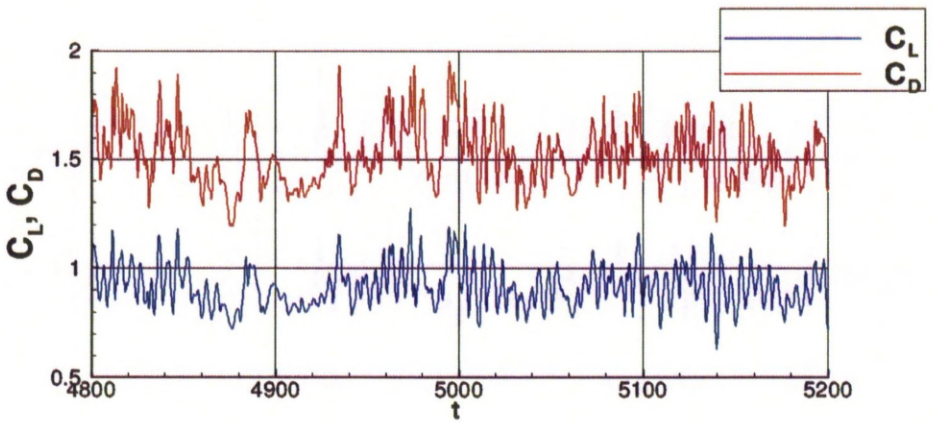

Figure 6.3: Time evolution of the wing lift and drag coefficients during the experiments by Swalwell *et al.* [119], obtained by integration from the pressure measurements.

Two peaks appeared after Fourier transformation of the experimental signals with their corresponding frequencies identified in [119]. The Reynolds and Mach numbers of the experiment were 2.7×10^5 and 0.10 respectively.

The European research program DESider used this experiment as a test case in order to assess the DES models. The chosen incidence of 60 degrees corresponds to an experimental lift coefficient of 0.931 and an experimental drag coefficient of 1.517. The first frequency peak corresponds to a Strouhal number of about 0.2 and the second to 0.4. The equivalent frequencies were 54.45Hz and 108.90Hz, respectively. The Strouhal number is the frequency non-dimensionalised with the reference length and speed. In this particular case, the freestream velocity and the chord length are used, so:

$$St = f\frac{c}{V_\infty}. \tag{6.1}$$

6.2 Predicted Flow Properties

The flow was computed on a grid with about 1.1 million nodes. The CFD model of the wing had unit chord and a span of 2 chords. An O-topology was used for the mesh. Symmetry boundary conditions are used on both planes at the tips of the wing. The far field of the CFD domain was located at 15 chords, and the trailing edge was sharpened for the calculation. The $2c$ span was chosen to be the length advised by Guenot[120]. Guenot's study was performed at an incidence of 45 degrees and DESider members found this length to be underestimated. The under-estimation is probably due to the change in the incidence. A more appropriate length of $2.8c$ should be considered though in this work the wingspan of $2c$ adopted in DESider was maintained.

The models that were tested in this work are all based on the SA model. The SALSA modification was first assessed before switching to the DES model, the DES model with the SALSA modification (DES SALSA), the DDES model, and finally the DDES model with the SALSA modification (DDES SALSA). The influence of the C_{DES} coefficient in DES was also assessed by using $C_{DES} = 0.325$ instead of the usual $C_{DES} = 0.65$. Finally, the results between the grid developed by the NTS was also used with DES to compare the results on both grids.

6.2.1 Flow Topology

Some instantaneous isosurfaces of the Q-criterion using the SA-DES turbulence model[61] as well as the pressure in slices orthogonal to the wing can be seen in Figure 6.4. The animation of the Q-criterion can be seen in the CD attached to this thesis. The flow develops a Kármán way in the wake. It is not 2D but fully 3D as some spatial irregularities can be seen in the Q-criterion. The wake structure is dominated by the leading and trailing edges vortices and does not change much from slide to slide.

Most of the DES models resulted in an unsteady fully 3D flow. In these cases, long stream-wise structures are visible through Q-criterion isosurfaces.

The low shedding activity is recognised with smaller variations of the lift coefficient as well as lower depressions in the vortices cores. This shedding activity variation is not predicted by all turbulence

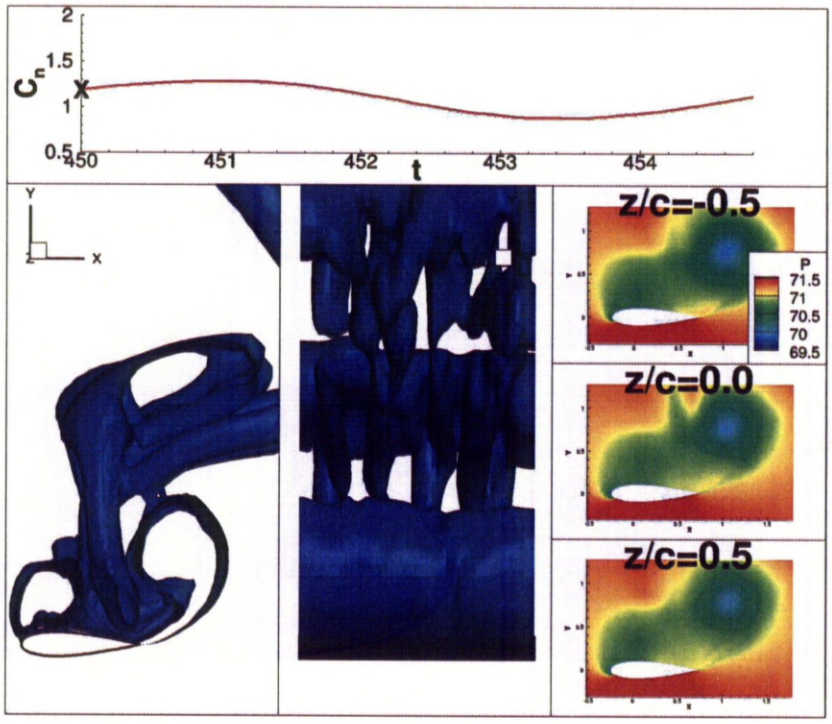

(a) $t = 450.0$

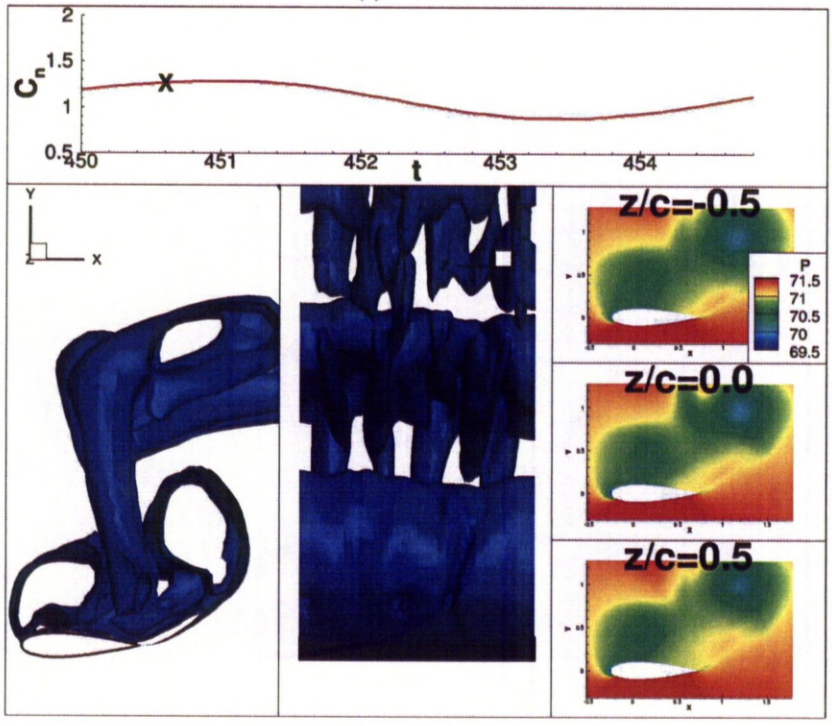

(b) $t = 450.6$

Figure 6.4: Instantaneous isosurfaces of the Q-criterion at 0.125 and pressure on slices perpendicular to the wing from a calculation with the DES turbulence model with a halved C_{DES} coefficient. The main frequency in the normal force coefficient corresponds to the shedding frequency. $\alpha_{inc} = 60^{o}$, $M_{\infty} = 0.10$ and $Re = 2.7 \times 10^{5}$. Continued.

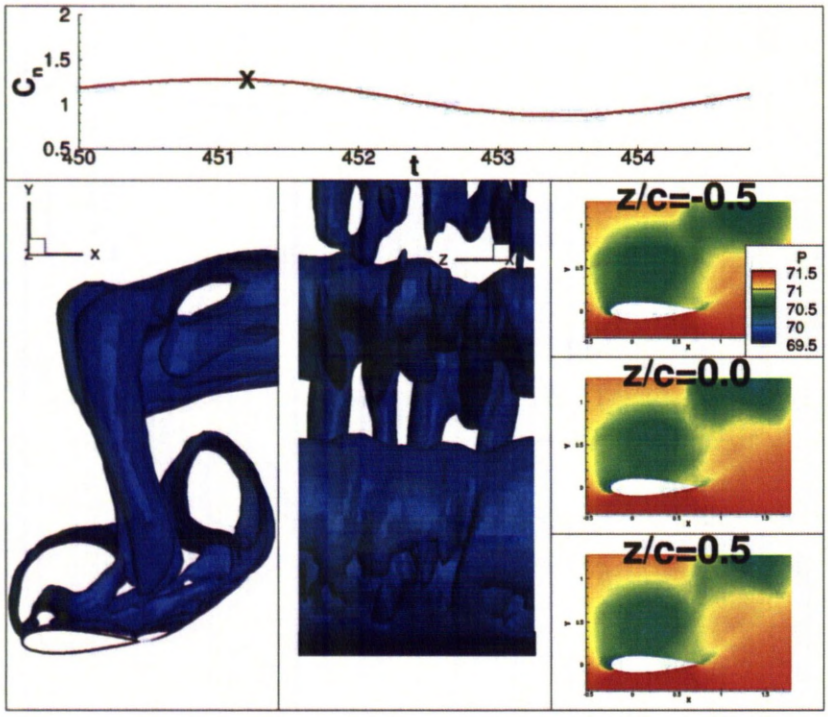

(c) $t = 451.2$

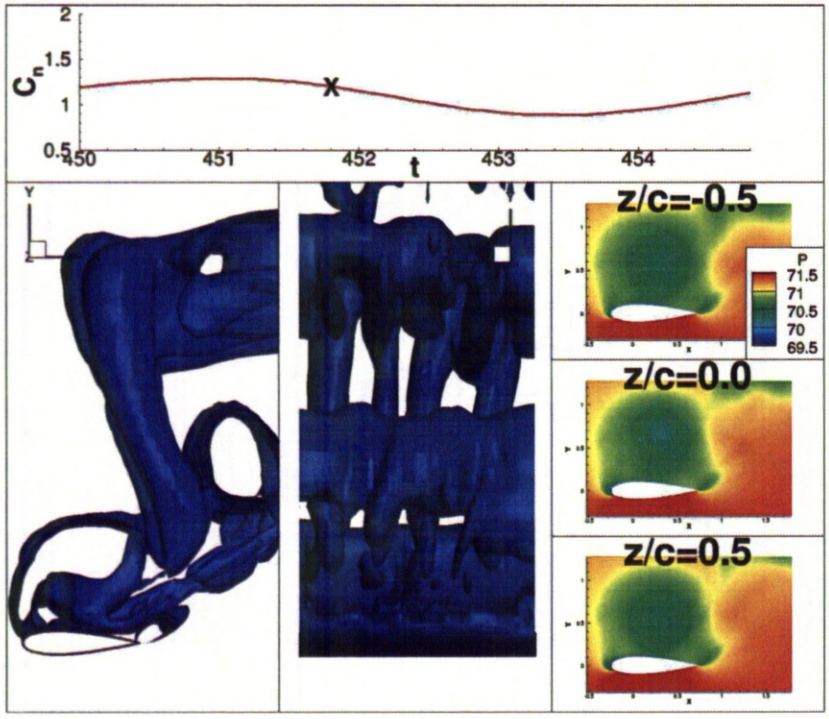

(d) $t = 451.8$

Figure 6.4: Instantaneous isosurfaces of the Q-criterion at 0.125 and pressure on slices perpendicular to the wing from a calculation with the DES turbulence model with a halved C_{DES} coefficient. The main frequency in the normal force coefficient corresponds to the shedding frequency. $\alpha_{inc} = 60^{\circ}$, $M_{\infty} = 0.10$ and $Re = 2.7 \times 10^5$. Continued.

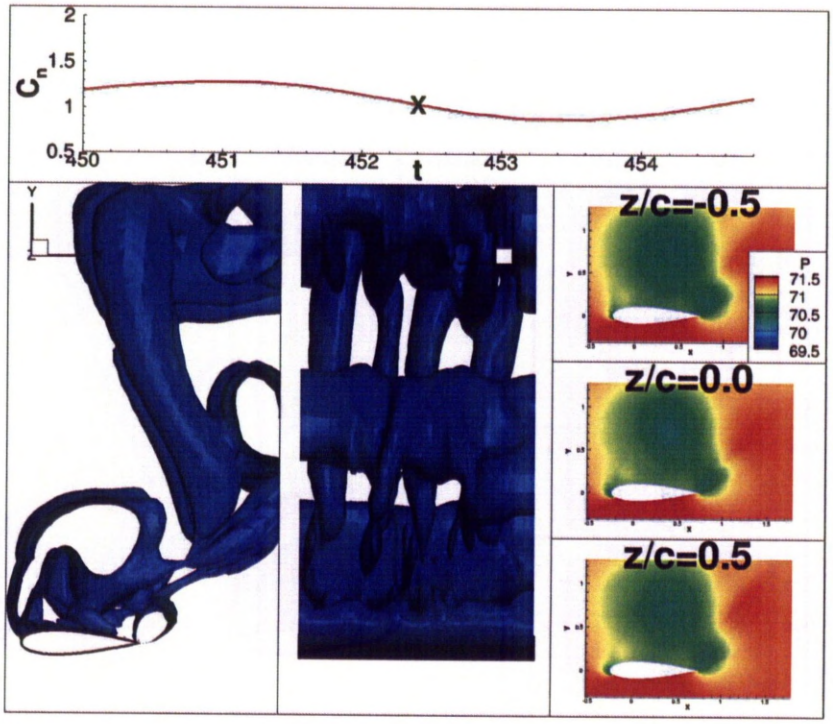

(e) $t = 452.4$

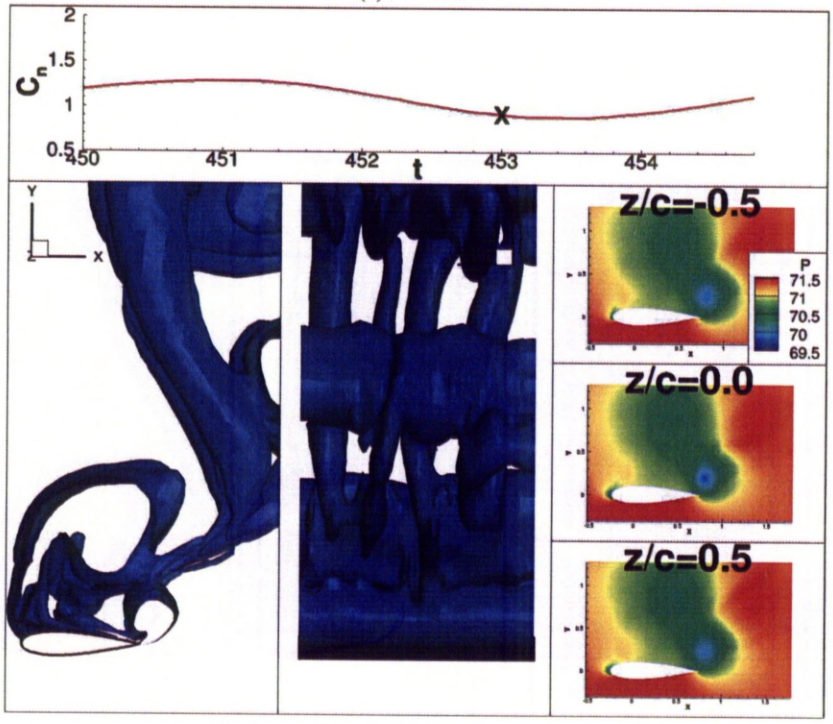

(f) $t = 453.0$

Figure 6.4: Instantaneous isosurfaces of the Q-criterion at 0.125 and pressure on slices perpendicular to the wing from a calculation with the DES turbulence model with a halved C_{DES} coefficient. The main frequency in the normal force coefficient corresponds to the shedding frequency. $\alpha_{inc} = 60^{o}$, $M_{\infty} = 0.10$ and $Re = 2.7 \times 10^{5}$. Continued.

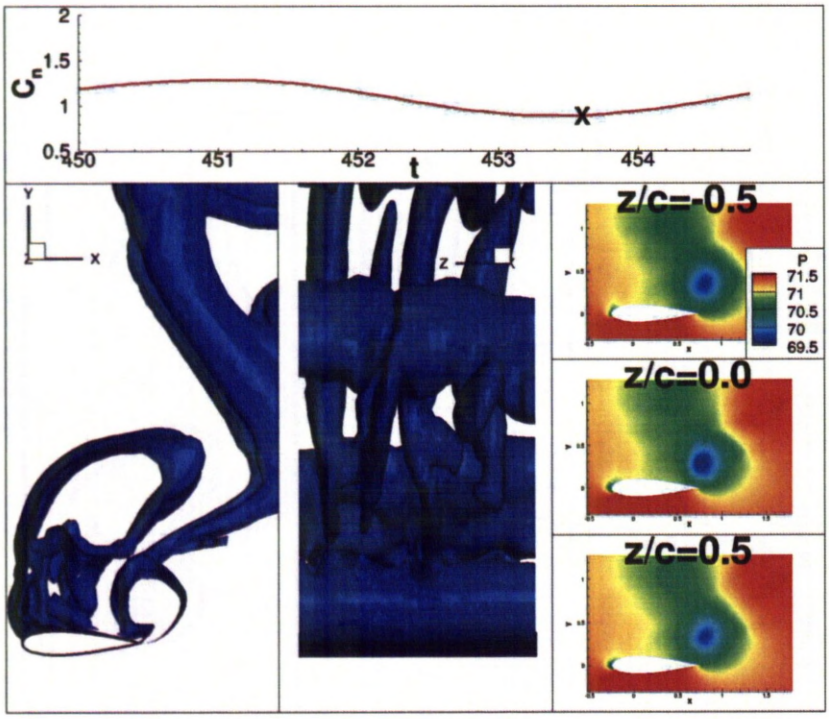

(g) $t = 453.6$

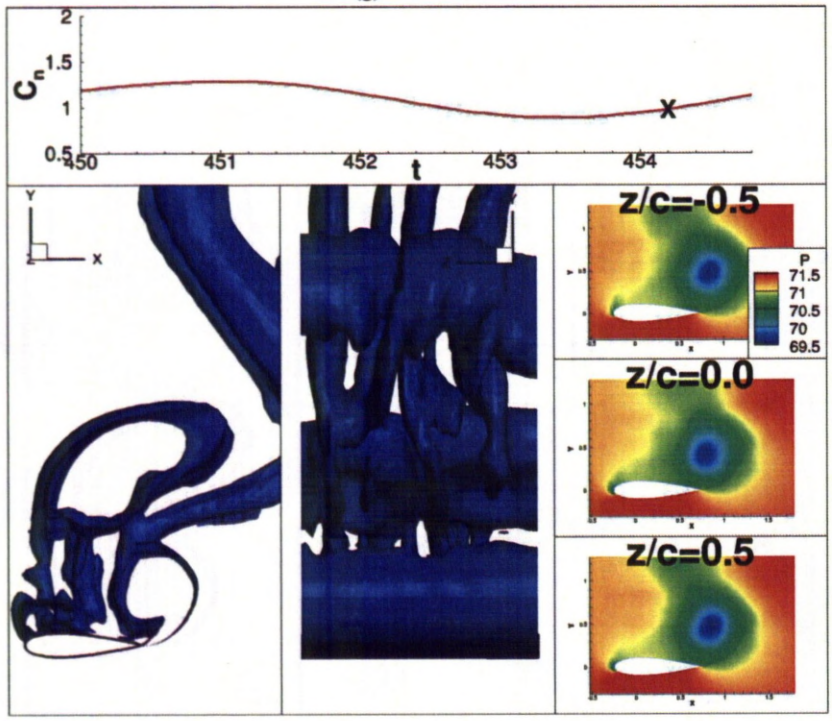

(h) $t = 454.2$

Figure 6.4: Instantaneous isosurfaces of the Q-criterion at 0.125 and pressure on slices perpendicular to the wing from a calculation with the DES turbulence model with a halved C_{DES} coefficient. The main frequency in the normal force coefficient corresponds to the shedding frequency. $\alpha_{inc} = 60°$, $M_\infty = 0.10$ and $Re = 2.7 \times 10^5$. Concluded.

models though, and at certain time steps, two small countra-rotating vortices are also created at the leading edge.

The mean pressure coefficient distribution on the aerofoil section is shown in Figure 6.5. The prediction is quite good but the suction on the upper surface is slightly under-predicted for the calculations that gave a steady flow and over-predicted by the rest. The experimental error bars, however, were not given and all the experimental values are located inside the computed RMS bars of the computed pressure coefficient for calculations with an unsteady result.

6.2.2 Mean Flow analysis

Spatial and temporal mean flows are shown in Figure 6.6. The flow is dominated by the main leading and trailing edges vortices, the leading edge vortex being bigger in size than the trailing one. The area between the two vortices is located between 65 and 75% of the chord. The mean flow topology is the same for all employed turbulence closures, whether these resulted in a steady or unsteady flow.

6.2.3 Analysis of Points Probes

Probes were added on the surface of the blade. 50 probes were put around each of three sections along the wing span. The distribution of the probes is shown in Figure 6.1, and the three sections are located at $z/c = -0.5$, $z/c = 0$ and $z/c = 0.5$.

The mean pressure was extracted out of these probes and compared with experiments. The results are shown in Figure 6.5. The predicted suction on the upper surface is slightly higher than the experimental one, therefore justifying a somehow higher lift coefficient prediction. The experimental results are still inside the RMS, however, the CFD and the experimental error margins are not known.

The correlation between the upper surface probes was also studied. Four locations on the aerofoil section were chosen on the upper surface in order to study the pressure on the upper surface due to the wake structure and their correlation. These probes are equally spaced and their locations are shown in Figure 6.1. The spanwise correlation was also studied, using probes in the middle section of the

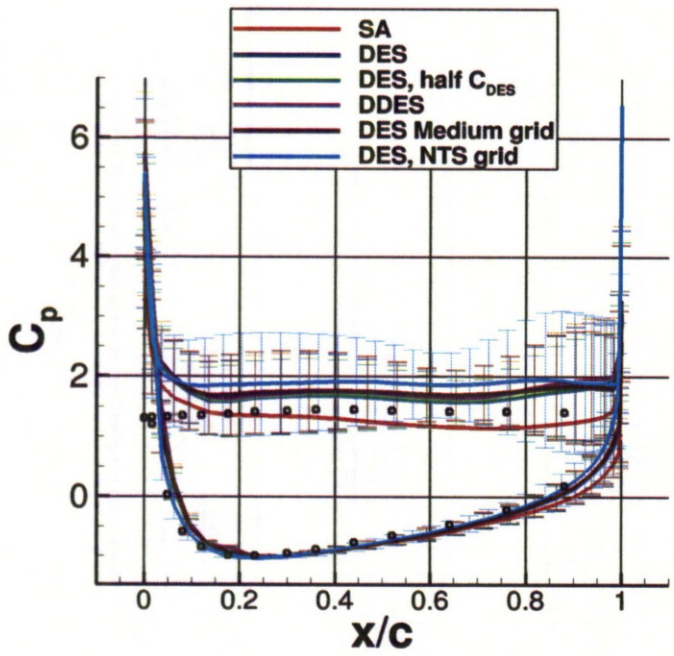

(a) SA-based models

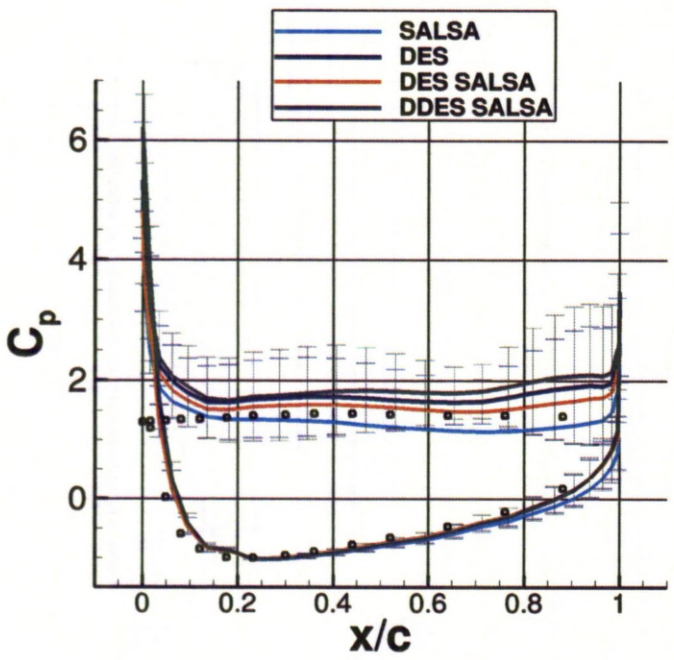

(b) SALSA-based models

Figure 6.5: Comparison of the mean pressure coefficient on the NACA0021 aerofoil. The error bars indicate the RMS of the pressure coefficient, computed by the DES models.

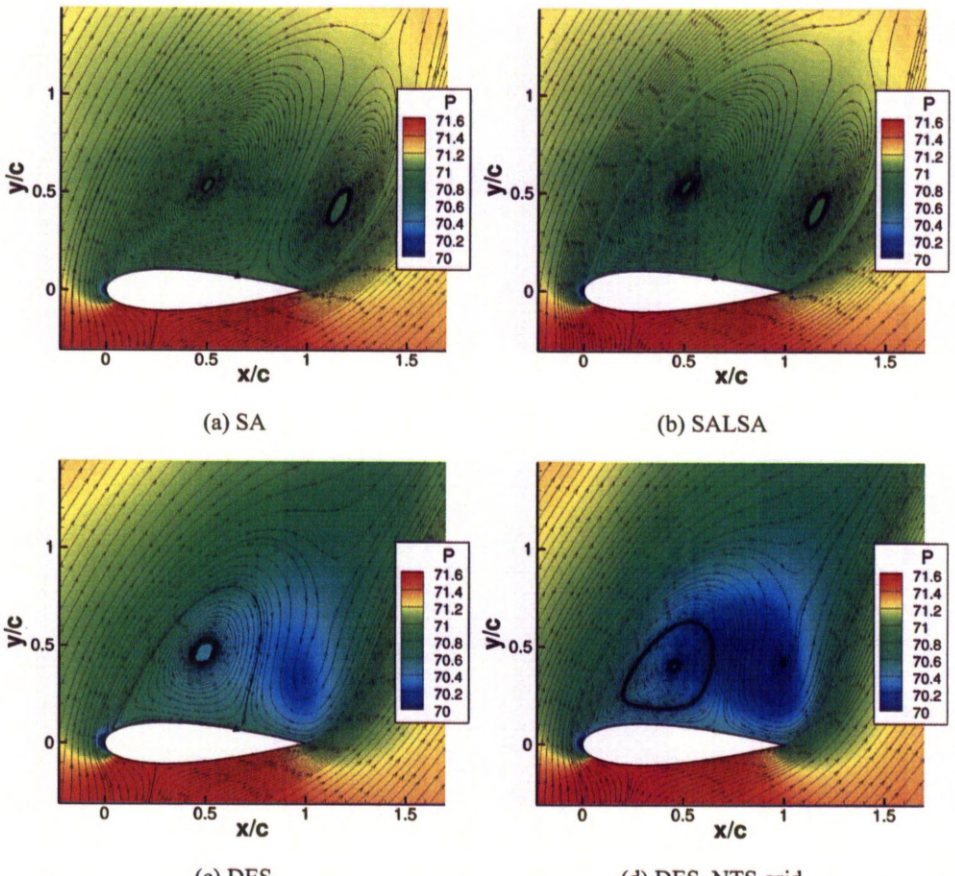

(a) SA

(b) SALSA

(c) DES

(d) DES, NTS grid

Figure 6.6: Comparison of the time-averaged pressure and flow in the midspan-plane obtained with various turbulence models. $\alpha_{inc} = 60^{o}$, $M_{\infty} = 0.10$ and $Re = 2.7 \times 10^{5}$. Continued.

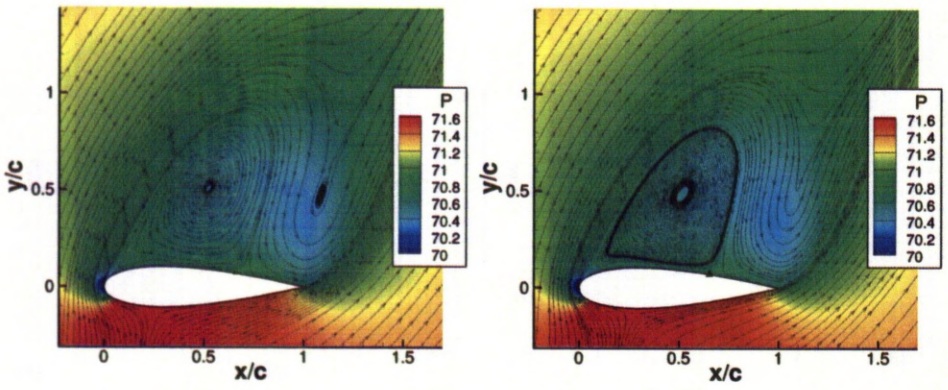

(e) DES SALSA (f) DES half C_{DES}

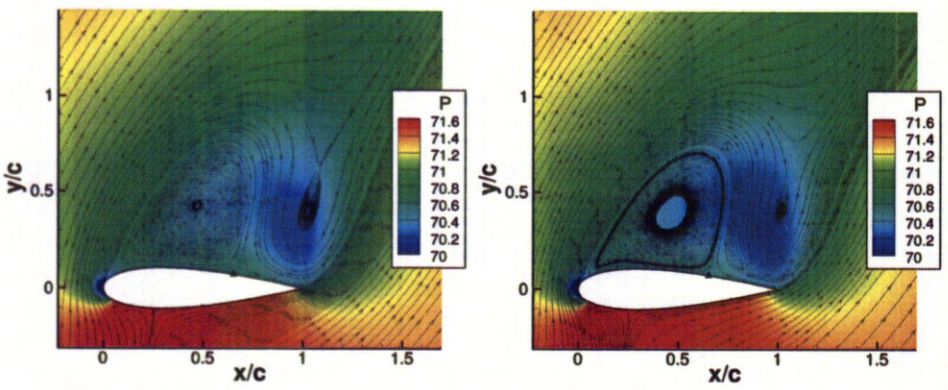

(g) DDES (h) DDES SALSA

Figure 6.6: Comparison of the time-averaged pressure and flow in the midspan-plane obtained with various turbulence models. $\alpha_{inc} = 60^{o}$, $M_{\infty} = 0.10$ and $Re = 2.7 \times 10^{5}$. Concluded.

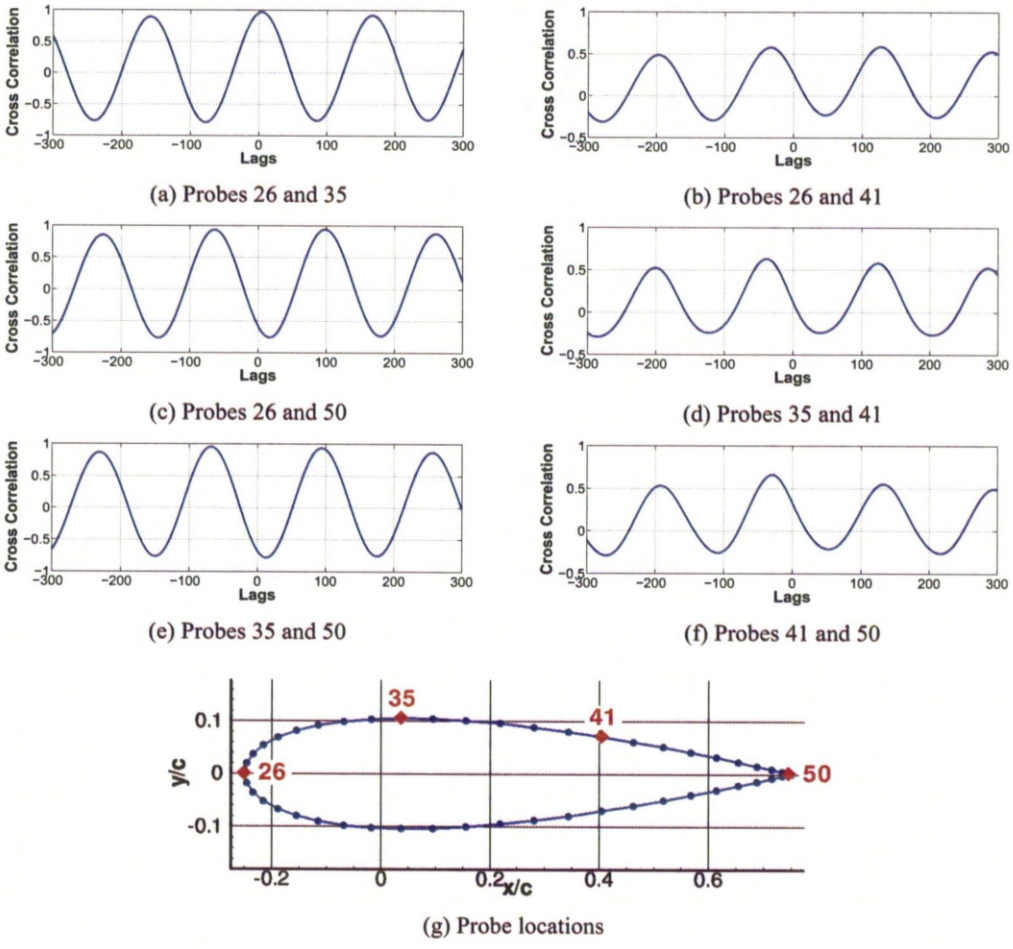

Figure 6.7: Correlation between various probes pressure measurement on the upper surface of the NACA0021 aerofoil at the middle section.

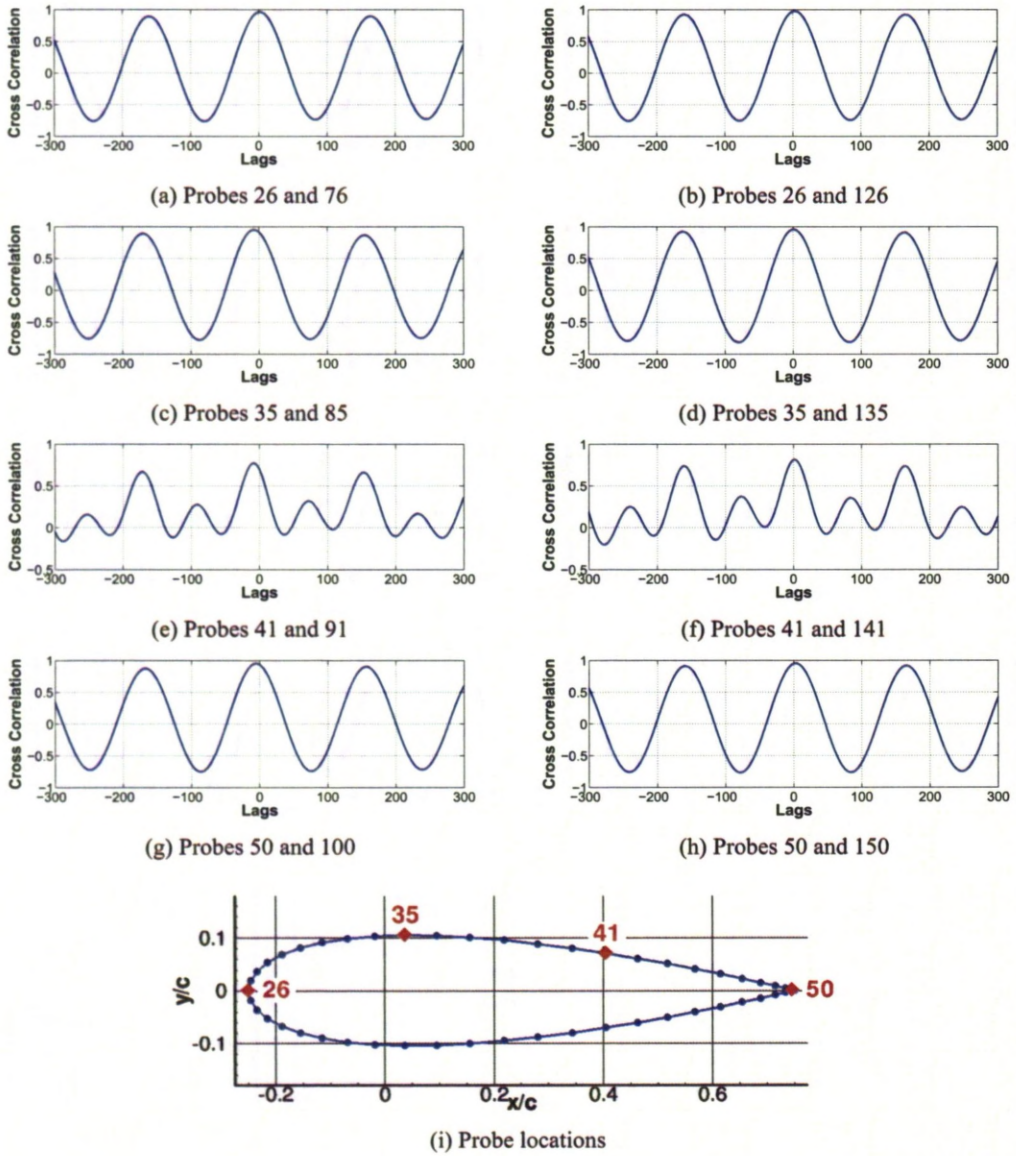

Figure 6.8: Correlation of pressure measurements at probes on the upper surface of the NACA0021 aerofoil. The probes 76, 85, 91 and 100 in section $z/c = -0.5$ correspond respectively to the locations of probes 26, 35, 41 and 50 on the described aerofoil section, and the probes 126, 135, 141 and 150 in section $z/c = 0.5$ correspond respectively to the locations of probes 26, 35, 41 and 50 on the aerofoil section.

wing ($z = 0$) and at two other sections located at $z/c = 0.5$ and $z/c = -0.5$, using the same four probes locations at each sections.

The first remark is the correlation at -1 (with a small lag) between the leading and trailing edges. This corresponds to the main wake vortices in the wake of the aerofoil and shows the formation of a vortex at the leading edge that is shed in the wake followed by a trailing edge vortex. The lower correlation between probes 35 and 41 seems to come from the fact that the limit between the trailing and leading edges vortices is located in between these probes and at least probe 41 is located near the area where the leading edge and trailing edge vortices are both dominant at alternating time instants.

The second remark deals with the spatial correlations in the spanwise direction, where some lag appears. The flow is fully 3D with some vortices formed perpendicular to the span-wise direction. There also seems to be a small wave along the span wise direction whose origin is unknown and this could be the reason for the lag appearing in this correlation. The frequency is doubled on the spatial correlation for probe 41 due to the presence of alternating leading and trailing edge vortices. The lower correlation peaks are due to the comparison at twice the shedding frequency and with every other peak being lower due to the comparison of the influence of the leading edge vortices and the trailing edge vortices.

6.3 Comparison of the Various Turbulence Models with the Experiment

The flow was computed with various revisions of the Spalart-Allmaras turbulence model: the URANS version of Spalart-Allmaras, the hybrids DES and DDES and the same models with the SALSA production term modification[99]. Furthermore, the DES model was also tested with a finer grid (2.2 million nodes instead of 1.1) and another calculation was carried out with the C_{DES} coefficient halved.

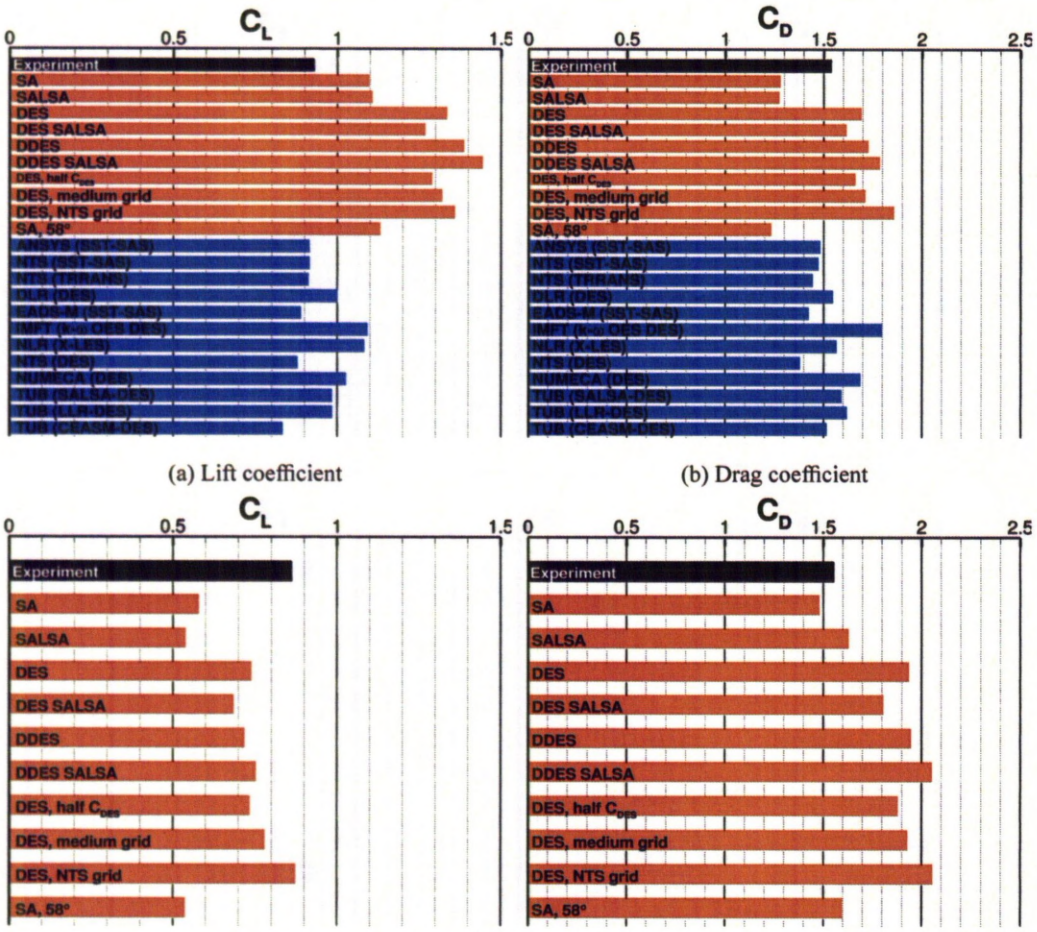

(a) Lift coefficient

(b) Drag coefficient

(c) Lift coefficient obtained by integration at the probe locations

(d) Drag coefficient obtained by integration at the probe locations

Figure 6.9: Comparison of the lift and drag coefficient of the NACA0021 aerofoil at an incidence of 60 degrees obtained with various turbulence models and the experimental value from Swalwell[119]. The coefficients obtained by other groups and presented in [121] are also added.

6.3.1 Comparison of the lift and drag coefficients

The mean lift and drag coefficients are presented in Figure 6.9. Two integration methods were used to calculate them: firstly, the pressure was integrated along the wing surface to obtain the force along the wing, and this technique was then compared to the integration of the mean pressure at the experimental tap locations. They show an overestimation of the lift as well as the drag. The reason of this estimation is not known, and the pressure distribution on the aerofoil surface appears otherwise normal. The DESider partners reached a better agreement with the experimental measurements, which can be due to the integration procedure. A grid dependency could also be the reason: the supplied NTS grid allowed for a better lift prediction, and was more refined in the separated flow area. However, the drag predictions was not improved by the use of this grid.

The first main difference between the calculations comes from the flow properties: while the URANS models converged to a steady output, the hybrids one converged to a fully unsteady flow, apart for the DES-SALSA which converged to a steady flow. The lift coefficient evolution during the unsteady calculations is shown in Figure 6.10. While the DES with a halved C_{DES} coefficient seems to accurately predict the evolution of the shedding activity with lows and highs, DDES-SALSA seemed to under-predict this variation. The DDES did not predict any evolution of the shedding activity.

An interesting comparison concerns the mean pressure coefficient shown in Figure 6.5. While all the models that predicted a steady flow under-predicted the suction on the upper surface, the unsteady flows appear to produce an over-prediction of this suction. The DES with a halved C_{DES} coefficient seems to give slightly better predictions while the differences between the DES and DDES are extremely small probably due to the coarseness of the grid. The DDES SALSA resulted in over-prediction.

The second interesting comparison is the power spectra of the lift and drag coefficients obtained with the various calculations with fully unsteady flow. The Power Spectrum Density (PSD) plots of the lift and drag coefficients during the unsteady calculations can be seen in Figures 6.11 and 6.12. The two first peaks in both coefficients at $St = 0.2$ and $St = 0.4$ are well predicted by all calculations that resulted in unsteady flows but tend to have a slightly higher amplitude than the experiment. Most of the models

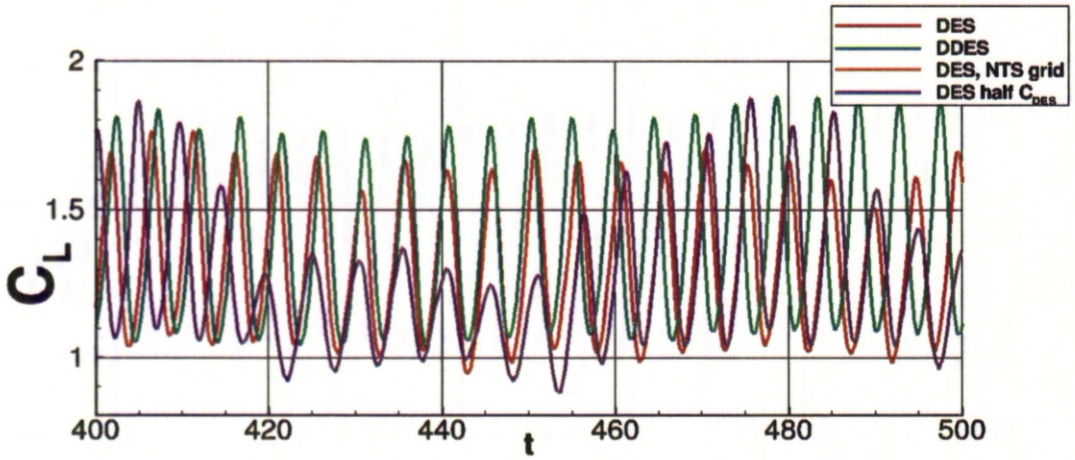

(a) SA-based models

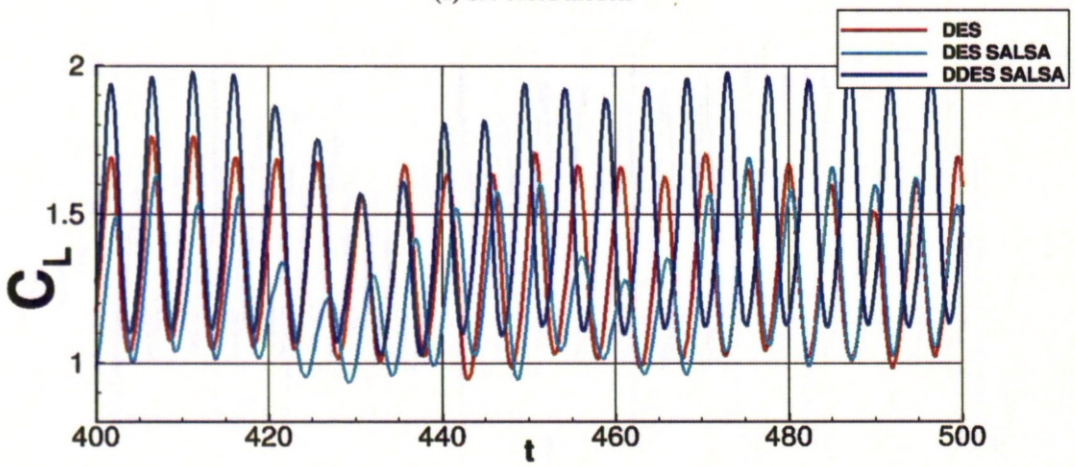

(b) SALSA-based models

Figure 6.10: Comparison of the evolution of the lift coefficient during the calculations as a function of time. The calculations resulting in a steady state flow are not shown.

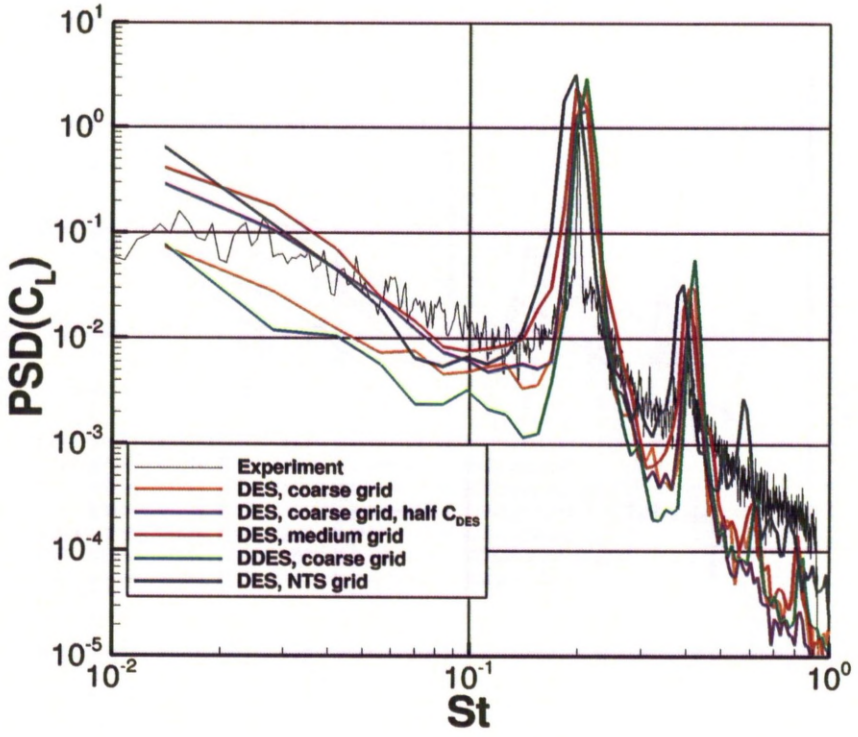

(a) SA-based models

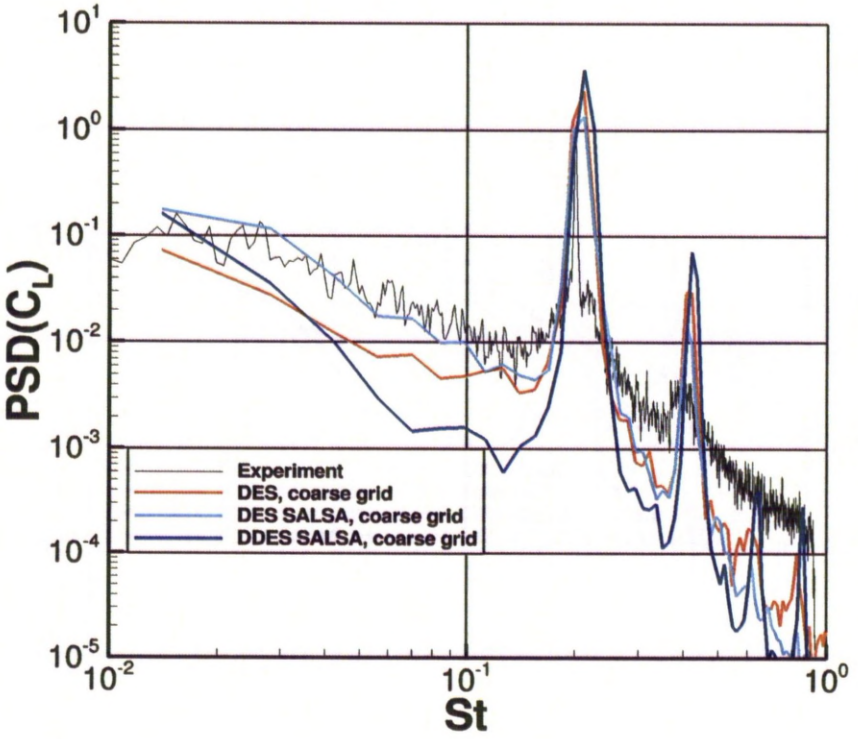

(b) SALSA-based models

Figure 6.11: Comparison of power spectral densities (PSDs) of the lift coefficients obtained with various turbulence models on the coarse and fine grids.

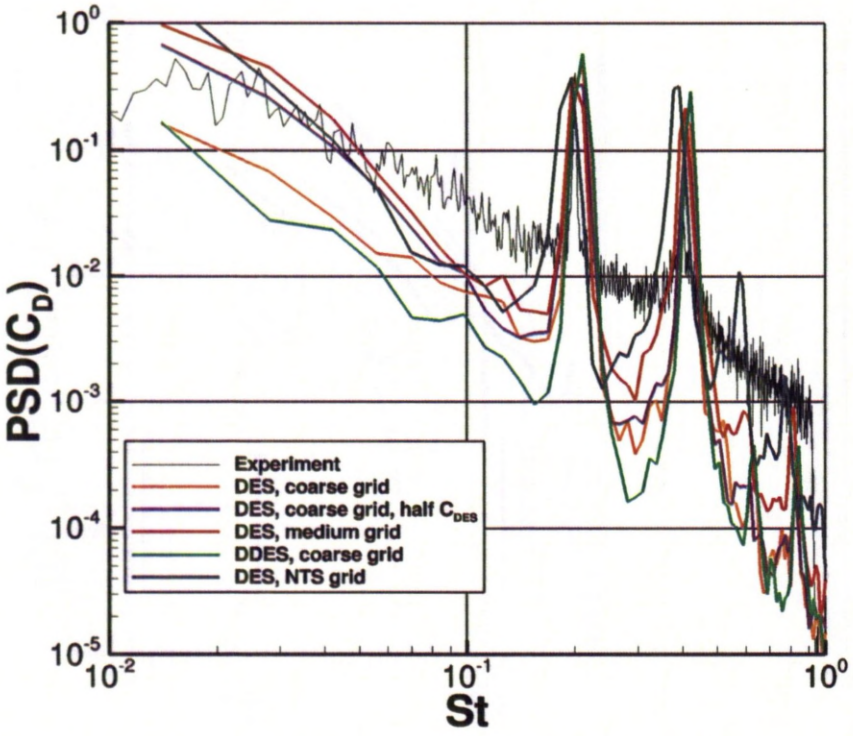

(a) SA-based models

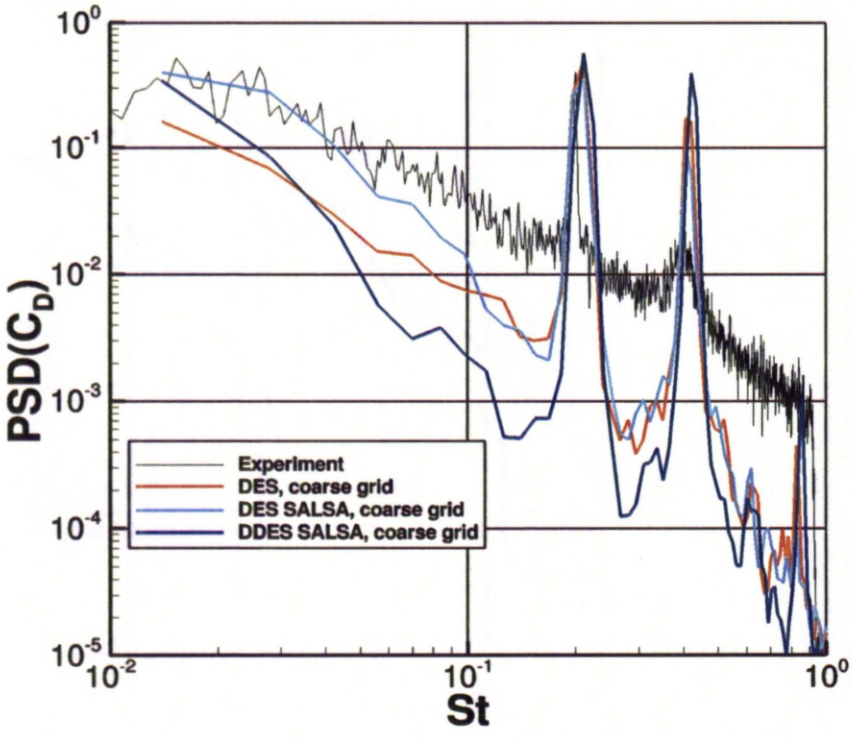

(b) SALSA-based models

Figure 6.12: Comparison of power spectral densities (PSDs) of the drag coefficients obtained with various turbulence models on the coarse and fine grids.

also predict other peaks at higher frequencies but these are not present in the experiment. Only the DES with halved C_{DES} coefficient did not predict these. Furthermore, the slope on the high frequencies of the spectra of the lift and drag coefficient higher frequencies is over-predicted, particularly in the case of the DDES-SALSA. This model also predicted the highest peaks at higher frequencies. The use of a lowered C_{DES} resulted better results. A more refined grid in the wake area allowed for a better slope as well, as shown by the use of the medium grid with the DES model, or the use of the NTS grid which is more refined there.

6.3.2 Flow and Probe Comparison

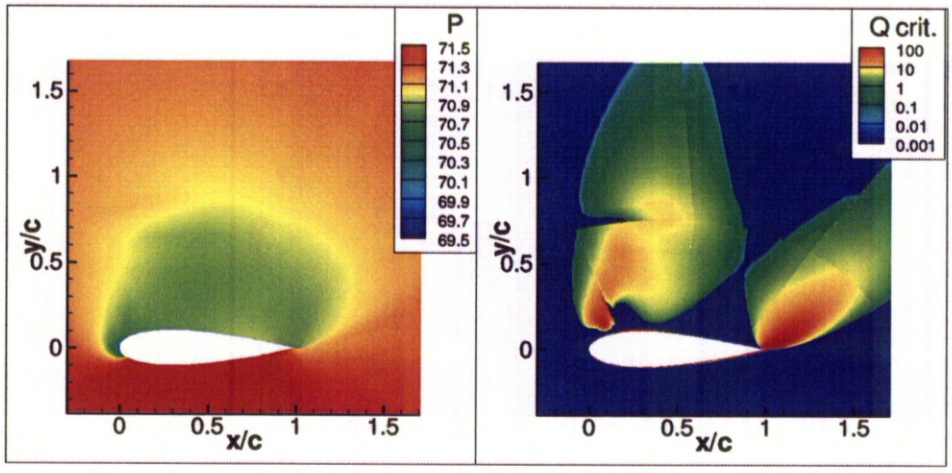

(a) SA

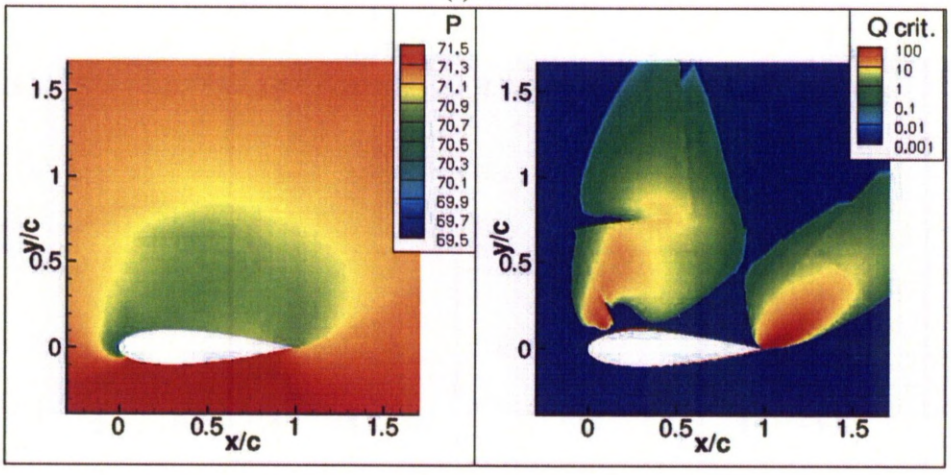

(b) SALSA

Figure 6.13: Instantaneous Q-criterion and pressure on the mid-span plane with both SA[40] and SALSA[99] turbulence models. $\alpha = 60_{inc}{}^{\circ}$, $M_{\infty} = 0.10$ and $Re = 2.7 \times 10^5$.

Instantaneous flow visualisation in the mid-plane of the domain, for computations that resulted in a steady flow are shown in Figure 6.13 and instantaneous isosurfaces of the Q-criterion obtained by the unsteady calculations as well as pressure distributions at slices perpendicular to the wing are shown in Figures 6.14.

A comparison of the mean flow for the various calculations shows that, while the mean flow structure is the same for every calculation, the leading edge vortex tends to be bigger in size and its centre moves further back when the calculation goes steady. A comparison of the mean flows streamlines and pressures is shown in Figure 6.6.

The effect of DES can also be seen when comparing the mean turbulent Reynolds number Re_T in slices perpendicular to the wing as shown in Figure 6.15. While the maximum of Re_T is almost 20000 in the steady predictions, the energy of the main vortices is not included in the unsteady predictions which leads to lower Re_T between 220 and 660, the lowest value appearing for the DES with a halved C_{DES} coefficient. This simulation is also the one that predicted stronger structures in the flow, that were filtered by the other models. These structures are not simply modelled, and when added to the turbulent energy the level of Re_T lowered.

The PSD of the pressure of the 4 probes selected earlier in Figure 6.1 is shown in Figures 6.16 and 6.17. The probes output in the DES calculation was damaged, therefore it does not appear in this comparison. The probes behave fairly similarly with every turbulence model. The first peak is dominant when the flow is driven by one vortex at the leading and one at trailing edge of the wing. The second peak becomes more and more important as the leading vortex alternates between the leading and trailing edge vortices. Depending on the turbulence model, some peaks also appear at higher frequencies. These models are also the ones showing peaks at high frequencies in the lift and drag coefficients spectra.

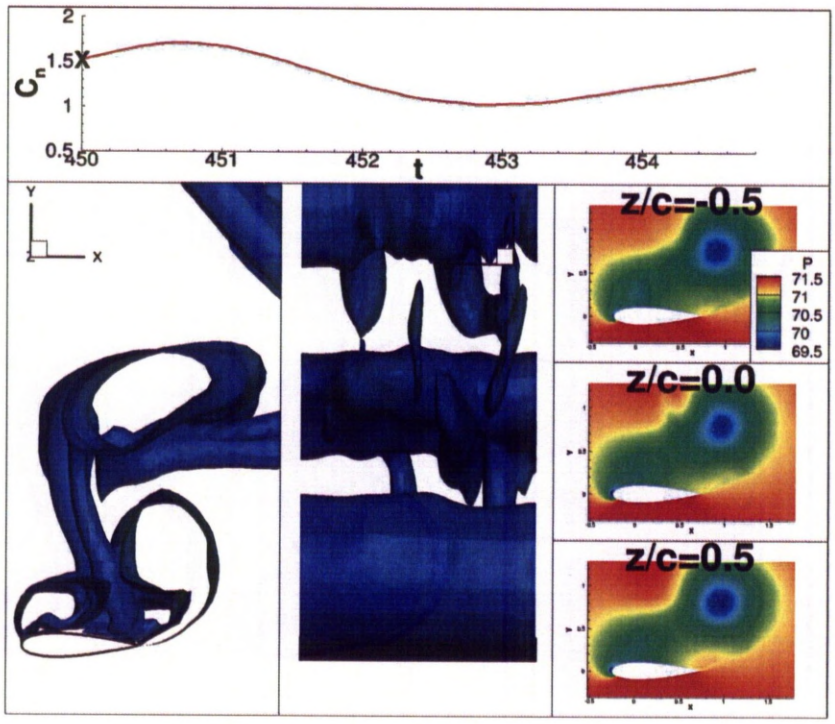

(a) DES

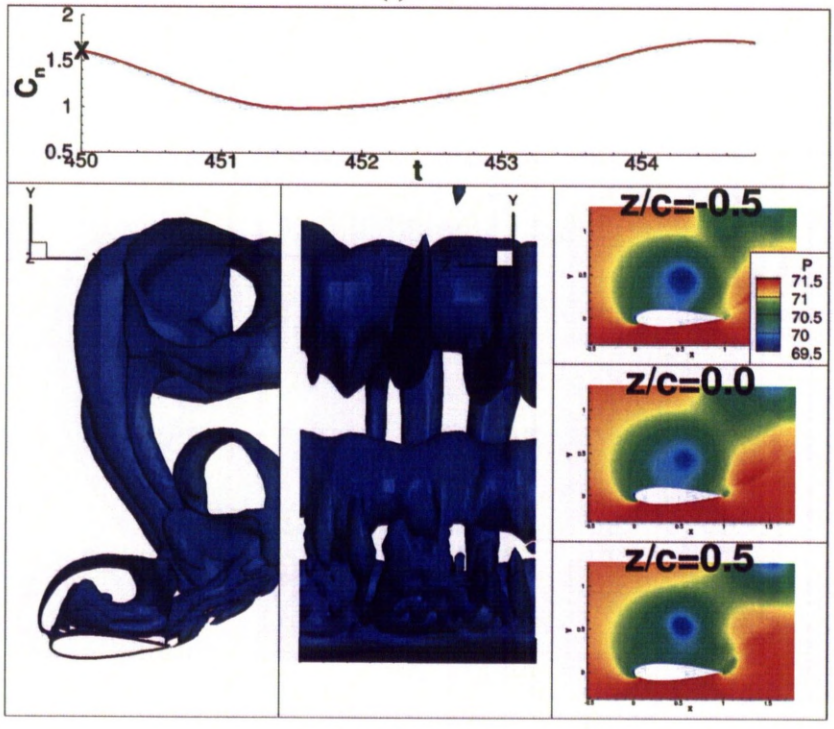

(b) DES, NTS grid

Figure 6.14: Comparison of instantaneous Q-criterion isosurfaces at 0.125 and pressure at mid-span. All flow visualisations are obtained at $t = 450$. $\alpha_{inc} = 60^{o}$, $M_{\infty} = 0.10$ and $Re = 2.7 \times 10^{5}$. Continued.

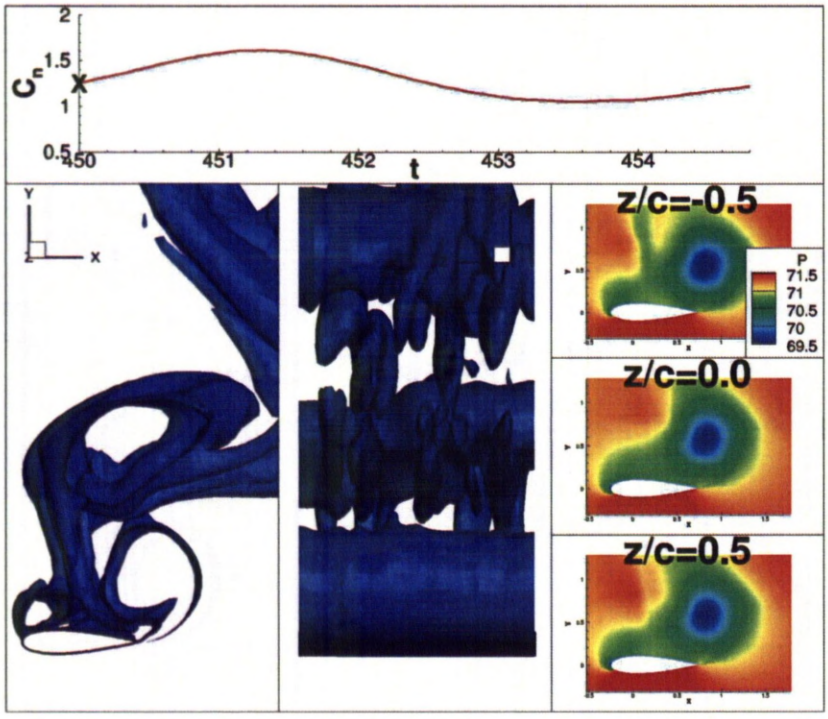

(c) DES SALSA

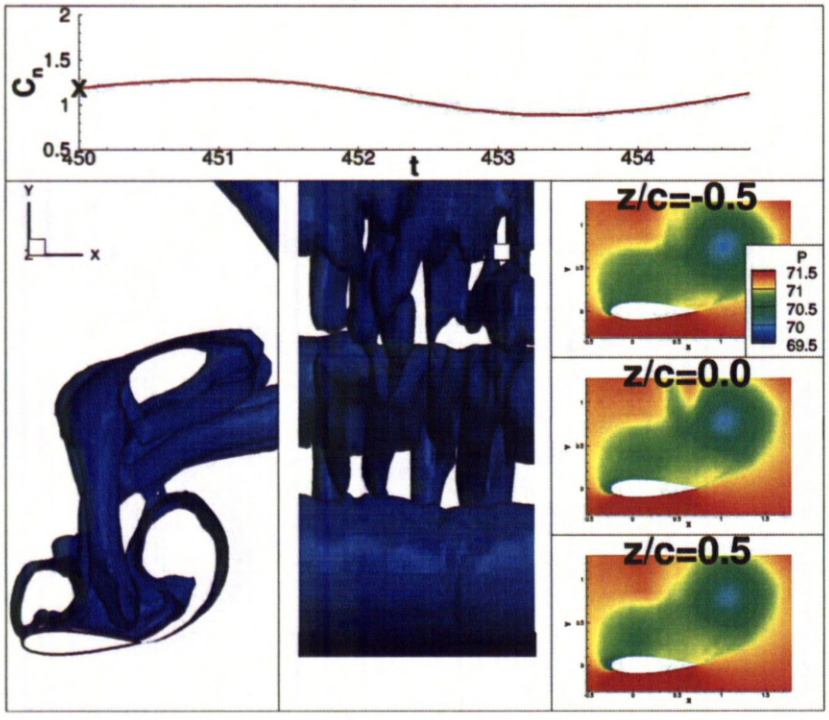

(d) DES with halved C_{DES}

Figure 6.14: Comparison of instantaneous Q-criterion isosurfaces at 0.125 and pressure at mid-span. All flow visualisations are obtained at $t = 450$. $\alpha_{inc} = 60^{o}$, $M_{\infty} = 0.10$ and $Re = 2.7 \times 10^{5}$. Continued.

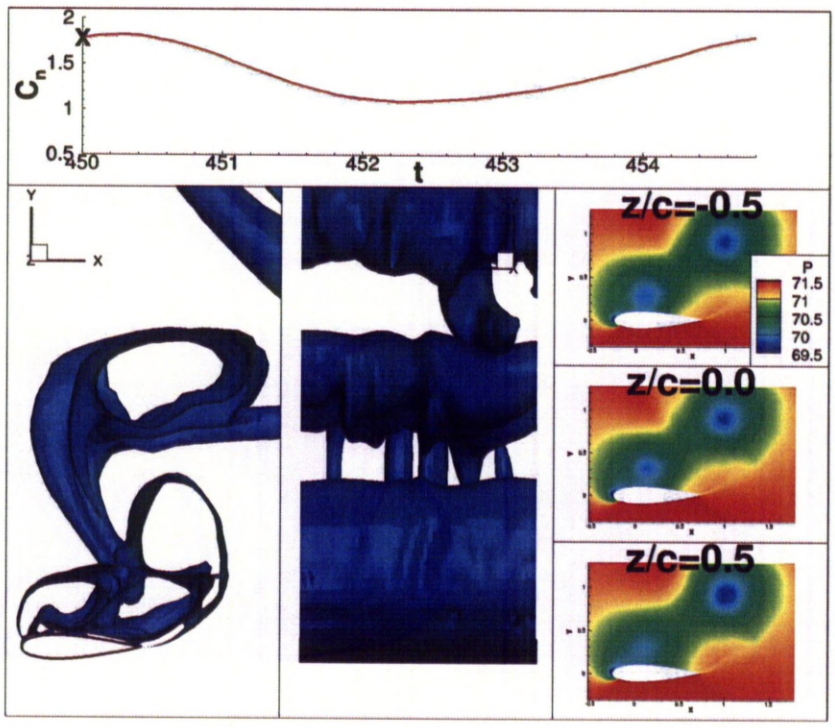

(e) DDES

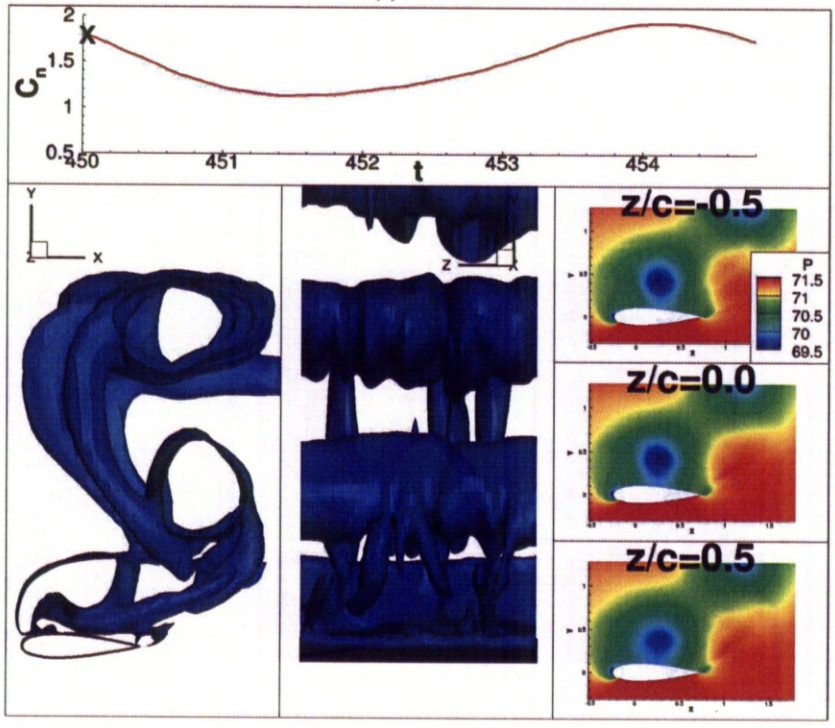

(f) DDES SALSA

Figure 6.14: Comparison of instantaneous Q-criterion isosurfaces at 0.125 and pressure at mid-span. All flow visualisations are obtained at $t = 450$. $\alpha_{inc} = 60^{o}$, $M_{\infty} = 0.10$ and $Re = 2.7 \times 10^{5}$. Concluded.

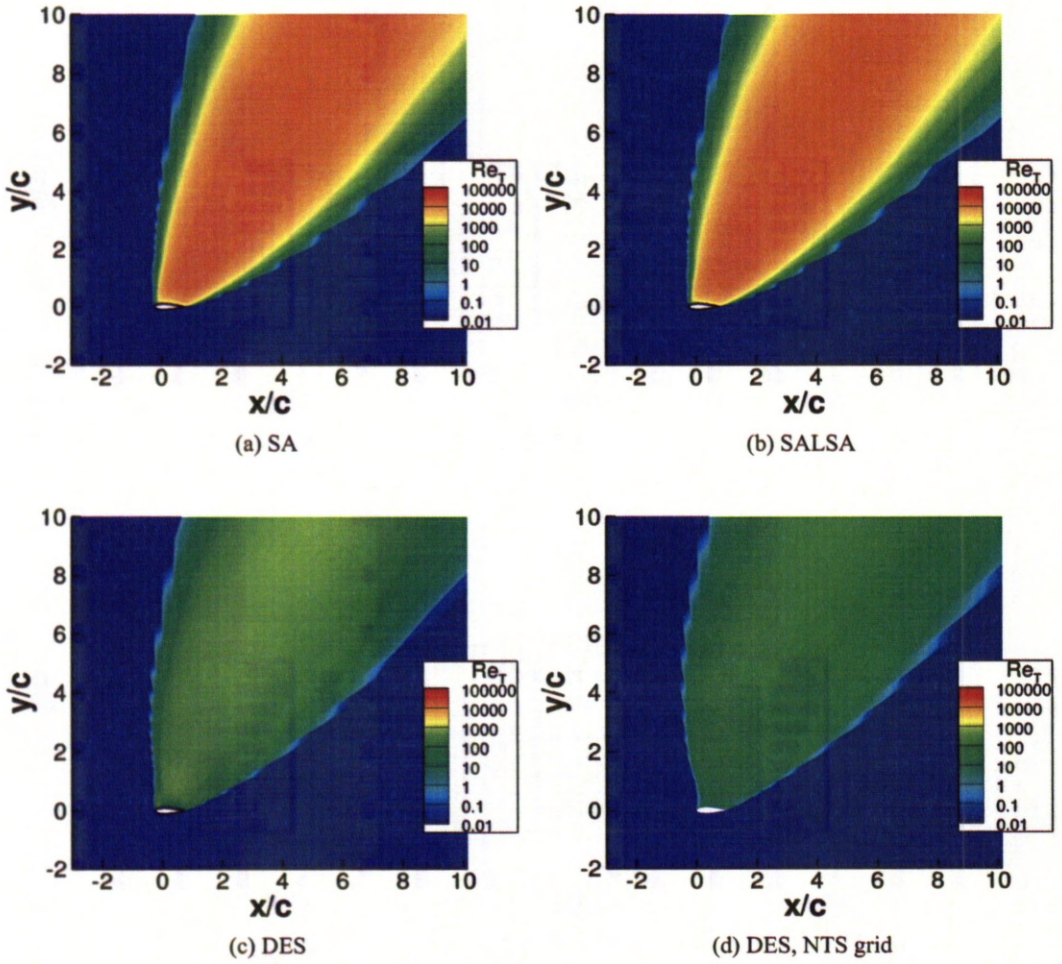

(a) SA (b) SALSA

(c) DES (d) DES, NTS grid

Figure 6.15: Comparison of the time-averaged turbulent Reynolds number on the mid-span plane as obtained with various turbulence models. $\alpha_{inc} = 60^{o}$, $M_{\infty} = 0.10$ and $Re = 2.7 \times 10^{5}$. Continued.

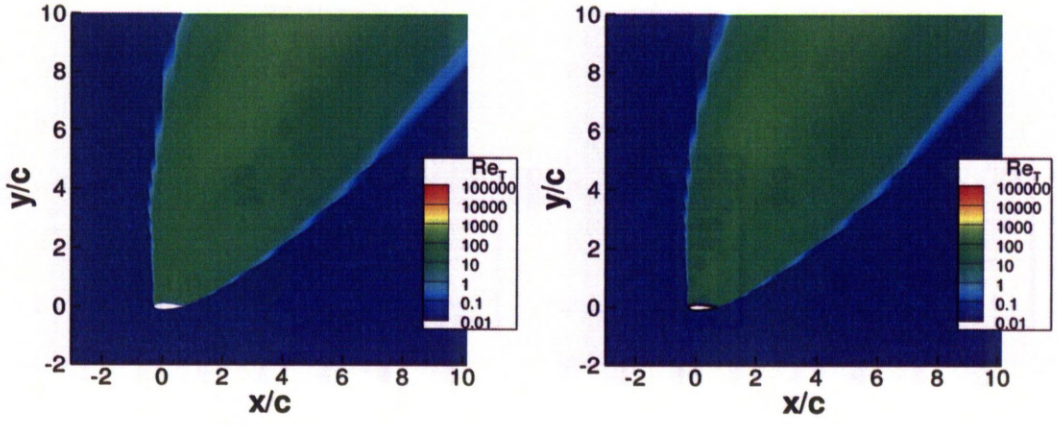

(e) DES SALSA (f) DES half C_{DES}

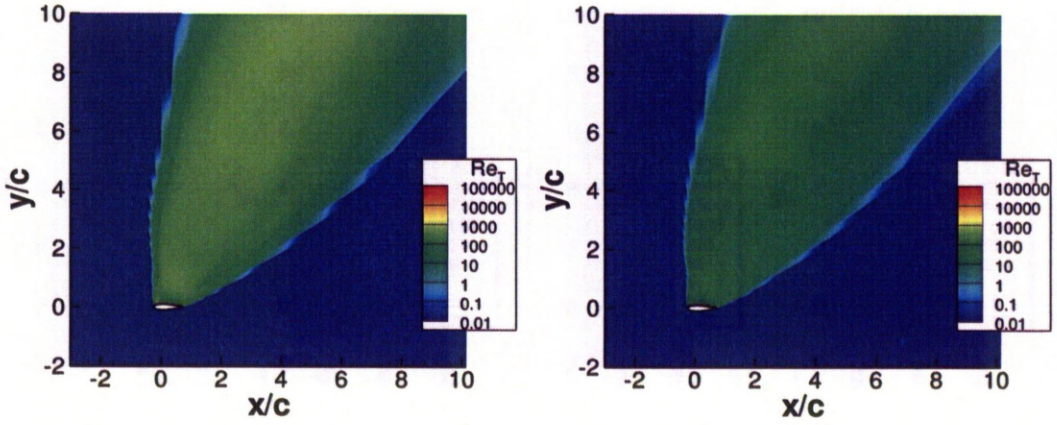

(g) DDES (h) DDES SALSA

Figure 6.15: Comparison of the time-averaged turbulent Reynolds number on the mid-span plane as obtained with various turbulence models. $\alpha_{inc} = 60^{o}$, $M_{\infty} = 0.10$ and $Re = 2.7 \times 10^{5}$. Concluded.

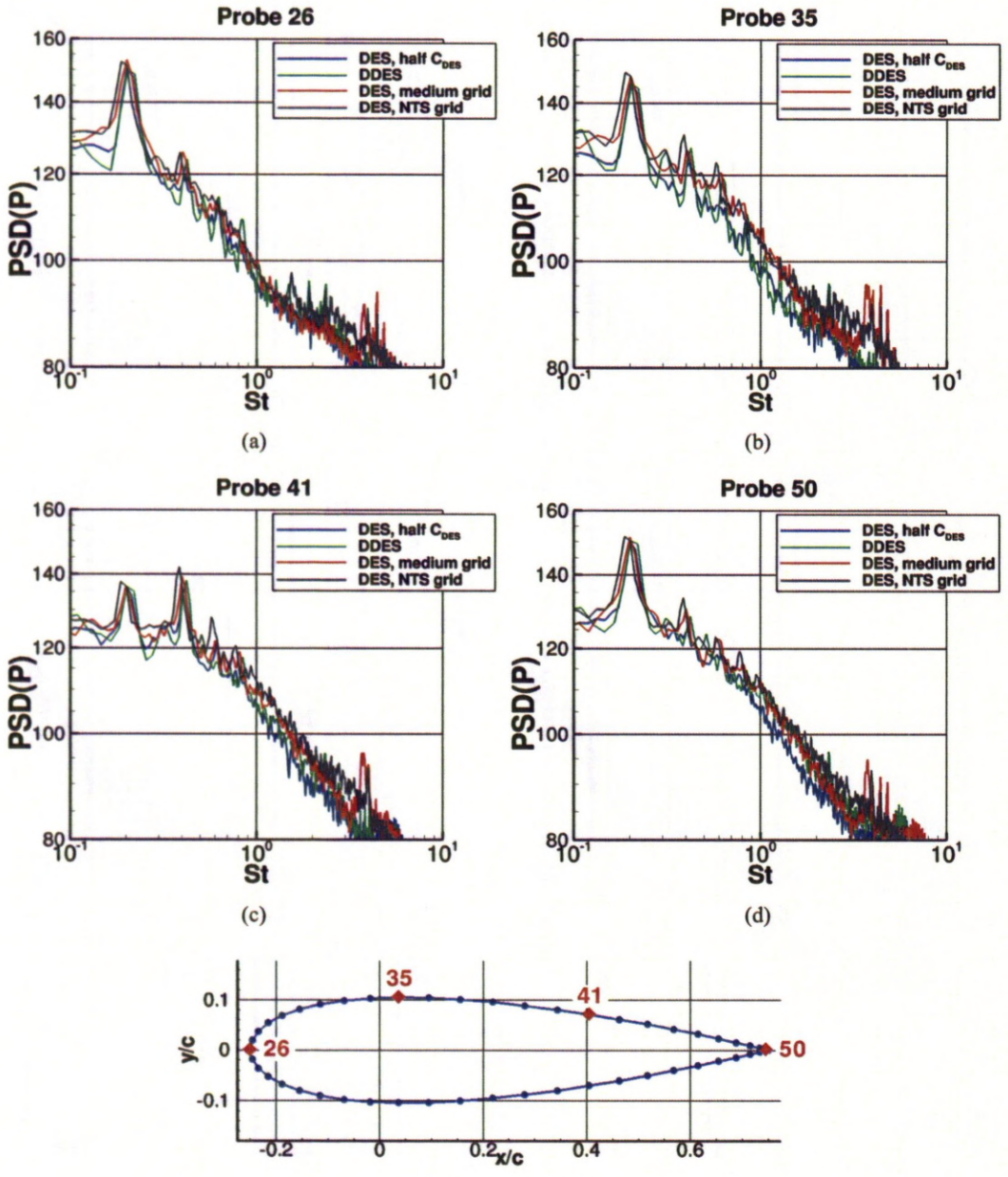

Figure 6.16: Comparison of the Pressure PSD on the aerofoil surface at various probe positions. SA-based models. Continued.

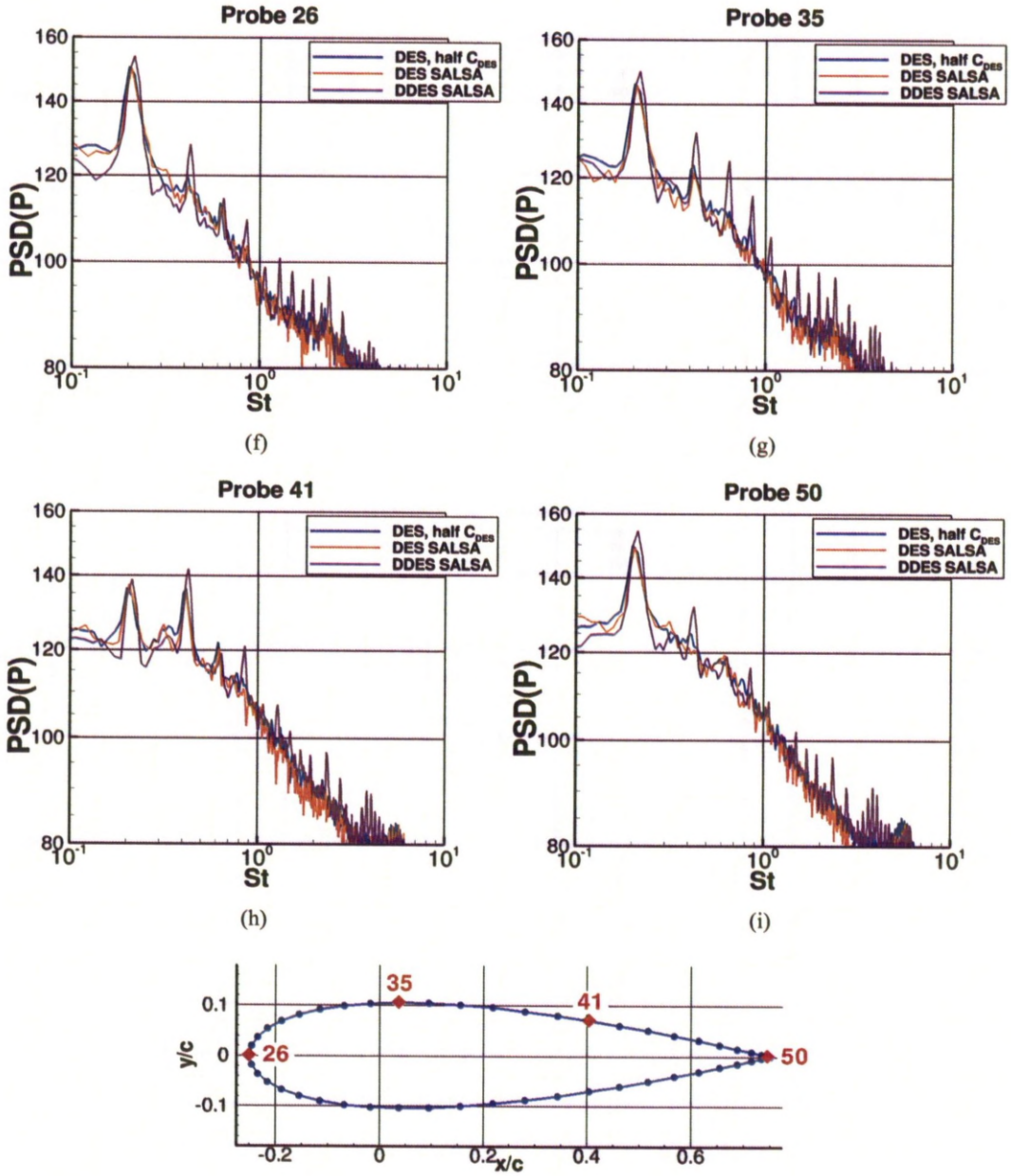

Figure 6.16: Comparison of the Pressure PSD on the aerofoil surface at various probe positions. SALSA-based models. Concluded.

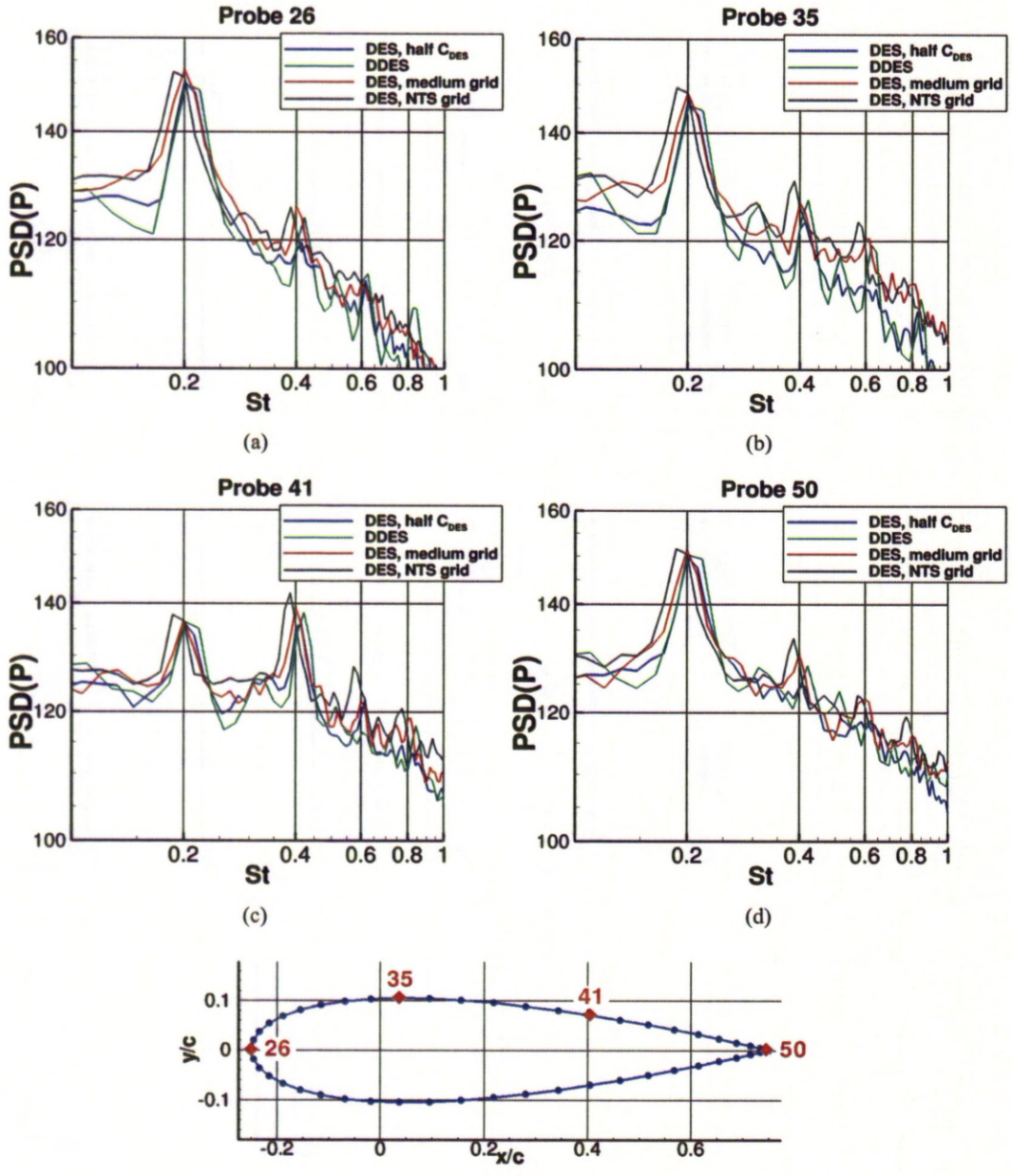

Figure 6.17: Comparison of the Pressure PSD on the aerofoil surface at various probe positions. SA-based models. Continued.

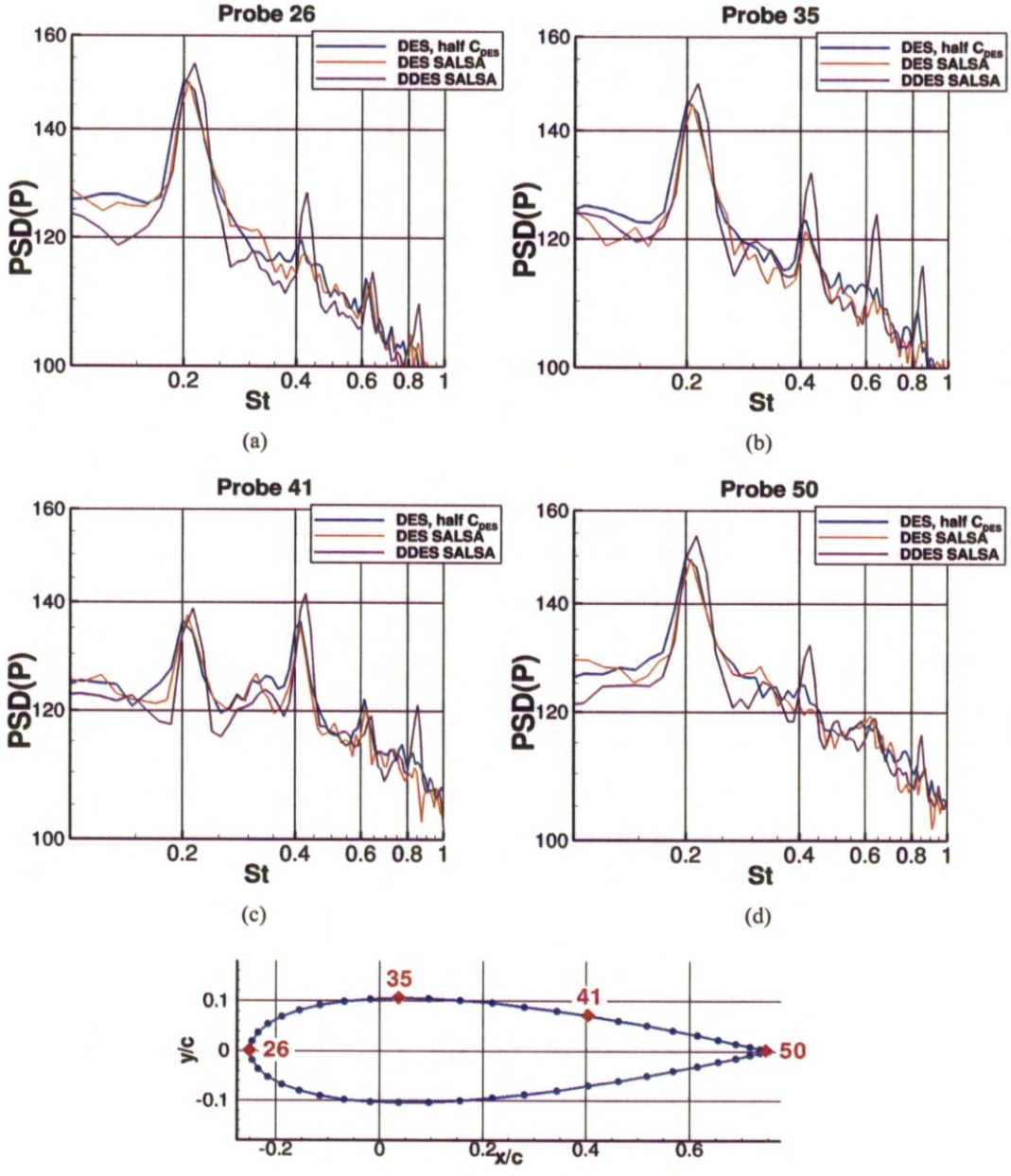

(e) Probe locations

Figure 6.18: Comparison of the Pressure PSD on the aerofoil surface at various probe positions. SALSA-based models. Concluded.

Chapter 7

Results and Discussion — Hovering Rotors

In this chapter, results obtained for rigid and elastic hovering rotors are presented and discussed. Firstly, the HART-II rotor is computed on grids of various densities to assess the grid convergence before being used to demonstrate the mesh deformation method. This is followed by an aeroelastic simulation of the UH-60A rotor. Hovering rotors are computed as steady-state, single-blade cases, allowing for shorter computations.

7.1 HART-II Rotor in Hover

7.1.1 Mesh Convergence Study

The first test case concerns the HART-II rotor in hover. Due to the lack of experimental data, the tip Mach number as well as the Reynolds number were chosen close to the HART-II experiment[49] tip Mach number of $M_{tip} = 0.641$ and tip Reynolds number of $Re_{tip} = 2.659 \times 10^6$. Furthermore, a high loading case was considered, leading to a collective at $\theta_0 = 12.5$ degrees. The coning angle was set at $\beta_0 = 2.2$ degrees.

Table 7.1: Integrated loads for the HART-II rotor as obtained for the grid convergence study.

Grid size	$C_T \times 10^2$	$C_{Q,P} \times 10^3$	$C_{Q,v} \times 10^5$	FM
3.3M	2.057	2.993	4.872	0.485
5.9M	2.095	2.769	4.973	0.538
11.2M	2.102	2.615	5.066	0.564
14.9M	2.116	2.567	5.060	0.588

Four grids were used to assess the grid convergence, ranging from 3.3 million nodes to 14.9 million nodes. Most of the grid refinement was localised under the rotor blade to improve the wake prediction. The spanwise distribution of the rotor integrated loads is shown in Table 7.1 for 4 grid densities. The predictions of the thrust coefficient showed a rapid convergence, while the torque coefficient increased with the grid size and the corresponding wake resolution. The figure of merit showed higher differences between the grids due to the sensitivity of this criterion to the torque coefficient. The torque coefficient changes were mainly driven by the pressure term, while the viscous term only showed limited changes. Furthermore, reaching convergence requested more iterations on the bigger grids, which increased even more the computational time. Overall, the differences between the grids appeared to decrease as the mesh density increased. For example, the 11.2M and 14.9M grids showed less difference than the 5.9M and 11.2M grids.

The evolution of the loads with the grid size is shown in Figure 7.1. While the normal loading reached convergence quickly, the sectional drag and moment would probably need even more refined grids. This is linked to the influence of the vortices in the wake. With more vortices predicted, their influence is also taken into account. The refinement of the grid in the spanwise direction also allowed for a better definition of the 3D-effects in the flow and their influence in the sectional drag and moments.

7.1.2 Mesh Deformation Method Assessment

It was also decided to use the hovering HART-II test case to demonstrate the efficiency of the mesh deformation method. Thus three calculations were performed, increasing the blade bending deformation: the first calculation used the undeformed blade, while the second and third ones computed a blade deformed according to the second flapping mode. The amplitudes of the deformation were set at about

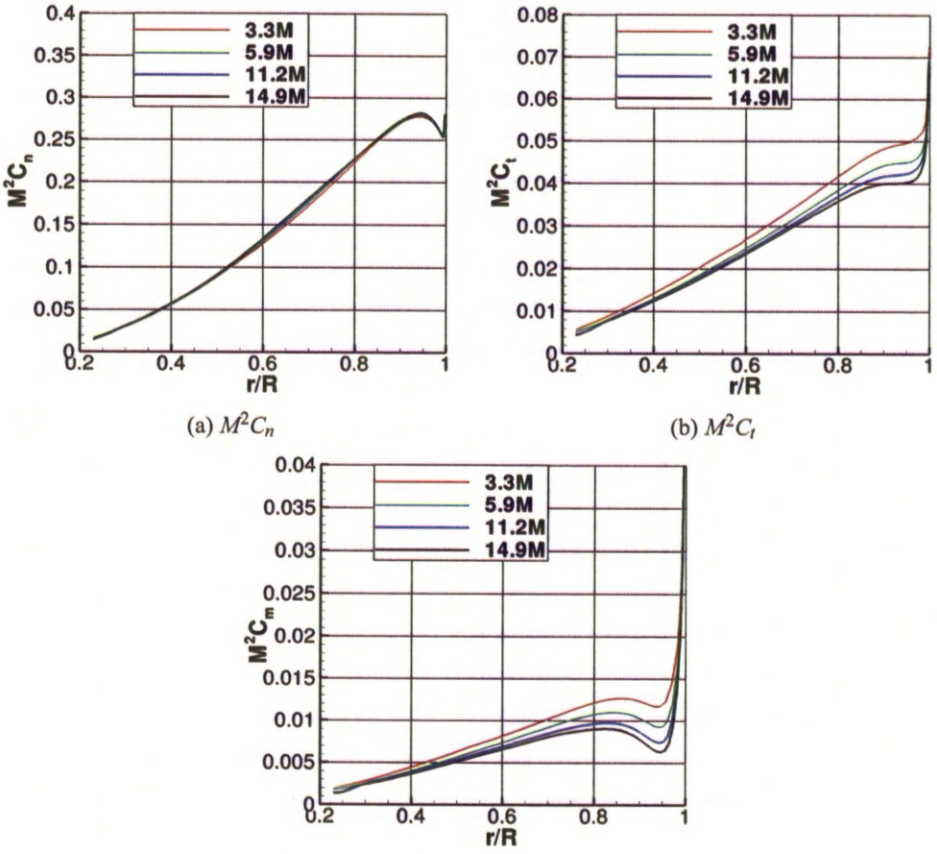

(a) M^2C_n (b) M^2C_t

(c) M^2C_m

Figure 7.1: Mach-scaled normal force (M^2C_n), tangential force (M^2C_t) and moment (M^2C_m) coefficients convergence along the HART-II blade depending on the grid size.

$0.3c$ and $0.6c$ at the tip respectively (called half-deformed and deformed blades respectively). Two collective values were tested: $\theta_0 = 8$ degrees and $\theta_0 = 12.5$ degrees. The grid quality for the strongest deformation at three sections of the blade (root, middle and tip) is shown in Figure 7.2. The cell volume changes were kept out of the C-part of the mesh (the mesh topologies were discussed in Chapter 3), and the results show that the cell skewness was kept close to the original.

A collective of $\theta_0 = 8$ degrees was first tested to check the mesh deformation method. The surface pressure coefficients on the deformed blade C_P are shown in Fig. 7.3. The deformation resulted in a higher suction at the tip. After switching from an absolute frame of reference to a relative one, streamlines are generated on the blade surface to identify the flow topology. At the root of the blade, the effect of the root vortex appears to be similar for all cases and is concentrated close to the root with the

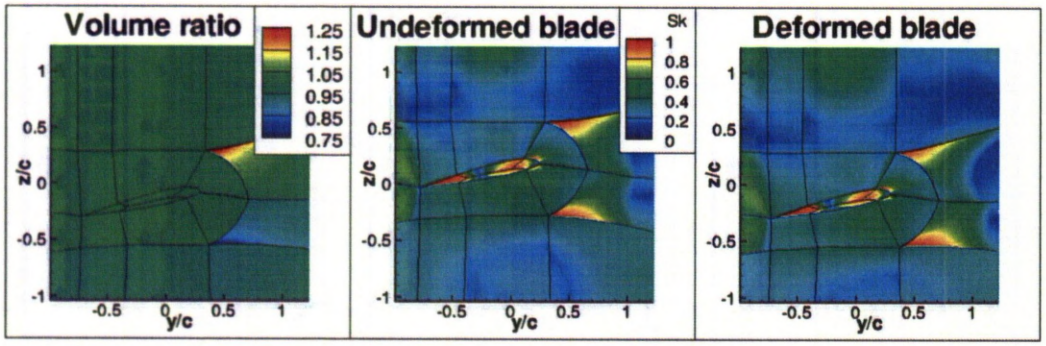

(a) Root of the blade

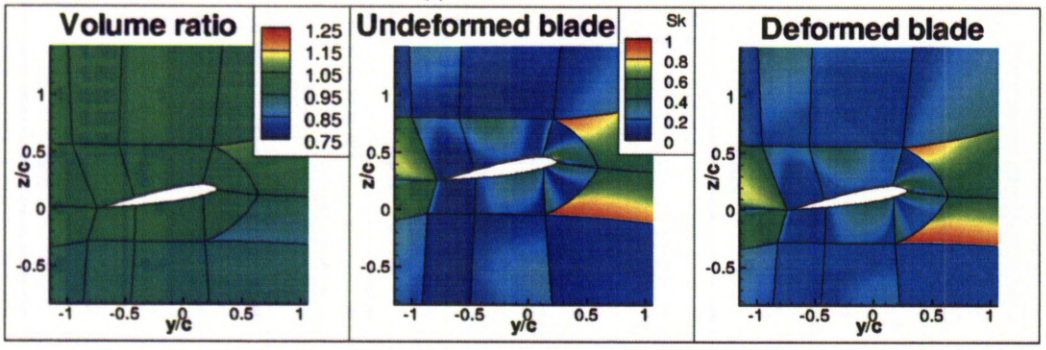

(b) Middle of the blade

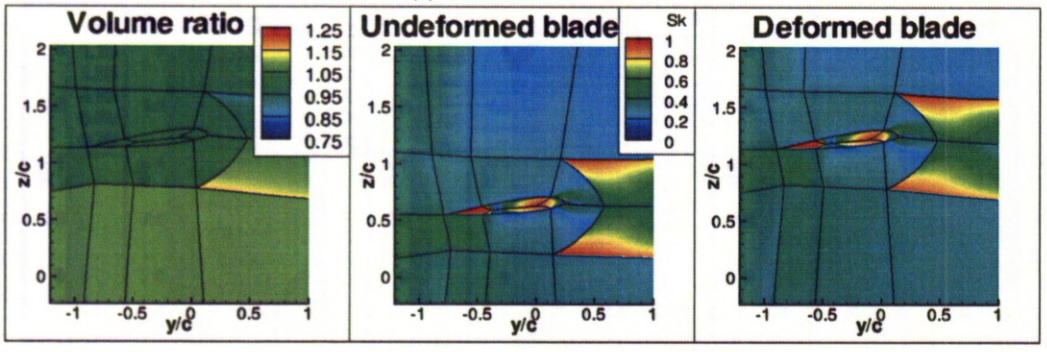

(c) Tip of the blade

Figure 7.2: HART-II rotor deformation following the second flapping mode with an amplitude of $0.6c$ at the tip. The first column shows the comparison of the cell volume ratio. The second and third columns show the skewness (Sk) of the undeformed and deformed grids. Three sections along the blade are shown: (a) root of the blade, (b) mid-span and (c) blade tip.

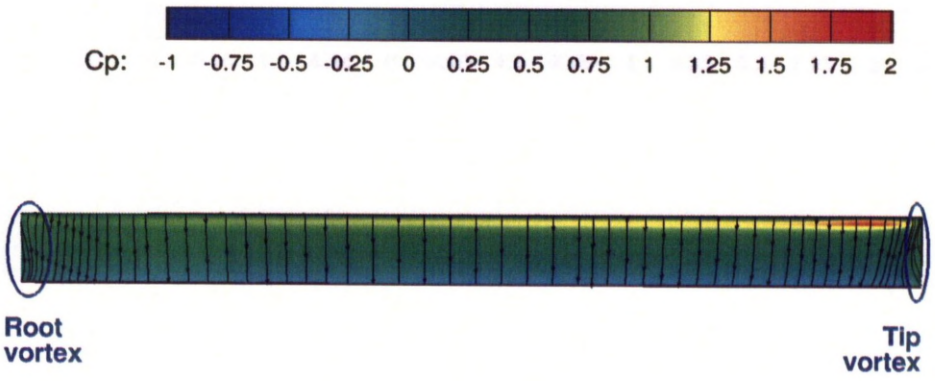

(a) Undeformed blade

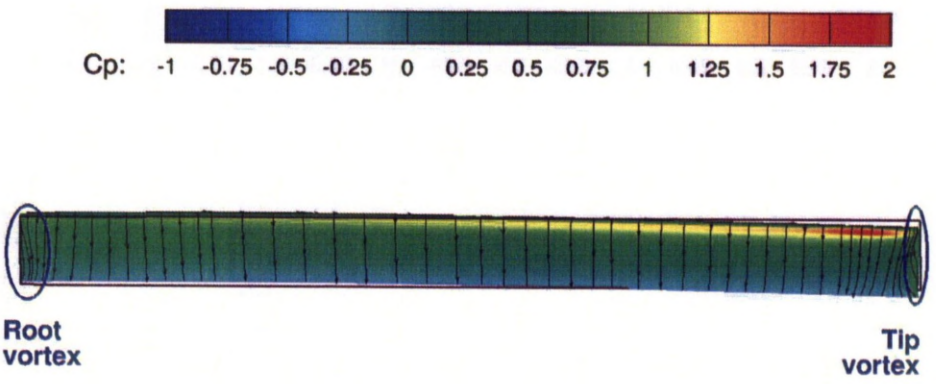

(b) Deformed blade, with the outline of the undeformed blade

Figure 7.3: Pressure coefficient distribution on the upper surface of the HART-II blade at $\theta_0 = 8$ degrees.

tip of the blade not affected. The flow was found to be attached on the whole blade.

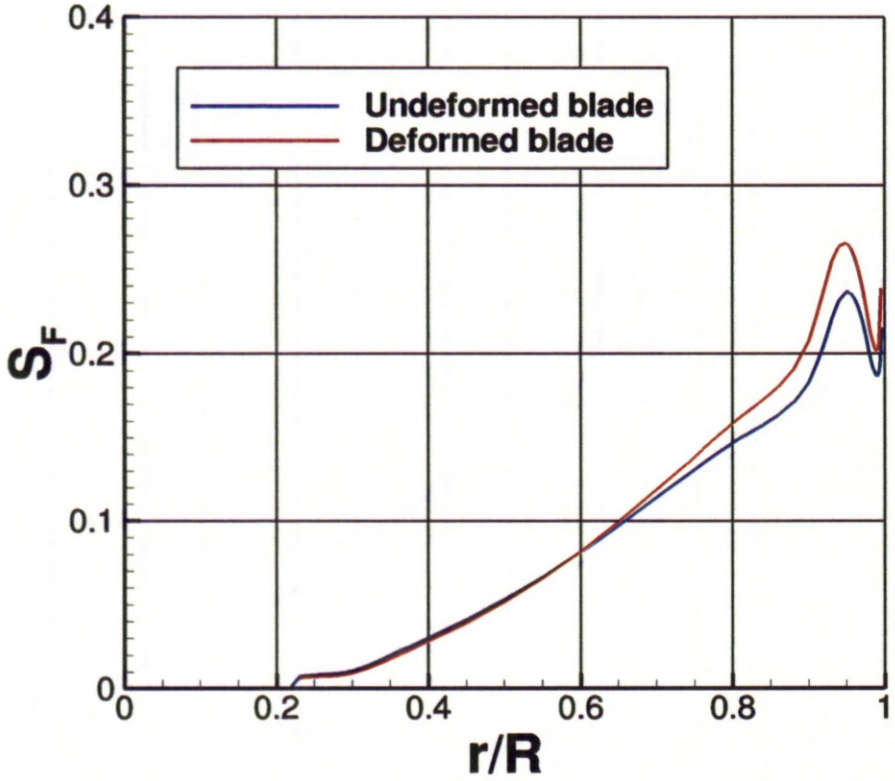

Figure 7.4: Comparison of the sectional force coefficient S_F along the blade span at $\theta_0 = 8$ degrees.

The increase in loading due to the higher suction at the tip is also visible in Fig. 7.4 which shows the distribution of the sectional force loading S_F along the span. Apart from the loading, the blade twist was extracted from the deformed mesh and plotted along with the geometric deflection of the blade on Figure 7.5. The results are consistent with the decrease of blade twist linked with the structural deformations. The effect of blade deformation is the opposite of what one would expect, when compared to the results by Yoon *et al.* [26]. They suggest a reduction in loading for the elastic blade with respect to the rigid one. However, the deformation applied here follows the second flapping mode which is coupled with a torsional mode resulting in less twist near the tip as shown by the geometric angle in Fig. 7.5, obtained by adding the blade twist to the collective and the torsional deformation from the second flapping mode deformation obtained through the structural analysis. Consequently, the loads were higher for the deformed blade. Overall, up to 3 degrees of difference in twist can be seen between

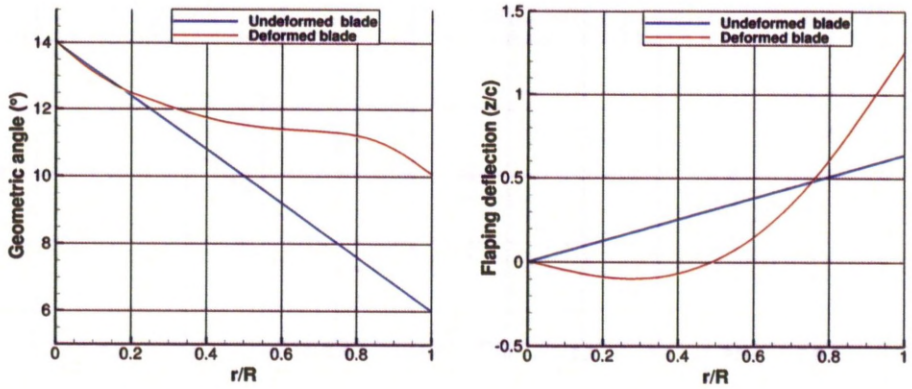

(a) Geometric angle (b) Flapping deflection

Figure 7.5: Deformation applied to the HART-II blade in hover at $\theta_0 = 8$ degrees.

the undeformed and the deformed blades with a maximum tip deflection.

The second case studied was at $\theta_0 = 12.5$ degrees. Fig. 7.6 shows, for the deformed blade, the pressure coefficient distribution C_P. Stalled conditions were selected so that the quality of the deformed mesh has a strong influence on the solution. In general, to resolve the velocity and pressure gradients encountered in flow recirculation regions , a higher quality mesh is needed. Again, an increase of the loading at the tip due to the deformation appears, represented by the increase of the size of the white surface. Looking at the streamlines, the flow is attached on most of the blade, however, a stall cell appears over the last 10% of the blade radius. At the tip of the blade, the footprint of the tip vortex can also be seen, and the stall cell is larger in the deformed blade case. The stall however is not caused by the deformation but the high collective of 12.5 degrees. On the other hand, the deformed blade has a more pronounced stall.

The above is shown in Fig. 7.7, where the span-wise sectional force coefficient S_F is computed along the blade. The tip is clearly stalled as suggested by the peak near 85%. Inboard of this peak, the effect of the deformation is more pronounced: the upward bending tip increases the blade loading over the undeformed value. Amongst the three configurations, the undeformed blade is less loaded near the tip and appears to have a slightly higher loading inboards as can be seen for r/R between 0.2 and 0.5. The blade deformation is shown in Figure 7.8. The equivalent twist suggests that the deformed blade maintains a relatively low twist between $r/R = 0.6$ and $r/R = 0.85$. This is related to the higher loading

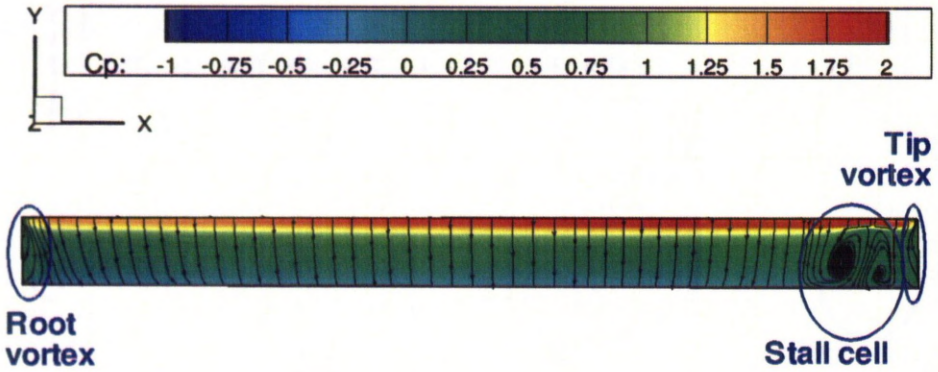

(a) Undeformed blade

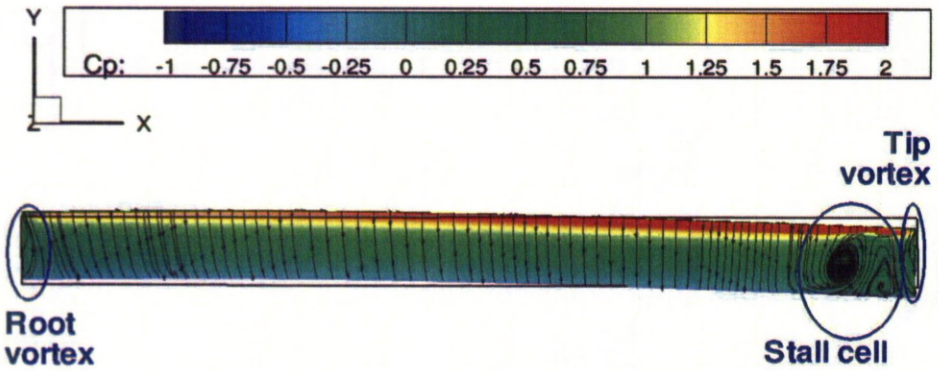

(b) Deformed blade, with the outline of the undeformed blade

Figure 7.6: Pressure coefficient distribution on the upper surface of the HART-II blade at $\theta_0 =$ 12.5 degrees.

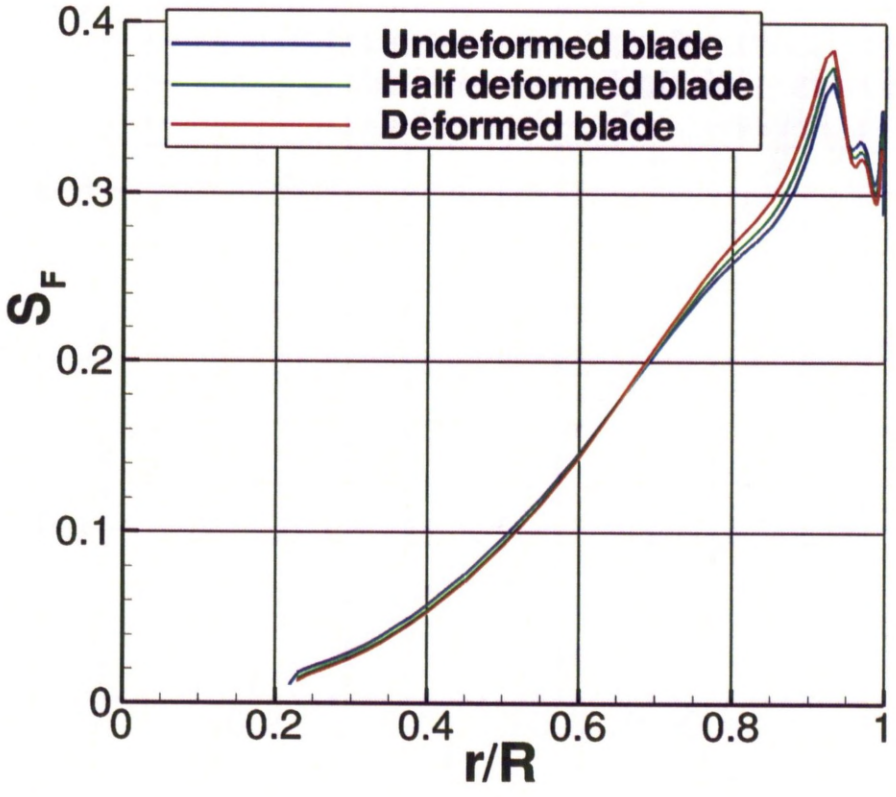

Figure 7.7: Comparison of the sectional force coefficient S_F along the blade span at $\theta_0 = 12.5$ degrees.

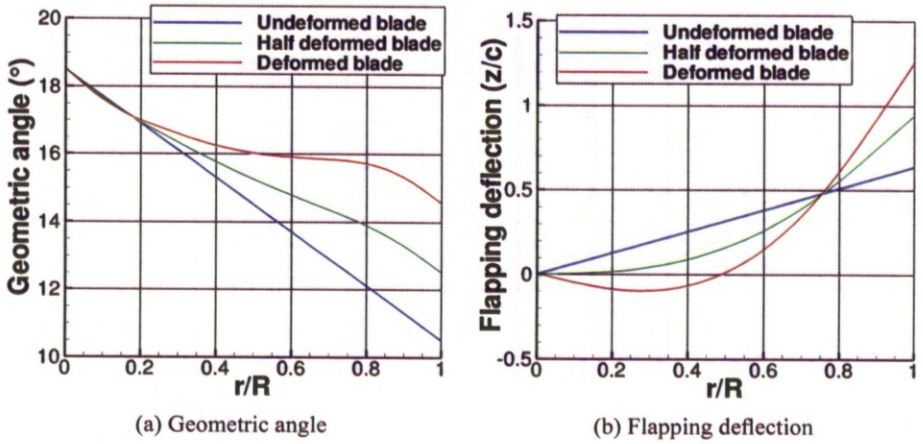

(a) Geometric angle

(b) Flapping deflection

Figure 7.8: Deformation applied to the HART-II blade in hover at $\theta_0 = 12.5$ degrees.

and more pronounced stall. In the other two cases, the twist is more linear, which offloads the tip further. However, the increased loading at the tip due to the blade deformation is less pronounced than for the attached flow case of Figure 7.3.

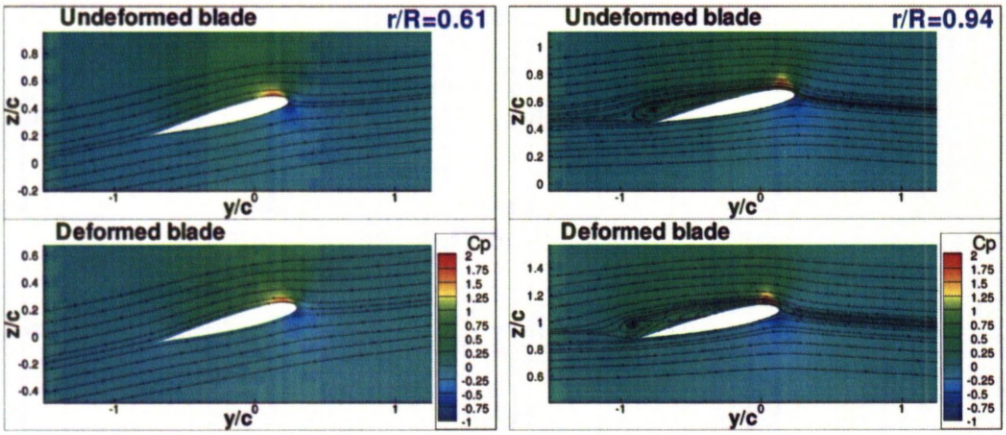

(a) $r/R = 0.61$ (b) $r/R = 0.94$

Figure 7.9: Comparison of the flow field at two blade sections at $r/R = 0.61$ and $r/R = 0.94$ for the undeformed and deformed blades.

Extracting the sectional flow field at two sections at $r/R = 0.64$ and $r/R = 0.94$ and converting the velocities from an absolute to a relative frame of reference as shown in Figure 7.9, one can see attached flow at $r/R = 0.64$ and separated flow at $r/R = 0.94$. The shape of the surface streamlines and the isobars suggest that the loading is similar for both cases. This is not the case further out where the stall is fully developed. The 3D pattern of the stall is evident from the surface streamlines and one can notice the larger extent of the stalled area on the deformed blade. Again, the same range of pressure contours is used and the deformed blade appears to be more loaded.

The pressure coefficient distribution at these two sections over the blade is extracted and compared in Figure 7.10. The difference between the cases on the section at $r/R = 0.61$ is minimal, with a slightly higher suction peak for the undeformed case, which suggests that the loading is similar for both cases. However, at $r/R = 0.94$, a mild shock forms on the upper surface, and moves forward compared to the original rigid blade. The flow behind the shock is stalled. The pressure appears to be lower for the deformed case. This difference in the pressure distribution is consistent with a change of incidence experienced by the airfoil.

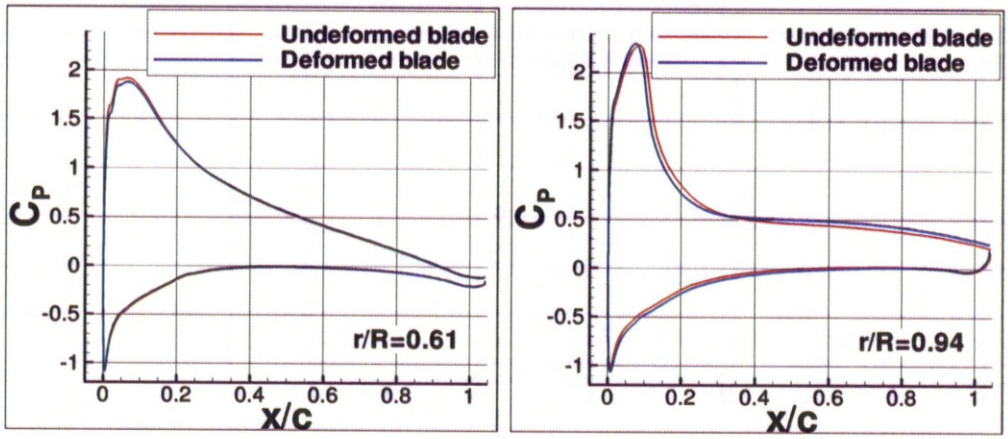

(a) $r/R = 0.61$ (b) $r/R = 0.94$

Figure 7.10: Comparison of surface pressure coefficient distributions at blade sections $r/R = 0.61$ and $r/R = 0.94$ for the deformed and undeformed blades.

The HART-II rotor was never tested in hover flight, therefore it is difficult to establish the stall boundary for the blade in hover flight. On the other hand, the obtained results appear reasonable and the performance of the mesh deformation method was very good with minimal overhead on the computational cost, only due to applying the grid deformation before starting the actual simulation.

7.2 Aeroelastic Computation of the UH-60A Rotor in Hover

A second test case to demonstrate and assess the aeroelastic coupling method used the UH-60A rotor. Wind-tunnel measurements were obtained by Lorber *et al.* [122,123] for a thrust coefficient of $C_T/\sigma = 0.170$ on a model rotor. This corresponds to $C_T = 0.01404$. The UH-60A rotor was Mach-scaled with a diameter 5.73 times smaller than the real rotor and some deformation was included in the blade to reflect the deformations undergone by the blade in flight. The exact geometry of the model blade along with its structural properties were not available, and there is some uncertainty about the blade twist[124]. Therefore, it was decided to compare the experimental results with a numerical simulation of the full scale rotor at the same thrust coefficient. The calculation was performed at tip Mach number of $M_{tip} = 0.63$, and Reynolds number based on the tip speed and chord length $Re_{tip} = 7.833 \times 10^6$. It was also decided to use a Reynolds number $Re_{tip} = 1.367 \times 10^6$ closer to the model experiments for

comparison, since viscous effects would influence the torque. This Reynolds number was assessed from the tip Mach number using ISA conditions. The experimental results contain integrated values including the thrust and torque moments and figure of merit, pressure taps along the blade span at 8 radial stations and the vortex position in the wake. The pressure taps, located at $r/R = 0.4$, 0.55, 0.675, 0.775, 0.865, 0.92, 0.945 and 0.965, were used for comparison.

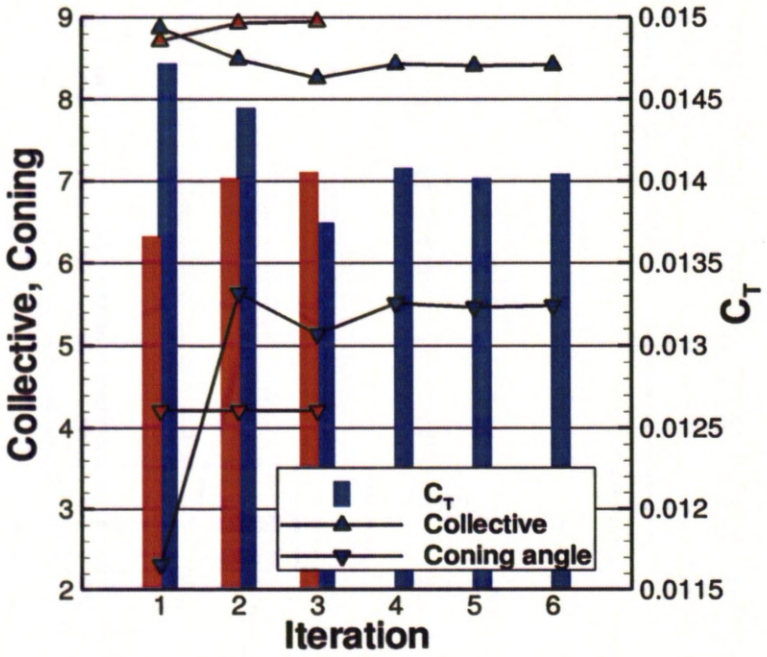

Figure 7.11: Trim convergence history for the UH-60A rigid (blue) and elastic (third iteration, red) blades in hover (viscous calculations at $Re_{tip} = 1.367 \times 10^6$, $M_{tip} = 0.63$).

The first calculation was done for an inviscid flow with a small grid (1.5 million nodes), while the following ones were on grids of 9 million nodes, with a viscous flow model and the $k-\omega$ BSL turbulence model of Menter[41]. The viscous calculation was first run for a rigid blade at each Reynolds number, and then structural deformations were introduced. Each calculation was trimmed to the experimental thrust coefficient. To obtain the coning angle from the trimmer, a lock number of 8 was used for both the full-scale and model blades, as used by Kim[125]. The structural model used corresponds to the real blade, due to the lack of properties for the model rotor. An example of rotor trimming is presented in Figure 7.11, where the trimming of the rigid and elastic (third aeroelastic coupling iteration) UH-60A blades with viscous flow model is presented. A converged trim state was obtained after seven iterations

for the rigid case and three for the elastic case, due to a better assessment of the initial collective angle based on the previous elastic iterations.

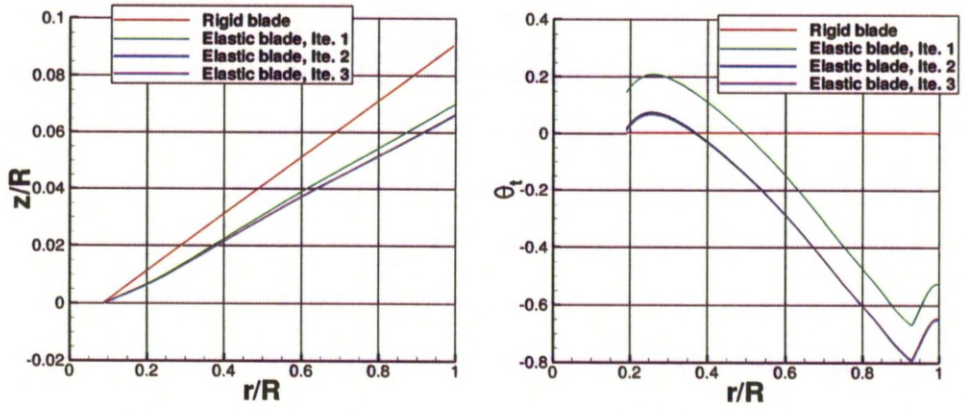

(a) Flapping deformation (b) Torsional deformation

Figure 7.12: UH-60A blade deformation obtained from viscous calculations at $C_T/\sigma = 0.170$ at $Re_{tip} = 1.367 \times 10^6$, taken at the quarter chord line.

The structural deformations were recomputed after each CFD simulation, and the convergence of the blade loads was quick: three elastic iterations allowed to get converged loads. The main difference between the inviscid and viscous results is located in the tip area, between $r/R = 0.70$ and $r/R = 1$. This is mainly due to the coarseness of the inviscid grid compared to the viscous: the flow features in the area near the sweep back were not well resolved by the inviscid case. The vertical loading of the elastic blade is slightly stronger in the main part of the blade than the loading of the rigid blade, while it is lower closer to the tip. The blade deformations at $Re_{tip} = 1.367 \times 10^6$ are shown in Figure 7.12. The loading is consistent with the torsion added to the blade due to the structural deformations, and the tip of the blade undergoes a torsion up to -0.8 degrees downwards. The trim state of each simulation is given in Table 7.2. The collective had to be increased by about 0.5 degrees for the deformed cases to compensate for the blade torsion. The coning was also higher for the rigid blade simulations. The relatively high coning angle for the rigid blade may be due to the simplified aeromechanics algorithm used in the trimmer. The obtained torque coefficients and figure of merit are compared to Lorber *et al.* [122,123]'s measurements in Figure 7.13 and show good agreement. The predicted torque coefficients for deformed and undeformed blades are very close at $C_T = 0.01404$ and these are mainly influenced by the Reynolds

Table 7.2: Trim state and integrated coefficients for the various UH-60A calculations.

Case	Reynolds number	θ_0	β_0	C_T	$C_{Q,P}$	C_Q	FM
Inviscid - Rigid blade	—	8.07	4.74	0.01374	0.001015	0.001015	0.7936
Viscous - Rigid blade	1.367×10^6	8.42	5.48	0.01403	0.001017	0.001083	0.7231
Viscous - Elastic blade	1.367×10^6	8.94	4.21	0.01406	0.001023	0.001157	0.7206
Viscous - Rigid blade	7.833×10^6	8.23	5.07	0.01402	0.000982	0.001070	0.7758
Viscous - Elastic blade	7.833×10^6	8.71	4.21	0.01403	0.000983	0.001072	0.7746

number. The structural deformation created some downward torsion at the tip of the blade, which had to be compensated by an increase of the collective. The influence of the structural deformation on the figure of merit is very limited (less than 3%). This low influence was already noticed by Schmitz *et al.* [124], but no more details about the differences between the rigid and elastic cases are detailed in this paper. However, at higher thrust, the effect of the blade deformation tends to be more important. even though not as important as viscosity. The required torque coefficient is then lower for the elastic blade, unlike what happened at lower thrust. These results are similar to solutions reported in the literature.

The sectional thrust C_t and the sectional torque coefficient C_q were extracted. Their distribution is compared with the experimental results of Lorber *et al.* [122, 123] in Figure 7.14. On the main part of the blade, the obtained results are very close to the experiment, however the peak at the tip is over predicted. This poor prediction may be due to the approximations on the blade shape, due to uncertainties on the blade shape, or the location of the preceeding blade tip vortex, which comes extremely close to the blade at about $r/R = 0.92$. The proximity of the vortex from preceeding blade with the following blade is clearly visible in Figure 7.15. It passes near the blade surface at about $r/R = 0.93$ and seems to have a strong influence on the air flow over the blade surface. However, the coning of the blade could not be compared to the experimental one, and neither is the position of the vortex from the preceeding blade relatively to the blade position. A study by Schmitz *et al.* [124] showed the effect of taking into account only the pressure at the tap locations and showed that the moment coefficient could be overestimated by more than 50% in the tip area. The influence of the Reynolds number was marginal, mainly at $r/R = 0.90$ where the sectional lift and moment coefficients were slightly increased.

The pressure coefficients along the blade are plotted against the chord position and are shown in

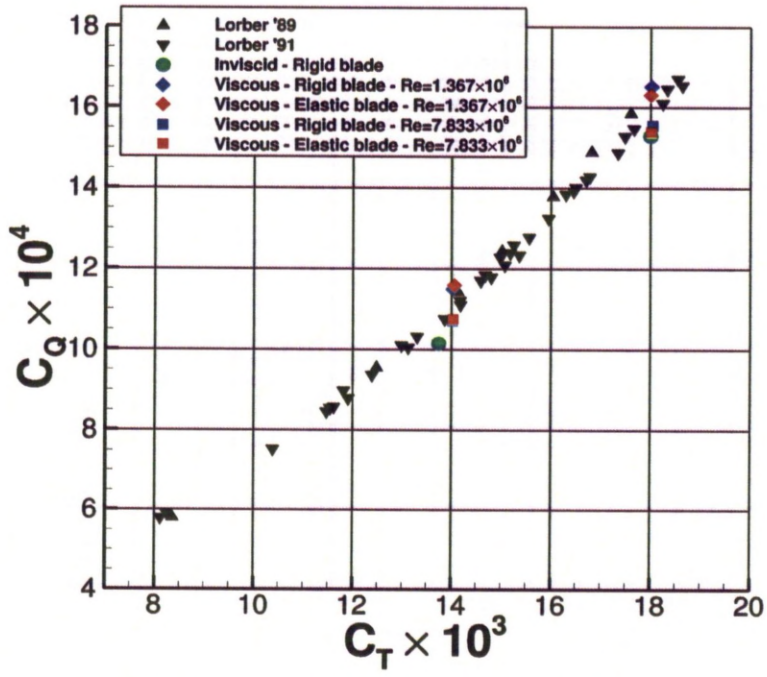

(a) Thrust coefficient C_T and torque coefficient C_Q

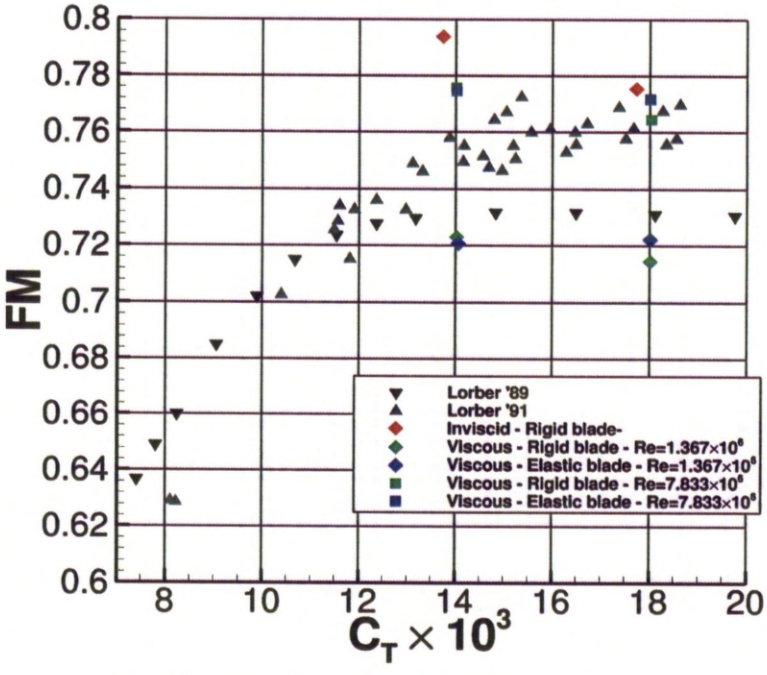

(b) Thrust coefficient C_T and figure of merit FM

Figure 7.13: Comparison of the thrust and torque coefficients (C_T and C_Q respectively), and the figure of merit (FM) with experimental measurements from Lorber *et al.* [122, 123].

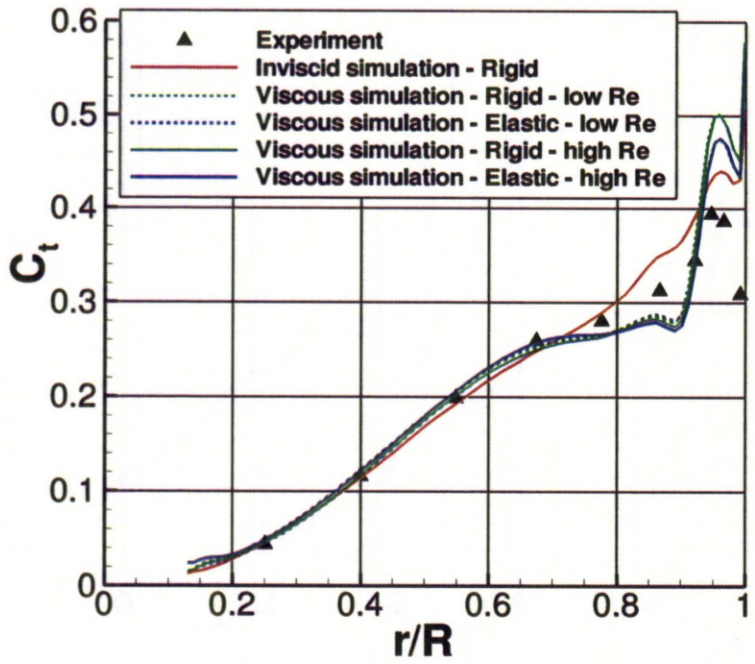

(a) Sectional thrust coefficient

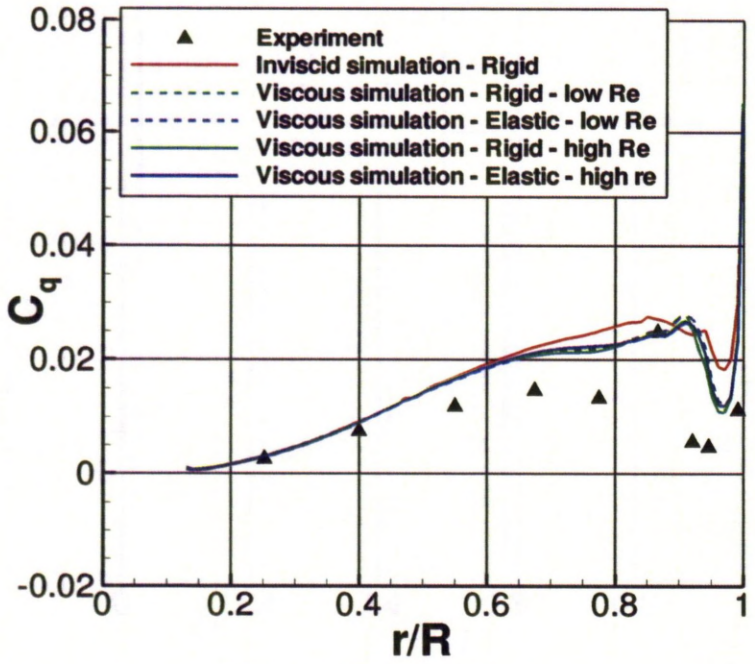

(b) Sectional moment coefficient

Figure 7.14: Comparison of the computed sectional thrust and moment coefficients (C_t and C_q respectively) along the rotor radius with the experiments from Lorber *et al.* [122,123].

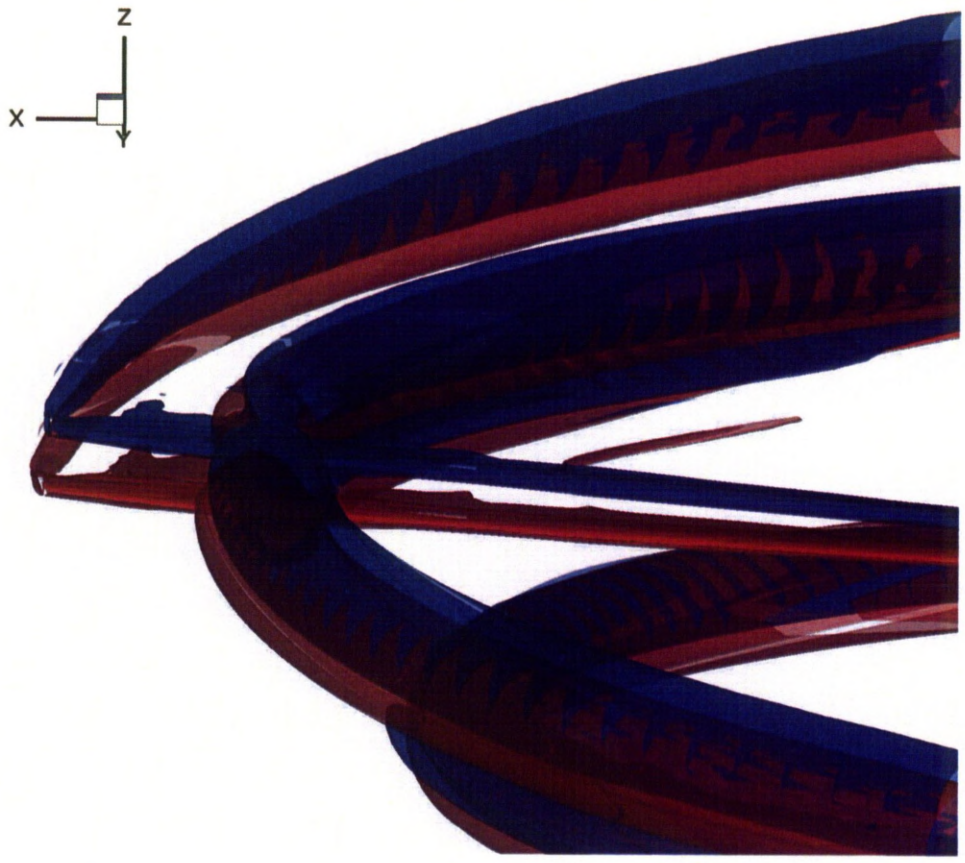

Figure 7.15: Wake visualisation in the tip area using the Q-criterion of hovering undeformed (blue) and deformed (red) UH-60A full-scale rotors at $C_T/\sigma = 0.170$.

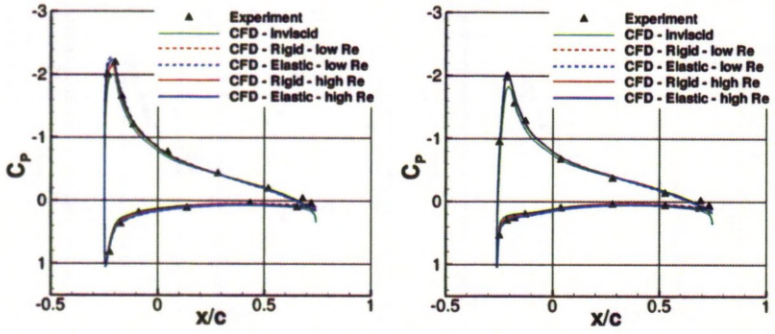

(a) $r/R = 0.40$ (b) $r/R = 0.55$

(c) $r/R = 0.675$ (d) $r/R = 0.775$

(e) $r/R = 0.865$ (f) $r/R = 0.92$

(g) $r/R = 0.945$ (h) $r/R = 0.965$

Figure 7.16: Comparison of the sectional pressure coefficients at various blade radial positions obtained with a rigid and elastic blade simulation with experimental measurements for hovering model (low Re) and full-scale (high Re) UH-60A rotors at $C_T/\sigma = 0.170$. Experiments by Lorber *et al.* [122]

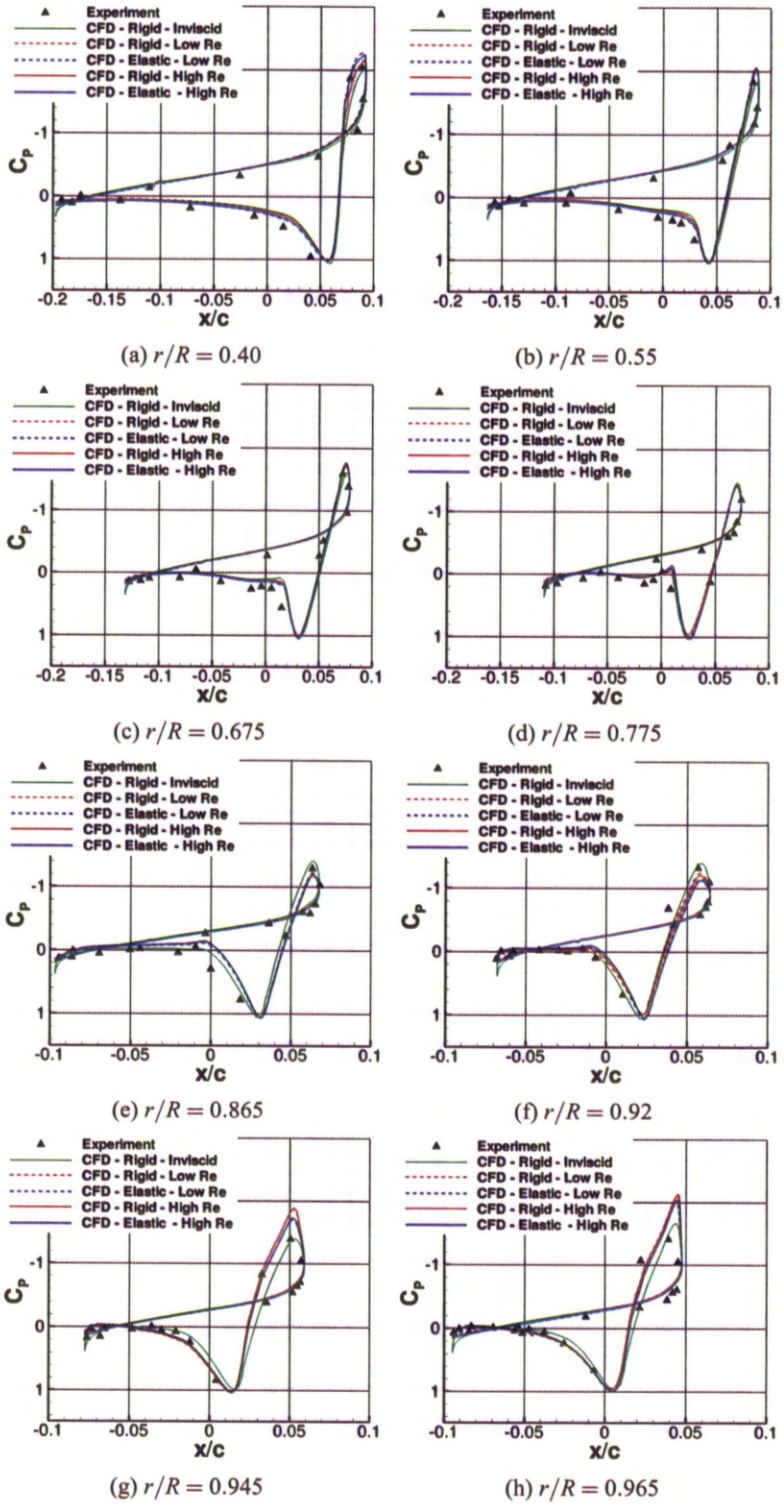

(a) $r/R = 0.40$ (b) $r/R = 0.55$

(c) $r/R = 0.675$ (d) $r/R = 0.775$

(e) $r/R = 0.865$ (f) $r/R = 0.92$

(g) $r/R = 0.945$ (h) $r/R = 0.965$

Figure 7.17: Comparison of the sectional pressure coefficients at various blade radial positions obtained with a rigid and elastic blade simulation with experimental measurements for hovering model (low Re) and full-scale (high Re) UH-60A rotors at $C_T/\sigma = 0.170$. The pressure coefficients are projected on the aerofoil thickness. Experiments by Lorber *et al.* [122]

Figure 7.16. The blade deformation increased the suction on the main part of the blade, but decreased it close to the tip, which is consistent with the torsional deformation undergone by the blade. The pressure coefficients from the simulations show good agreement with the experimental measurements up to the station at $r/R = 0.675$. The higher suction peak predicted on the elastic blade was closer to the experiment, particularly at $r/R = 0.40$. However, between $r/R = 0.775$ and $r/R = 0.92$, the suction peak was under predicted and the pressure side showed a lower C_P. This explains the lower load in this part of the blade on the thrust distribution of Figure 7.17. After $r/R = 0.945$, the suction on the upper surface is over predicted, explaining the higher predictions of the sectional thrust coefficient in the tip area in Figure 7.14a. These results could be due to a poor interpretation of the local twist of the original blade, or the position of the vortex from the preceeding blade, as explained previously. The predicted pressure coefficients show an equivalent angle of attack lower than the experimental predictions at the section $r/R = 0.865$ and higher at the sections $r/R = 0.945$ and $r/R = 0.965$. This is consistent with the vortex effect around $r/R = 0.92$ increasing the downwash at sections before $r/R = 0.92$ and decreasing it at sections after $r/R = 0.92$. The effect of the Reynolds number was limited on the pressure coefficients. Similar results for the chordwise pressure distribution were obtained by Wake and Baeder[17] and Schmitz *et al.* [124]. Schmitz *et al.* [124] also projected their pressure distribution along the aerofoil thickness, and better agreement was obtained, particularly for sections inboard of $r/R = 0.675$, probably due to a better interpretation of the local twist of the original blade.

When the pressure coefficients are projected along the thickness of the aerofoil, as shown in Figure 7.17, the differences between the simulation and experimental results appear clearer. This projection shows the effect of the pressure coefficient on the sectional torque of the rotor, and therefore the bigger the differences, the worse the prediction of the rotor torque. Due to the few measurement locations on the sections, some important features are not well captured, like the stagnation point. This lack of resolution can explain the important differences between the predicted and experimental sectional torque seen in Figure 7.14b.

The vortex core location in the wake of the rotor has also been measured and compared to experimental results in Figure 7.18. The effect of the Reynolds number on the vortex trajectory was

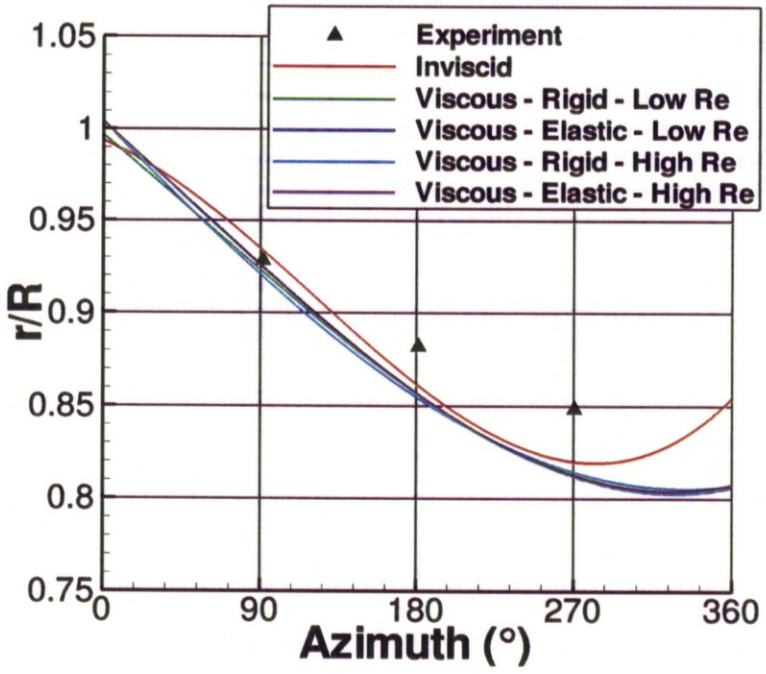

(a) Radial position

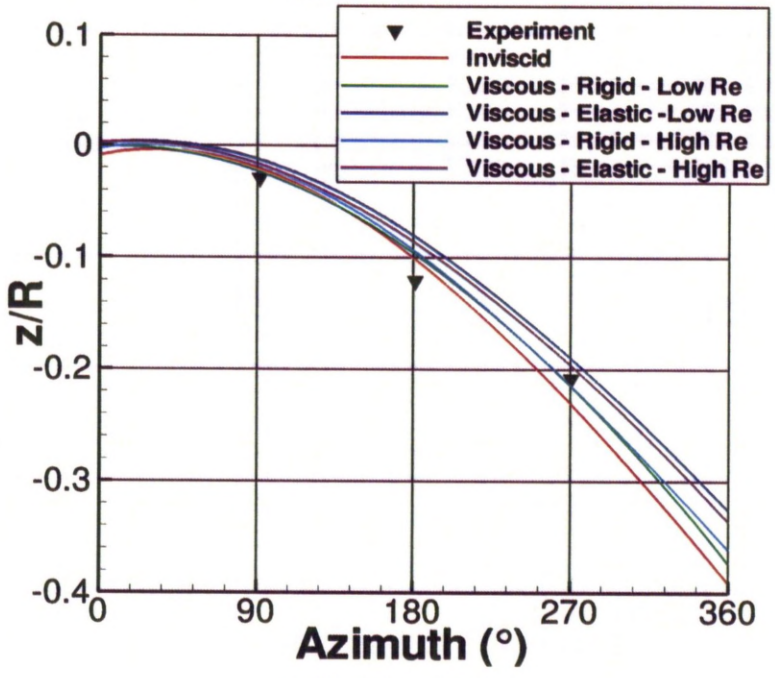

(b) Vertical position

Figure 7.18: Vortex radial and vertical location in the wake of hovering UH-60A model (low Re) and full-scale (high Re) rotors at $C_T/\sigma = 0.170$. Experiments by Lorber *et al.* [122]

marginal. The vortex vertical displacement is well predicted, while in the horizontal plane, the vortices tend to come slightly too fast inboard. Furthermore, after 270 degrees, the grid cells become too loose to accurately predict the location of the vortex cores and this explains the lack of agreement at the higher azimuth angles.

Overall, the flow predictions showed very good agreement with the experimental data on the main part of the blade, with some discrepancies with experiments near the tip. These are apparently due to uncertainties in the blade definition. The lack of structural data for the model blade or the unknown blade shape during the experiment did not allow for a further investigation of this problem. The mesh deformation and trimming methods were found to be robust and needed a minimal increase of CPU cost. For the rigid rotor, 135,000 steady iterations allowed to get a converged flow at a settled collective, and an additional 60,000 were required to trim the rotor to the correct thrust coefficient. A further 100,000 iterations allowed for a trimmed aeroelastic solution.

Chapter 8

Results and Discussion — Rotors in Forward Flight

Forward flight simulations were also carried out using moving meshes of the complete rotor as described in Chapter 3. A steady flow field is first computed around a static rotor and then, the blades are accelerated to their final speed within 90 degrees of azimuth. The ONERA 7A and 7AD rotors were first analysed using DES to evaluate its potential for rotorcraft flows, and this is combined with a study of the mesh deformation method using the ONERA 7A rotor. The UH-60A rotor in high-speed flight was subsequently used to demonstrate and validate the aeroelastic coupling method. The very demanding HART-II rotor case was finally used with DES and prescribed deformations.

8.1 7A/7AD Rotors in Forward Flight — DES Assessment

Encouraged by the DES results for the stalled aerofoil case, rotors in forward flight were then attempted. Due to its popularity in CFD works and the availability of experimental data from several wind tunnel campaigns, the ONERA 7A/7AD rotors, described in Section 3.3.3, were considered. Table 8.1 shows the selected test cases from the database of the HELISHAPE campaign[45]. For this complex mesh

topology, there was less flexibility to optimise the mesh for DES computations like for the NACA0021 cases, though care has been taken to refine the mesh near the blades while maintaining some of the mesh orthogonality at the rotor disk plane where the wake is expected to be concentrated.

Table 8.1: ONERA 7A and 7AD flight conditions and trimming for the various simulations. The angles are given in degrees.

Case	μ	M_∞	C_T	α_S	θ_0	θ_{1c}	θ_{1s}	β_0	β_{1c}	β_{1s}
Case 1	0.1673	0.1031	0.007	2.0	4.87	−2.2	3.1	2.13	0.11	0.32
Case 2	0.355	0.2180	0.0105	−5.0	8.57	1.89	7.56	2.12	0.12	0.51
Case 3	0.390	0.2399	0.005	11.0	14.0	−2.0	4.5	0.0	4.5	0.0

The computation was undertaken using 16.8 million nodes with good load balancing and due to CPU time limitations only three rotor revolutions were attempted using an azimuthal step of 0.25 degrees. This time is close to what is used for URANS computations though further refinement would lead to overwhelmingly expensive computations.

The results obtained from the URANS and the DES solutions are compared against experimental data[45] in Figure 8.1 for case 3 of Table 8.1. Three stations are shown corresponding to 0.7, 0.825 and 0.9 of the rotor radius. Inboards, the flow appears to be well-resolved by both DES and URANS solutions and the overall agreement for the Mach-scaled normal force coefficient is fair on the advancing side of the blade and the rear of the disk. Some differences exist on the retreating side and the DES solution fares somehow better in that region. This is especially true for the pitching moment coefficient. At the $r/R = 0.825$ station, the situation shows some of the DES benefits though these are mainly concentrated on the retreating side. For the selected test case, the experimental data show the presence of some blade-vortex-interaction near 100 degrees of azimuth. None of the employed models captured the BVI and this is apparently due to the lack of spanwise mesh resolution as well as the selected azimuthal step of 0.25 degrees. Interestingly, the dip of the normal force coefficient on the advancing side of the rotor is well-captured in terms of magnitude and phase by both models. This issue is revisited later on in the thesis for the HART-II rotor case. For the third available station ($r/R = 0.975$) the URANS and DES results are fairly close for the pitching moment and normal force coefficients. Again, it is interesting to see that regardless of some minor differences near the advancing side, both models follow the trend of

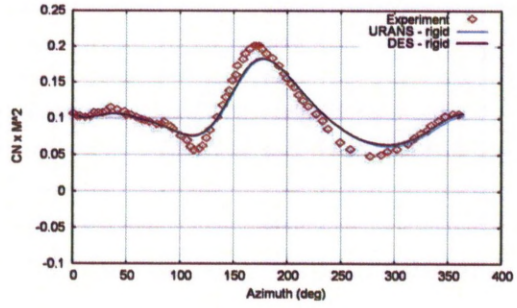

(a) M^2C_n, $r/R = 0.7$

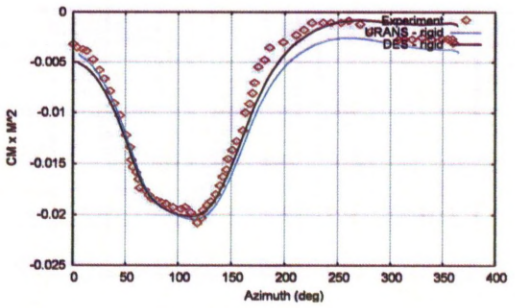

(b) M^2C_m, $r/R = 0.7$

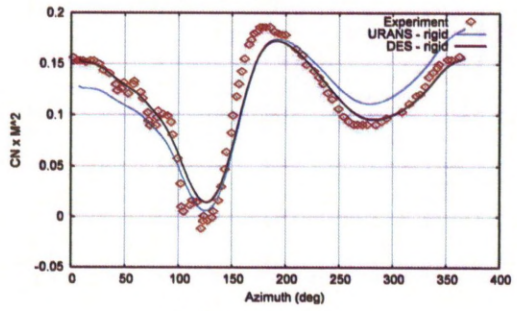

(c) M^2C_n, $r/R = 0.825$

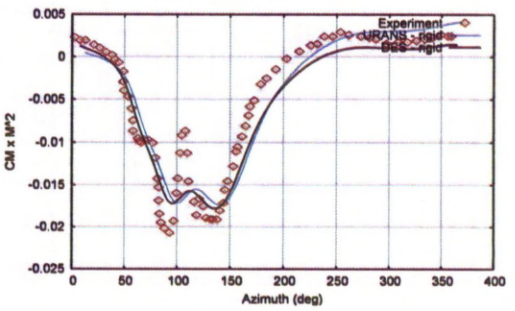

(d) M^2C_m, $r/R = 0.825$

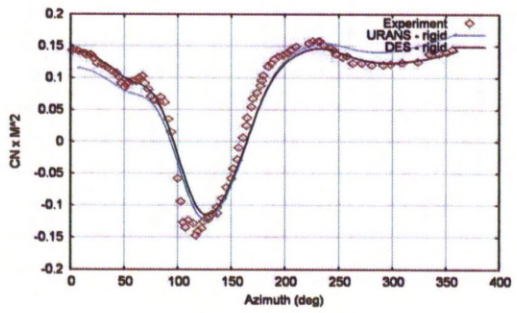

(e) M^2C_n, $r/R = 0.975$

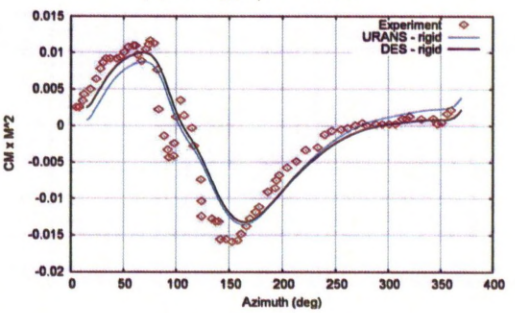

(f) M^2C_m, $r/R = 0.975$

Figure 8.1: Comparison of the Mach scaled normal and moment coefficients at three sections obtained with URANS and DES turbulence models during a revolution with the experiment for an ONERA 7A rotor in case 3 conditions.

the experiments quite accurately.

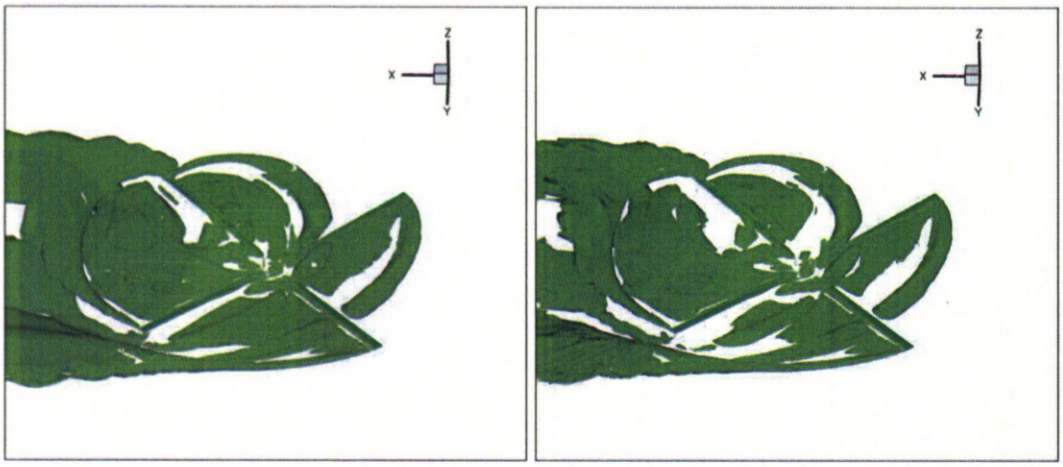

(a) URANS (b) DES

Figure 8.2: λ_2 isosurfaces comparison for URANS and DES turbulence models simulations in case 2 conditions.

Further insight in the differences and similarities of the models can be obtained by looking at the λ_2-criterion iso-surfaces for case 2 in Figure 8.2. The overall distribution and shape of the surfaces look similar between URANS and DES. The DES solution, however, appears to have more fine structures super-imposed on some mean flow field. This prompted further investigation in the data and for this reason, the mean blade loads as well as the first harmonic were removed from the rotor-integrated forcing. The results are shown in Figure 8.3 and it appears that at the front of the disk as well as the advancing side, the two solutions are very close to each other. For the back of the disk, the situation is different. The DES solution shows higher peak-to-peak variations and higher level of oscillations that diminish as the inflow of the rotor disk is approaching. This suggests that since no inflow forcing[126] has been used for the computations near the free-stream, the DES behaved more-or-less like URANS for that part of the flow domain. The presence of the vortices and the complex wake further downstream has triggered the LES part of the DES model and much reduced levels of eddy-viscosity were observed. For this reason, more and more flow structures were resolved on the relatively coarse DES mesh.

From the available experiment, it is difficult to extract information about the level of turbulence present around the rotor. The use of DES is therefore only suitable for qualitative comparisons. On the other hand, based on the simpler cases studied for flows around aerofoils, DES appears to have

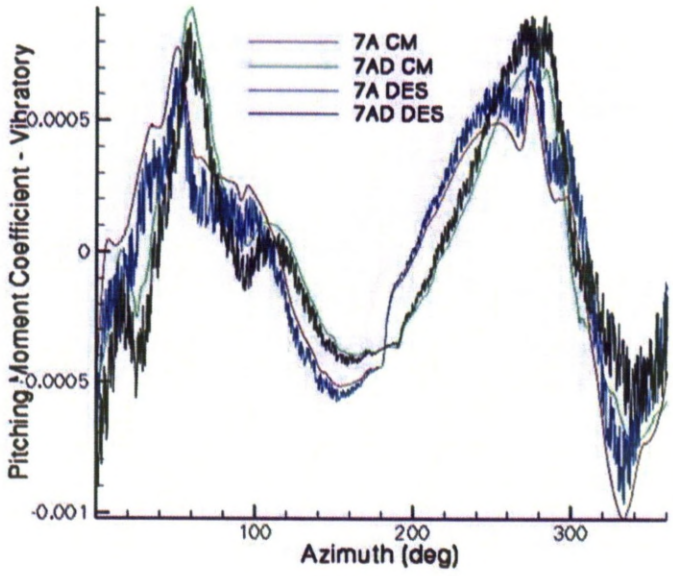

(a) Case 1

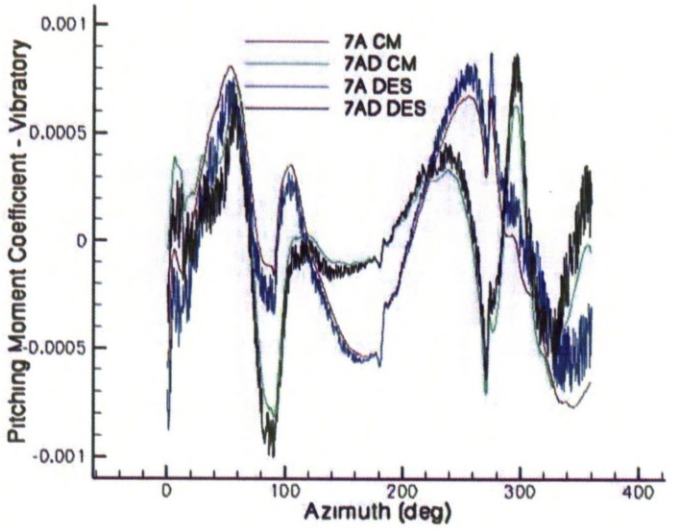

(b) Case 2

Figure 8.3: Comparison of the pitching moments vibratory part for the 7A and 7AD rotors during a revolution for two test cases.

some merit. Clearly, experiments providing detailed spectra are needed to screen DES models and help improve the predictions of CFD. The use of a more suitable case is deemed necessary and this will be attempted in Section 8.4.

8.2 7A Rotor in Forward Flight — Mesh Deformation Method Assessment

The proposed mesh deformation method was also tested for a forward flying ONERA 7A rotor. The chosen test point for the calculations was Datapoint 156 of the HELISHAPE experiments[45], which corresponds to a moderately high speed flight. The advance ratio is set to $\mu = 0.35513$. The free stream Mach number equals $M_\infty = 0.219$ and the thrust coefficient is set to $C_T/\sigma = 0.08415$, where $\sigma = 0.085$. The control angles used for this calculation are summarised in Table 8.2. The pressure on the blade

Table 8.2: ONERA 7A and 7AD flight conditions and trimming for the various simulations. The angles are given in degrees.

μ	M_∞	C_T/σ	α_S	θ_0	θ_{1c}	θ_{1s}	β_0	β_{1c}	β_{1s}
0.35515	0.219	0.08415	−4.98	7.37	−2.16	6.23	2.12	−0.12	−0.51

was measured at five sections: $r/R = 0.5$, 0.7, 0.82, 0.92 and 0.98. The tip displacement was extracted from the HART experiment and it was arbitrarily decided to use the second and third flapping modes for the mean tip deformation, using an amplitude of half the mean displacement at the tip for each mode. Then the five first harmonics were extracted from the HART-II tip displacement. The one- and two-per-revolution harmonics were introduced using the second flapping mode, while the three- to five-per-revolution harmonics were introduced using the third flapping mode. This was necessary due to the lack of structural deformation for the 7A rotor. However, the 7A and HART-II rotors were of similar construction.

The comparison of the Mach scaled normal coefficient at various spanwise sections shown in Figure 8.4 showed some important differences despite the low torsional deformations of the blade. The introduced flapping deformation tended to largely modify the Mach-scaled normal force and moment

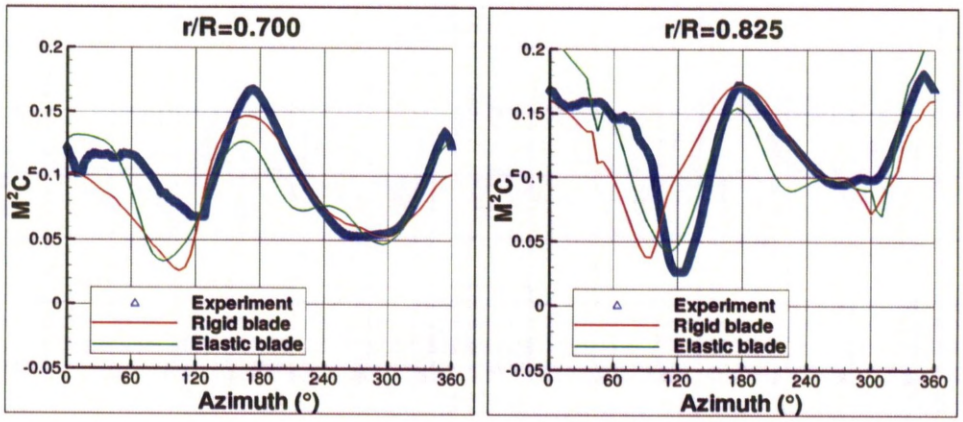

(a) $r/R = 0.70$

(b) $r/R = 0.825$

(c) $r/R = 0.915$

Figure 8.4: Comparison of the Mach scaled normal force coefficients of the elastic and rigid 7A blades with wind tunnel test data at various sections.

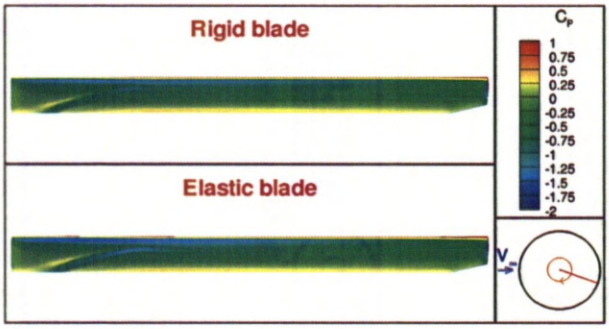

(a) $\Psi = 10$ degrees

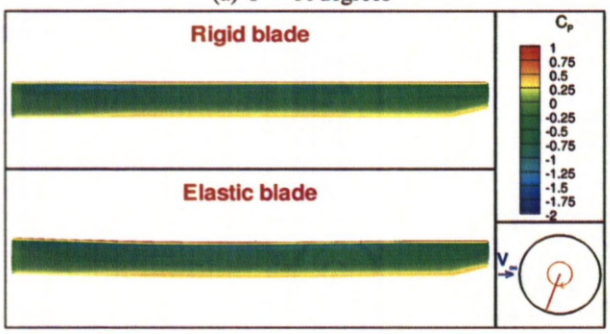

(b) $\Psi = 100$ degrees

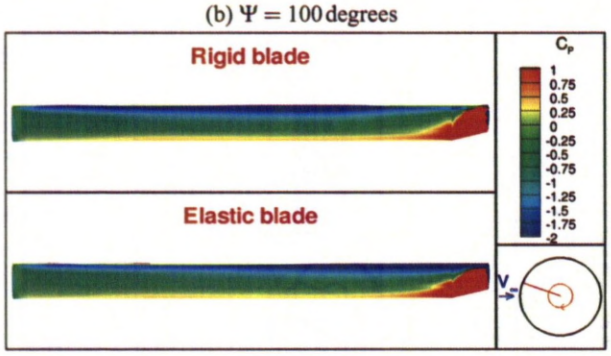

(c) $\Psi = 190$ degrees

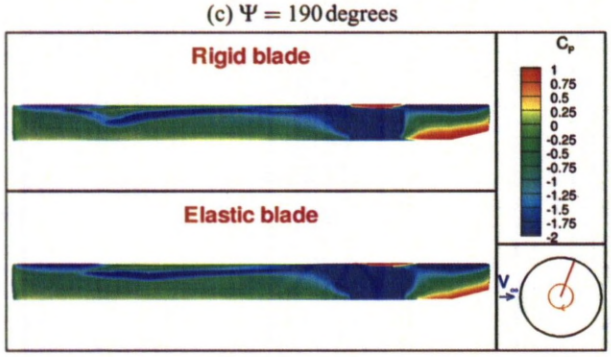

(d) $\Psi = 280$ degrees

Figure 8.5: Comparison of the pressure coefficients on the upper surface of the 7A blade at four azimuthal positions for Datapoint 156.

coefficients. The differences appear to be located at the most outboard section of the blade: the down peak has been delayed and the force coefficient reaches a far lower level, which is closer to experimental results. On the most inboard station, due to the low flapping amplitude, the differences due to the introduced deformation are small and mainly located at the front and the back of the disk. The pressure coefficient at various azimuthal stations is shown in Figure 8.5. The suction is increased on the blade at an azimuth of 190 degrees and the stalled area at an azimuth of 280 degrees is bigger on the elastic blade.

8.3 Coupling Method Assessment on the UH-60A Rotor in Forward Flight

The UH-60A rotor was chosen to assess the aeroelastic coupling strategy. This rotor was tested in flight by NASA and the US Army (see Section 1.2.5). In the high-speed flight (Flight Counter 8534), it has been shown[117,127] that the torsional deformation played an important role in the loading predictions. This torsional deformation is triggered by the movement of a shock on the advancing-side and the formation of a shock on the blade lower surface. This case was used by Steijl *et al.* [127], who showed that the inclusion of torsional deformation extracted from flight test data allowed for an improvement of the loads on the advancing side, that were mainly driven by a high amplitude pitch-down torsion around $\Psi = 140$ degrees. It was therefore deemed as an interesting test-case to assess the coupling method.

Table 8.3: UH-60A flight conditions and trimming for flight counter 8534. The angles are given in degrees.

μ	M_∞	Re_∞	α_S	θ_0	θ_{1c}	θ_{1s}	β_0	β_{1c}	β_{1s}
0.368	0.256	2.735×10^6	-7.31	11.6	-2.39	8.63	3.43	-0.70	-1.00

The flight conditions and control angles are summarised in Table 8.3. The grid contained 8.0 million nodes. A first simulation was carried out using a structural damping of $\zeta = 0.3$ for every structural mode and an azimuthal step of $\Delta\Psi = 0.25$ degree. The implicit coupled method was used. The first half of the revolution was run as a rigid case, before the blade was allowed to elastically deform. Three

revolutions allowed for convergence on the deformations.

The blade geometry was estimated from publications in the literature, however, uncertainties are left on the exact blade geometry, twist distribution and structural model, and those are therefore approximates.

8.3.1 Deformation and Loads Analysis

The blade deformations were extracted from the coupled simulations and are shown in Figure 8.6. The most noticeable property of the blade deformation was the strong dip at $\Psi = 160$ degrees in torsion deformation. This deformation was caused by a shock formed on the lower surface, shown in Figure 8.7. With the torsional deformation, the shock was moving on the lower surface and increased the amplitude of the blade deformation. The blade recovered from the torsional deformation when the local free stream velocity decreased enough. Small oscillations also appeared on the retreating side and a slight increase of torsion was also noticed at $\Psi = 25$ degrees. The amplitude of second torsional mode seemed negligible compared to the amplitude of the first torsional mode. The flapping deformation also seemed to be dominated by the second flapping mode, with a strong 1/Rev component, leading to a dip of the tip flapping at $\Psi = 135$ degrees.

The Mach-scaled sectional normal force and pitching moments were extracted. The influence of the torsional deformation around $\Psi = 160$ degrees is clearly visible, with the normal force being negative. High frequency oscillations can also be noticed on the advancing side. These were caused by BVIs. Looking at the pitching moments, the transitions between aerofoil sections and the start of the sweep can be noticed through the moment discontinuities in the radial direction. The BVI area is also visible with the high-frequency changes on the advancing side. The higher moments due to the SC1094-R8 seemed to trigger the dip in the torsional moment, due to the higher amplitude of the pitching moment between $\Psi = 45$ degrees and $\Psi = 120$ degrees.

The sectional normal force was compared with flight-test measurements[51] at $r/R = 0.675$ and $r/R = 0.865$. The dip in the sectional forces on the advancing side showed much stronger in the simulations than in flight test measurements, and was delayed by 15 degrees. However, the loads on the

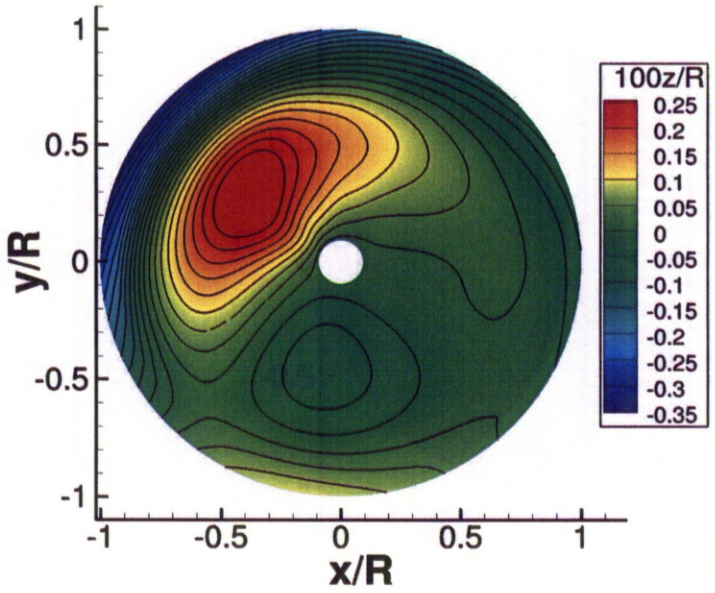

(a) Elastic flapping

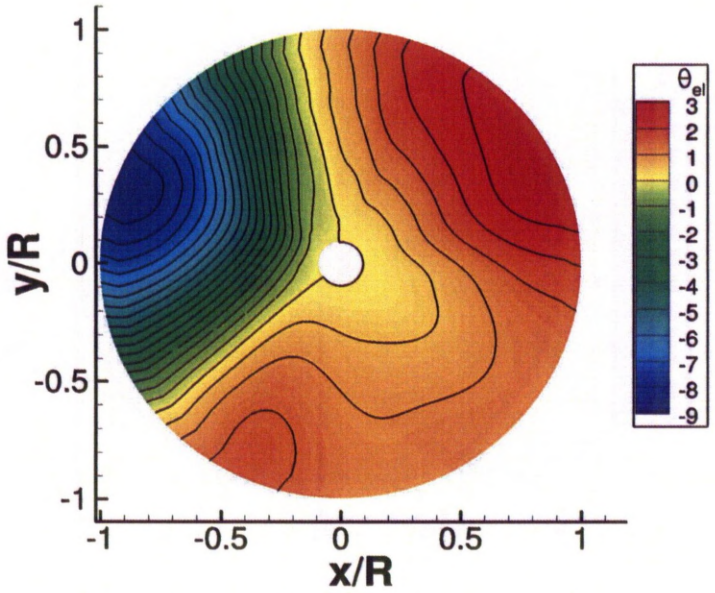

(b) Elastic torsion

Figure 8.6: Predicted UH-60A blade deformation during a revolution for Flight Counter 8534.

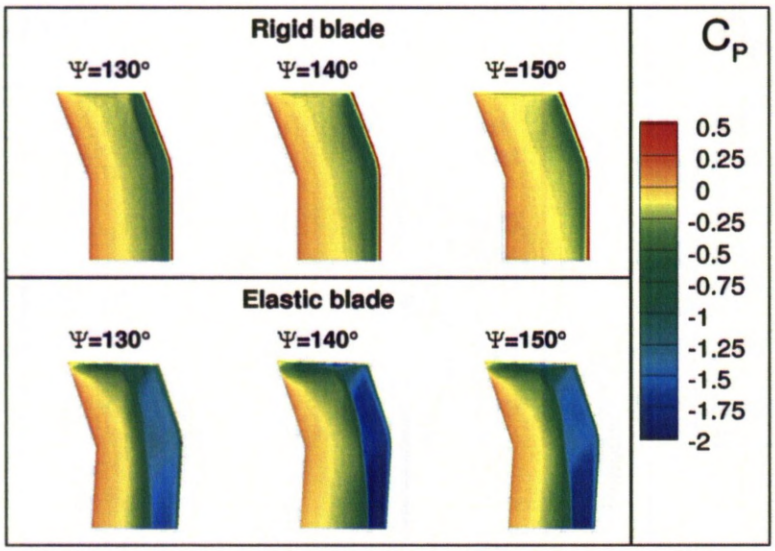

Figure 8.7: Comparison of the pressure coefficient on the blade lower surface between a rigid blade assumption and an elastic blade for Flight Counter 8534.

retreating side agreed well with the flight test measurements. At $r/R = 0.675$, the BVIs predicted by the simulations did not seem to occur in the flight tests on the advancing-side, but at $r/R = 0.865$, their locations and amplitudes seemed to agree with the flight test data. The mean normal force in the first quadrant is, however, over-predicted. The predicted loads were also compared to the ones obtained with a rigid blade and the ones obtained by Steijl *et al.* [127], using a prescribed torsion based on the flight tests. The effect of the blade in-flight deformation was mainly located on the advancing side. On the retreating side, the only difference between the simulations occurred in the coupled one, predicting a higher increase of the Mach-scaled loading in the forth quadrant, in better agreement with flight test measurements. On the advancing-side, the differences in the dip amplitude and phase between the coupled simulation and the flight test measurements appeared to be due to different torsional levels between the coupled simulation and the flight test data, as the simulation with a prescribed torsion agreed well with the flight test data. The BVIs around $\Psi = 85$ degrees also appeared to be stronger in the coupled simulation compared to the others, which may come from the inclusion of the flapping deformation. Clearly, the approximate blade shape and the lack of detailed data for the structural properties have an influence on the results. The mesh deformation method, however, managed to produce good quality grids.

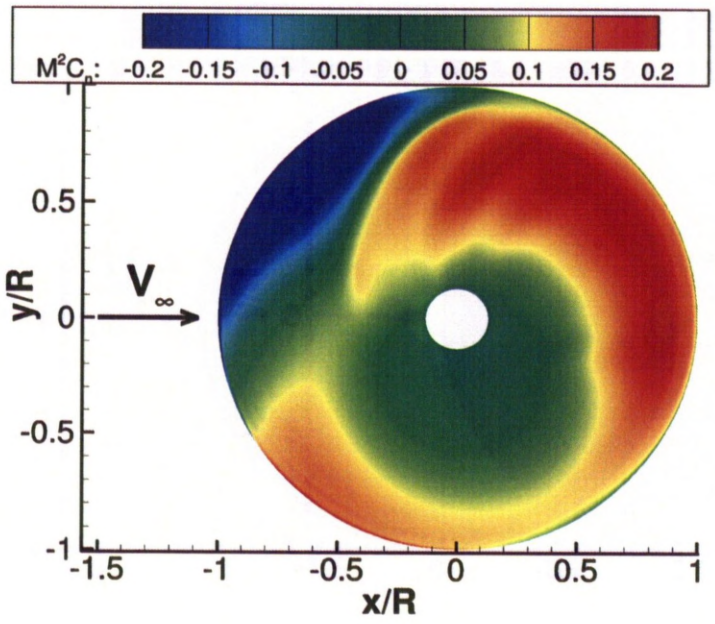

(a) M^2C_n

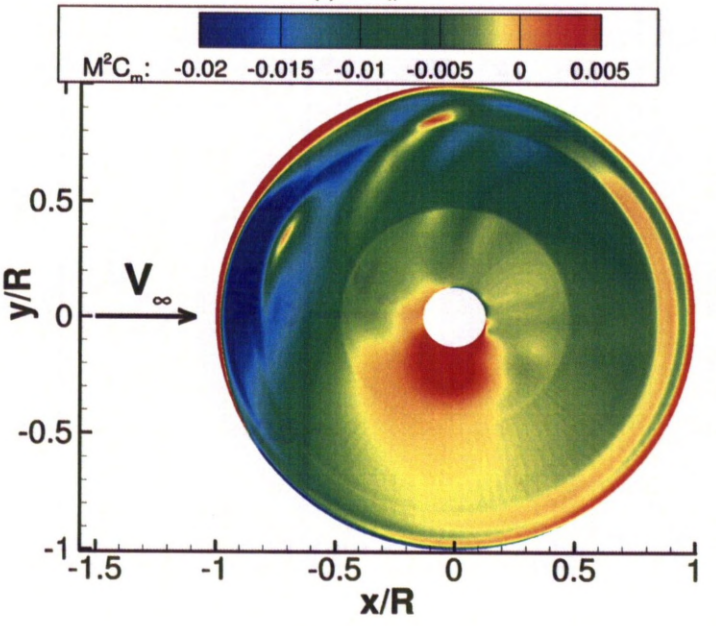

(b) M^2C_m

Figure 8.8: Loading of the UH-60A for Flight Counter 8534.

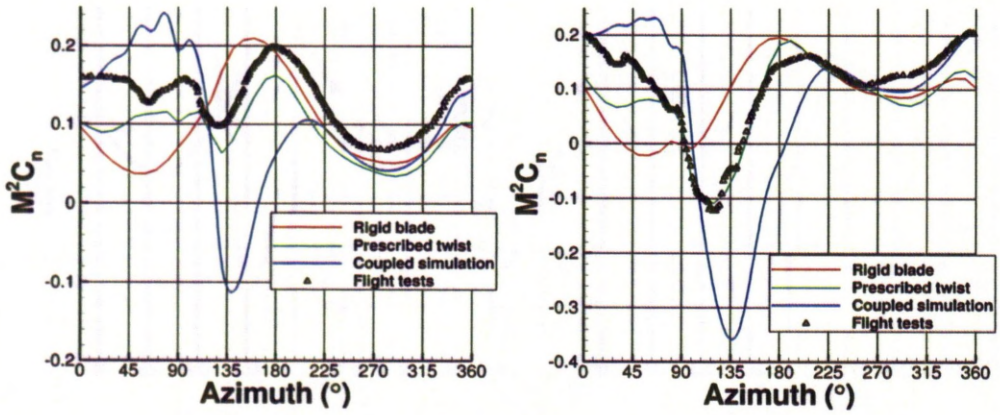

(a) $r/R = 0.675$ (b) $r/R = 0.865$

Figure 8.9: Comparison of the sectional normal force of the UH-60A with flight test measurements for Flight Counter 8534. The prescribed twist predictions were obtained by Steijl *et al.* [127].

8.3.2 Evolution of the Blade Deformation with the Structural Damping Coefficient

It was decided to study the influence of the structural damping coefficient ζ (see Equation 4.2) on the blade in-flight deformation. Therefore, $\zeta = 0.1$ and $\zeta = 0.02$ were compared to the original value of

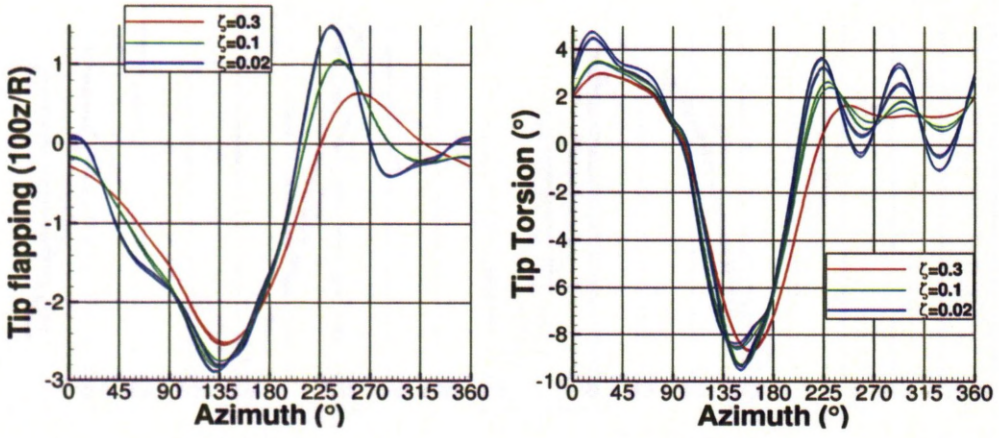

(a) Tip flapping (b) Tip torsion

Figure 8.10: Evolution of the predicted UH-60A blade tip deformation with the structural damping coefficient ζ during a revolution for Flight Counter 8534.

0.3. The evolution of the blade tip deformation with the damping coefficient can be seen in Figure 4.2. The main features of the blade deformation did not change. The tip flapping showed a difference in

the recovery from the dip on the advancing side. With the lower damping, the recovery happened at a higher speed, and the overshoot was also more important. Higher differences can also be noticed on the tip torsion. The first remark deals with the converged state. While all the blade converged to the same equilibrium state at $\zeta = 0.3$, it can be noticed that, for lower damping coefficients, the converged deformation of blades 1 and 3 was different from the one of blades 2 and 4. This difference appeared mainly in the amplitude and the azimuth of the down-peak as well as the oscillations on the retreating side. Also, the aerodynamic damping of the oscillations on the retreating side proved low, and a decrease in the structural damping allowed the blade to vibrate at the frequency of the first torsional mode.

8.3.3 Evolution of the Blade Deformation with the Azimuthal Time Step

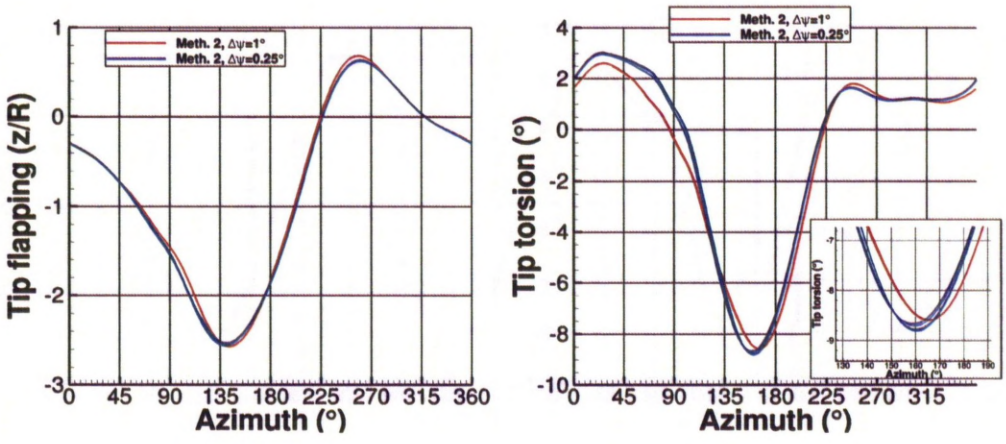

(a) Tip flapping

(b) Tip torsion

Figure 8.11: Evolution of the predicted UH-60A blade tip deformation with the time step $\Delta\Psi$ during a revolution for Flight Counter 8534. Method 2 is the implicit coupled method.

The influence of the azimuthal time step was also studied, using $\Delta\Psi = 1$ degree and $\Delta\Psi = 0.25$ degree. The difference in the blade deformation predictions was limited, showing just a slight difference on the advancing side in tip torsion. This was the result of a higher gradient predicted between $\Psi = 315$ degrees and $\Psi = 360$ degrees.

8.3.4 Evolution of the Blade Deformation with the Coupling Method

The two methods introduced in Section 5.2.2 for the strong coupling strategy were also compared for this case. Two time steps $\Delta\Psi = 1$ degree and $\Delta\Psi = 0.25$ degree were used. Figure 8.12 shows the tip

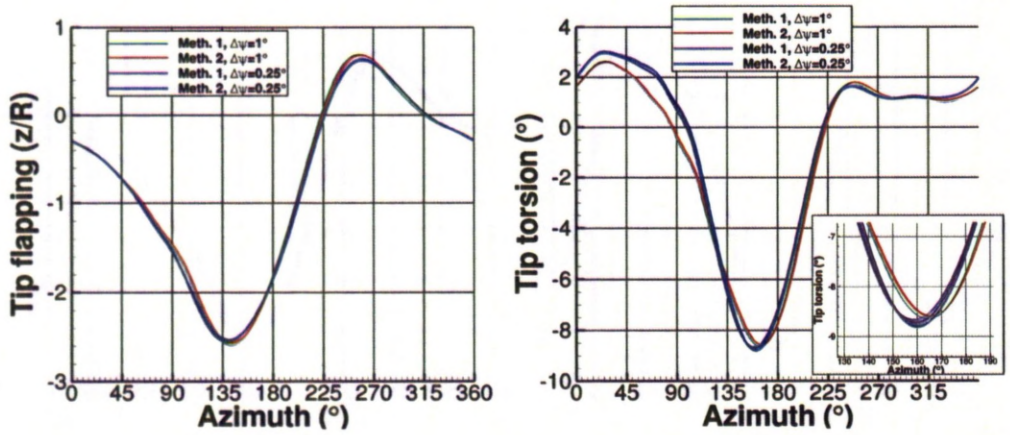

(a) Tip flapping (b) Tip torsion

Figure 8.12: Evolution of the predicted UH-60A blade tip deformation with the time step $\Delta\Psi$ and the coupling method during a revolution for Flight Counter 8534. Method 1 represents the leap-frog method and Method 2 the implicit coupled method.

deformation for the two methods. The difference between the two methods proved limited. Although the leap-frog scheme predicted slightly higher gradients before the dip, leading to a slightly earlier dip. The offset did not exceed 3 degrees and the amplitude of the dip were the same.

8.4 HART-II in Forward Flight

The deformation method was also applied to the HART-II rotor in forward flight, with experiments carried out by Van der Wall *et al.* [49]. The rotor was flying at a low advance ratio of 0.1508, a free stream Mach number of $M_\infty = 0.0963$ and a tip Reynolds number of $Re_\infty = 2.88 \times 10^5$. These particular flight conditions were chosen to create blade-vortex interactions (BVIs) and study the effect of the BVIs on the loads and the flow field around the rotor. The measurements included the blade loading as a function of the azimuth at $r/R = 0.87$, the blade in-flight deformation and PIV planes at the core of vortices. More details about the experiment can be obtained in Section 1.2.5. This test case is nowadays

considered the hardest test for rotor CFD.

The blade deformation was measured using the SPR technique, and was projected against the blade eigenmodes by Van der Wall[128]. These modal amplitudes were used with the mode shapes predicted with NASTRAN as described in Section 4.3.3 to prescribe the blade deformation in the CFD simulations. The induced torsional deformation in the flapping modes was also corrected when recomputing the modal amplitudes. The resulting blade deformations are shown in Figure 8.13. The elastic flapping deflections were dominated by the second flapping mode, with the blade tip bending down on the advancing side and up on the retreating side. The chordwise bending was also dominated by a 1/Rev frequency, while the torsional deformation was dominated by a 2/Rev component, with peaks of lower torsion around the areas where the BVIs occurred (around $\Psi = 90$ degrees and $\Psi = 270$ degrees). The prescribed deformation at the blade tip is compared to experimental measurements in Figure 8.14. The flapping deformation agreed well with experimental measurements. The chordwise deformation was, however, offset. The tip torsion also tended to be slightly under-estimated on the advancing side, particularly the down-peak at $\Psi = 170$ degrees.

Table 8.4: Control angles for the HART-II rotor simulation, in degrees.

Case	α_S	θ_0	θ_{1s}	θ_{1c}
untrimmed	4.5	2.96	0.97	−1.57
trimmed	4.5	2.96	1.47	−1.57

During the simulations, a fine grid containing 34.8M nodes was used. This fine grid was also used to assess the interest in DES, therefore two simulation were run: one using the SA model and the other one the DES model. It was noticed during the simulation that an increase in amplitude of the sinus component of the cyclic allowed for a better trimming and loading. This second simulation was called *trimmed* in this section. The trim states used for the HART are summarised in Table 8.4. Due to the higher DES requirements, the simulations were run with an azimuthal time step $\Delta\Psi = 0.1$ degrees. This is perhaps a harder test for the method since most researcher trim and re-trim the rotor to obtain good agreement with tests even if at different C_T than the experiments.

Iso-surfaces of the λ_2-criterion from the *trimmed* DES simulation are shown in Figure 8.15 and

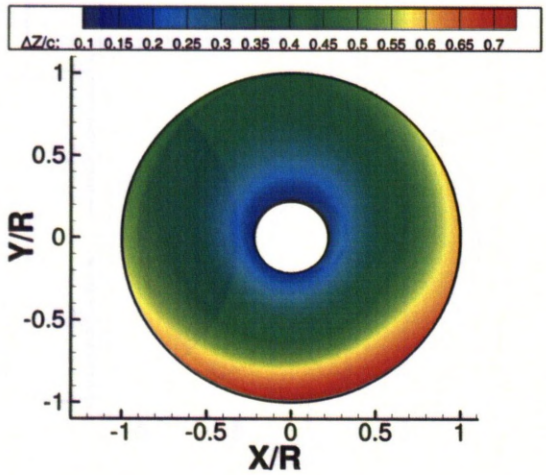

(a) Flapping deflection

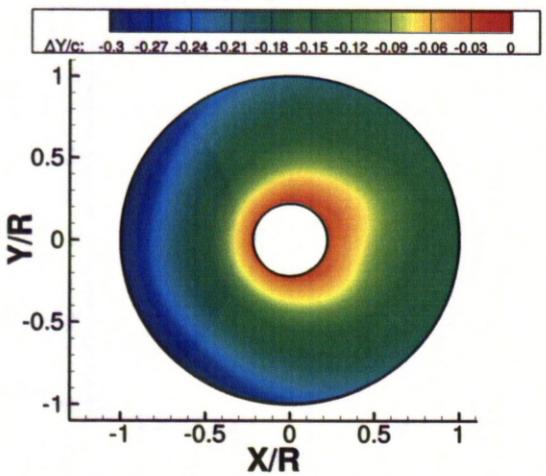

(b) Chordwise deflection

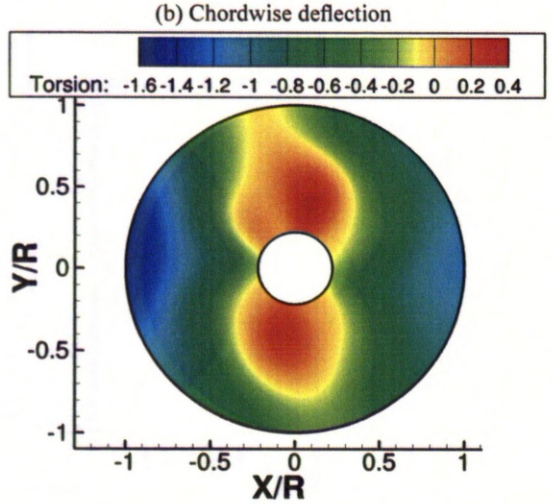

(c) Torsional deformation (degrees)

Figure 8.13: Prescribed deflections to a HART-II blade during a revolution.

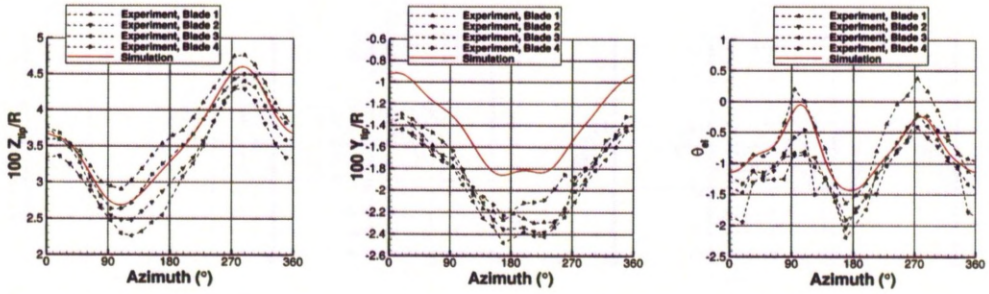

(a) Flapping deflection (b) Chordwise deflection (c) Torsional deformation

Figure 8.14: Comparison of a HART-II blade tip deformation with experimental measurements by Van der Wall *et al.* [49].

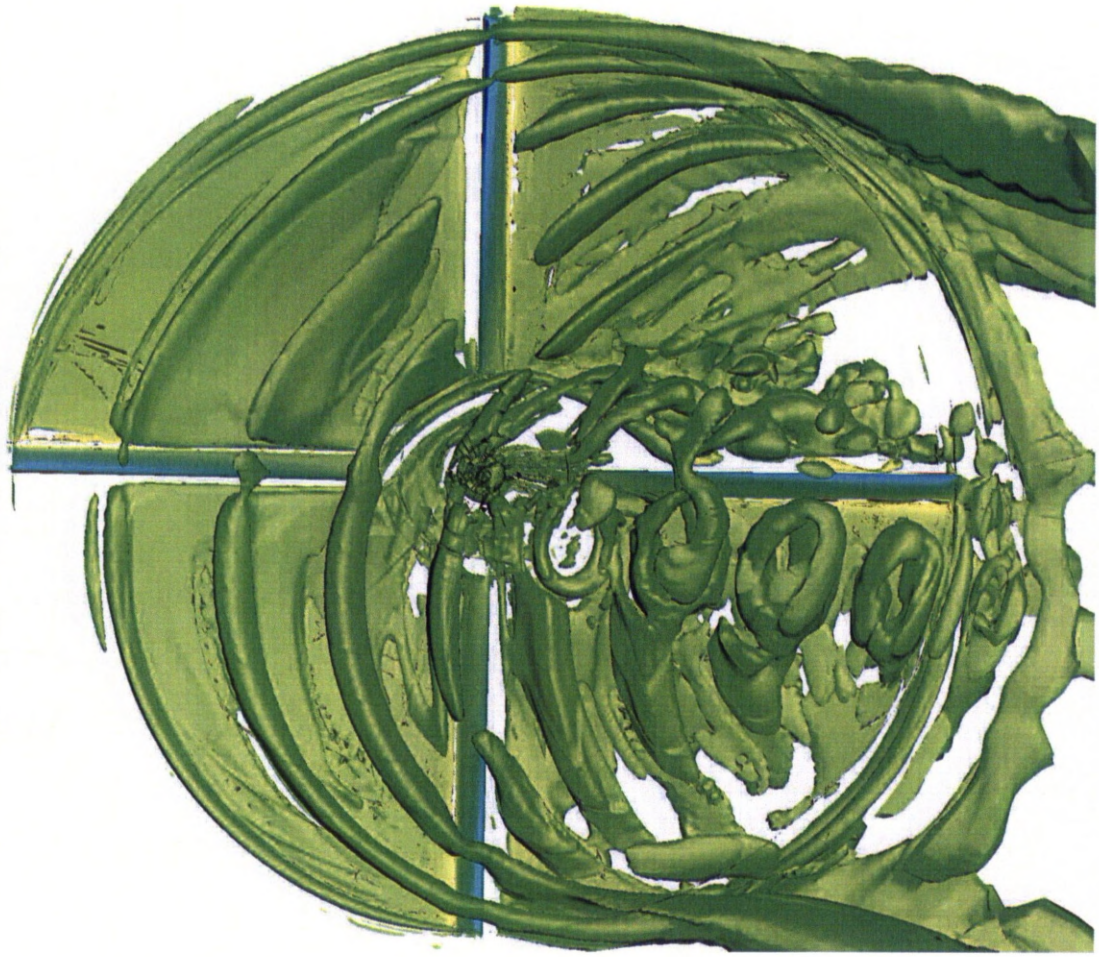

Figure 8.15: λ_2-criterion iso-surfaces for the flow around the HART-II rotor, coloured with the pressure. View from the top of the rotor.

animated in the CD attached to this thesis, showing the location of the vortices. Due to the low thrust coupled with the backward shaft angle, the vortices generated by the blades at the front of the disk pass over the rotor before moving downward and crossing the rotor disk at the rear. Due to the low advance-ratio, the vortices are progressing very slowly along the rotor. The hub wake as well as the blade root vortices are also clearly visible and interact with the blade in the rear of the disk.

8.4.1 Loads Comparison

Figure 8.16 presents the computed Mach-scaled normal force coefficient along the span during the rotation of the HART-II rotor using both the DES and SA turbulence models. Both simulation predicted BVIs around $\Psi = 80$ degrees and $\Psi = 270$ degrees, as the strong oscillations in the normal coefficient indicate. The interaction of the blade with the wake of the hub is also clearly visible at the back of the disk. The predictions from the SA and DES turbulence models were very similar, and the main differences are located in the BVIs area where differences reached 5% of the peak-to-peak variation of the Mach-scaled normal force coefficient.

The Mach-scaled pitching moment coefficients were also extracted and are shown in Figure 8.17. Once again, the difference between the two simulations was limited to the areas were the BVIs occur, mainly on the advancing-side. The maximum difference between the DES and SA simulations reached 10% of the peak-to-peak variation of the Mach-scaled pitching moment coefficient.

The loading at section $r/R = 0.87$ was then extracted and compared with experimental measurements in Figure 8.18. The BVIs are clearly visible around $\Psi = 80$ degrees and $\Psi = 280$ degrees, with large variations in amplitude. While the predictions followed the experimental trend, the down-peak at $\Psi = 150$ degrees tended to be over-predicted. The loads in the first quarter of a revolution were also under-predicted. The *trimmed* solution improved the predictions on the advancing side, with an upward peak around $\Psi = 90$ degrees following the experimental values instead of being higher. This improvement proved limited when focusing on the vibratory part of the loads. The BVIs from the CFD simulations tend to happen more forward in the rotor disk. This might be linked to the higher thrust from the rotor ($C_T = 0.0140$ in the simulations, and $C_T = 0.00886$ in the experiments) which brought

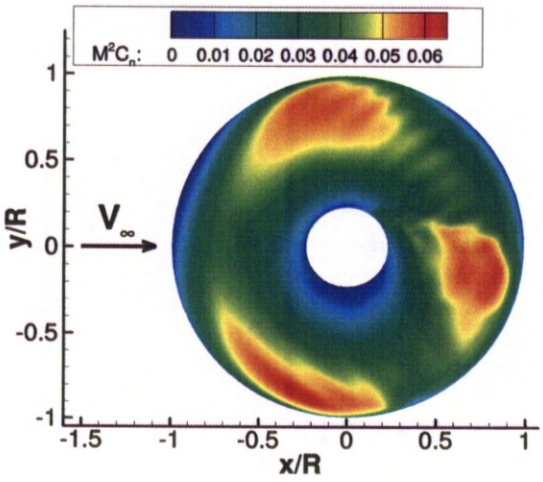

(a) SA

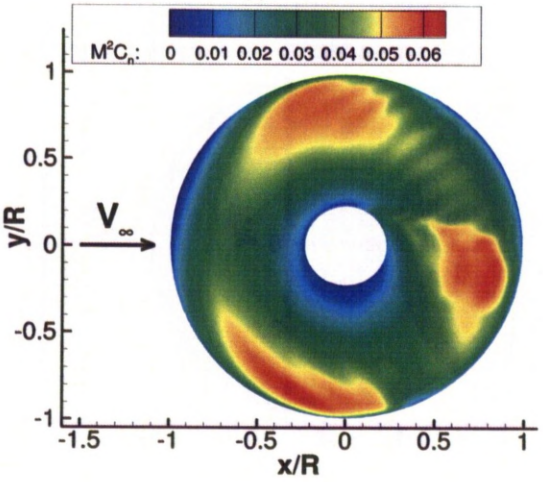

(b) DES

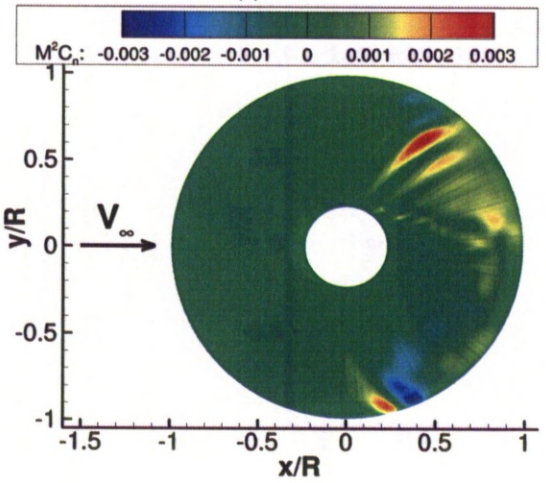

(c) Difference (DES-SA)

Figure 8.16: Mach-scaled normal force coefficient for the HART-II rotor, using the SA and DES turbulence models

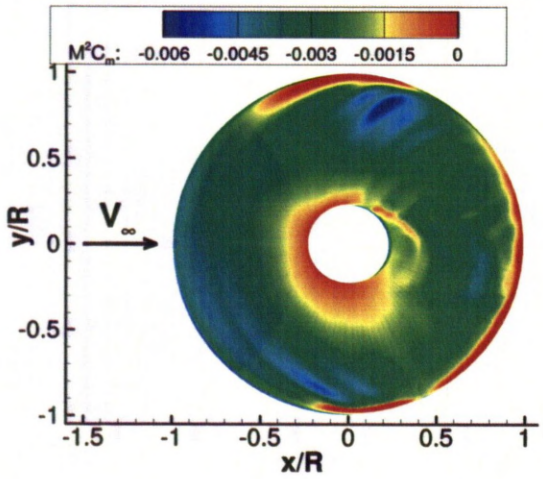

(a) SA

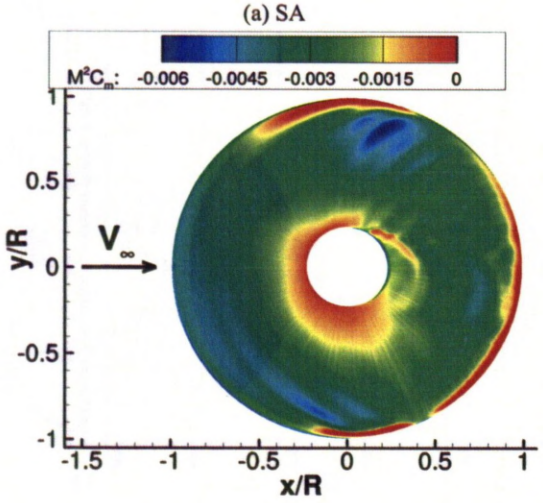

(b) DES

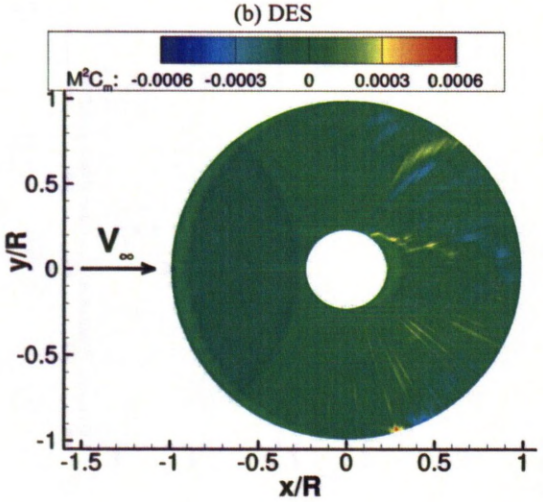

(c) Difference (DES-SA)

Figure 8.17: Mach-scaled pitching moment coefficient for the HART-II rotor, using the SA and DES turbulence models

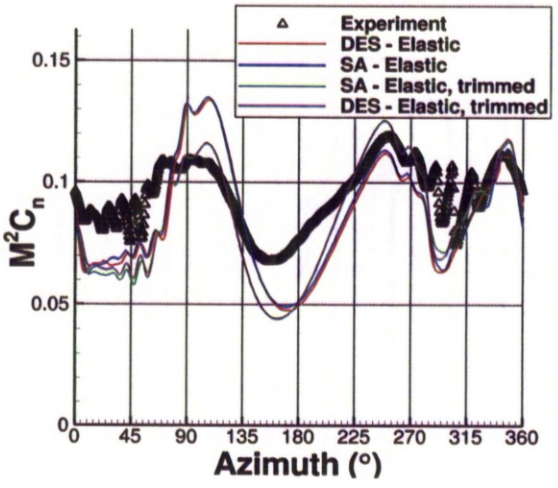

(a) M^2C_n

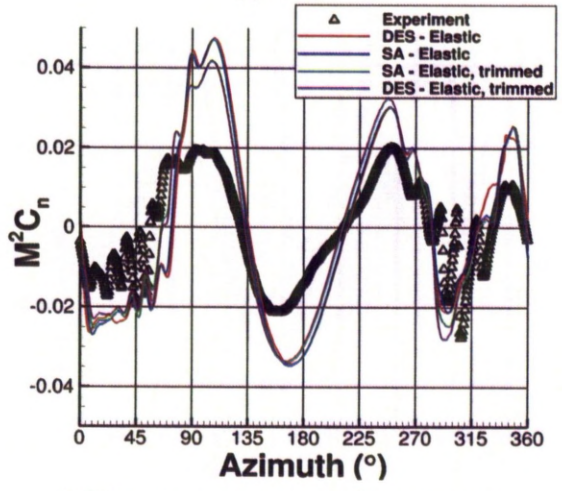

(b) Vibratory part (mean and 1 /Rev removed)

Figure 8.18: Comparison of the Mach-scaled normal force coefficient for the HART-II rotor at $r/R = 0.87$. Experiments by Van der Wall *et al.* [49].

the vortices through the rotor disk earlier. The amplitude of the loads variations was also smaller in the CFD simulations. This might come from the numerical dissipation of the vortex, despite the use of a fine mesh.

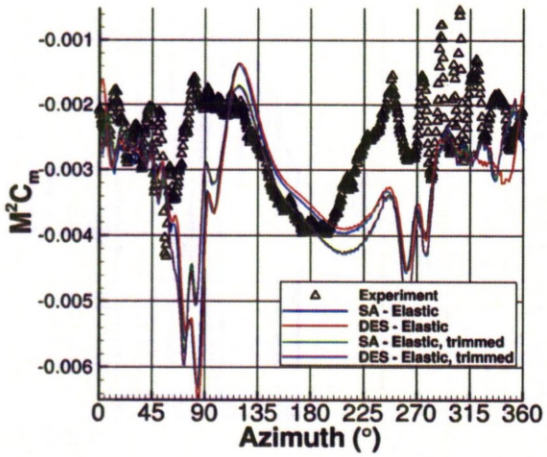

(a) M^2C_m

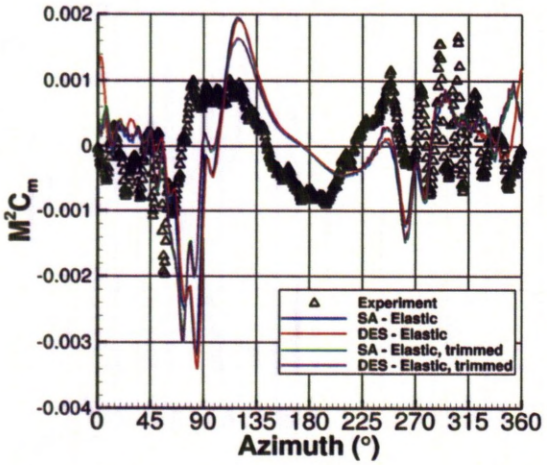

(b) Vibratory part (mean and 1/Rev removed)

Figure 8.19: Comparison of the Mach-scaled pitching moment coefficient for the HART-II rotor at $r/R = 0.87$. Experiments by Van der Wall *et al.* [49].

The Mach-scaled moment coefficient at section $r/R = 0.87$ was also extracted and is compared with experimental measurements in Figure 8.19. The sectional moment tended to be under-predicted during the whole revolution. A very strong peak, that did not appear in the experiment, was predicted around azimuth $\Psi = 80$ degrees. The *trimmed* solution however reduced the amplitude of the peak and improved the predictions on the advancing side, but the sectional moments were still under-predicted.

Again, the amplitude of the variations due to the BVIs was under-predicted, particularly on the retreating side. In the literature, several authors have recently attempted this case and the present results are in broad agreement with all published simulations. This shows the difficulty in obtaining accurate results for this extreme test case.

8.4.2 Comparison with PIV Data

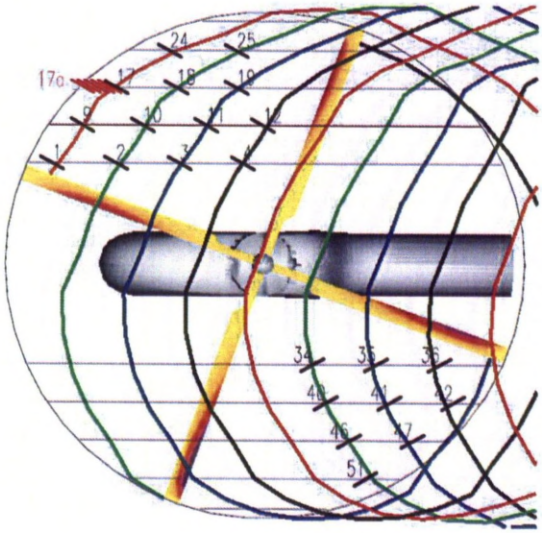

Figure 8.20: Location of the PIV planes in the wake of the HART-II rotor when the first blade is at $\Psi = 70$ degrees, from [128].

In order to assess the numerical dissipation of the vortex cores linked with the mesh refinement, planes perpendicular to the vortex cores were extracted and compared with PIV measurements on the HART-II model by Van der Wall *et al.* [49]. The plane positions for the PIV are shown in Figure 8.20. Plane 17 is the most important and proved popular in the literature for comparison. Planes 17 and 18 were extracted when the first blade was located at $\Psi = 70$ degrees. The measured vortices were generated by the blades at $\Psi = 160$ degrees and $\Psi = 250$ degrees, respectively. The cores of the vortex were located in the plane $y/R = 0.7$ and the planes were oriented such that they were perpendicular to the vortex. For the experimental measurements, an angle of 30.47 degrees was used. Therefore, the measured vortices had an age of about 28 degrees and 118 degrees.

The comparison of the predictions for plane 17 with experimental measurements is shown in

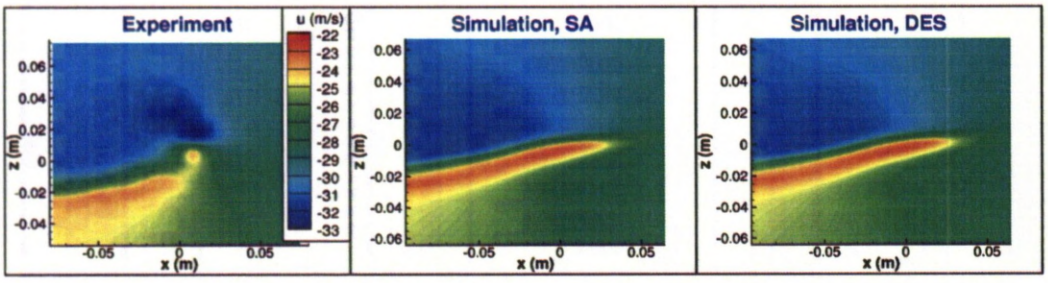

(a) U

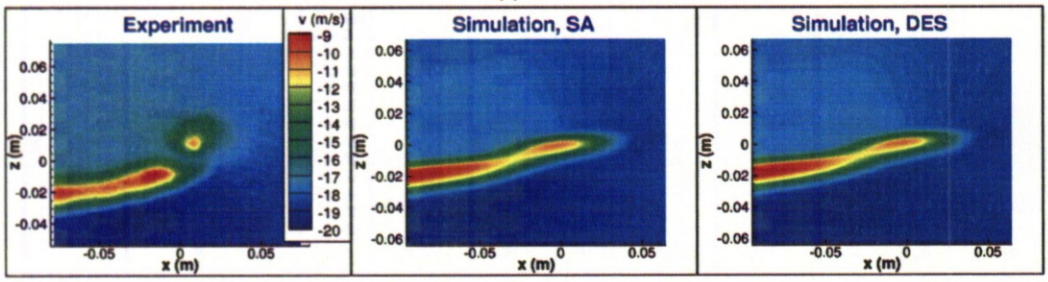

(b) V

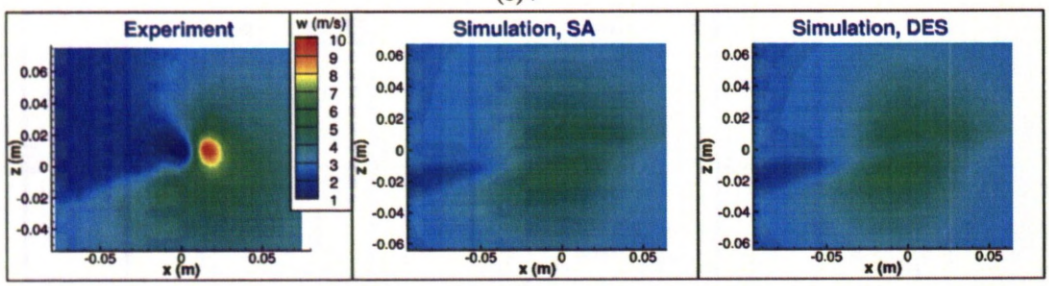

(c) W

Figure 8.21: Comparison of the flow velocities measured in Plane 17 obtained from the SA and DES simulations with PIV measurements. Experiments by Van der Wall *et al.* [49].

Figure 8.21. The V and W components were corrected by subtracting 2 m/s and 5.5 m/s due to differences in trim. The differences between the SA and DES simulations proved limited. The comparison with the PIV measurements however showed that the small core of the vortex was already wider in the simulations, as shown in the V component. The separation between the lifting sheet and the vortex core is still visible, but was milder than the one in the PIV measurements. The high gradients visible in the measurements on the U and W components were much smaller in the simulations, showing the numerical dissipation, even for the 34.8 million nodes grid. Recently, improvements were showed by Lim and Strawn[129], using a 113 million nodes mesh.

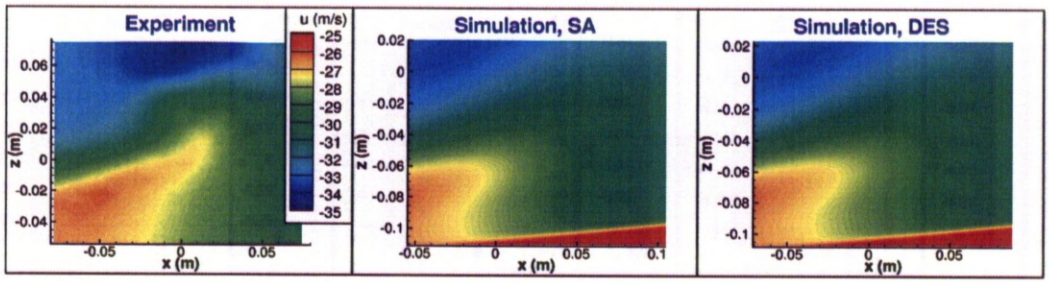

(a) U

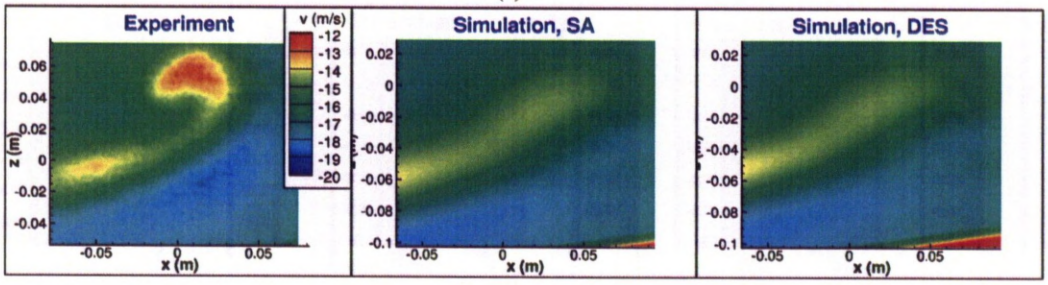

(b) V

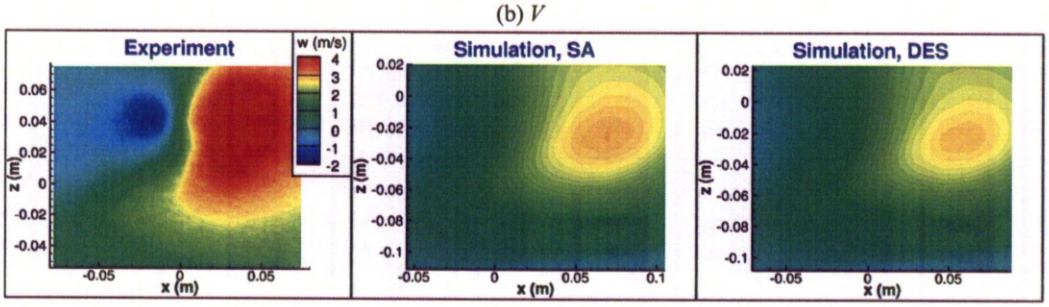

(c) W

Figure 8.22: Comparison of the flow velocities measured in Plane 18 obtained from the SA and DES simulations with PIV measurements. Experiments by Van der Wall *et al.* [49].

The comparison of the CFD simulations with the PIV measurements in plane 18 is shown in

Figure 8.22. The V and W components were corrected by subtracting 1 m/s and 5 m/s. The difference between the DES and SA simulations is once again limited. On this older vortex, the amplitude of the V component was smaller then the experimental one and the gradients on the U and W were much smaller at the core of the vortex, showing the dissipation of the vortex. This dissipation in the vortex could explain the lack of the strength in the loads oscillations due to the BVI.

For this case, a mesh refinement near the core would certainly provide better comparison. On the other hand, HMB showed no lack of stability or convergence due to the new mesh deformation method.

Chapter 9

Conclusions

9.1 Summary and Conclusions

In this thesis, an aeroelastic coupling strategy was developed, using HMB as the CFD solver and NASTRAN as the structural solver. Rotor blade models tend to use the beam theory, meaning that the number of nodes is very low while the blade surface in a CFD grid is usually represented using 20,000 nodes or more. Therefore, a method has to be used to interpolate the deformation of the structure to the fluid grid, and adapt the fluid grid to the new blade shape. In order to address this issue, a new mesh deformation method was developed. The grids employed by HMB have certain requirements related to the blade actuation. Due to this, the mesh deformation method had to respect the tagging of blocks as rigid or deformable, or blade fixed, or fuselage-fixed. It was therefore necessary to build the maximum possible flexibility in the mesh deformation method and this was achieved using a combination of techniques.

The final method was based on the use of CVT[116], SAM[19] and TFI[118]. The CVT interpolated the blade deformation from the structural model based on triangular elements, and proved able to deal with large blade deformations. Although CVT has been used in the past, this is the first time that it is employed on rotor blades for cases with large deformations and, due to its limitations, it is restricted to

the blade surface only. The SAM was used to move the block vertices of all blocks in the computational domain. This restricted use of the SAM resulted in CPU economies, since SAM is an iterative technique, without compromising the final grid quality. TFI is finally used to recompute the inner part of the blocks. TFI is renowned for its efficiency and since this applies to blocks that already have deformed solid surfaces and solid vertices, the final mesh quality is high. The hybrid mesh deformation method was applied to a range of rotors and proved able to deal with usual blade in-flight deformations. In addition to rotor cases, the method was used to calculate the static deflections for wind turbine cases as well as the dynamic deformation of the fins of missiles at high speed.

Once the mesh deformation method was developed, efforts were directed towards development test cases with available experimental data. This proved difficult. So, a lot of weight was put on the verification of the solution, in terms of mesh convergence, size of the computational domain and time convergence for unsteady calculations. A first study on the grid convergence for a hovering rotor showed that a fine grid in the rotor wake is required to accurately capture the rotor wake and thus the rotor performance, and more specifically the torque coefficient.

A demonstration of the hybrid mesh deformation method on a highly-loaded HART-II rotor showed that the grid quality was maintained after the transformation, leading to similar stall predictions. The method showed no overhead in terms of CPU-cost, and no loss of stability. The method was also demonstrated for the ONERA 7A rotor in forward flight, showing the effect of prescribed flapping deformations. The blade deformation led to important changes in phase and amplitude of the main flow features in the blade loading, mainly in the normal force dip on the advancing side.

The aeroelastic coupling was applied to a hovering UH-60A rotor. An iterative method was adopted, based on exchange of data between the FEM and fluid flow domains. Sectional loadings were extracted from the fluid simulation and used in NASTRAN to compute the blades static structural deformation. This structural deformation was then imposed on the blade, and the rest of the CFD grid had to be updated using the new hybrid method. After convergence, the aerodynamic loads were transferred again to NASTRAN and the cycle was repeated until a final blade shape was reached. The method needed three iterations to converge. The resulting blade deformation was small, which induced

limited changes to the aerodynamic loads. However, the trend in the evolution of the Figure of Merit with the thrust coefficient was improved by the inclusion of aeroelastic effects. The agreement of the results with experimental measurements was good on the main part of the blade, but the tip loading in the area where the blade crossed the vortex from the preceeding blade showed discrepancies with experimental data. Uncertainties on the blade geometry and the structural properties could account for these differences. Overall, the performance of the hybrid method was adequate and the results from tests where large deformations were imposed on the blade did not show any substantial limitations of the method.

Moving on from the development of the structural deformation method, a study on the impact of DES on rotorcraft flow predictions was also carried out. The aim was to assess the capability of DES in predicting higher frequency content of the aerodynamic loading, which, in turn, might improve the predictions for the structural stimulations and vibration levels. The DES was first assessed on a stalled flow, using a NACA0021 wing with an incidence of 60 degrees. DES was able to improve the frequency content of the loads, capturing the Kármán way in the wake of the aerofoil, while URANS only predicted a steady flow. DES was also able to predict spanwise variations of the loads and this was a further improvement over the URANS method. The integrated loads also showed improvement. While URANS was predicting limited time variation, DES managed to deliver results in broad agreement with the experiments across the frequency spectrum. The shedding frequency of the vortices was captured and the results were in fair agreement with experiments. In the literature, several versions of DES have recently been proposed. It was therefore challenging to find out a DES method that is particularly suited for stalled flows. The challenge was harder because of the limitations in grid size and run times throughout this PhD study. There were differences between the various DES models predictions, with some models giving similar results. However, the DES model with a halved C_{DES} coefficient was more suitable for predicting the structures in the flow when used in coarse grids. For rotorcraft flows, the ability of DES models to predict the stalled flow behind a stalled aerofoil should in principle improve the predictions of the flow in the wake of the hub, at the root of the blades and at stalled sections, where detached flows appear. Similar shedding could be captured thanks to DES and interact with the flow

around a blade in the back of the disk, therefore improving the predictions. This could be particularly useful in vibration predictions and acoustics where higher frequencies need to be accurately captured.

DES was then applied to forward flying rotors. A first study on the ONERA 7A and 7AD rotors showed a high level of vibrations at very high frequency at the back of the disk. This high variation due to the flow turbulence were expected, because the rotor was flying through the wake it generated. Regardless of this positive results, new test cases had to be solved, since the ONERA 7A and 7AD rotors did not have adequate experimental data to be compared against DES. For this reason, more recent experiments were identified in the literature. DES was then applied to the HART-II rotor in slow descending flight. The blade elastic deformation were prescribed, using experimental measurements. The mesh deformation showed no lack of stability, and a limited overhead in terms of CPU-cost. Thanks to the fine grid, strong BVIs were captured at the rear of the disk. They agreed with experimental measurements, but appeared slightly more forward in the disk. This appeared to come from the rotor trim state, that did not match the experimental one. The amplitude of the loads vibration was also smaller than in the experiments. The differences between DES and URANS showed limited, despite the use of a finer grid and smaller time steps. Slight improvements in the BVI amplitudes were however noted on the rear of the disk. A comparison of the vortex cores with PIV-measurements showed that the numerical dissipation of the vortices strength lead to lower loads vibration in the BVIs. To realise the full potential of DES, finer grids and further reductions in the time step of the simulations are necessary.

As a final test for the employed methods, the well-known experiments of NASA/US Army were used, where the solver was asked to predict both the aerodynamics and the shape of the blade. A strong aeroelastic coupling strategy was chosen. In general, with a structural damping level at $\zeta = 0.3$, three revolutions were enough to reach convergence on the deformations. The aeroelastic coupling method proved able to capture the characteristic dip in the normal force on the advancing side, due to the high torsional deformation, which was already shown in previous works in the literature. The study showed the dependency of the results to many parameters. The most important ones were the time step and mesh sizes. The structural damping was also shown to have an influence on the blade deformation, due to the low aerodynamic damping. Out of these calculations, the first conclusion was that the coupling

method, implicit or leap-frog, did not have a strong influence on the obtained results. On the other hand, the time step and mesh size appeared to have an influence. This conclusion agrees with what was found from our DES studies where, again, the employed grid and time step were perhaps not enough to fully resolve the complex rotor flow.

9.2 Suggestions for Future Work

Future studies shall look at the effect of the trim state and develop a trimming method compatible with the current strong coupling method. The current trim method, changing the trim step between two time steps, may introduce oscillations in the simulation that need long time to be damped out. The effect of the grid size should also be studied. The influence of the fuselage in some flight conditions, as well as the hub wake could also improve the predictions, mainly at the back of the disk where the blade passes over the tail of the helicopter and in the wake of the hub. Clearly, multi-million nodes grids are required to resolve vortex cores and fine scales of turbulence.

Acoustic predictions should also be looked at. Aeroelastic deformations have been shown to have an effect on the location and the strength of the BVIs, which lead to high noise levels. Their prediction could be improved by the inclusion of aeroelastic effects, especially if combined with a high order spatial scheme of low dispersion and fine grids.

The availability of comprehensive data at usual flight conditions in the open literature could improve the validation of the aeroelastic coupling. The BVI conditions used in the HART-II test case led to costly simulations. Comprehensive measurements at more standard flight conditions would allow for affordable validation of the coupling method. At present, no such data is available.

A further study of DES should be carried out. The minimum grid and step size to obtain noticeable differences between URANS predictions and DES ones should be investigated. However, such a study would require extremely high computational resources.

The aeroelastic coupling method should also be generalised to other flows. Studies are in progress in Liverpool to assess the influence of aeroelastic deformation for flows around wind-turbines

and missiles inside a cavity. Other domains of application could also be envisioned, such as turbomachinery and propeller flows.

Bibliography

[1] J.G. Leishman, *Principles of Helicopter Aerodynamics*. Cambridge University Press, Cambridge, UK, second edition, 2000.

[2] D.H. Hodges, X. Shang, and C.E.S. Cesnik, Finite Element Solution of Nonlinear Intrinsic Equations for Curved Composite Beams, *Journal of the American Helicopter Society*, 41(4):313–321, October 1996.

[3] W.K. Wilkie, P.H. Mirick, and C.W. Langston, Rotating Shake Test and Modal Analysis of a Model Helicopter Rotor Blade, Technical Memorandum NASA-TM-4760, NASA, June 1997.

[4] K.S. Hamade and R.M. Kufeld, Modal Analysis of UH-60A Instrumented Rotor Blades, Technical Memorandum NASA-TM-4239, NASA, 1990.

[5] E.C. Smith and I. Chopra, Aeroelastic Response, Loads and Stability of a Composite Rotor in Forward Flight, *AIAA Journal*, 31(7):1265–1273, July 1993.

[6] A.D. Stemple and S.W. Lee, Large Deflection Static and Dynamic Finite Element Analysis of Composite Beams with Arbitrary Cross Sectional Warping, In *AIAA 30th Structures, Structural Dynamics and Materials Conference, Mobile, AL*, 3–5 April 1989, AIAA-1989-1363.

[7] J.C. Ho, H. Yeo, and R.A. Ormiston, Investigation of Rotor Blade Structural Dynamics and Modeling Based on Measured Airloads, *Journal of Aircraft*, 45(5):1631–1642, September–October 2008.

[8] K.V. Truong, Dynamics Studies of the ERATO blade, based on Finite Element Analysis. 31th European Rotorcraft Forum, Florence, Italy, September 13–15 2005, Paper 94.

[9] A. Datta and W. Johnson, A Multibody Formulation for Three Dimensional Bick Finite Element Based Parallel and Scalable Rotor Dynamic Analysis, In *American Helicopter Society 66th Annual Forum, Phoenix, AZ*, May 11–13 2010.

[10] H. Yeo and W. Johnson, Comparison of Rotor Structural Loads Calculated Using Comprehensive Analysis, In *31st European Rotorcraft Forum, Florence, Italy*, September 13–15 2005.

[11] D.M. Tang and E.H. Dowell, Experimental and theoretical study for nonlinear aeroelastic behaviour of a flexible rotor blade, *AIAA Journal*, 31(6):1133–1142, June 1993.

[12] D.H. Hodges and E.H. Dowell, Nonlinear Equations of Motion for the Elastic Bending and Torsion of Twisted Nonuniform Rotor Blades, Technical Note NASA TN D-7818, NASA, December 1974.

[13] S.R. Turnour and R. Celi, Modeling of Flexible Rotor Blades for Helicopter Flight Dynamics Applications, *Journal of the American Helicopter Society*, 41(1):52–66, January 1996.

[14] D.M. Tang and E.H. Dowell, Nonlinear rotor aeroelastic analysis with stall and advanced wake dynamics, *Journal of Aircraft*, 34(5):679–687, September–October 1997.

[15] P. Beaumier, N. Jobard, M. Costes, C. Tung, S. Low, and L. Dadone, Evaluation of Airload Prediction Methodologies Using BH-360 Test Data, In *American Helicopter Society 53rd Annual Forum, Virginia Beach, VA*, pages 1017–1027, April 29–May 1 1997.

[16] L. Dadone, S. Dawson, D. B. Boxwell, and D. Ekquist, Model 360 Rotor Test at DNW, In *American Helicopter Society 43rd Annual Forum, St Louis, MO*, May 18–20 1987.

[17] B.E. Wake and J.D. Baeder, Evaluation of a Navier-Stokes Analysis Method for Hover Performance Prediction, *Journal of the American Helicopter Society*, 41(1):7–17, January 1996.

[18] M. Dietz, M. Kessler, and E. Krämer, Trimmed simulation of a complete helicopter configuration using fluid-structure coupling, In *High Performance Computing in Science and Engineering '07*, pages 487–501. Springer Berlin Heidelberg, 2008.

[19] F.J. Blom, Considerations on the Spring Analogy, *International Journal for Numerical Methods in Fluids*, 32(6):647–668, 2000.

[20] A. Dugeai, Aeroelastic Developments in elsA Code and Unsteady RANS Applications. nternational Forum on Aeroelasticity and Structural Dynamics' 2005, Munich, Germany, June 28–July 1 2005, IFASD-2011-079.

[21] B. Ortun, D. Petot, K.V. Truong, and R. Ohayon, Towards a New Generation of Rotorcraft Comprehensive Analysis; Coupling with CSM and CFD, In *34th European Rotorcraft Forum, Liverpool, UK*, September 16–18 2008, Paper 6a2.

[22] M.J. Smith, D.H. Hodges, and C.E.S. Cesnik, Evaluation of Computational Algorithms Suitable for Fluid-Structure Interactions, *Journal of Aircraft*, 37(2):282–294, March–April 2000.

[23] T.C.S. Rendall and C.B. Allen, Unified Fluid-Structure Interpolation and Mesh Motion Using Radial Basis Functions, *International Journal for Numerical Methods in Fluids*, 74:1519–1559, 2008.

[24] Thomas Gerhold and Jens Neumann, The Parallel Mesh Deformation of the DLR TAU-Code, In *New Results in Numerical and Experimental Fluid Mechanics VI*, volume 96 of *Notes on Numerical Fluid Mechanics and Multidisciplinary Design*, pages 162–169. Springer Berlin / Heidelberg, 2008.

[25] R.T. Biedron and E. Lee-Rausch, Rotor Airloads Prediction Using Unstructured Meshes and Loose CFD/CSD Coupling, In *AIAA 26th Applied Aerodynamics Conference, Honolulu, HI*, August 18–21 2008, AIAA-2008-7341.

[26] S.-H. Yoon, J.S. Kwak, S.J. Shin, and C. Kim, Loosely Coupled CFD/CSD Analysis for a Helicopter Rotor in Hover and Forward Flight, In *American Helicopter Society Specialists' Conference on Aeromechanics, San Francisco, California*, January 20–22 2010.

[27] X. Liu, N. Qin, and H. Xia, Fast Dynamic Deformation Based on Delaunay Graph Mapping, *Journal of Computational Physics*, 211(2):405–423, January 2006.

[28] G. Servera, P. Beaumier, and M. Costes, A Weak Coupling Method Between the Dynamics Code HOST and the Unsteady Euler Code WAVES, *Aerospace Science and Technology*, 5(6):397–408, September 2001.

[29] P. Beaumier, E. Chelli, and K. Pahlke, Navier-Stokes Predictions of Helicopter Rotor Performance in Hover Including Aeroelastic Effects, *Journal of the American Helicopter Society*, 46(4):301–309, 2001.

[30] A.R.M. Altmikus, S. Wagner, P. Beaumier, and G. Servera, A Comparison: Weak versus Strong Modular Coupling For Trimmed Aeroelastic Rotor Simulations, In *American Helicopter Society 58th Annual Forum*, June 2002.

[31] K. Pahlke and B.G. van der Wall, Chimera Simulations of Multibladed Rotors in High-Speed Forward Flight With Weak Fluid-Structure-Coupling, *Aerospace Science and Technology*, 9(5):379–389, July 2005.

[32] D.C. Wilcox, Simulation of Transition with a Two-Equation Turbulence Model, *AIAA Journal*, 32(2):247–255, February 1994.

[33] H.S. Dol, J.C. Kok, and B. Oskam, Assessment of Explicit Algebraic Stress Models in Transonic Flows, In *AIAA 40th Aerospace Sciences Meeting and Exhibit, Reno, Nevada*, January 14–17 1999, AIAA-2002-843.

[34] H. Pomin and S. Wagner, Aeroelastic Analysis of Helicopter Rotor Blades on Deformable Chimera Grids, *Journal of Aircraft*, 41(3):577–584, May–June 2004.

[35] H. Pomin and S. Wagner, Navier-Stokes Analysis of Helicopter Rotor Aerodynamics in Hover and Forward Flight, *Journal of Aircraft*, 39(5):813–821, September–October 2002.

[36] K.G. Pahlke, The GOAHEAD Program, In *33rd European Rotorcraft Forum, Kazan, Russia*, September 11–13 2007.

[37] M. Potsdam, H. Yeo, and W. Johnson, Rotor Airloads Prediction Using Loose Aerodynamic/Structural Coupling, In *American Helicopter Society 60th Annual Forum, Baltimore, MD*, pages 497–518, June 7–10 2004.

[38] J. Sitaraman and B. Roget, Prediction of Helicopter Maneuver Loads Using a Fluid-Structure Analysis, *Journal of Aircraft*, 46(6):1957–1964, November–December 2009.

[39] R.T. Biedron and E. Lee-Rausch, Computation of UH-60A Airloads Using CFD/CSD Coupling On Unstructured Meshes, In *American Helicopter Society 67th Annual Forum, Virginia Beach, VA*, May 3–5 2011.

[40] Ph. Spalart and S.R. Allmaras, A One-Equation Turbulence Model for Aerodynamic Flows, *La Recherche Aérospatiale*, 1:5–21, 1994.

[41] F.R. Menter, Two-Equation Eddy-Viscosity Turbulence Models for Engineering Applications, *AIAA Journal*, 32(8):1598–1605, August 1994.

[42] M. Sanchez-Rocha, *Wall-Models for Large Eddy Simulation Based on a Generic Additive-Filter Formulation*, PhD thesis, Georgia Institute of Technology, Atlanta, GA, May 2009.

[43] J.D. Singleton and W.T Yeager, Important Scaling Parameters for Testing Model-Scale Helicopter Rotors, *Journal of Aircraft*, 37(3):396–402, May–June 2000.

[44] P.P. Friedmann, Aeroelastic Scaling for Rotary-Wing Aircraft with Applications, *Journal of Fluids and Structures*, 19(5):635–650, June 2004.

[45] K.J. Schultz, W. Splettstoesser, B. Junker, W. Wagner, G. Arnaud, E. Schoell, D. Fertis, E. Mercker, and K. Pengel, A Parametric Windtunnel Test on Rotorcraft Aerodynamics and Aeroacoustics (Helishape) — Test Procedures and Representative Results, *Aeronautical Journal*, 101(1004):143–154, April 1997.

[46] O.D. Wong, A.N. Watkins, and J.L. Ingram, Pressure Sensitive Paint Measurements on 15% Scale Rotor Blades in Hover, In *AIAA 35th Fluid Dynamics Conference and Exhibit*, June 6–9 2005, AIAA-2005-5008.

[47] R.J. Flemming, An Experimental Evaluation of Advanced Rotorcraft Airfoils in the NASA Ames Eleven-Foot Transonic Wind Tunnel, Technical Report CR-166587, NASA, September 1984.

[48] K.W. Noonan, Jr W.T. Yeager, J.D. Singleton, M.L. Wilbur, and P.H. Mirick, Wind Tunnel Evaluation of a Model Helicopter Main Rotor Blade With Slotted Airfoils at the Tip, Technical Report NASA/TP-2001-211260, NASA Technical Publication, December 2001.

[49] B.G. van der Wall, C.L. Burley, Y. Yu, H. Richard, K. Pengel, and P. Beaumier, The HART II Test — Measurement of Helicopter Rotor Wakes, *Aerospace Science and Technology*, 8(4):273–284, June 2004.

[50] C.P. Coleman and W.G. Bousman, Aerodynamic Limitations of the UH-60A Rotor, Technical Memorandum TM-110396, NASA, August 1996.

[51] J.G.M. Leung, M.Y. Wei, and M. Aoyagi, UH-60A Airloads Data Acquisition and Processing System, In *AIAA/IEEE 13th Digital Avionics Systems Conference*, pages 206–211, October 30–November 3 1994.

[52] R.M. Kufeld, D.L. Balough, J.L. Cross, K.F. Studebaker, C.D. Jennison, and W.G. Bousman, Flight Testing of the UH-60A Airloads Aircraft, In *American Helicopter Society 50th Annual Forum, Alexandria, VA*, May 1994, .

[53] D.C. Wilcox, Multiscale Model for Turbulent Flows, *AIAA Journal*, 26(11):1311–1320, November 1988.

[54] T. Rung, H. Lübcke, M. Franke, L. Xue, F. Thiele, and S. Fu, Assessment of Explicit Algebraic Stress Models in Transonic Flows, In *4th International Symposium on Engineering Turbulence Modelling and Measurements, Corsica, France*, pages 659–668, May 24–26 1999.

[55] M. Dietz and O. Dieterich, Towards Increased Industrial Application of Rotor Aeroelastic CFD, In *35th European Rotorcraft Forum, Hamburg, Germany*, September 2009, Paper 101185.

[56] S. Borie, J. Mosca, L. Sudre, C. Benoit, and S. Péron, Influence of Rotor Wakes on Helicopter Aerodynamic Behaviour, In *35th European Rotorcraft Forum, Hamburg, Germany*, September 22–25 2009, Paper No 1205.

[57] M. Potsdam, M. Smith, and T. Renaud, Unsteady Computations of Rotor-Fuselage Interaction, In *35th European Rotorcraft Forum, Hamburg, Germany*, September 22–25 2009, Paper 1230.

[58] W. Khier, Numerical Simulation of Air Flow Past a Full Helicopter Configuration, In *35th European Rotorcraft Forum, Hamburg, Germany*, September 22–25 2009, Paper 1207.

[59] T. Renaud, D. O'Brien, M. Smith, and M. Potsdam, Evaluation of Isolated Fuselage and Rotor-Fuselage Interaction Using Computational Fluid Dynamics, *Journal of the American Helicopter Society*, 53(3):3–17, January 2008.

[60] B.-Y. Min, L.N. Sankar, N. Rajmohan, and J.V.R. Prasad, Computational Investigation of Gurney Flap Effects on Rotors in ForwardFlight, *Journal of Aircraft*, 46(6):1957–1964, November–December 2009.

[61] P. Spalart, W.H. Jou, M.Kh. Strelets, and S.R. Allmaras, Comments on the Feasibility of LES for Wings, and on a Hybrid RANS/LES Approach, In *First AFOSR International Conference on DNS/LES, Columbus, OH*, August 1997.

[62] R. Steijl and G. Barakos, Computational Study of Helicopter Rotor-Fuselage Aerodynamin Interactions, *AIAA Journal*, 47(9):2143–2157, September 2009.

[63] M.J. Smith, N.D. Ligett, and B.C.G. Koukol, Aerodynamics of Airfoils at High and Reverse Angles of Attack, *Journal of Aircraft*, 48(6):2012–2023, November–December 2011.

[64] G.N. Barakos, *Study of Unsteady Aerodynamics Phenomena Using Advanced Turbulence Closure*, PhD thesis, University of Manchester Institute of Science and Technology, April 1999.

[65] Ph. Spalart, Strategies for Turbulence Modelling and Simulations, *International Journal of Heat and Fluid Flow*, 21(3):252–263, June 2000.

[66] A. Juneja, D.P. Lathrop, K.R. Sreenivasan, and G. Stolovitzky, Synthetic Turbulence, *Physical Review E*, 49(6):5179–5194, June 1994.

[67] G. Martinat, R. Bourguet, Y. Hoarau, F. Dehaeze, B. Jorez, and M. Braza, Numerical Simulation of the Flow in the Wake of Ahmed Body Using Detached Eddy Simulation and URANS Modeling, In *Advances in Hybrid RANS-LES Modelling*, volume 97 of *Notes on Numerical Fluid Mechanics and Multidisciplinary Design*, pages 125–131. Springer Berlin / Heidelberg, 2008.

[68] J.S. Batten, U.C. Goldberg, and S.R. Chakravarthy, Sub-Grid Turbulence Modeling for Unsteady Flow with Acoustic Resonance, In *AIAA 38th Aerospace Sciences Meeting, Reno, NV*, January 10–13 2000, AIAA-00-0473.

[69] P. Nayyar and G. Barakos, A Summary of Turbulence Modelling Approaches in CFD, Aerospace Engineering Report 0206, University of Glasgow, September 2002.

[70] P. Spalart, S. Deck, M.L. Shur, K.D. Squires, M.Kh. Strelets, and A. Travin, A New Version of Detached-Eddy Simulation, Resistant to Ambiguous Grid Densities, *Theoretical and Computational Fluid Dynamics*, 20:181–195, 2006.

[71] S. Deck, P. Weiss, M. Pamiès, and E. Garnier, On the Use of Stimulated Detached Eddy Simulation (SDES) for Spatially Developing Boundary Layers, In *Advances in Hybrid RANS-LES Modelling*, volume 97 of *Notes on Numerical Fluid Mechanics and Multidisciplinary Design*, pages 67–76. Springer Berlin / Heidelberg, 2008.

[72] M.L. Shur, P. Spalart, M.Kh. Strelets, and A. Travin, A Hybrid RANS-LES Approach with Delayed-DES and Wall-Modelled LES Capabilities, *International Journal of Heat and Fluid Flow*, 29(2008):1638–1649, 2008.

[73] O. Reynolds, On the Dynamical Theory of Incompressible Viscous Fluids and the Determination of the Criterion, *Philosophical Transactions of the Royal Society of London*, A(186):123–164, 1895.

[74] J. Boussinesq, *Théorie de l'Écoulement Tourbillonant et Tumultueux des Liquides dans des Lits Rectilignes à Grande Section, Tome I-II*. Gaulthier-Villars, Paris, France, first edition, 1897.

[75] A. Jameson, Time Dependent Calculations Using Multigrid, with Applications to Unsteady Flows Past Airfoils and Wings, In *10th Computational Fluid Dynamics Conference, Honolulu, HI*, 1991, AIAA-91-1596.

[76] S. Osher and S. Chakravarthy, Upwind Schemes and Boundary Conditions with Applications to Euler Equations in General Geometries, *Journal of Computational Physics*, 50:447–481, January–February 1983.

[77] P.L. Roe, Approximate Riemann Solvers, Parameter Vectors, and Difference Schemes, *Journal of Computational Physics*, 43(2):357–372, October 1981.

[78] B. van Leer, Flux-vector splitting for the euler equations, In *Eighth International Conference on Numerical Methods in Fluid Dynamics*, volume 170 of *Lecture Notes in Physics*, pages 507–512. Springer Berlin / Heidelberg, 1982.

[79] O. Axelsson, *Iterative Solution Methods*. Cambridge University Press, Cambridge, MA, edition, 1994.

[80] M. Woodgate, K. Badcock, B. Richards, and R. Gatiganti, A Parallel 3D Fully Implicit Unsteady Multiblock CFD Code Implemented on a Beowulf Cluster, In *Parallel CFD 1999, Williamsburg, VA, USA*, 1999.

[81] UK Research Councils, HECToR: UK National Supercomputing Service, http://www.hector.ac.uk/, 2007.

[82] P. Chassaing, *Turbulence en Mécanique des Fluides*. Cépaduès-Éditions, Toulouse, France, first edition, 2000.

[83] M.V. Morkovin, Effects of Compressibility on Turbulent Flows, *Mécanique de la Turbulence*, 108:367–380, 2007. Coll. CNRS, CNRS, Paris.

[84] T. Cebeci and A. M. O. Smith, *Analysis of Turbulent Boundary Layers*. Number 15. Applied Mathematics and Mechanics. Academic Press, New York, NY, 1974.

[85] B. Baldwin and H. Lomax, Thin-layer Approximation and Algebraic Model for Separated Turbulent Flows, In *AIAA 16th Aerospace Sciences Meeting, Huntsville, AL.*, January 16–18 1978.

[86] B. S. Baldwin and T. J. Barth, A One-Equation Turbulence Transport Model for High Reynolds Number Wall-Bounded Flows, Technical Memorandum NASA-TM-102847, NASA, August 1990.

[87] W.P Jones and B.E Launder, The Prediction of Laminarization with a Two-Equation Model of Turbulence, *International Journal of Heat and Mass Transfer*, 15(2):301–314, 1972.

[88] S. Moir and A. Gould, VoTMATA — British Aerospace Default Model, Technical report, BAE SYSTEMS, 1998.

[89] K. Hanjalić and B. E. Launder, A Reynolds Stress Model of Turbulence and its Application to Thin Shear Flows, *Journal of Fluid Mechanics*, 52:609–638, 1972.

[90] P. A. Durbin, Near-Wall Turbulence Closure Modeling without Damping Functions, *Theoretical and Computational Fluid Dynamics*, 3(1):1–13, 1991.

[91] T.J. Craft, B.E. Launder, and K. Suga, Development and Application of a Cubic Eddy-Viscosity Model of Turbulence, *International Journal of Heat and Fluid Flow*, 17(2):108–115, 1996.

[92] T. P. Sommer, R. M. C. So, and H. S. Zhang, A Near-Wall Four-Equation Turbulence Model for Compressible Boundary Layers, Technical Report NASA-CR-4436, NASA, April 1992.

[93] P. Malecki, *Étude de Modèles de Turbulence pour les Couches Limites Tridimensionnelles*, PhD thesis, ENSAE, Toulouse, France, 1994.

[94] K. Hanjalic, B. E. Launder, and R. Schiestel, Multiple-Time-Scale Concepts in Turbulent Transport Modeling, In *Von Karman Institute for Fluid Dynamics Measurements and Predictions of Complex Turbulent Flows*, volume 1, 1980.

[95] S.-W. Kim, Numerical Investigation of Separated Transonic Turbulent Flows with a Multiple-Time-Scale Turbulence Model, Technical Memorandum NASA-TM-102499, NASA, January 1990.

[96] C.P. Chen, A Non-Isotropic Multiple-Scale Turbulence Model, Technical Report NASA-CR-184217, NASA, September 1990.

[97] S. Deck, Ph. Duveau, P. d'Espiney, and Ph. Guillen, Development and Application of Spalart-Allmaras One Equation Turbulence Model to Three-Dimensional Supersonic Complex Configurations, *Aerospace Science and Technology*, 6(3):171–183, March 2002.

[98] P.R. Spalart and M. Shur, On the Sensitization of Turbulence Models to Rotation and Curvature, *Aerospace Science and Technology*, 1(5):297–302, July 2002.

[99] T. Rung, U. Bunge, M. Schatz, and F. Thiele, Restatement of the Spalart-Allmaras Eddy-Viscosity Model in Strain-Adaptative Formulation, *AIAA Journal*, 74(7):1396–1399, July 2003.

[100] A.N. Kolmogorov, Equations of Turbulent Motion of an Incompressible Turbulent Fluid, *Izvestiya Akademii Nauk SSSR, Seriya Fizicheskaya*, 6(1–2):56–58, 1942.

[101] F. H. Harlow and P. I. Nakayama, Turbulence Transport Equations, *Journal of Fluid Mechanics*, 10(11):2323–2332, 1967.

[102] D.B. Spalding, The Prediction of Two-Dimensional, Steady Turbulent Flows, Technical Report Heat Transfer Section Report EF/TN/A/16, Imperial College, 1969.

[103] C.G. Speziale and P.S. Bernard, The Energy Decay in Self-Preseving Isotropic Turbulence Revisited, *Journal of Fluid Mechanics*, 241:645–667, 1992.

[104] D.A. Johnson and L.S. King, A Mathematically Simple Turbulence Closure Model for Attached and Separated Turbulent Boundary Layers, *AIAA Journal*, 23(11):1684–1692, November 1985.

[105] M. Strelets, Detached Eddy Simulation of Massively Separated Flows, In *AIAA 39th Aerospace Sciences Meeting and Exhibit, Reno, NV*, January 8–11 2001, AIAA-2001-0879.

[106] N. A. Ridhwan Nik Mohd and G. N. Barakos, Computational Aerodynamics of Hovering Helicopter Rotors, In *RAeS Aerodynamics Conference 2010, Bristol, UK*, July 27–28 2010.

[107] R. Steijl, G. Barakos, and K. Badcock, A Framework for CFD Analysis of Helicopter Rotors in Hover and Forward Flight, *International Journal for Numerical Methods in Fluids*, 51(8):819–847, 2006.

[108] P. Beaumier, J. Decours, and T. Lefebvre, Aerodynamic and Aero-Acoustic Design of Modern Tilt-Rotors: the ONERA Experience, In *26th International Congress of the Aeronautical Sciences, Anchorage, AK*, September 14–19 2008, ICAS 2008-1.7.4.

[109] P. Crozier, Tests on ADYN and TILTAERO Rotor Blades Performed in S1 Modane Wind Tunnel, Technical Report PV 1/10971 DAAP/DSMA, Modane-Avrieux Wind Tunnels Department, February 2007.

[110] P. Arcidiacono and R. Zincone, Titanium UTTAS Main Rotor Blade, *Journal of the American Helicopter Society*, 21(2):12–19, 1976.

[111] MSC.Software Corporation, *MSC.Nastran 2005 Release Guide*. Macmillan, 2005.

[112] G.H. Golub and C.F. van Loan, *Matrix Computations*. The Johns Hopkins University Press, Baltimore, MD, third edition, 1996.

[113] Robert M. Kufeld and David M. Nguyen, Full-Scale UH-60A Rotor Blade Nonrotating Modal Analysis Shake test, Technical Memorandum NASA-TM-101005, NASA, November 1989.

[114] A.R.S. Bramwell, G. Done, and D. Balmford, *Bramwell's Helicopter Dynamics*. Butterworth Heinemann, Oxford, UK, second edition, 2001.

[115] B.G. van der Wall, 2nd HHC Aeroacoustic Rotor Test (HART II) — Part I: Test Doumentation, Technical Report IB-111-2003/31, German Aerospace Center (DLR), 2003.

[116] G.S.L. Goura, K.J. Badcock, M.A. Woodgate, and B.E. Richards, Implicit Method for the Time Marching Analysis of Flutter, *Aeronautical Journal*, 105(1046), April 2001.

[117] A. Datta, J. Sitaraman, I. Chopra, and J.D. Baeder, CFD/CSD Prediction of Rotor Vibratory Loads in High-Speed Flight, *Journal of Aircraft*, 43(6):1698–1709, November–December 2006.

[118] L. Dubuc, F. Cantariti, M.A. Woodgate, B. Gribben, K.J. Badcock, and B.E. Richards, A Grid Deformation Technique for Unsteady Flow Computations, *International Journal for Numerical Methods in Fluids*, 32(3):285–311, 2000.

[119] K.E. Swalwell, J. Sheridan, and W.H. Melbourne, Frequency Analysis of Surface Presssures on an Airfoil After Stall. AIAA 21st Applied Aerodynamics Conference, Orlando, Florida, June 23–26 2003, AIAA-2003-3416.

[120] D. Guenot, *Simulation des Effets Instationnaires a Grande Échelle dans les Écoulements Décollés*, PhD thesis, SUPAERO, Toulouse, France, 2004.

[121] W. Haase, M. Braza, and A. Revell, *DESider — A European Effort on Hybrid RANS-LES Modelling*, volume 103 of *Notes on Numerical Fluid Mechanics and Multidisciplinary Design*. Springer Berlin / Heidelberg, 2009.

[122] P.F. Lorber, R.C. Stauter, and A.J. Landgrebe, A Comprehensive Hover Test of the Airloads and Airflow of an Extensively Instrumented Model Helicopter Rotor, In *American Helicopter Society 45th Annual Forum, Boston, MA*.

[123] P.F. Lorber, Aerodynamic Results of a Pressure-Instrumented Model Rotor Test at the DNW, *Journal of the American Helicopter Society*, 36(4):12–19, October 1991.

[124] S. Schmitz, M. Bhagwat, M.A. Moulton, F.X. Caradonna, and J.-J. Chattot, The Predictions and Validation of Hover Performance and Detailed Blade Loads, *Journal of the American Helicopter Society*, 54(1):1–12, 2009.

[125] K.C. Kim, Analytical Calculations of Helicopter Torque Coefficient (C_Q) and Thrust Coefficient (C_T) Values for the Helicopter Performance (HELPE) Model, Technical Report ARL-TR-1986, Army Research Laboratory, June 1999.

[126] S.J. Lawson and G.N. Barakos, Review of Numerical Simulations for High-Speed, Turbulent Cavity Flows, *Progress in Aerospace Sciences*, 47(3):186–216, April 2011.

[127] R. Steijl, G.N. Barakos, and K.J. Badcock, Computational Study of the Advancing-Side Lift-Phase Problem, *Journal of Aircraft*, 45(1):246–257, January–February 2008.

[128] B.G. van der Wall, Mode Identification and Data Synthesis of HART II Blade Deflection Data, Technical Report IB-111-2007/28, German Aerospace Center (DLR), 2007.

[129] J.W. Lim and R.C. Strawn, Computational Modeling of HART II Blade-Vortex Interaction Loading and Wake System, *Journal of Aircraft*, 45(3):923–933, May–June 2008.

[130] N. O. Myklestad, *Vibration Analysis*. McGraw-Hill Book Company, New York, NY, 1944.

Appendix A

Additional Blade Properties

During this research, CFD grids and structural models were also developed for several rotors. They are presented in this appendix, as evidence of the flexibility and robustness of the developed methods.

A.1 The HIMARCS Rotor

The HIMARCS is a four-bladed rotor. The properties of the HIMARCS blade were obtained from Noonan *et al.* [48]. Two aerofoil sections are used along the span. The inboard sections up to $r/R = 0.8$ uses the RC(4)-10 aerofoil. Between $r/R = 0.85$ and the tip, a RC(6)-08 aerofoil is used, and a linear transition is added between $r/R = 0.80$ and $r/R = 0.85$. The blade has a diameter of 56.224 in and a chord of 4.454 in, leading to an aspect ratio $\lambda = 12.6$. The blade has a built-in twist of 8 degrees/R. The blade geometry is shown in Figure A.1. The blade structural properties were obtained from Noonan *et al.* [48], and are shown in Figure A.2.

The structural model consists of 27 CBEAM elements along the quarter-chord line. The NASTRAN model is shown in Figure A.3. The frequencies of the seven first blade modes were extracted and compared to experimental measurements from Noonan *et al.* [48] for a cantilever blade in Table A.1. While the frequency of the first modes was accurately predicted, the error increased quickly with the frequency. The first torsional mode frequency was underestimated by 37%, which could lead to problems when

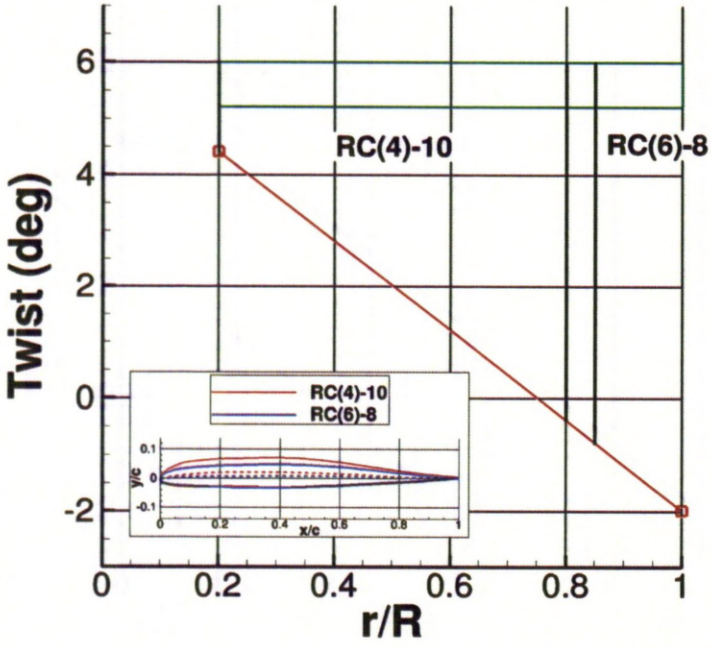

Figure A.1: Geometry of the HIMARCS blade.

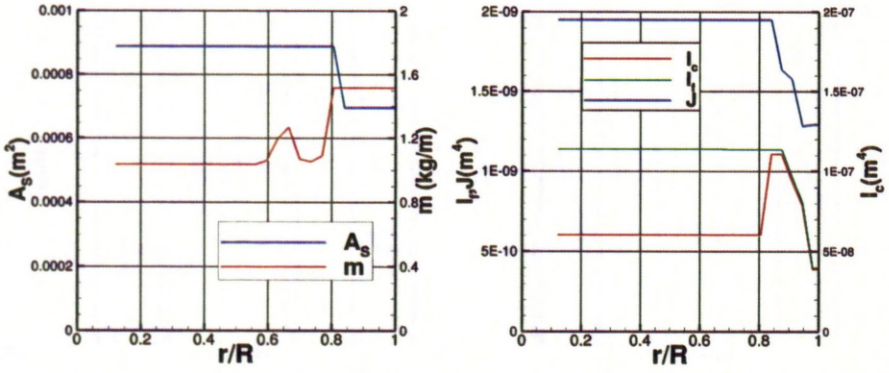

(a) Sectional area and linear mass distribution (b) Chordwise, flapwise and torsional area moment of inertia

Figure A.2: Structural properties of the HIMARCS blade.

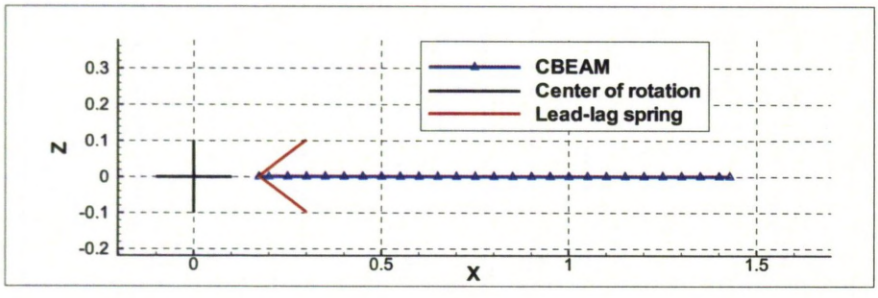

Figure A.3: Structural model of the HIMARCS blade.

used in a coupled simulation due to the importance of the torsion in the blade in-flight deformations.

Table A.1: Comparison of the natural frequencies of the HIMARCS cantilever blade between NASTRAN simulation and experimental measurements by Noonan *et al.* [48], in Hertz.

Mode	NASTRAN	Experiments
First flap	3.23	3.75
First chord	17.99	17.50
Second flap	21.21	23.50
Third flap	48.57	62.25
Second chord	58.09	n/a
First torsion	61.95	98.50
Forth flap	92.77	n/a

The evolution of the predicted natural frequencies with the rotational speed is shown in Figure A.4.

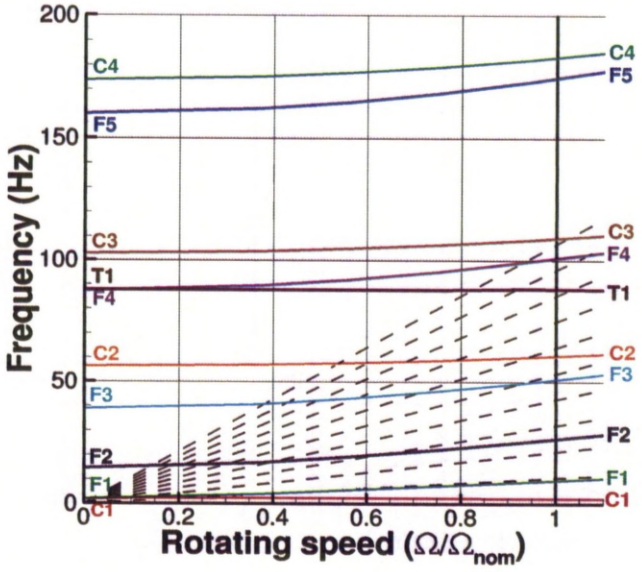

Figure A.4: Evolution of the natural frequencies of HIMARCS blade with the rotational speed. $\Omega_{nom} =$ 640 RPM. F denotes a flapping mode, C a chordwise mode and T a torsional mode.

A.2 The SO-1 Rotor

The SO-1 rotor contains four blades, with a RAE 9646 aerofoil section along the whole span. It has a radius of 1.5 m and a chord of 0.12 m, leading to an aspect ratio $\lambda = 12.5$. The blade geometry is shown

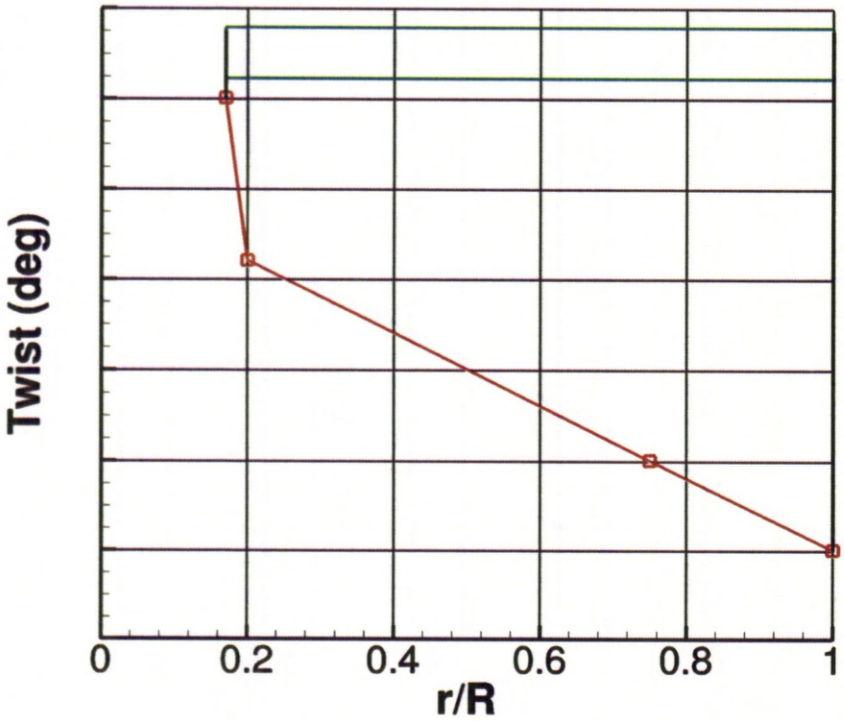

Figure A.5: Geometry of the SO-1 blade.

in Figure A.5. The structural properties of the blade were obtained from QinetiQ. They are shown in Figure A.6.

Table A.2: Natural frequencies of the SO-1 blade obtained by NASTRAN.

Mode	NASTRAN
First chord	2.49
Second flap	28.84
Third flap	78.28
Second chord	119.32
First torsion	136.15
Forth flap	163.62

The SO-1 blade was modelled in NASTRAN using 30 CBEAM elements. Young's modulus was tuned to get the second flapping mode frequency to match experimental measurements. A lead-lag damper was added, with a strength of 155.9N/rad. The NASTRAN model is shown in Figure A.7. The frequencies of the six first blade modes are shown in Table A.1.

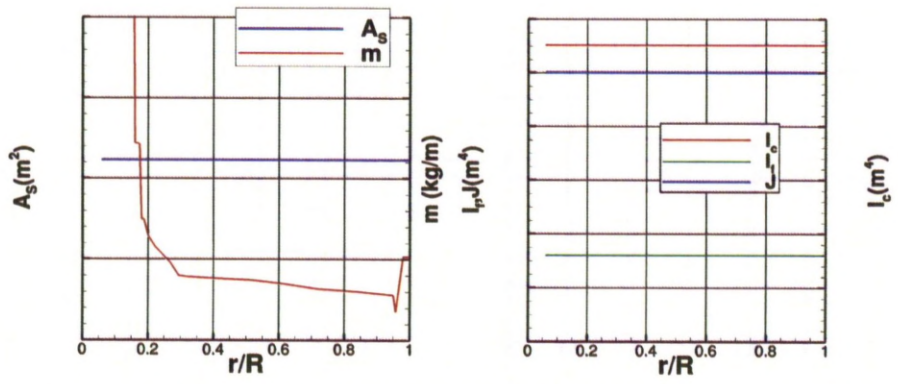

(a) Sectional area and linear mass distribution (b) Chordwise, flapwise and torsional area moments of inertia

Figure A.6: SO-1 blade structural properties.

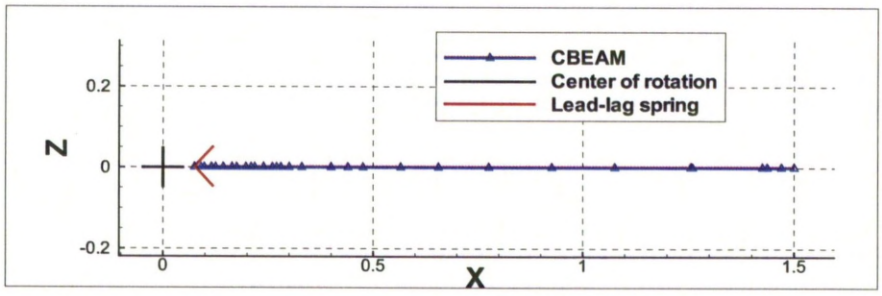

Figure A.7: Structural model of the SO-1 blade.

The evolution of the predicted natural frequencies with the rotational speed is shown in Figure A.8. A flapping spring with a stiffness of 155.9N/rad had to be added for ensuring the convergence of the NASTRAN calculation.

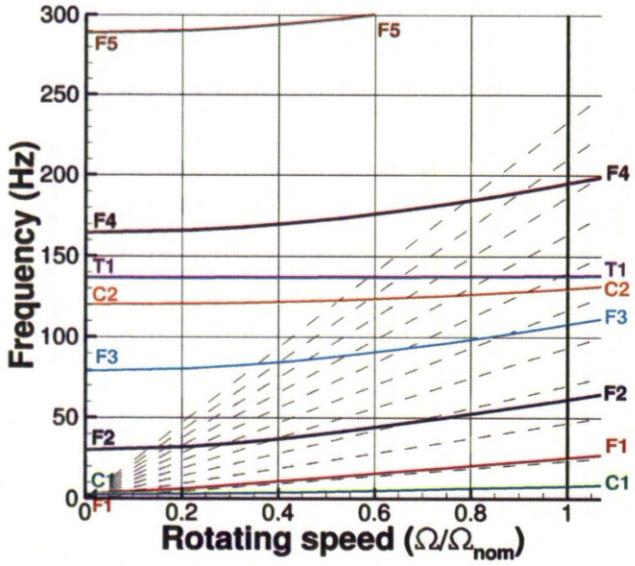

Figure A.8: Evolution of the natural frequencies of SO-1 blade with the rotational speed. $\Omega_{nom} = 1400$RPM. F denotes a flapping mode, C a chordwise mode and T a torsional mode.

A.3 The PM-3 and PM-4 Rotor

The PM-3 and PM-4 rotors have four blades with an advanced plan shape, featuring the BERP technology.

A.4 Model Main Rotors

Models for two main rotors (SK-1 and SK-2) were also developed. The blade geometries are shown in Figure A.9. Both blades have an aspect ratio of $\lambda = 20.4$. The structural properties of the two blades were obtained as follows: the structural properties of the UH-60A blade were extracted at mid-span and scaled using the sectional area of the SK-1 aerofoil section. Furthermore, the blade properties were scaled by the local chord at the tip of the SK-2 blade. The resulting structural properties are shown in

Figure A.10.

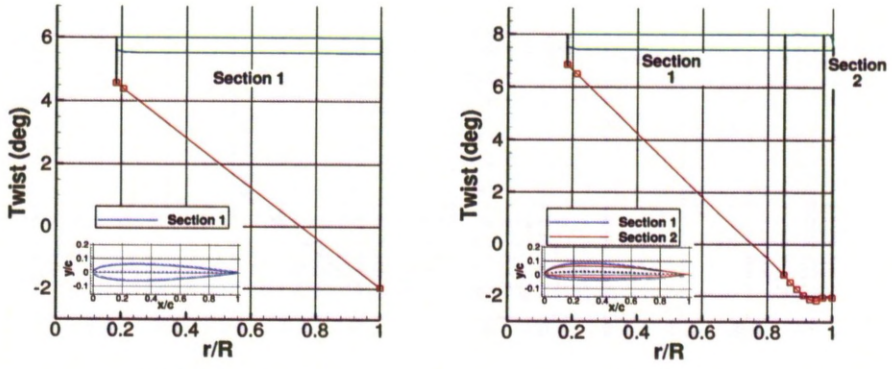

(a) SK-1 blade (b) SK-2 blade

Figure A.9: Geometry of the SK-1 and SK-2 blades.

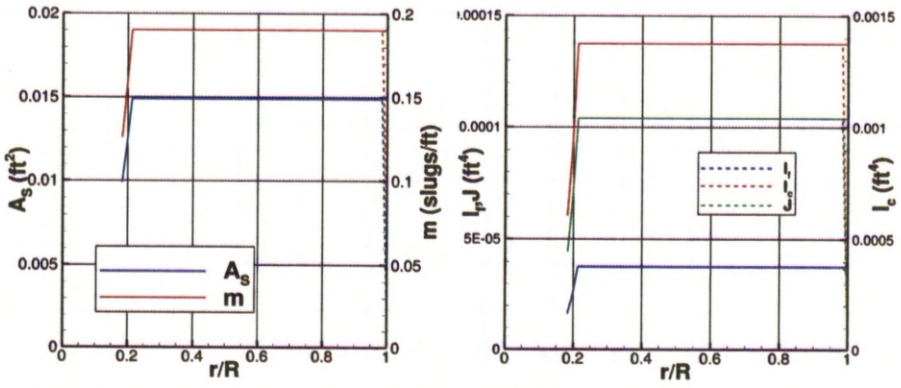

(a) Sectional area and linear mass distribution ($1\,ft^2 = 0.0929\,m^2$ and $1\,slug/ft = 47.88\,kg/m$) (b) Chordwise, flapwise and torsional area moments of inertia($1\,ft^4 = 0.00863\,m^4$)

Figure A.10: SK-1 (solid) and SK-2 (dashed) blades structural properties.

The SK blades were modelled in NASTRAN using 50 CBEAM elements. A lead-lag damper was added, with a strength of 353 lbf/rad (478.6 Nm/rad) as the UH-60A one. A flapping spring with a stiffness of 353 lbf/rad (478.6 Nm/rad) was also added in order to ensure the convergence of the calculation.

The evolution of the predicted natural frequencies with the rotational speed is shown in Figure A.12. Due to the different tip properties and twist, the difference between the natural frequencies showed limited when the blade was not rotating but increased with the rotational speed. At high rotational speed, the blade did not behave the same way anymore.

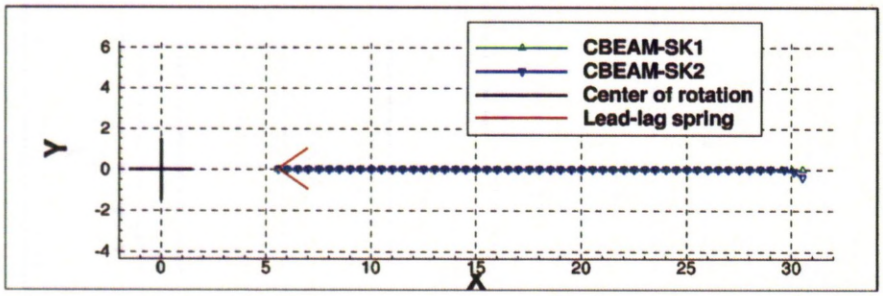

Figure A.11: Structural model of the SK-1 and SK-2 blades.

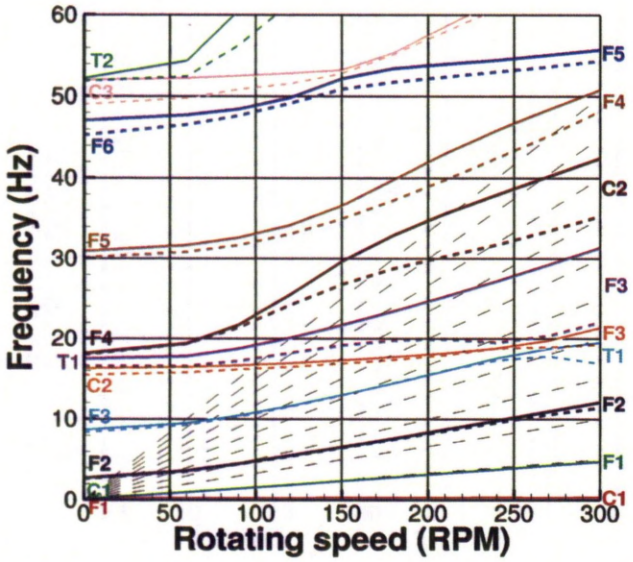

Figure A.12: Evolution of the natural frequencies of the SK-1 (solid) and SK-2 (dashed) blades with the rotational speed.

Appendix B

Myklestad's Method

Myklestad's method was developed to predict the natural frequencies of a beam. The beam is discretised, and stimulated at a frequency of ω. The boundary conditions allow for finding the natural frequencies.

B.1 Theory

B.1.1 Uncoupled Bending

A first method presented in [130] aims at obtaining the blade eigenmode shapes and frequencies for a bending blade, without coupled torsion. The blade is discretised in b nodes. The deformation is represented through the y_n and β_n parameters, that represent the vertical displacement and bending angle of the blade at the n-th node. as shown in Figure B.1. The beam is modelled by a mass distribution on

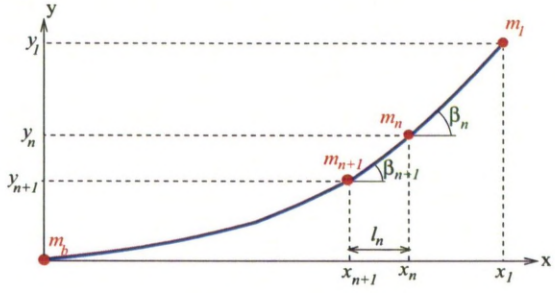

Figure B.1: Myklestad's method notations for the blade deformation.

each node on the elastic axis. The deformations obtained through a unit force or moment are calculated at each section, using the notations described in Figure B.2.

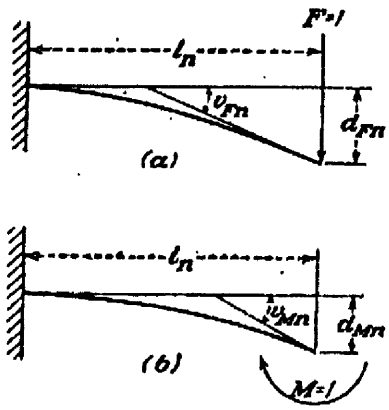

Figure B.2: Notations for the properties of the n-th section of the beam: deformation of the section for an unit bending force and moment applied at the tip[130].

For a rotating beam, the shear force and bending moment at the n-th node, noted S_n and M_n, equal:

$$S_n = \sum_{i=1}^{n} m_i \omega^2 y_i - \beta_n \sum_{i=1}^{n} m_i x_i \Omega^2 \tag{B.1}$$

$$M_n = \sum_{i=1}^{n-1} m_i \omega^2 y_i (x_i - x_n) - \sum_{i=1}^{n-1} m_i x_i \Omega^2 (y_i - y_n) \tag{B.2}$$

β is supposedly small, so the centrifugal force is parallel to the straight beam axis. Therefore, the beam deformation can be expressed as:

$$\beta_{n+1} = \beta_n - v_{Fn} S_n - v_{Mn} M_n \tag{B.3}$$

$$y_{n+1} = y_n - l_n \beta_{n+1} - d_{Fn} S_n - d_{Mn} M_n \tag{B.4}$$

which, using S_n and M_n definitions in B.1 and B.2, gives:

$$\beta_{n+1} = \beta_n \left(1 + v_{Fn} \sum_{i=1}^{n} m_i x_i \Omega^2 \right) - v_{Fn} \sum_{i=1}^{n} m_i \omega^2 y_i - v_{Mn} \sum_{i=1}^{n-1} \left[m_i \omega^2 y_i (x_i - x_n) - m_i x_i \Omega^2 (y_i - y_n) \right] \tag{B.5}$$

$$y_{n+1} = y_n - \beta_n \left[l_n + (l_n v_{Fn} - d_{Fn}) \sum_{i=1}^{n} m_i x_i \Omega^2 \right] + (l_n v_{Fn} - d_{Fn}) \sum_{i=1}^{n} m_i \omega^2 y_i + (l_n v_{Mn} - d_{Mn}) \sum_{i=1}^{n-1} \left[m_i \omega^2 y_i (x_i - x_n) - m_i x_i \Omega^2 (y_i - y_n) \right] \tag{B.6}$$

The blade deformation is computed for a tip displacement $y_1 = 1$ and a tip bending angle $\beta_1 = \varphi_{tip}$. Because of the linear character of the problem, β_n and y_n can be projected on the $(\beta_1 = \varphi_{tip}, y_1 = 1)$ basis:

$$\beta_n = f_{\varphi n}\varphi_{tip} - f_n \tag{B.7}$$

$$y_n = -g_{\varphi n}\varphi_{tip} + g_n \tag{B.8}$$

The following notation is now introduced:

$$l_n v_{Fn} - d_{Fn} = u_{Fn} \tag{B.9}$$

$$l_n v_{Mn} - d_{Mn} = u_{Mn} \tag{B.10}$$

$$\sum_{i=1}^{n} m_i x_i \Omega^2 = a_n \tag{B.11}$$

$$1 + v_{Fn} a_n = A_n \tag{B.12}$$

$$l_n + u_{Fn} a_n = A_n' \tag{B.13}$$

Variables φ_{tip} and y_1 are independent, so Equations B.5 and B.6 lead to:

$$f_{\varphi n+1} = A_n f_{\varphi n} + v_{Fn} G_{\varphi n} + v_{Mn} G_{\varphi n}' \tag{B.14}$$

$$f_{n+1} = A_n f_n + v_{Fn} G_n + v_{Mn} G_n' \tag{B.15}$$

$$g_{\varphi n+1} = g_{\varphi n} + A_n' f_{\varphi n} + u_{Fn} G_{\varphi n} + u_{Mn} G_{\varphi n}' \tag{B.16}$$

$$g_{\varphi n+1} = g_n + A_n' f_n + u_{Fn} G_n + u_{Mn} G_n' \tag{B.17}$$

where:

$$G_{\varphi n} = \sum_{i=1}^{n} m_i \omega^2 g_{\varphi i} \tag{B.18}$$

$$G_n = \sum_{i=1}^{n} m_i \omega^2 g_i \tag{B.19}$$

$$G_{\varphi n}' = \sum_{i=1}^{n-1} \left[l_i G_{\varphi i} + a_i \left(g_{\varphi i+1} - g_{\varphi i} \right) \right] \tag{B.20}$$

$$G_n' = \sum_{i=1}^{n-1} \left[l_i G_i + a_i \left(g_{i+1} - g_i \right) \right] \tag{B.21}$$

These equations can be solved iteratively to obtain the tip bending angle φ_{tip} by assuming no displacement at the root ($y_b = 0$):

$$\varphi_{tip} = \frac{g_b}{g_{\varphi b}} \tag{B.22}$$

Then the natural frequencies are located by using the boundary conditions at the root: no bending ($\beta_b = 0$) for a cantilever beam, or no moment ($M_b = 0$) for an articulated blade, with:

$$\beta_b = f_{\varphi b}\varphi_{tip} - f_b \tag{B.23}$$

$$M_b = G_B' - G_{\varphi b}'\varphi_{tip} \tag{B.24}$$

B.1.2 Coupled Bending-Torsion

If the shear centre and the elastic axis are offset, torsional deformations along the span will appear aside the bending ones. A sectional torsion moment T_n is added, modifying the sectional torsion angle θ_n. The previous notations are used, but in this case, the n-th mass is located at a distance s_n from the shear centre, and the torsional stiffness is J_n. The additional notations are shown in Figure B.3.

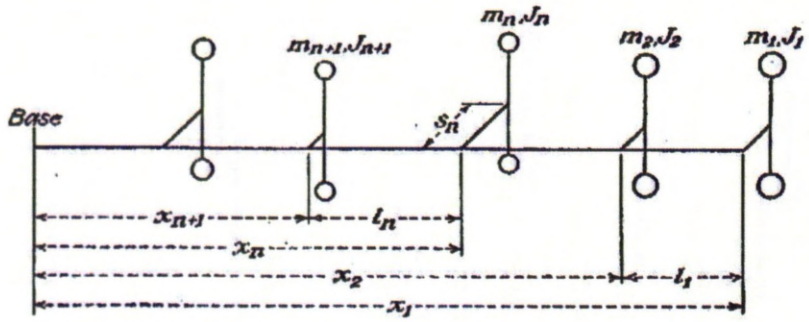

Figure B.3: Notations for a beam with coupled bending and torsional deformations[130].

The same notations are used for the displacement due to an unit bending force or moment on the n-th section, and a torsion angle ν_{Tn} is added for a unit torsion moment at the tip of the n-th section, as shown in Figure B.4.

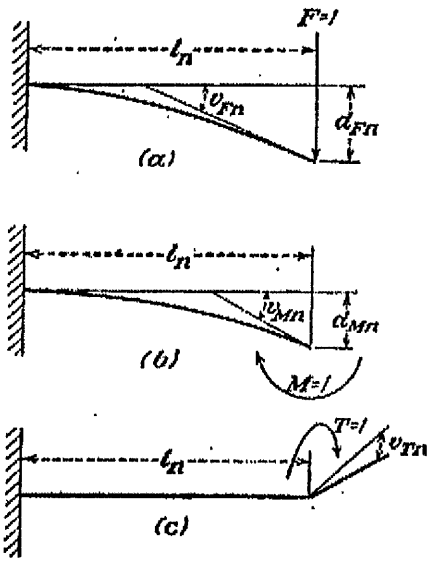

Figure B.4: Notations for the deformation of the n-th section of the beam for an unit bending force, bending moment and torsional moment[130].

The new shear force, bending and torsion moment are expressed as:

$$S_n = \sum_{i=1}^{n} m_i\omega^2 (y_i + s_i\theta_i) - \beta_n \sum_{i=1}^{n} m_i x_i \Omega^2 \tag{B.25}$$

$$M_n = \sum_{i=1}^{n-1} m_i\omega^2 (y_i + s_i\theta_i)(x_i - x_n) - \sum_{i=1}^{n-1} m_i x_i \Omega^2 (y_i + s_i\theta_i - y_n - s_n\theta_n) \tag{B.26}$$

$$T_n = \sum_{i=1}^{n} (m_i s_i y_i + J_i\theta_i)\omega^2 - \beta_n \sum_{i=1}^{n} m_i x_i s_i \Omega^2 \tag{B.27}$$

β is supposedly small, so the centrifugal force is parallel to the straight beam axis. Therefore, the beam deformation can be expressed as:

$$\beta_{n+1} = \beta_n - v_{Fn}S_n - v_{Mn}M_n \tag{B.28}$$

$$y_{n+1} = y_n - l_n\beta_{n+1} - d_{Fn}S_n - d_{Mn}M_n \tag{B.29}$$

$$\theta_{n+1} = \theta_n - v_{Tn} \tag{B.30}$$

S_n, M_n and T_n are replaced using Equations B.25, B.26 and B.27:

$$\beta_{n+1} = \beta_n \left(1 + v_{Fn} \sum_{i=1}^{n} m_i x_i \Omega^2\right) - v_{Fn} \sum_{i=1}^{n} m_i \omega^2 (y_i + s_i \theta_i) - v_{Mn} \sum_{i=1}^{n-1} \left[m_i \omega^2 (y_i + s_i \theta_i)(x_i - x_n) - m_i x_i \Omega^2 (y_i + s_i \theta_i - y_n - s_n \theta_n)\right] \quad \text{(B.31)}$$

$$y_{n+1} = y_n - \beta_n \left[l_n + (l_n v_{Fn} - d_{Fn}) \sum_{i=1}^{n} m_i x_i \Omega^2\right] + (l_n v_{Fn} - d_{Fn}) \sum_{i=1}^{n} m_i \omega^2 (y_i + s_i \theta_i) + (l_n v_{Mn} - d_{Mn}) \sum_{i=1}^{n-1} \left[m_i \omega^2 (y_i + s_i \theta_i)(x_i - x_n) - m_i x_i \Omega^2 (y_i + s_i \theta_i - y_n - s_n \theta_n)\right] \quad \text{(B.32)}$$

$$\theta_{n+1} = \theta_n + \beta_n v_{Tn} \sum_{i=1}^{n} m_i x_i s_i \Omega^2 - v_{Tn} \sum_{i=1}^{n} (m_i s_i y_i + J_i \theta_i) \omega^2 \quad \text{(B.33)}$$

The blade deformation is computed for a tip displacement $y_1 = 1$ and tip bending and torsional angles $\beta_1 = \varphi_{tip}$ and $\theta_1 = \psi_{tip}$. Because of the linear character of the problem, y_n, β_n and θ_n can be projected on the $(\beta_1 = \varphi_{tip}, \theta_1 = \psi_{tip}, y_1 = 1)$ basis:

$$\beta_n = f_{\varphi n} \varphi_{tip} - f_n - f_{\psi n} \psi_{tip} \quad \text{(B.34)}$$

$$y_n = -g_{\varphi n} \varphi_{tip} + g_n + g_{\psi n} \psi_{tip} \quad \text{(B.35)}$$

$$\theta_n = h_{\varphi n} \varphi_{tip} - h_n + h_{\psi n} \psi_{tip} \quad \text{(B.36)}$$

The following notation is now introduced:

$$l_n v_{Fn} - d_{Fn} = u_{Fn} \quad \text{(B.37)}$$

$$l_n v_{Mn} - d_{Mn} = u_{Mn} \quad \text{(B.38)}$$

$$\sum_{i=1}^{n} m_i x_i \Omega^2 = a_n \quad \text{(B.39)}$$

$$1 + v_{Fn} a_n = A_n \quad \text{(B.40)}$$

$$l_n + u_{Fn} a_n = A_n' \quad \text{(B.41)}$$

$$\sum_{i=1}^{n} m_i x_i s_i \Omega^2 = b_n \quad \text{(B.42)}$$

$$v_{Tn} b_n = B_n \quad \text{(B.43)}$$

Variables y_1, φ_{tip} and ψ_{tip} are independent, so Equations B.28, B.29 and B.30 lead to:

$$f_{\varphi n+1} = A_n f_{\varphi n} + v_{Fn} G_{\varphi n} + v_{Mn} G_{\varphi n}' \tag{B.44}$$

$$f_{n+1} = A_n f_n + v_{Fn} G_n + v_{Mn} G_n' \tag{B.45}$$

$$f_{\psi n+1} = A_n f_{\psi n} + v_{Fn} G_{\psi n} + v_{Mn} G_{\psi n}' \tag{B.46}$$

$$g_{\varphi n+1} = g_{\varphi n} + A_n' f_{\varphi n} + u_{Fn} G_{\varphi n} + u_{Mn} G_{\varphi n}' \tag{B.47}$$

$$g_{\varphi n+1} = g_n + A_n' f_n + u_{Fn} G_n + u_{Mn} G_n' \tag{B.48}$$

$$g_{\varphi n+1} = g_{\psi n} + A_n' f_{\psi n} + u_{Fn} G_{\psi n} + u_{Mn} G_{\psi n}' \tag{B.49}$$

$$h_{\varphi n+1} = h_{\varphi n} + B_n f_{\varphi n} + v_{Tn} H_{\varphi n} \tag{B.50}$$

$$h_{\varphi n+1} = h_n + B_n f_n + v_{Tn} H_n \tag{B.51}$$

$$h_{\varphi n+1} = h_{\psi n} + B_n f_{\psi n} + v_{Tn} H_{\psi n} \tag{B.52}$$

where:

$$G_{\varphi n} = \sum_{i=1}^{n} m_i \omega^2 \left(g_{\varphi i} - s_i h_{\varphi i}\right) \tag{B.53}$$

$$G_n = \sum_{i=1}^{n} m_i \omega^2 \left(g_i - s_i h_i\right) \tag{B.54}$$

$$G_{\psi n} = \sum_{i=1}^{n} m_i \omega^2 \left(g_{\psi i} - s_i h_{\psi i}\right) \tag{B.55}$$

$$H_{\varphi n} = \sum_{i=1}^{n} \left(m_i s_i \omega^2 g_{\varphi i} - J_i \omega^2 h_{\varphi i}\right) \tag{B.56}$$

$$H_n = \sum_{i=1}^{n} \left(m_i s_i \omega^2 g_i - J_i \omega^2 h_i\right) \tag{B.57}$$

$$H_{\psi n} = \sum_{i=1}^{n} \left(m_i s_i \omega^2 g_{\psi i} - J_i \omega^2 h_{\psi i}\right) \tag{B.58}$$

$$G_{\varphi n}' = \sum_{i=1}^{n-1} \left[l_i G_{\varphi i} + a_i \left(g_{\varphi i+1} - g_{\varphi i} + s_i h_{\varphi i} - s_{i+1} h_{\varphi i+1}\right)\right] \tag{B.59}$$

$$G_n' = \sum_{i=1}^{n-1} \left[l_i G_i + a_i \left(g_{i+1} - g_i + s_i h_i - s_{i+1} h_{i+1}\right)\right] \tag{B.60}$$

$$G_{\psi n}' = \sum_{i=1}^{n-1} \left[l_i G_{\psi i} + a_i \left(g_{\psi i+1} - g_{\psi i} + s_i h_{\psi i} - s_{i+1} h_{\psi i+1}\right)\right] \tag{B.61}$$

This equations can be solved iteratively, giving the tip bending angle φ_{tip} and the tip torsion angle ψ_{tip}

by forcing no root displacement ($y_b = 0$):

$$\varphi_{tip} = \frac{g_b h_{\psi b} + g_{\psi b} h_b}{g_{\varphi b} h_{\psi b} + g_{\psi b} h_{\varphi b}} \tag{B.62}$$

$$\psi_{tip} = \frac{g_{\varphi b} h_b - g_b h_{\varphi b}}{g_{\varphi b} h_{\psi b} + g_{\psi b} h_{\varphi b}} \tag{B.63}$$

Then the natural frequencies are located by using the boundary conditions at the root: $\beta_b = 0$ for a cantilever beam, or $M_b = 0$ for an articulated blade, with:

$$\beta_b = f_{\varphi b}\varphi_{tip} - f_b - f_{\psi b}\psi_{tip} \tag{B.64}$$

$$M_b = G_B{}' - G_{\varphi b}{}'\varphi_{tip} + G_{\psi b}{}'\psi_{tip} \tag{B.65}$$

B.2 Computation of the Sectional Displacements from the Beam Theory

The beam theory can be used to extract the displacement and angular deformation of a section due to an unit force or moment. For an unit force, d_{Fn} and v_{Fn} become:

$$d_{Fn} = \frac{l_n^3}{3E_y I} \tag{B.66}$$

$$v_{Fn} = \frac{l_n^2}{2E_y I} \tag{B.67}$$

where E_y is the Young's modulus and I is the moment of inertia of the beam cross section. For an unit bending moment, d_{Mn} and v_{Mn} become:

$$d_{Mn} = \frac{l_n^2}{2EI} \tag{B.68}$$

$$v_{Mn} = \frac{l_n}{EI} \tag{B.69}$$

In the case of an unit torsional moment, v_{Tn} becomes:

$$v_{Tn} = \frac{2(1+\nu) l_n}{EI_p} \tag{B.70}$$

where ν is the Poisson's ratio and I_p the torsional moment of inertia.

B.3 Implementation of the Method

B.3.1 Uncoupled Bending

The following programs reads in the blade properties at various sections, and processes these sectional properties to obtain the elementary displacements due to an unit force or moment, and then applies the method to compute the boundary condition value.

```
/*
 * Read in structural info
 */
data = fopen("new_data_with_torsion.txt", "r");
node = 1;
while((fscanf(data,"%lf %lf %lf %lf %lf %lf",&m[node],
              &r[node],&I[node],&Ip[node],&s[node],&J[node]))!=EOF){
   node++; }
nn=node-1;
ne=nn-1;
for(node=1;node<=nn-1;node++) {
   l[node]=r[node]-r[node+1];
   uf[node]=l[node]*l[node]*l[node]/(3.*E*I[node]);
   um[node]=l[node]*l[node]/(2.*E*I[node]);
   vf[node]=um[node];
   vm[node]=l[node]/(E*I[node]);
   vt[node]=2*(1+nu)*l[node]/(E*Ip[node]);

plot = fopen("plot", "w");

/* location of each node */
x[nn]=0;
for(node=nn-1;node>=1;node--) {
   x[node]=x[node+1]+l[node];}
/* mx/100 */
for(node=1;node<=nn;node++) {
   mx[node]=m[node]*x[node];}
/* ms  */
for(node=1;node<=nn;node++) {
   ms[node]=m[node]*s[node];}
/* elastic coefficients uf x 10^6 um x 10^6*/
for(element=1;element<=ne;element++) {
   uf[element]=l[element]*vf[element]-df[element];
   um[element]=l[element]*vm[element]-dm[element];}
/* centrifugal component alpha */
alphasum=0.;
for(node=1;node<=nn;node++) {
   alpha[node]=alphasum+m[node]*r[node]*Omega*Omega;
   alphasum=alpha[node];}
/* A and A'*/
for(element=1;element<=ne;element++) {
   A[element]=1.+vf[element]*alpha[element];
   AA[element]=l[element]+uf[element]*alpha[element];}
/* centrifugal component beta */
betasum=0.;
for(node=1;node<=nn;node++) {
```

```
   beta[node]=betasum+m[node]*r[node]*Omega*Omega*s[node];
   betasum=beta[node];}
/* B */
for(element=1;element<=ne;element++) {
   B[element]=vt[element]*beta[element];}

/* start solving the problem */
while (omega <= stop_omega) {
   omega2=omega*omega;
   /* sweep  tip to root  */
   fphi=1.;
   f=0;
   fpsi=0;
   gphi=0;
   g=1.;
   gpsi=0;
   hphi=0;
   h=0;
   hpsi=1.;
   Gphin=0;
   Gn=0;
   Gpsin=0;
   GGphin=0;
   GGn=0;
   GGpsin=0;
   Hphin=0;
   Hn=0;
   Hpsin=0;
   for(node=1;node<=nn-1;node++) {
      Gphin=Gphin+m[node]*omega2*(gphi-s[node]*hphi);
      Gn   =Gn   +m[node]*omega2*(g   -s[node]*h);
      Gpsin=Gpsin+m[node]*omega2*(gpsi+s[node]*hpsi);

      Hphin=Hphin+omega2*(ms[node]*gphi-J[node]*hphi);
      Hn   =Hn   +omega2*(ms[node]*g   -J[node]*h);
      Hpsin=Hpsin+omega2*(ms[node]*gpsi+J[node]*hpsi);

      dgphi=AA[node]*fphi+uf[node]*Gphin+um[node]*GGphin;
      dg   =AA[node]*f   +uf[node]*Gn   +um[node]*GGn;
      dgpsi=AA[node]*fpsi+uf[node]*Gpsin+um[node]*GGpsin;

      dhphi= B[node]*fphi+vt[node]*Hphin;
      dh=    B[node]*f   +vt[node]*Hn;
      dhpsi=-B[node]*fpsi-vt[node]*Hpsin;

      /* store for plotting */
         gstore[node]=g;
      gphistore[node]=gphi;
      gpsistore[node]=gpsi;

         hstore[node]=h;
      hphistore[node]=hphi;
      hpsistore[node]=hpsi;

      fphi=A[node]*fphi+vf[node]*Gphin+vm[node]*GGphin;
      f   =A[node]*f   +vf[node]*Gn   +vm[node]*GGn;
      fpsi=A[node]*fpsi+vf[node]*Gpsin+vm[node]*GGpsin;
```

```
      GGphin=GGphin+l[node]*Gphin+alpha[node]*(dgphi-s[node]*dhphi);
      GGn   =GGn+l[node]*Gn   +alpha[node]*(dg   -s[node]*dh);
      GGpsin=GGpsin+l[node]*Gpsin+alpha[node]*(dgpsi+s[node]*dhpsi);

      gphi=gphi+dgphi;
      g   =g   +dg;
      gpsi=gpsi+dgpsi;

      hphi=hphi+dhphi;
      h   =h   +dh;
      hpsi=hpsi+dhpsi; }

      gstore[node]=g;
   gphistore[node]=gphi;
   gpsistore[node]=gpsi;

      hstore[node]=h;
   hphistore[node]=hphi;
   hpsistore[node]=hpsi;

   aa=gpsi*h   +g   *hpsi;
   bb=gphi*hpsi+gpsi*hphi;
   cc=gphi*h   -g   *hphi;

   var=-GGphin*aa/bb +GGn +GGpsin*cc/bb;
   fprintf(plot," %e \t %e \n", omega/2/PI, var);

   /* calculate displacement y */
   for(node=1;node<=nn;node++) {
          y[node]=( gstore[node]-gphistore[node]*aa/bb
                    +gpsistore[node]*cc/bb);
      theta[node]=(-hstore[node]+hphistore[node]*aa/bb
                    +hpsistore[node]*cc/bb);
   omega=omega+interval; }
}
close(plot);
```

B.3.2 Coupled Bending-Torsion

A similar implementation was developed for the coupled bending-torsion method:

```
/*
 * Read in structural info
 */
data = fopen("new_data_with_torsion.txt", "r");
node = 1;
while((fscanf(data,"%lf %lf %lf %lf %lf %lf",
      &mF[node],&r[node],&I[node],&Ip[node],&s[node],&J[node]))!=EOF){
   node++; }
nn=node-1;
ne=nn-1;
for(node=1;node<=nn-1;node++) {
   l[node]=r[node]-r[node+1];
   uf[node]=l[node]*l[node]*l[node]/(3.*E*I[node]);
   um[node]=l[node]*l[node]/(2.*E*I[node]);
   vf[node]=um[node];
   vm[node]=l[node]/(E*I[node]);
```

```
   vt[node]=2*(1+nu)*l[node]/(E*Ip[node]);}

plot = fopen("plot", "w");

/* location of each node */
x[nn]=0;
for(node=nn-1;node>=1;node--) {
   x[node]=x[node+1]+l[node];}
/* mx/100 */
for(node=1;node<=nn;node++) {
   mx[node]=m[node]*x[node];}
/* ms  */
for(node=1;node<=nn;node++) {
   ms[node]=m[node]*s[node];}
/* elastic coefficients uf x 10^6 um x 10^6*/
for(element=1;element<=ne;element++) {
   uf[element]=l[element]*vf[element]-df[element];
   um[element]=l[element]*vm[element]-dm[element];}
/* centrifugal component alpha */
alphasum=0.;
for(node=1;node<=nn;node++) {
   alpha[node]=alphasum+m[node]*r[node]*Omega*Omega;
   alphasum=alpha[node];}
/* A and A'*/
for(element=1;element<=ne;element++) {
   A[element]=1.+vf[element]*alpha[element];
   AA[element]=l[element]+uf[element]*alpha[element];}
/* centrifugal component beta */
betasum=0.;
for(node=1;node<=nn;node++) {
   beta[node]=betasum+m[node]*r[node]*Omega*Omega*s[node];
   betasum=beta[node];}
/* B */
for(element=1;element<=ne;element++) {
   B[element]=vt[element]*beta[element];}

/* start solving the problem*/
while (omega <= stop_omega) {
   omega2=omega*omega;
   /* sweep  tip to root  */
   fphi=1./omega2;
   f=0;
   fpsi=0;

   gphi=0;
   g=1./omega2;
   gpsi=0;

   hphi=0;
   h=0;
   hpsi=1./omega2;

   Gphin=0;
   Gn=0;
   Gpsin=0;

   GGphin=0;
   GGn=0;
```

```
GGpsin=0;

Hphin=0;
Hn=0;
Hpsin=0;

for(node=1;node<=nn-1;node++) {
   Gphin=Gphin+m[node]*(gphi-s[node]*hphi);
   Gn   =Gn   +m[node]*(g-s[node]*h);
   Gpsin=Gpsin+m[node]*(gpsi+s[node]*hpsi);

   Hphin=Hphin+ms[node]*gphi-J[node]*hphi;
   Hn   =Hn   +ms[node]*g   -J[node]*h;
   Hpsin=Hpsin+ms[node]*gpsi+J[node]*hpsi;

   dgphi=AA[node]*fphi+uf[node]*Gphin+um[node]*GGphin;
   dg   =AA[node]*f   +uf[node]*Gn   +um[node]*GGn;
   dgpsi=AA[node]*fpsi+uf[node]*Gpsin+um[node]*GGpsin;

   dhphi= B[node]*fphi+vt[node]*Hphin;
   dh=    B[node]*f   +vt[node]*Hn;
   dhpsi=-B[node]*fpsi-vt[node]*Hpsin;

   /* store for plotting */
      gstore[node]=g;
   gphistore[node]=gphi;
   gpsistore[node]=gpsi;

      hstore[node]=h;
   hphistore[node]=hphi;
   hpsistore[node]=hpsi;

   fphi=A[node]*fphi+vf[node]*Gphin+vm[node]*GGphin;
   f   =A[node]*f   +vf[node]*Gn   +vm[node]*GGn;
   fpsi=A[node]*fpsi+vf[node]*Gpsin+vm[node]*GGpsin;

   GGphin=GGphin+l[node]*Gphin+alpha[node]*(dgphi-s[node]*dhphi);
   GGn      =GGn+l[node]*Gn   +alpha[node]*(dg   -s[node]*dh);
   GGpsin=GGpsin+l[node]*Gpsin+alpha[node]*(dgpsi+s[node]*dhpsi);

   gphi=gphi+dgphi;
   g   =g   +dg;
   gpsi=gpsi+dgpsi;

   hphi=hphi+dhphi;
   h   =h   +dh;
   hpsi=hpsi+dhpsi; }

   gstore[node]=g;
gphistore[node]=gphi;
gpsistore[node]=gpsi;

   hstore[node]=h;
hphistore[node]=hphi;
hpsistore[node]=hpsi;

aa=gpsi*h   +g   *hpsi;
bb=gphi*hpsi+gpsi*hphi;
```

```
    cc=gphi*h    -g    *hphi;

    var=-(GGphin*aa/bb +GGn +GGpsin*cc/bb);
    fprintf(plot," %e \t %e \n", omega/2/PI, var);

    /* calculate displacement y */
    for(node=1;node<=nn;node++) {
            y[node]=omega2*( gstore[node]-gphistore[node]*aa/bb
                             +gpsistore[node]*cc/bb);
       theta[node]=omega2*(-hstore[node]+hphistore[node]*aa/bb
                             +hpsistore[node]*cc/bb);}
    omega+=interval; }
}
close(plot);
```

B.4 Demonstration of the Method

The method was implemented and tested, using the examples supplied by Myklestad[130]. Both the uncoupled bending and coupled bending-torsion methods were tested for a rotating cantilever beam.

B.4.1 Uncoupled Bending

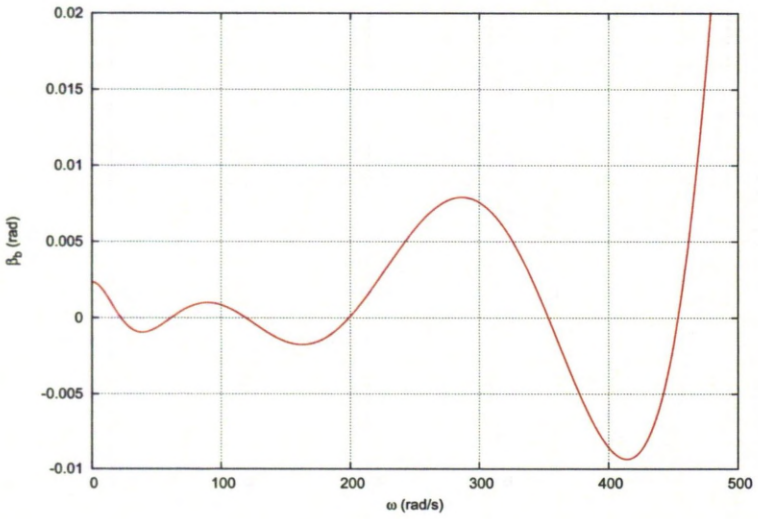

Figure B.5: Evolution of the root bending angle β_b with the frequency

The Myklestad example, described in [130], consists of a cantilever beam rotating at 10rad/s. Figure B.5 shows the variation of the root bending angle β_b with the frequency. The natural frequencies

are found when the tested mode has no bending angle at the root ($\beta_b = 0$), due to the cantilever boundary condition. Six modes were captured between 0 and 500 rad/s. The three first bending modes were extracted and are shown in Figure B.6.

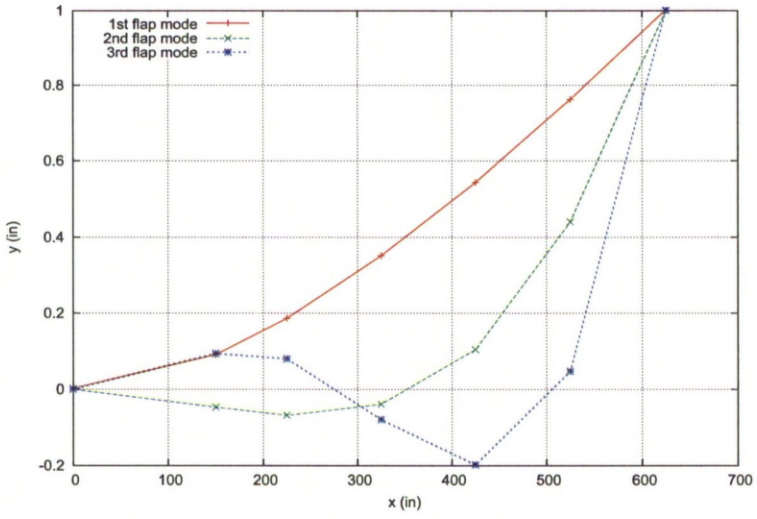

Figure B.6: First three eigenmodes obtained by the bending only approach.

B.4.2 Coupled Bending-Torsion

The Myklestad example described in [130] consists of a beam rotating at 10 rad/s. Figure B.7 shows the variation of the root bending angle β_b with the frequency. The natural frequencies are found when the tested mode has no bending angle at the root ($\beta_b = 0$), due to the cantilever boundary condition. Nine modes were captured between 0 and 500 rad/s. The three first bending modes as well as the first torsional mode were extracted and are shown in Figure B.8.

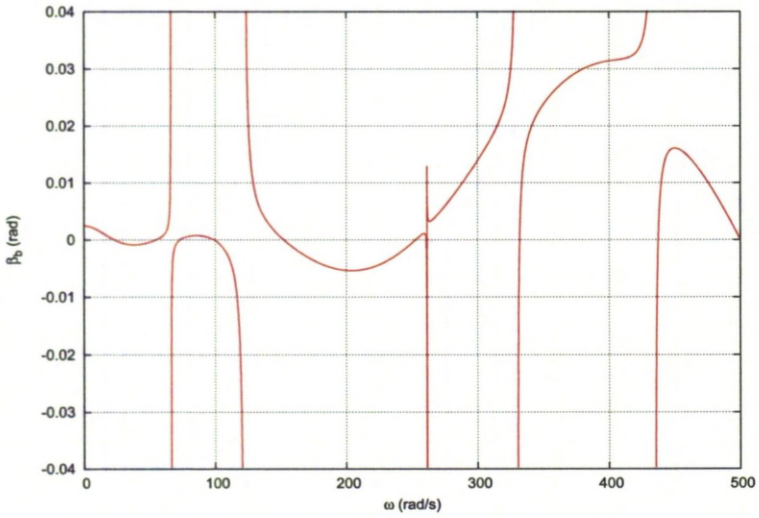

Figure B.7: Evolution of the root bending angle β_b with the frequency

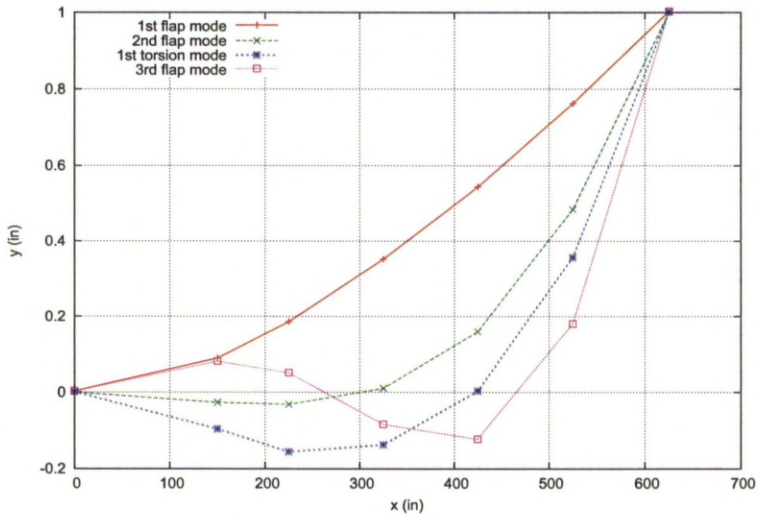

(a) Bending deformation

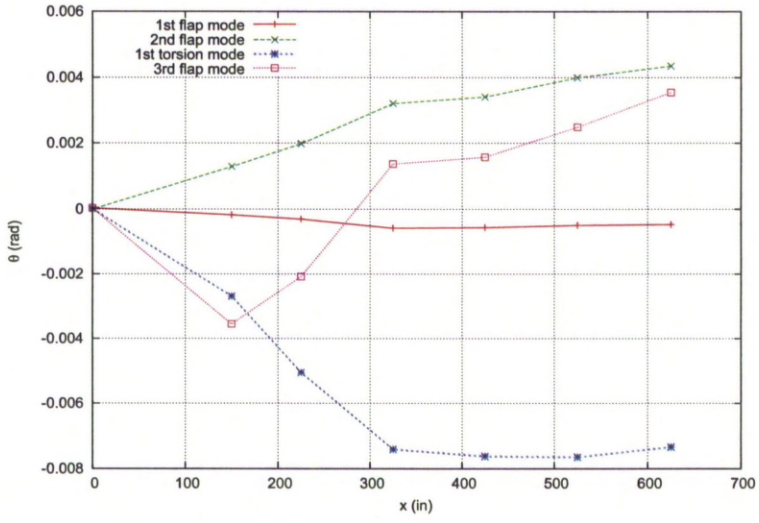

(b) Torsional deformation

Figure B.8: First four eigenmodes obtained by the coupled bending-torsion approach.

Appendix C

Simulation of a Tiltrotor and its Nacelle

The tiltrotor test case was introduced in the TILTAERO European research program. Two blade geometries were experimentally tested in the ONERA wind tunnel of Modane. The first TILTAERO blade was optimised by Beaumier *et al.* [108] to obtain the ADYNE blade. The optimisation process dealt with the hover flight efficiency, while trying to keep the cruise flight efficiency of the TILTAERO blade.

The TILTAERO blade has a non-linear twist distribution. The diameter of the rotor is 7.4 m meters with a thrust weighted mean blade chord of 0.522 m, leading to an aspect-ratio of $\lambda = 6.9$. The aerofoil sections came from the aerofoil database of Agusta and had thicknesses between 7 and 12%. The ADYNE blade has the same length as the TILTAERO one, but the aerofoils were modified using ONERA sections. The quarter-chord line has a double sweep angle: a forward sweep on the main part of the blade and backward sweep at the tip. The twist distribution was also modified, and an anhedral angle of about 15 degrees was added at the tip. The TILTAERO and ADYNE shapes were compared in Section 3.2.

C.1 Simulation without Nacelle

The tiltrotor simulation was for high-speed cruise conditions at Mach $M_\infty = 0.52$. The rotational speed was set to 1100RPM, leading to an advance ratio of $\mu = 1.07$. The Reynolds number was set to $Re_\infty = 2 \times 10^6$ based on the root chord. The collective was trimmed to reach $C_T = 0.13$. The first simulations were carried out with a long spinner running down to the outflow surface, as previously shown in Section 3.2.

Table C.1: Integrated loads from the pressure on the TILTAERO and ADYNE rotors without nacelle. $M_\infty = 0.52$, $Re = 2 \times 10^6$, $C_T = 0.013$ and $\mu = 1.07$.

Rotor	*CTA*	*CCM*	*ETAA*
ADYNE $\theta_0 = 55.6$degrees	0.0915	0.0847	0.5741
TILTAERO $\theta_0 = 56.1$degrees	0.0563	0.0671	0.4457
TILTAERO $\theta_0 = 58.1$degrees	0.1097	0.1011	0.5774
TILTAERO $\theta_0 = 57.6$degrees	0.0979	0.0915	0.5688

The computed integrated loads, using a propeller norm, are compared in Table C.1. Unlike experimental measurements, the efficiency *ETAA* is found to be higher for the ADYNE rotor. However, this difference proved limited, less than 1%.

Iso-surfaces of Q-criterion were used to localise the vortical structures in Figure C.1. An animation of these iso-surfaces around the TILTAERO rotor is also available in the CD attached to the thesis. Strong tip vortices were created by the blades. Another vortex was created where the trailing edge of the blade is becoming sharp. A shoe horse vortex was created at the root of the blade, due to the interaction of the blade root with the spinner. Due to the cylindrical shape of the blade root, a Kármán way is convected down stream close to the spinner.

The pressure coefficient, scaled by the local free-stream velocity V_{loc} was extracted on both blade surfaces, and is shown in Figure C.2. Higher suction was visible at the root on both sides of the ADYNE blade compared to the TILTAERO.

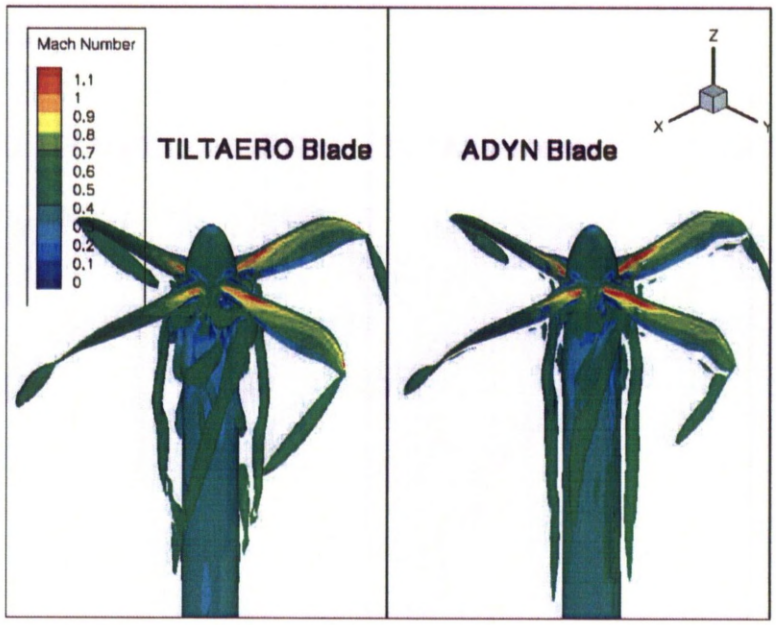

(a) General view

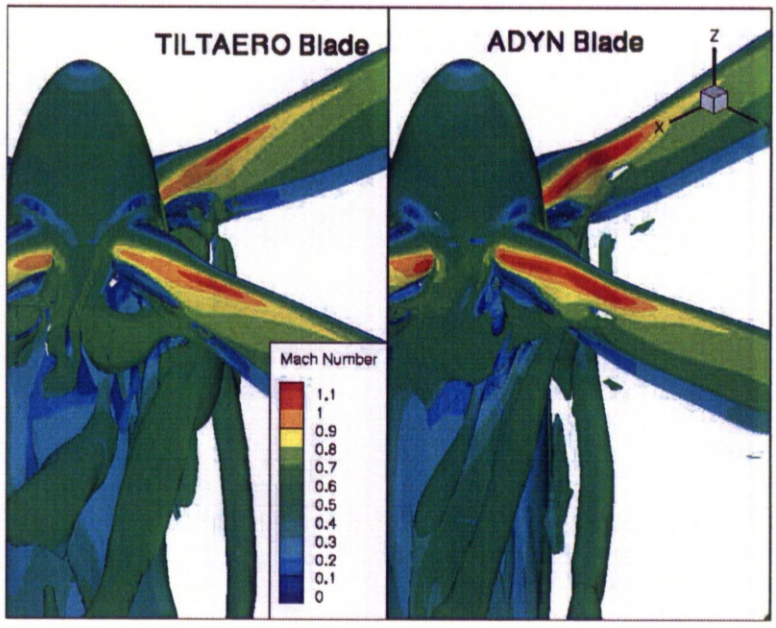

(b) Zoom on the blade root

Figure C.1: Comparison of Q-criterion iso-surfaces at 0.5 around the TILTAERO and ADYN rotors at the same time azimuth. $M_\infty = 0.52$, $Re = 2 \times 10^6$, $C_T = 0.013$ and $\mu = 1.07$.

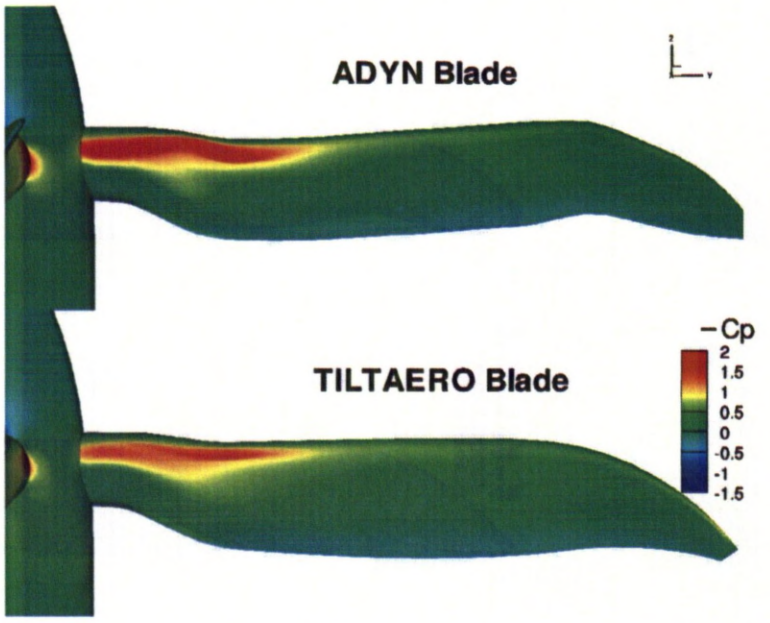

(a) Upper surface

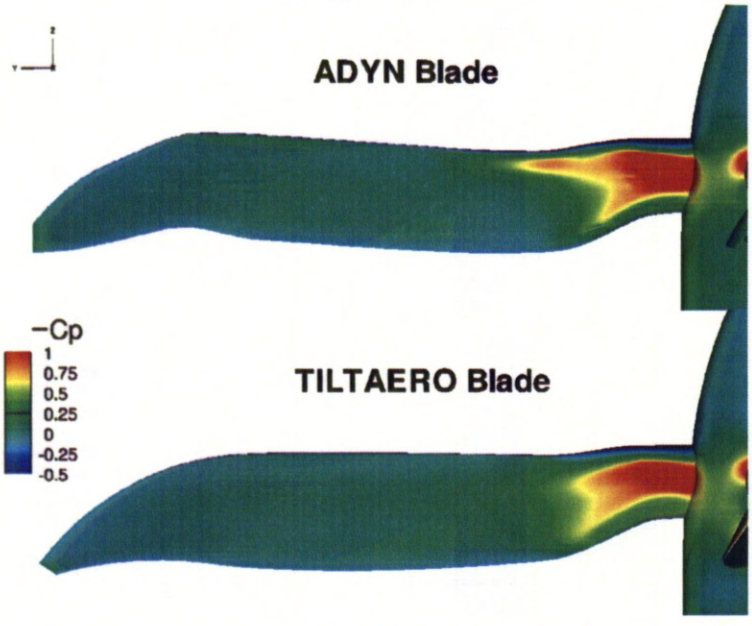

(b) Lower surface

Figure C.2: Comparison of the pressure coefficient on the TILTAERO and ADYNE blade surfaces. $M_\infty = 0.52$, $Re = 2 \times 10^6$, $C_T = 0.013$ and case)$\mu = 1.07$.

C.2 Simulation with Nacelle

The nacelle used in the experiments was bulky and was not a solid of revolution. Therefore, it was decided to investigate its effects. The nacelle geometry was not rotating, leading to the use of sliding planes between the rotor and the nacelle, as described in Section 3.2. Due to the shape of the nacelle, the sliding plane geometry was complex and was located close to the blade trailing edge. The same collective as in the case without nacelle was used.

Table C.2: Thrust and torque coefficients, and Figure of Merit of the two tiltrotor geometries with and without nacelle. $M_\infty = 0.52$, $Re = 2 \times 10^6$, $C_T = 0.013$ and $\mu = 1.07$.

Rotor case		C_T	C_Q	FM
ADYNE	without nacelle	0.0123	0.0210	0.586
	with nacelle	0.0230	0.0308	0.747
TILTAERO	without nacelle	0.0127	0.0232	0.547
	with nacelle	0.0231	0.0334	0.692

The integrated loads on the rotor were extracted and compared to the ones from the simulations without nacelle in Table C.2. The effect of the nacelle on the forces proved important: the thrust and the torque coefficient were increased by a factor of 1.5 to 2 and the Figure of Merit largely increased by the addition of the nacelle, despite using the same collective in both simulations. This brings the question of the mesh quality at the sliding plane: the cell size on each side of the sliding plane might increase by a high factor in either the vertical and horizontal direction, while it is located very close to the blade. A finer mesh around the nacelle may have improved the predictions and lowered the differences.

An animation of iso-surfaces of the λ_2 criterion for both rotors with nacelle is available in the CD attached to the thesis. The influence of the nacelle on the tip vortices was limited, but the nacelle strongly modified the convection of the structures close to the blade root. The structures were only convected along the flattened part of the nacelle.

The sectional loads were extracted. The variation of the sectional loads for both blades is shown in Figures C.3 and C.4. Unlike the case without nacelle, small oscillations in amplitude appear on the whole blade span. The oscillations proved stronger on the ADYNE blade. Heavy load fluctuations at a

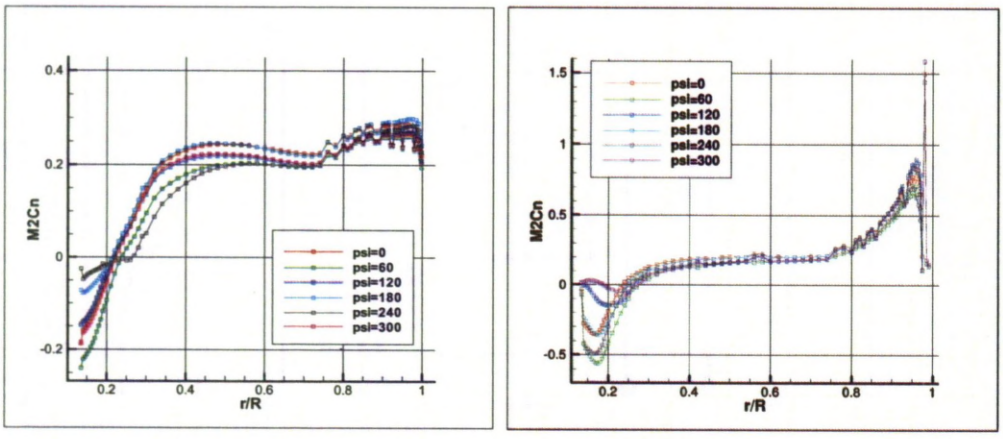

(a) ADYNE blade (b) TILTAERO blade

Figure C.3: Variation of the span-wise distribution of the Mach-scaled normal coefficient every 60 degrees of azimuth when the nacelle was included. $M_\infty = 0.52$, $Re = 2 \times 10^6$, $C_T = 0.013$ and $\mu = 1.07$.

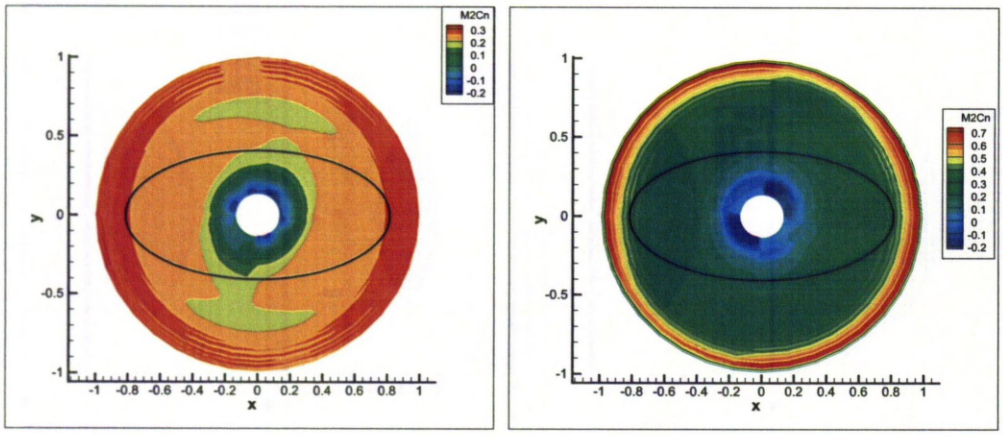

(a) ADYNE blade (b) TILTAERO blade

Figure C.4: Variation of the Mach-scaled normal coefficient with the azimuth when the nacelle was included. $M_\infty = 0.52$, $Re = 2 \times 10^6$, $C_T = 0.013$ and $\mu = 1.07$.

frequency of $2/Rev$ appeared close to the blade root, directly linked to the presence of the nacelle.

Sectional pressure coefficients were extracted and compared to see the effect of the nacelle, as shown in Figure C.5 for the ADYNE blade and Figure C.6 for the TILTAERO blade. Despite the use of the same collective in both simulations, the suction on the blades with nacelle was always much higher than the ones without nacelle, explaining the difference in the integrated coefficients. Higher variations of the blade coefficient at the root of the blade can be noticed for both rotors when the nacelle was added to the simulation.

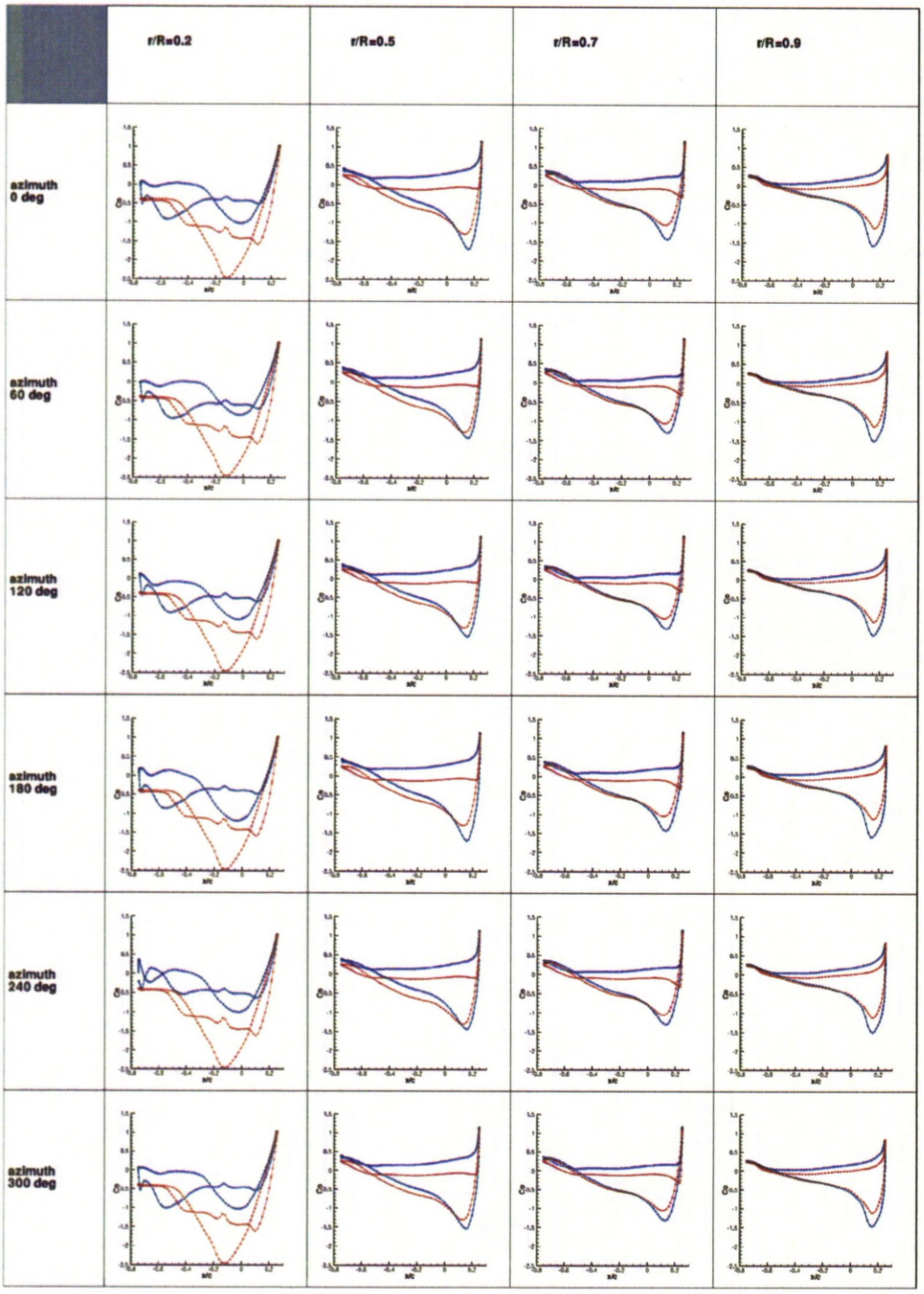

Figure C.5: Evolution of the sectional pressure coefficients along span with the azimuth on the ADYNE blade, without and with nacelle (red and blue, respectively). $M_\infty = 0.52$, $Re = 2 \times 10^6$, $C_T = 0.013$ and $\mu = 1.07$.

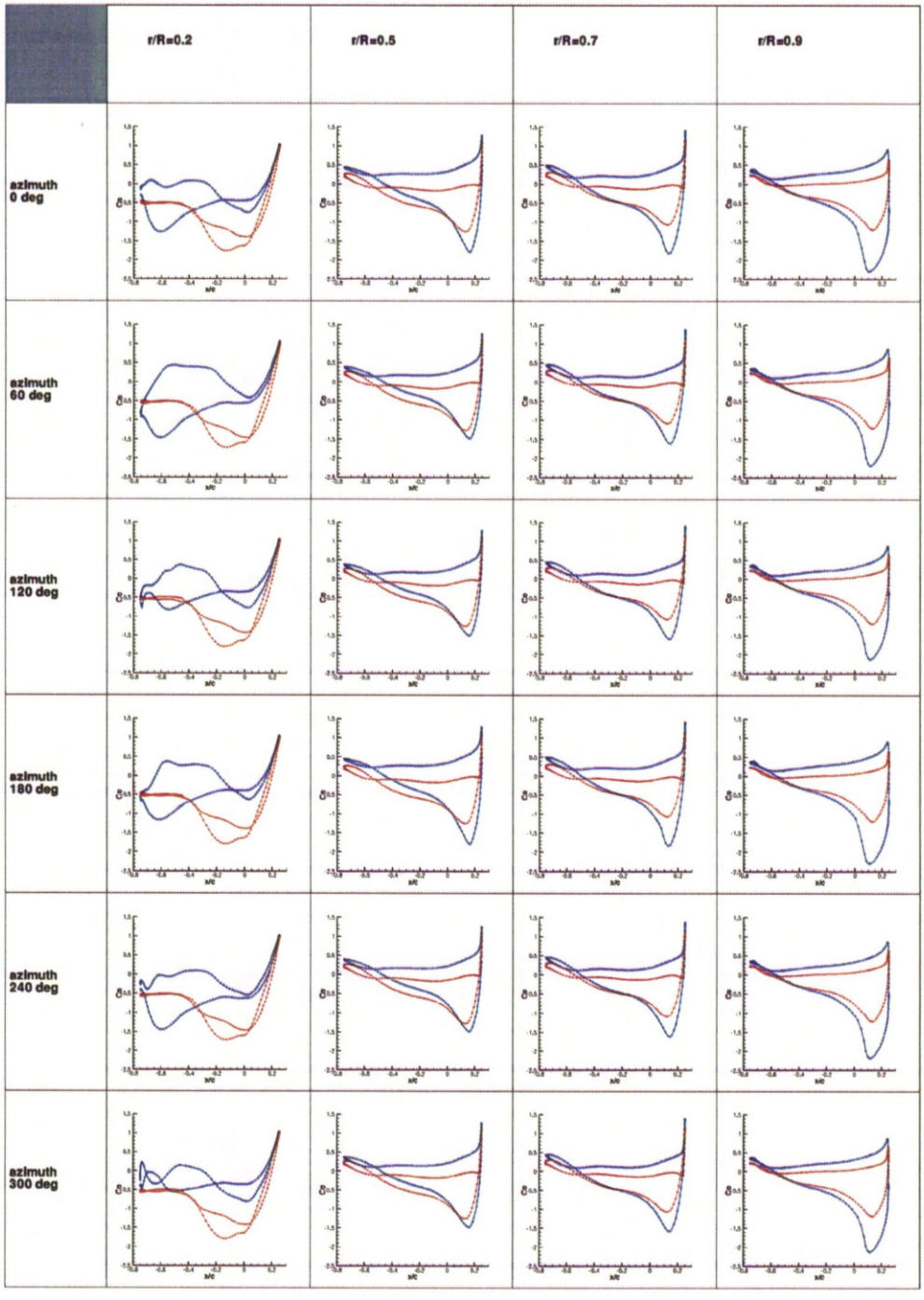

Figure C.6: Evolution of the sectional pressure coefficients along span with the azimuth on the TILTAERO blade, without and with nacelle (red and blue, respectively). $M_\infty = 0.52$, $Re = 2 \times 10^6$, $C_T = 0.013$ and $\mu = 1.07$.